Title
Amorphous and structurally disordered quantum materials

Author
Corbae, Paul

Publication Date
2022

Amorphous and structurally disordered quantum materials

by

Paul Joseph Corbae

A dissertation submitted in partial satisfaction of the

requirements for the degree of

Doctor of Philosophy

in

Engineering- Materials Science and Engineering

in the

Graduate Division

of the

University of California, Berkeley

Committee in charge:

Professor Frances Hellman, Chair
Professor Ramamoorthy Ramesh
Professor Joel Moore

Fall 2022

Amorphous and structurally disordered quantum materials

Abstract

Amorphous and structurally disordered quantum materials

by

Paul Joseph Corbae

Doctor of Philosophy in Engineering- Materials Science and Engineering

University of California, Berkeley

Professor Frances Hellman, Chair

Crystalline symmetries have played a central role in the identification and understanding of quantum materials. The use of symmetry indicators and band representations have enabled a classification scheme for crystalline topological materials, leading to large scale topological materials discovery. Amorphous materials lack long-range order and therefore fall outside of this classification scheme, casting them aside for consideration as topological quantum materials. The work described in this thesis suggests that amorphous systems provide a good materials space to study the topological and quantum properties of the electronic structure. The basis of this observation lies in the fact that amorphous materials have a well defined local environment. Due to this environment, it will be shown that an amorphous material can have dispersive, spin-momentum locked surface states, which can be a consequence of a topological electronic structure. I will also show that by modifying this local environment in a trivial material, a topological phase transition can be achieved with disorder. Nanocrystalline materials also lack long range order, however work shown in this thesis suggests that nanocrystals are detrimental for topological properties since the grain boundaries lack a well defined environment. These systems aren't devoid of interesting properties, the disorder can increase electronic interactions. Given that amorphous materials can host topological states, a method to predict which amorphous materials will be topological with chemical specificity is developed.

In this work an amorphous analog of a well known three-dimensional strong topological insulator, which lies beyond this classification due to the lack of long-range structural order, is investigated and our experimental observations suggest it has topological properties in the solid state. Amorphous Bi_2Se_3 thin films are studied, which show metallic behavior and high bulk resistance. The observed low field magnetoresistance due to weak antilocalization demonstrates a significant number of two-dimensional surface conduction channels. Our angle-resolved photoemission spectroscopy data is consistent with a dispersive two-dimensional surface state that crosses the bulk gap. Spin resolved photoemission spec-

troscopy shows this state has an anti-symmetric spin texture, confirming the existence of spin-momentum locked surface states. These experimental results are discussed in light of a theoretical photoemission spectra obtained with an amorphous tight-binding topological insulator model, contrasting it with an alternative Rashba explanation. The discovery of spin-momentum locked surface states in amorphous materials suggests new ways to characterize amorphous matter. The dispersive, spin-momentum locked states motivates the study of an overlooked subset of amorphous quantum materials outside of current classification schemes, as a novel route to develop promising scalable quantum devices.

Much of our world is comprised of amorphous materials, which lack periodicity and long-range order but retain short-range ordering such as bond-lengths and preferred local environments. Here, it is demonstrated that, even in the absence of long range order, a well-defined real-space length scale is sufficient to produce dispersive band structures. Moreover, for the first time, a repeated Fermi surface structure of duplicated annuli is observed, reminiscent of Brillouin zone-like repetitions. Our simulations using amorphous Hamiltonians reveal that the typical momentum scale where repetitions occur is the inverse average nearest-neighbour distance, the direct fingerprint of the local order of the underlying atomic structure. Many electronic phenomenon rely on momentum-dependence such as momentum pairing or spin-orbit coupling and therefore, under this description, amorphous materials can be reevaluated as a source for generating novel phases.

We investigate using local structural disorder to induce a topologically nontrivial phase in a solid state system. Using first-principles calculations, structural disorder is introduced in the trivial insulator BiTeI and observe the emergence of a topological insulating phase. By modifying the bonding environments, the crystal-field splitting is enhanced, with spin-orbit interactions producing a band inversion in the bulk electronic structure. Analysis of the Wannier charge centers and the surface electronic structure reveals a strong topological insulator with Dirac surface states. Finally, a prescription for inducing topological states from disorder in crystalline materials is proposed. Understanding how local environments produce topological phases is a key step for predicting disordered and amorphous topological materials.

Strong disorder has a crucial effect on the electronic structure in quantum materials by increasing localization, interactions, and modifying the density of states. In this work amorphous $\mathrm{Bi}_x\mathrm{TeI}$ thin films were grown at various compositions and growth temperatures in order to study the effect of structural disorder on electronic properties. By decreasing the growth temperature, the structural disorder is increased and we observe a metal-insulator transition as a function of composition in films grown both at room temperature and 230 K. By tuning the disorder of several compositions with growth temperature, a several magnitudes decrease in the conductivity is observed. The metal-insulator transition is accompanied by a disappearance of weak-antilocalization and increased electron-electron interactions. This work shows that disorder can be used to study strongly correlated topological materials. Disorder is controlled to study the effect of interactions and localization in quantum materials with strong spin-orbit coupling, and by doing so we shed light on how quantum materials can be tuned for spin transport with disorder.

While topological phases of matter are not restricted to crystals, there is no efficient method for predicting which amorphous solids are topological. In order to enable a high-throughput screening of amorphous topological materials, it is desirable to find a computationally efficient indicator of topology, compatible with first-principles calculations. In this work, the structural spillage is introduced, an indicator that predicts the unknown topological phase of an amorphous solid by comparing it to a known reference crystal. To illustrate its potential, it is benchmarked using tight-binding and first-principles calculations of amorphous bismuth models. Using DFT the structural spillage predicts that amorphous bilayer bismuth is topological, and thus a novel topological material. Our work sets the basis to predict topological amorphous solids efficiently, opening up a novel and large material class to high-throughput searches of topological materials.

Contents

List of Figures

List of Tables

Acknowledgments

Firstly, I would like to thank my advisor Professor Frances Hellman for taking me on as a student, teaching me all there is to know about amorphous materials, enabling me to conduct innovative research, and helping me to grow into the scientist I am now. Above all, Frances allowed me to have academic freedom to pursue novel and interesting ideas. I am grateful Frances opened my eyes to the world of amorphous materials.

In addition to the guidance from Frances, I was lucky enough to have the guidance of Dr. Adolfo Grushin and Dr. Sinéad Griffin throughout my Ph.D. Adolfo was critical in the development of my understanding of topology in amorphous materials. Not only did he help conceptualize the main ideas behind my thesis, he has cemented himself as a leader in the field of amorphous topological phases. Similarly, Sinéad has enabled my scientific career to grow and has also provided me with immense mentorship. Sinéad gave me the opportunity to run first-principles calculations and took the time to teach me, this has led to many projects and fruitful results. Sinéad has also helped me in every step of career planning. I am grateful to consider Adolfo and Sinéad friends.

I would like to thank Professor Lu Li at the University of Michigan - Ann Arbor for introducing me to advanced Physics in the classroom and well as in his lab.

To Dr. Samuel Ciocys, you are truly one of the most creative people I have met and the only person I know crazy enough to have accepted doing ARPES on an amorphous material. My Ph.D. work would be much different had I not met you.

I would like to thank the entire Hellman lab past and present. Dr. Manel Molina Ruiz has been critical in my development as an experimentalist and film grower. I would like to thank Dr. Daniel Varjas, Daniel Munoz Segovia, and Nicolai Taufertshöfer for being influential in my studies. I would like to thank Professor Alessandra Lanzara for working with me and helping to elucidate the electronic structure in amorphous materials as well as serve on my qualification committee. I would like to thank Professor Joel Moore for discussions and insight into topological materials as well as serving on my Dissertation and qualification committee. I would like to thank Professor Ramamoorthy Ramesh for serving on my Qualification and Dissertation Committee. Professor Mary Scott, Ellis Kennedy, and Steven Zeltmann for working with me and helping me to ”see” amorphous structures with my own eyes.

To Fiona, you are the best and have supported in every way possible. I am grateful to my friends Dylan, Jack, Dr. Eric Parsonnet, Dr. Abel Fernandez, and Michael for having the most fun together while I was in my Ph.D. Especially, Eric and Abel who helped making my Ph.D. more fun talking at lunch and commiserating through the hard times, I am forever grateful.

Finally, I would like to thank my family for supporting me the entire way. To my mom who always let me know everything would be fine. To my dad for inspiring me to be in academia and for his helpful guidance. To Bethany for always being the smartest child. To Elena for thinking physics is also cool and inspiring me by making your own path in the field.

Chapter 1

Background and Motivation

Topological materials have been an exciting field of research over the past two decades. They are robust to disorder and have quantize physical responses. Recently, a classification scheme has discovered that around 30% of the materials around us could have topological bands [1, 2, 3]. However an even larger percentage of the materials around us are amorphous. Topological properties have not been explored in amorphous systems until recently due to the lack of translational invariance. In the field of topological materials it has been shown theoretically that topological properties exist in the amorphous phase. In this thesis, I present an experimental observation of spin-momentum locked surface states providing evidence of topological states in an amorphous solid state system. Amorphous materials have many benefits for technology and topological materials are key for next generation technology. Therefore the intersection of these two fields is very exciting.

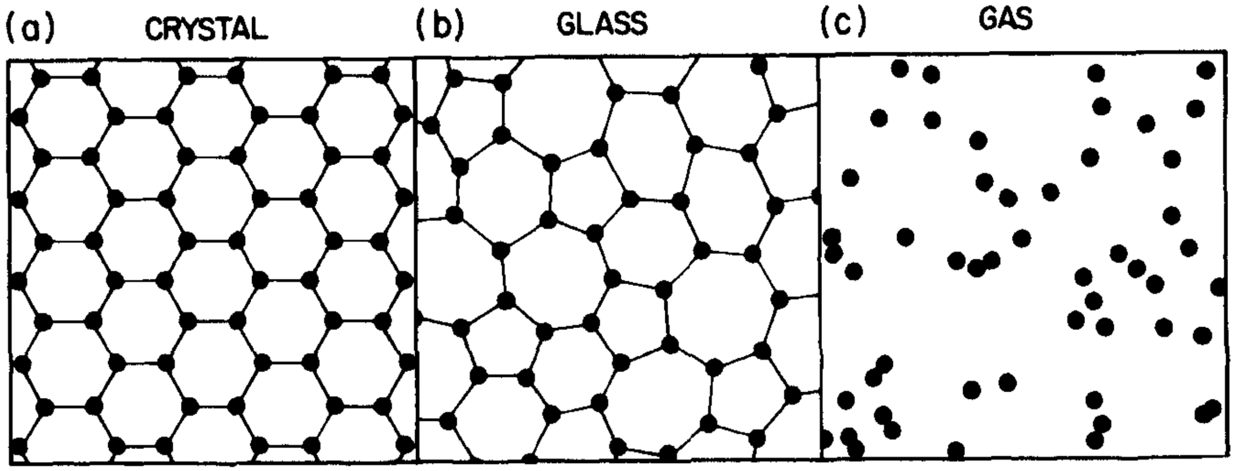

Figure 1.1: Cartoon version of different atomic structural arrangements. (a) A crystalline structure. (b) An amorphous solid. (c) A random distribution such as a gas. Taken from [4]

Material	Crystal T_c	Amorphous T_c
Bi	10^{-4} K	6 K
Ba	0.026 K	9.9 K
Mo	0.9 K	9 K

Table 1.1: T_c in elemental crystals and their amorphous counterparts

1.1 Amorphous Materials

Amorphous materials make up a large portion of the tangible world around us from window glass to golf clubs to solar cells. However, due to the lack of translational symmetry amorphous materials do not benefit from the full machinery that has been developed for solid state physics. For this reason, they are typically not considered when discussing quantum materials. Amorphous materials are not expected to have any electronic states with well-defined momenta, but are nonetheless known to support metallic conduction and superconductivity. Table 1.1 shows three elemental superconductors Bi, Ba, and Ge that have higher critical temperatures for the superconducting state (T_c) in the amorphous phase than the crystalline phase. This is due to an increased density of states at Fermi level and increased electron phonon coupling [5].

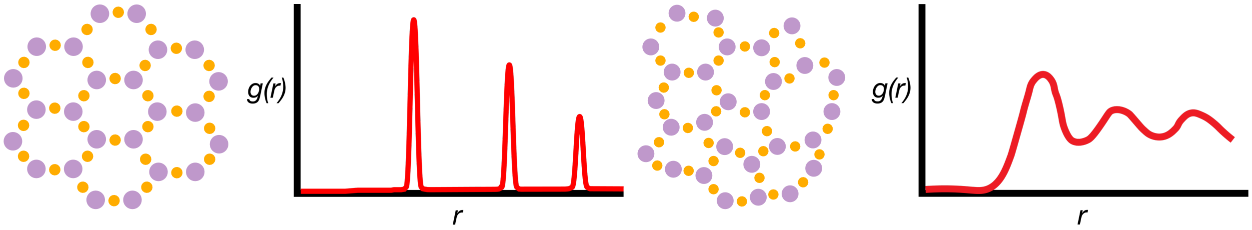

Figure 1.2: Cartoon version of different atomic structural arrangements and the resultant radial distribution function.

Structure

It is important to understand the structure of amorphous materials before discussing the relevant features of the electronic structure. Amorphous materials are materials where long-range order is absent and the equilibrium positions of the atoms are not translationally periodic as in a crystal, Fig. 1.1. However, there exists short-range order (SRO) (well defined nearest neighbor) and even medium-range order (MRO) (second and third nearest neighbor). The short range order manifests itself as preferred bond lengths and angles as well as a well defined coordination environment (well defined number of nearest neighbors). This is a result of the electronic configuration of the atoms involved in bonding. For example, covalent bonding typically leads to a lower coordination number z. The nature of chemical bonding and the electronic states is implicit in producing short range order. One way to characterize the structure of the amorphous solid is by considering the radial distribution function (rdf). The SRO manifests itself as peaks in the radial distribution function which is the probability that an atom will be found at a distance r from another atom. Picking an atom as the origin we can consider its nearest and next nearest neighbors. These well defined coordination environments and distances lead to the peaks in $g(r)$, Fig. 1.2. For a crystal with well defined long range order the rdf is a sum of delta functions which correspond to well defined coordination shells. For amorphous materials where nearest and next nearest (and even third) neighbors are defined, the rdf shows peaks corresponding to these coordination shells but broadened. The structure of amorphous solids is picked up in diffraction where the well defined interatomic spacing from the short-range order leads to a larger diffraction amplitude at certain angles leading to diffuse rings in the diffraction pattern. Additionally, medium range order exists further away from short range order from weaker but longer range interactions. This is the next-level structural organization beyond the SRO, for example, how the local structural 'units' are connected and arranged to fill three-dimensional (3D) space. Operationally, we define medium-range order as physical structure beyond the length scale which produces peaks in g(r), but below the length scale which yields Bragg peaks in the structure factor. In summary, the local environment in amorphous and crystalline solids are very similar and the structural difference lies in the lack of long range order. Nanocrystalline systems also do not have long range order, but are quite different from amorphous systems. There is no continuous pathway from the crystalline phase to amorphous phase but instead a discontinuous phase transformation associated with the nucleation of crystalline domains. The presence of grain boundaries and the atomic disorder associated with them makes nanocrystalline systems inherently more disordered than amorphous films with lack long range order but retain well defined atomic environments.

Electronic structure

We lose the ability to write the wavefunctions as Bloch states, which are periodic in the lattice, due to the lack of translational invariance. However this does not mean amorphous materials are devoid of interesting and important electronic properties. The electronic density of states $N(E)$ is equally valid for crystalline and non-crystalline materials. $N(E)$ has been shown through experiment to not drastically vary between crystalline and non-crystalline systems. However, disorder produces band tails which are localized states at the top of the valence band or bottom of the conduction band. The localized states are separated from the extended states at an energy called the mobility edge. Amorphous Germanium is an example of the primacy of the short range order in the electronic structure of an amorphous solid. In this system the local ordering resulting from chemical bonding is similar which produces similar $N(E)$ seen in Fig. 1.3. The similarity in the density of states results in similar experimental measured quantities such as the reflectivity. This is a result of the overall

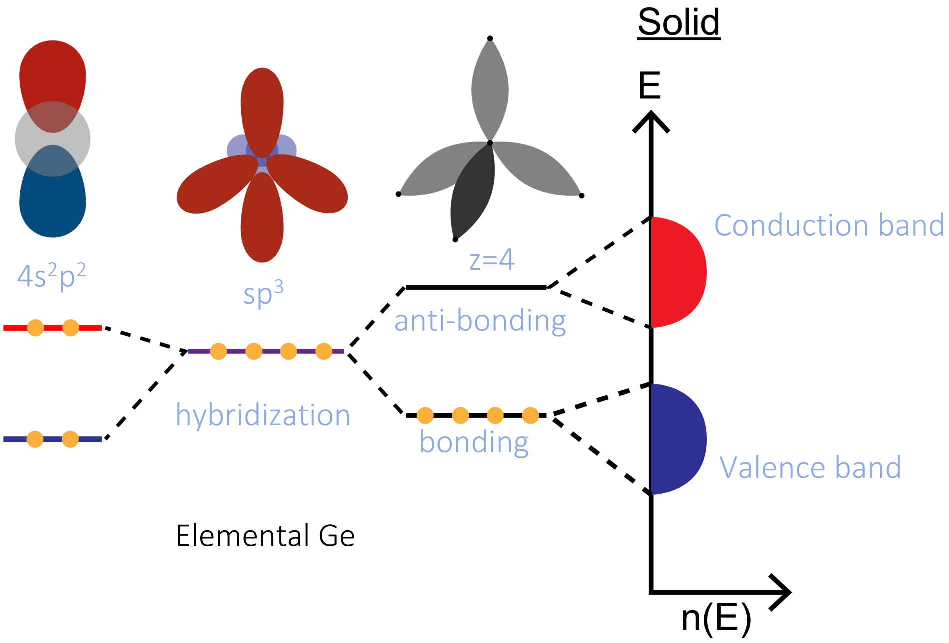

Figure 1.3: Cartoon of how local ordering affects the electronic structure in elemental Germanium.

density of states and electronic structure arises from short range order. Long-range disorder produces states in the gap but the overall features remain the same. The well-defined local environment and subsequent electronic structure in amorphous systems has important implication on the topological properties. The local environment (similar crystal field environment) determines the coarse properties of the density of states such as spectral gaps (allowing for observation of band inversions), while long-range correlations or periodicity, determine the finer details. If the local environment produces an electronic structure with a band inversion then this system cant be adiabatically connected to an atomic insulator. Also in non-crystalline materials if the Fermi wavevector k_F is large (since the mean free path is $\sim 1\AA$) such that the Ioffe-Regel limit is $k_F l >> 1$, then the magnitude of the wavevector $\mathbf{k}$ is still a good quantum number (due to its relationship to energy) and a Fermi surface can still be defined for metallic systems. The Fermi surface will be spherical because of the isotropic nature of the amorphous system. If the is a deviation from free electron form then this concept breaks down. This will be important for how we interpret our photoemission data.

The reasons for use of amorphous materials in the field of quantum materials and for use in technology is that they can be grown under less stringent conditions than single crystals require. Secondly, they can be grown in a range of compositions rather than an exact composition that a crystalline compound requires for a given crystal structure.

Anderson Localization

Anderson's famous discovery states that electrons traveling in an amorphous solid will become localized due to the random potential they see from the random atomic positions. The electrons will become localized around a well and the wavefunction decays exponentially with r. This occurs when the ratio of the disorder potential and the bandwidth V_0/B approaches a critical value. The wavefunctions of the localized states take the form:

$$\psi = \sum A_n \phi(\mathbf{r} - \mathbf{R}) e^{-\alpha r}. \tag{1.1}$$

Anderson showed that disorder introduces localization which has important implications on the electronic structure [6]. A random potential will produce localized states in the bandtail, Fig. 1.4. There is a critical energy that separates the localized from extended states E_C called the 'mobility edge' where the conductivity $\sigma(T \to 0) = 0$ below E_C. If the Fermi energy lies blow the mobility edge then there are two forms of conduction above $T = 0$: 1) the electrons have thermally activated hopping from one site to another called Variable Range Hopping (VRH) or 2) the electrons are thermally excited above the mobility edge. VRH can be nearest neighbor hopping or to distances much larger than nearest neighbor and depends on the overlap of the wavefunctions. The conductivity in the VRH regime takes the form [7]:

$$\sigma = Ae^{-(T_0/T)^{1/4}}. \tag{1.2}$$

Structural disorder in electronic systems is typically accompanied by electronic interactions (structural disorder in bosonic systems is not accompanied by interactions and is the only place that Anderson localization is observed in the original sense). Coulomb interactions create a gap in $N(E)$ and causes the problem to require a many body approach, i.e. quasiparticle description does not work. In the case of interactions Efros and Shklovskii showed the conductivity in the VRH regime takes the form [8]:

$$\sigma = Ae^{-(T_0/T)^{1/2}}. \tag{1.3}$$

.

1.2 Topological Materials

Topology enters condensed matter and specifically insulators since we can separate all gapped Hamiltonian's into different topological classes, only are they in the same class if they can be smoothly connected without closing the bulk gap [9]. To provide a reference, insulators are labeled trivial if their Hamiltonians can be smoothly brought back to the atomic limit, which corresponds to a bandstructure that admits localized atomic orbitals when the separation is taken to infinity. Therefore, topological materials present an obstruction to the atomic limit. Topological phases are defined such that the wavefunctions cannot be described by purely localized orbitals, or there is an obstruction to create localized Wannier functions.

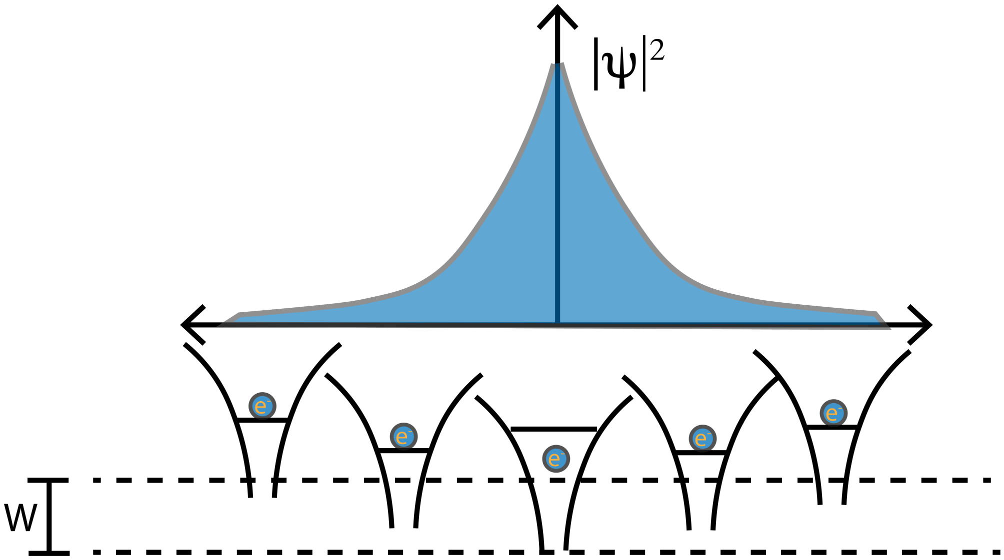

Figure 1.4: Cartoon of Anderson Localization. Anderson modeled the disorder as random well depths which localize the electron wavefunction around a well.

Since the information about these phases is non-local and spread amongst the entire system, their physical properties are robust to local perturbations (as long as they obey symmetry), making them some of the most robust phases of matter.

Wannier Functions

In solid state physics we traditionally deal with $E_n(\mathbf{k})$ dispersion's for a band in the Brillouin zone resulting from the Bloch functions $\psi_{n\mathbf{k}}$. The Fourier transformed partner to the Bloch functions are known as Wannier functions and live in three dimensional real space. They are defined as:

$$|w_{n\mathbf{R}}\rangle = \frac{V_{cell}}{2\pi^3}\int_{BZ} e^{-i\mathbf{k}\cdot\mathbf{R}}\,|\psi_{n\mathbf{k}}\rangle\,d^3k, \tag{1.4}$$

$$|\psi_{n\mathbf{k}}\rangle = \sum_{\mathbf{R}} e^{i\mathbf{k}\cdot\mathbf{R}}\,|w_{n\mathbf{R}}\rangle\,. \tag{1.5}$$

The Wannier functions can be thought of as the Fourier components of the Bloch functions expanded in a plane wave basis set. We assume the Bloch functions are smooth functions of $\psi_{n\mathbf{k}}(\mathbf{r})$; this means the Wannier functions are localized in real space since the Fourier components will be large for a few $\mathbf{R}$ near the origin ($w_{n\mathbf{R}}(\mathbf{r})$ decays rapidly with $|\mathbf{r}-\mathbf{R}|$ for a given $\mathbf{R}$). Since the Fourier transform above is a unitary transformation, the Bloch and Wannier states provide two different basis for the same manifold of states of an electron band. There are four properties of Wannier functions worth mentioning:

1. They are localized. $w_{n\mathbf{R}}(\mathbf{r}) \to 0$ with increasing $|\mathbf{r} - \mathbf{R}|$ for a given $\mathbf{R}$
2. $w_{n\mathbf{R}}(\mathbf{r}) = w_{n\mathbf{0}}(\mathbf{r} - \mathbf{R})$
3. $\langle w_{n\mathbf{R}'} | w_{n\mathbf{R}} \rangle = \delta_{\mathbf{R}'\mathbf{R}}$
4. The Wannier functions span the same subspace of the Hilbert space as the Bloch functions from which they were constructed. The projection operator is:

$$P_n = \frac{V_{cell}}{2\pi^3} \int_{BZ} |\psi_{n\mathbf{k}}\rangle \langle \psi_{n\mathbf{k}}| \, d^3k = \sum_{\mathbf{R}} |w_{n\mathbf{R}}\rangle \langle w_{n\mathbf{R}}| \,. \tag{1.6}$$

The Hamiltonian matrix elements being $\langle w_{n\mathbf{0}}|H|w_{n\mathbf{R}}\rangle = E_{n\mathbf{R}}$ means that Wannier functions reproduce the tight-binding representation of $E_n(\mathbf{k})$. The position operator $\mathbf{r}$ matrix elements are:

$$\langle w_{n\mathbf{0}}|\mathbf{r}|w_{n\mathbf{R}}\rangle = e^{-i\mathbf{k}\cdot\mathbf{R}} \langle u_{n\mathbf{k}}|i\nabla_{\mathbf{k}} u_{n\mathbf{k}}\rangle \, d^3k, \tag{1.7}$$

this will be important when discussing Berry phases. Another important quantity is the Wannier center of charge $\overline{\mathbf{r}}_n = \langle w_{n\mathbf{0}}|\mathbf{r}|w_{n\mathbf{0}}\rangle$.

Hybrid Wannier functions (HWF) are very useful to calculate topological invariants along planes in the Brillouin zone. HWF's are obtained by doing the Fourier transform in only one direction:

$$|h_{n,k_1k_2l_3}\rangle = \frac{1}{2\pi} \int_0^{2\pi} e^{-il_3k_3} |\psi_{nk_1k_2k_3}\rangle \, dk \tag{1.8}$$

$$|\psi_{nk_1k_2k_3}\rangle = \sum_{l_3} e^{ik_3l_3} |h_{n,k_1k_2l_3}\rangle \,. \tag{1.9}$$

This means the states are localized in one direction and extended in the others.

Berry Phases

The notion of a geometrical phase is central to defining topological invariants. The Berry phase is such a phase is defined as the global phase evolution of a complex vector as it is carried around a closed loop in a complex vector space. The vectors are taken to be the wavefunctions of the quantum system. The Berry phase is defined as

$$\phi = -\mathrm{Im}\ln \left[\langle u_0|u_1\rangle \langle u_1|u_2\rangle \ldots \langle u_{N-1}|u_N\rangle\right] \tag{1.10}$$

where the $|u_i\rangle$ are the N representative vectors around the loop and $|u\rangle_0 = |u_N\rangle$. The Berry phase can be described in terms of the parallel transport gauge. This is where we choose the representative vectors in such a way to have a positive, real inner product. This means $\mathrm{Im}\ln\left[\langle u_i|u_{i+1}\rangle\right] = 0$. On a loop $|u_0\rangle$ and $|u_N\rangle$ describe the same state but the phase will be different because $|u_N\rangle$ was chosen to be positive and real with $|u_{N-1}\rangle$. This phase difference is exactly the Berry phase and seen in Fig. 1.5. Since $|u_N\rangle$ and $|u_0\rangle$ only differ by a phase:

$$\phi = -\mathrm{Im}\ln\left[\langle u_0|u_1\rangle \langle u_1|u_2\rangle \ldots \langle u_{N-1}|u_N\rangle \langle u_N|u_0\rangle\right] \tag{1.11}$$

so that the Berry phase becomes:

$$\phi = -\mathrm{Im}\ln\left[\langle u_N|u_0\rangle\right] \tag{1.12}$$

because all of the inner products were chosen to be real and positive. In the continuum the Berry phase is written as $\phi = \oint \langle u_\lambda|i\partial_\lambda u_\lambda\rangle\, d\lambda$ where λ is some parameter of the quantum system that varies on the path [10]. The Berry connection

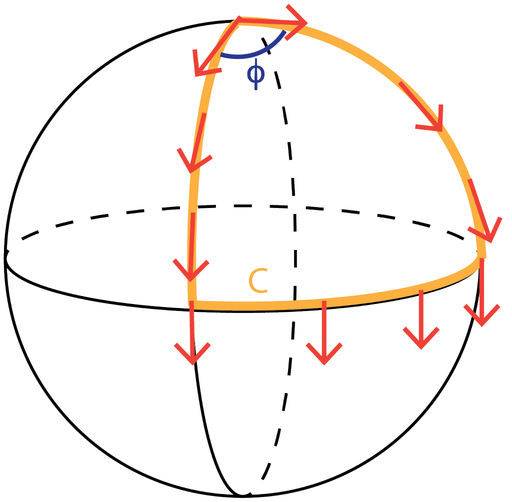

Figure 1.5: Parallel Transport. The vector (red) picks up a geometric phase as it is taken around a closed path C. This phase is the Berry phase.

$$A(\lambda) = \langle u_\lambda|i\partial_\lambda u_\lambda\rangle \tag{1.13}$$

is not gauge invariant. This is seen by performing a gauge transformation $|\overline{u}_\lambda\rangle = e^{-i\beta(\lambda)}\,|u_\lambda\rangle$, which makes the Berry connection

$$\overline{A}(\lambda) = \langle u_\lambda|i\partial_\lambda u_\lambda\rangle\, d\lambda + d\beta/d\lambda \tag{1.14}$$

. This leads to the Berry phase being $\overline{\phi} = \phi + 2\pi m$ meaning the Berry phase is gauge invariant modulo $2\pi m$ with m being an integer, therefore its gauge invariant when thought of as a phase angle. The fact that the Berry phase is gauge invariant means it is physical and can have direct implications via interference effects. The possible gauge transformations $(e^{-i\beta})$ that lead to different integers m can be classified topologically and the integer m is called the winding number. It tells how many times $e^{-i\beta}$ winds around the unit circle as λ varies around the closed path. The Berry phase can also be derived by inserting $|\psi_n(t)\rangle$ into the time dependent Schrodinger equation with a geometric phase included.

The Berry curvature is defined as the the Berry phase per unit area in the parameter space $(\lambda_x, \lambda_y, \lambda_z)$ and can be thought of as a magnetic field. It is defined as;

$$\Omega_{\mu\nu} = \partial_\mu A_\nu - \partial_\nu A_\mu \tag{1.15}$$

. If the parameter space is three dimensional then in vector form (related to the tensor via the Levi-Civita tensor) it is:

$$\boldsymbol{\Omega}_n(\boldsymbol{\lambda}) = \nabla_\lambda \times A_n(\boldsymbol{\lambda}) \tag{1.16}$$

. This now enables the use of stokes theorem to compute the Berry phase

$$\phi = \int_S \boldsymbol{\Omega} \cdot d\mathbf{S} = \oint_P \mathbf{A} \cdot d\boldsymbol{\lambda} \tag{1.17}$$

where dS is the differential surface element. The Chern theorem states that the integral of the Berry curvature over a 2D closed manifold is $2\pi C$ for some integer C. C, also known and the Chern number, can be thought of as a topological invariant for the manifold of states $|u\rangle_\lambda$ defined on the surface S. On a torus, the Chern number can be viewed as the winding of the Berry phase.

Applying all of this to electrons in a solid, we can use the wavevector $\mathbf{k}$ as the parameter which we vary our states. The Berry phase, connection, curvature, and Chern number are now defined as follows:

$$\phi = \oint \mathbf{A}_n(\mathbf{k}) \cdot d\mathbf{k} \tag{1.18}$$

$$\mathbf{A}_{n\mu}(\mathbf{k}) = \langle u_{n\mathbf{k}}(\mathbf{k}) | i\partial_\mu u_{n\mathbf{k}} \rangle \tag{1.19}$$

$$\boldsymbol{\Omega}_n(\mathbf{k}) = \nabla_k \times \mathbf{A}_n(\mathbf{k}) \tag{1.20}$$

$$C_n = \frac{1}{2\pi} \int_{BZ} \boldsymbol{\Omega}_n d^2\mathbf{k} \tag{1.21}$$

. If the system has inversion symmetry $\boldsymbol{\Omega}_n(\mathbf{k}) = \boldsymbol{\Omega}_n(-\mathbf{k})$. If the system has time-reversal symmetry $\boldsymbol{\Omega}_n(\mathbf{k}) = -\boldsymbol{\Omega}_n(-\mathbf{k})$. If both time-reversal and inversion are present then $\boldsymbol{\Omega}_n(\mathbf{k}) = 0$. In the presence of spin-orbit coupling the Berry quantities are computed using spinor wavefunctions. Recall that the Wannier charge center is defined as

$$\bar{\mathbf{r}}_n = \frac{V_{cell}}{2\pi^3} \int_{BZ} \langle u_{n\mathbf{k}} | i\nabla_{\mathbf{k}} u_{n\mathbf{k}} \rangle \, d^3k = \frac{V_{cell}}{2\pi^3} \int_{BZ} \mathbf{A}_n(\mathbf{k}) d^3k \tag{1.22}$$

which means that the Wannier charge centers are related to the Berry phase and in some cases are equal (in addition to some scaling factors)! This will become useful for calculating topological invariants.

Topological invariants

A topological invariant is a quantized property that cannot be changed without changing the topological phase. An example of this would be the genus for closed, orientable two-dimensional surfaces. In real materials, we need an object on which to define topological properties. This ends up being a set of bands, typically the occupied set of bands $\{|u_{n,\mathbf{k}}\rangle\}_{\in \text{occupied}}$. This set of states span a vector space $V_{\mathbf{k}}$ and the smoothness of this vector space can be broken if the order of the states changes. To avoid this, topological properties are defined on a isolated set of bands separated by an energy gap. Another constraint for topological insulators imposed is that when smoothly changing the Hamiltonian the band gap must not close to stay in the same topological class. The boundary consists of points in space between the topological phase and vacuum which is connected to the atomic limit (trivial). To smoothly change the Hamiltonian between these two topologically distinct phases the band gap needs to close, making the boundary states gapless. This argument only depends on bulk band gaps and symmetries which makes these boundary states insensitive to local perturbations.

The Chern number can be calculated by tracking the Berry phase along lines of constant k in the Brillouin zone. This is done constructing the Wilson loop which is matrix that maps the states are some starting $\mathbf{k}_i$ onto their images along the $\mathbf{k}$ line in the Brillouin zone

$$W(C) = M^{\mathbf{k}_0,\mathbf{k}_1}...M^{\mathbf{k}_{N-1},\mathbf{k}_N} \tag{1.23}$$

$$M^{\mathbf{k}_i,\mathbf{k}_j}_{m,n} = \langle u_{m,\mathbf{k}_i}|u_{n,\mathbf{k}_j}\rangle \tag{1.24}$$

. The Berry phase is computed by taking the sum of the argument of the Wilson loop eigenvalues ($\phi = \sum \arg\lambda_i$). As we saw earlier the Berry phase is also related to the Wannier functions. Therefore the Chern number can be calculated by calculated using hybrid Wannier functions ($\phi = \frac{2\pi}{a}\sum \overline{x}_n$). This approach provides more provides more intuition since it is understood that as the electrons move through Brillouin zone by varying k their average position changes. They must come back to the same place in the unit cell after a cycle, but it can be a different unit cell, therefore this process is charge pumping C electrons to the neighboring unit cell.

Since the Chern number is attached to a set of Bloch states in the 2D Brillouin zone, these states can be classified topologically and the Chern number is used as the topological invariant. Haldane [11] proposed a model that allows for the consequences of topology to be easily seen. By varying a hopping parameter, a band inversion is introduced where the character of the states in the valence and conduction bands have changed. The system went from a trivial insulator to topologically nontrivial since the two cant be connected without a band closing. This is accompanied by a Chern number jump from 0 to 1 and the nontrivial winding of the Wannier functions. Regarding bulk-boundary correspondence, the winding of the Wannier centers has a corresponding flow of surface states due to charge conservation.

Topological phases can be enhanced in the presence of symmetry. One important symmetry is time-reversal (TR) symmetry where $t \to -t$. In the presence of time reversal symmetry the topological classification is different to the one described above. There are different approximations that allow us to understand the classification of a system with time-reversal symmetry and spin-orbit coupling. One is where we consider spin-orbit coupling only using the σ_z term in $H_{SOC} = \frac{\hbar}{4m^2c^2}\sigma \cdot \nabla V(\mathbf{r} \times \mathbf{p})$ which decouples the spin-up and spin-down system. Obviously this is less physical but we will see by adding σ_x and σ_y terms the conclusions don't change. Time-reversal symmetry reverses $\mathbf{p}$, meaning $H_\uparrow$ is interchanged with $H_\downarrow$, but time-reversal also flips the spin. So compounding these two actions, time-reversal symmetry is still present. This means that the spin-up Chern number is equal and opposite to the spin down Chern number and the total Chern number is zero because TR is present. We consider a system with $(C_\uparrow, C_\downarrow) = (1, -1)$ as a pair of Haldane systems with one being a complex conjugated partner. Therefore we know there is a nontrivial winding of the Wannier functions and a gapless edge mode. Kramer's theorem states that in the presence of time reversal symmetry that each Bloch state $|\psi_{n,\mathbf{k}}\rangle$ is degenerate with $|\psi_{n,-\mathbf{k}}\rangle$. The time-reversal invariant momenta in the Brillouin zone come in degenerate pairs. The Wannier charge centers also come in degenerate pairs at the TRIM. Now due to Kramer's theorem, we expect time reversed partners in the Wannier function spectrum and edge state dispersion's. Another consequence of Kramer's theorem is that even when consider the full effect of SOC the degenerate pairs at the TRIM stay degenerate. These degeneracies cant be gapped out by any TR perturbation and they cant be moved out of the gap in the bulk continuum.

The above discussion tells us that by taking what we know from Haldane's model with the Chern number as the topological invariant, the Wannier spectrum flow and boundary dispersion are crucial for classifying the topology of the bulk. Applying this to systems with TRS, we now discuss the $\mathbb{Z}_2$ topological classification. By analyzing the edge state dispersion in the half Brillouin zone or the Wannier charge centers across the entire BZ we notice there will be an even number of crossings of a line for trivial states and an odd for topological states Fig. 1.6. The Hamiltonian of system with even number of crossings (N_c) cannot be adiabatically connected to a system with an odd number without closing the bulk gap. Now we have a $\mathbb{Z}_2$ classification where the invariant is $\{0, 1\}$ or $N_c \bmod 2$. Computing the $\mathbb{Z}_2$ invariant boils down to calculating the Wannier center flow of the bulk Hamiltonian when inversion symmetry isn't present or the Fu-Kane criterion [12] in the presence of inversion symmetry. In three dimensions one would calculate the $\mathbb{Z}_2$ invariant for one of the six TR invariant planes in the Brillouin zone which generates the topological index set $\nu = (\nu_0; \nu_1\nu_2\nu_3)$ where ν_0 is the strong topological index and $\nu_{1,2,3}$ are the weak indices [13, 14].

Classification of crystalline topological materials

The field is at a point where we can classify the topological properties of all crystalline materials using the symmetry in each space group and by combining real and momentum

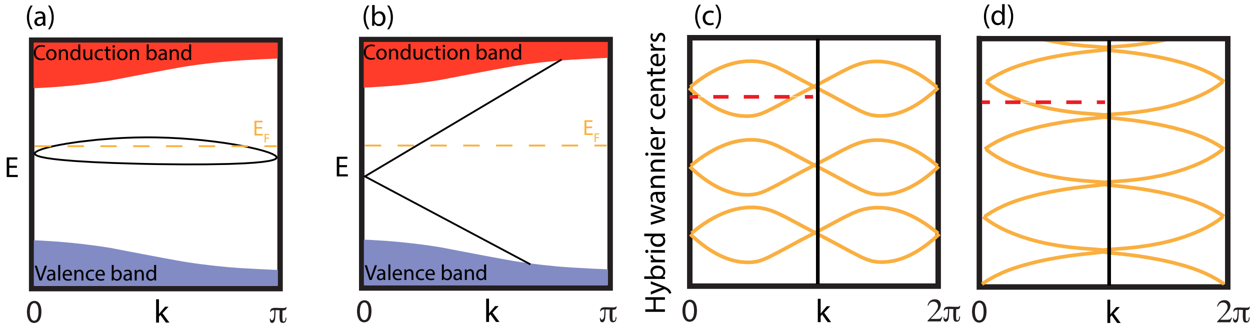

Figure 1.6: Cartoon version of the band structure and hybrid Wannier center flow for trivial and topological systems. (a) A trivial band structure. The boundary states that lie in the bulk gap can be pushed into the bulk continuum with a perturbation. (b) A topological band structure. The boundary states that lie in the bulk gap cannot be pushed into the bulk continuum with a perturbation. (c) A trivial Wannier spectrum flow where a line will cross the hybrid Wannier centers an even number of times. (c) A topological Wannier spectrum flow where a line will cross the hybrid Wannier centers an odd number of times. This corresponds to charge pumping into another unit cell as well as an obstruction to constructing localized Wannier functions.

space pictures of the electronic structure, with Wannier functions provide the link between the topology of Bloch functions in momentum space and the localized orbital description of chemical compounds [2, 15]. To do this we need three things: the crystals space group, description of the orbitals, and the positions of the orbitals. With this we map between the locations of atoms and orbitals within the crystal unit cell and allowed band structures. To identify topological crystals one asks if the band representations of a particular space group admit a trivial insulator limit (exponentially localized Wannier functions) compatible with the crystal symmetries. So basically one takes the bands arising from a global momentum space picture and compares them to the band representations generated in real space and topological crystalline bands are those that do not admit a description in terms of localized Wannier functions. From this one can also use symmetry indicators directly from the crystal symmetry like the Fu Kane criterion to enable the ability to directly diagnose the topological phases. However, many materials are not classified due to the lack of a crystal lattice. We now shift focus to the idea of topological states in non crystalline materials, specifically amorphous and disordered systems. Noncrystalline materials fall outside of this classification because they do not have a space group. While we don't have a crystal lattice we still have orbitals and the position of those orbitals are well defined. We cant calculate band structures or use the symmetry indicators of the crystal lattice but the DOS is well defined. So do amorphous topological materials exist? It isn't a question of if they exist but in what solid state systems can we discover them.

1.3 Topology in non-crystalline materials

It is commonly discussed theoretically that strong disorder will close the bulk band gap and create a trivial topological phase. However there is never a random distribution of atoms with arbitrary potential well depths - there is always a hard sphere core distance and some local order. "Strong disorder" means disorder in the depths of potential wells that are comparable to their depth, which typically does not happen. Topological phases can survive even in the absence of a crystal lattice. Theoretically, amorphous solids can be topological since there are non-spatial symmetries that protect topological phases, such as time-reversal symmetry. In this case, topological states remain robust and do not localize, so long as disorder respects time reversal symmetry and there is a non-zero mobility gap [16].

Topological Anderson insulators have been discussed in the context of disorder and topological systems. Remarkably disorder actually creates a nontrivial topological bulk [17]. In these systems random onsite disorder renormalizes the onsite energy pushing a topologically trivial system that is close to being topological to have a topologically nontrivial gap. Two similar works by Agarwala and Shenoy [18] as well as Mitchell, et al. [19] showed that topological states exist in amorphous systems. Agarwala and Shenoy approached the problem theoretically and defined their tight-binding Hamiltonian as;

$$H = \sum_{i\alpha} \sum_{j\beta} (t(r) T_{\alpha\beta}(\hat{\mathbf{r}}) + \epsilon_{\alpha\beta}\delta_{ij}) c^{\dagger}_{i\alpha} c_{j\beta} \tag{1.25}$$

where the hoppings depend on the angular part T and the distance part t. The authors then formulated the onsite and hopping terms to enable a topological bulk (such as a Chern insulator) when the lattice sites come from a random point set. They saw that by tuning some of the parameters and the atomic density that with open boundary conditions there are states that fill the band gap which are localized to the edge. When the Fermi level is brought into gap the conductivity is quantized to Ce^2/h. Additonally they computed a topological marker called the Bott index to prove the bulk is topologically nontrivial. They also generalized the model to the 10 different symmetry classes given by the Altland–Zirnbauer periodic table. Separately Mitchell, et al. performed similar theoretical as well as experimental work on a mechanical metamaterial of coupled gyroscopes showing the possibility of a topological phase in an amorphous mechanical system. They provided additional insight by constructing different point sets and applying connectivity rules to each site more closely resembling a real amorphous material. They show in most cases that a topological Chern insulator phase was realized. Now the field has taken off theoretically with many new works [18, 25, 26, 19, 27, 28, 29, 30, 31, 20, 21, 22, 23, 24]. The most realistic model for amorphous topological phases was created by Marsal, et al. [30] where they retained the most important aspects of amorphous materials: a coordination environment that closely resembles the crystal. They show with a well defined local environment and fixed coordination that they were able to analytically and numerically compute the energy spectrum and saw was that the the local environment of a site is enough to determine the broad spectral features, and where the gap closures appear. They also were able to the apply the concept of symmetry indicators to an amorphous system since the model has equivalence between orbitals and fixed coordination.

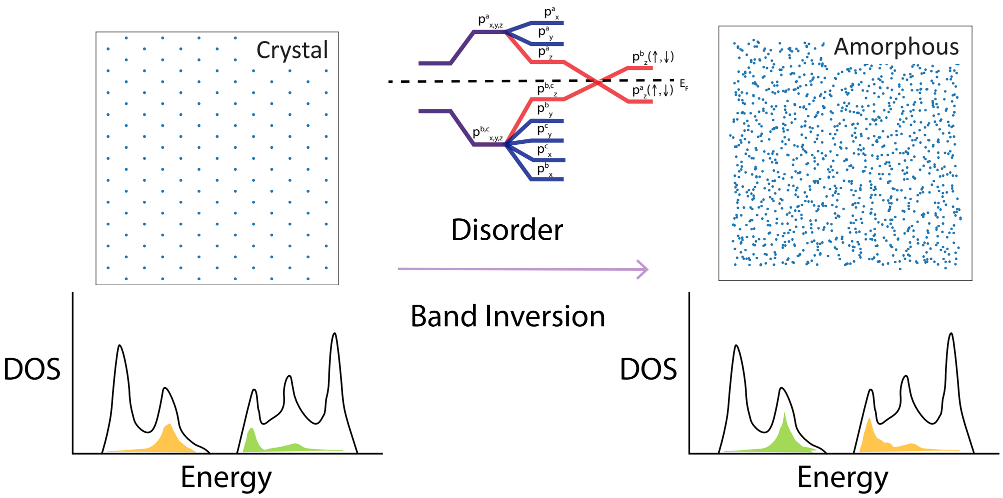

Figure 1.7: Cartoon of how modifying the local environment and subsequent electronic DOS could produce a band inversion.

Topological order must reflected in the electronic structure of systems where $\boldsymbol{k}$ is not defined. Our interpretation of how topological physics arises in amorphous materials is based on the similarity of the local environment of sites. The chemical bonding and connectivity produce the relevant aspects of the electronic structure for discussing band inversions and topology. We also rely on the definition of a topological phase: one that cannot be adiabatically connected to an atomic insulator without closing the bulk gap. This can be coupled with "topological markers" that are rely on many of the above expression but formulated in real space. For a system where the crystalline phase is topological, if the amorphous phase retains the local environment of the crystal then the density of states should resemble the crystalline phase (maybe lacking some sharp features). In this case if the adjustment of the atomic sites to make the system amorphous does not close the mobility gap then the inverted band gap can still exist. In the case of a trivial crystal to topological amorphous system, if the local environment in a trivial crystal changes in a way that does not allow the electronic structure in the amorphous state to be connected to the atomic limit then there can be topological states in an amorphous system that are not present in the crystalline system. Upon increasing disorder and removing the long range order associated with the crystalline atomic positions, the new local environment in the amorphous system can create a new crystal field that can push the states closer together in energy, similar to the effect of pressure. The incorporation of SOC then can invert these states producing a topologically nontrivial bulk. A cartoon of this shown in Fig. 1.7. In some cases localization can also increase the impact of SOC, likely to increase band inversion due to increased wavefunction mixing.

Chapter 2

Techniques

2.1 Thin films and Physical Vapor Deposition

Thin film growth is a critical technique in developing materials for technological advancements. Thin films are deposited onto bulk materials, substrates, to achieve properties the bulk materials cannot achieve alone. Thin films have been critical in science by being able to tune the thickness/dimensionality of materials or used for coatings in experiments such as LIGO. Thin films enable the growth of some materials that aren't achievable in bulk form, by stabilizing the structure using lattice matching or protecting it from atmospheric degradation with capping layers. It also enables heterostructures where the properties of an adjacent thin films influence each other. They also have been critical for technological applications such as magnetic memory. There are many different thin film techniques such as Physical Vapor Deposition (PVD), Chemical vapor deposition, Sputtering, etc. The principles of PVD are vapor transport to the substrate in an Ultra High Vacuum (UHV) chamber. Pure elemental sources are made into a vapor form via many different techniques such as effusion cells or electron beam evaporators. Then this vapor is transported to the substrate by various means like a vacuum, plasma, or liquid. The vapor arrives at the substrate and is deposited depending on many factors such as surface condition, reactivity, and energy. The vapor phase techniques have significant advantages. They are applicable to any material, the substrate temperature is variable, and the surface is accessible during deposition.

PVD is a particularly useful growth technique regarding amorphous materials and has been found to make amorphous (glassy) materials which are not available by liquid quenching, and in some cases to produce "better" amorphous materials than are found by the best liquid quenching techniques. The standard way to produce amorphous materials are: cooling from the liquid state (slow cooling, moderate quenching, rapid quenching) and PVD. PVD has several advantages in this realm since we can tune many knobs such as the substrate temperature, growth rate (affects the time absorbed atoms have to diffuse to ideal positions), irradiation, and chemical dopants to frustrate crystallization. Modifying the substrate temperature enables the growth of amorphous films with different local ordering and produces what is called an ”ideal glass” [32, 33].

Substrate Prep

The substrates used in this thesis are 300 nm of amorphous SiN_x on top of 500 micron Si(100) (10x10x0.5mm^3). Stoichiometric Silicon Nitride has a composition of Si_3N_4, but the LPCVD Silicon Nitride used in our lab is not stoichiometric, slightly Si rich of stoichiometric, which enables it to be low stress and hence able to be used as a thin membrane after removing the Si substrate. The substrates are cleaned in a sonicator using a sequence of solvents: first acetone, then methanol, finally isopropanol. After this each substrate was taken out of the beaker with UHV tweezers and blow dried with Nitrogen gas. The substrates were then mounted onto a sample plate with clips, Fig. 2.1. Once introduced to the UHV chambers the substrates are heated to 150 ^{o}C to remove any atmospheric contaminants that impinged on the surface while moving from flow hood to UHV chamber.

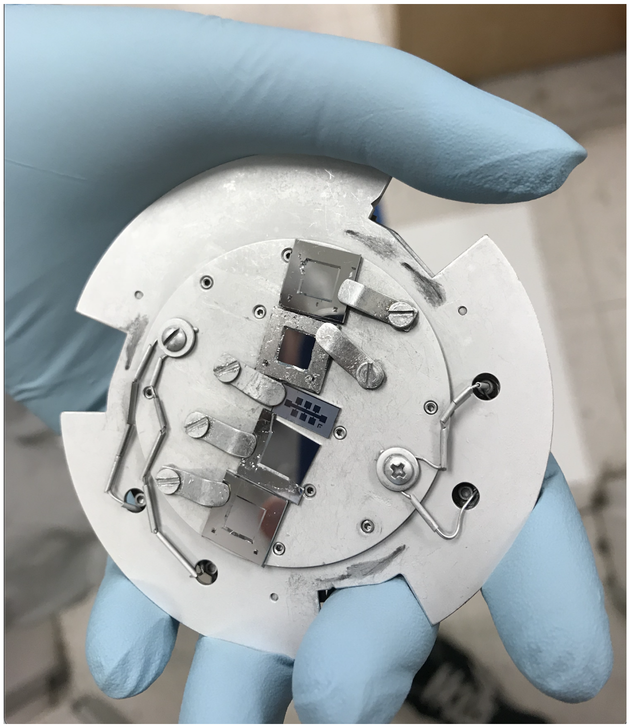

Figure 2.1: Sample plate post deposition.

For TEM measurements a 10 nm thick SiN_x membrane was used. The window array TEM grid has 9 evenly-spaced 0.1×0.1mm square windows (in a 3×3 array pattern) centered on a 200µm thick circular or octagon shaped silicon frame that fits inside a 3mm diameter circle. These windows aren’t cleaned in the sonicator or heated in the chamber (expansion and contraction) due to the delicate nature of the membrane. The membranes are fabricated in a cleanroom and determined to be UHV clean. After sample mounting they are gently blown with nitrogen gas to remove any dust.

Growth

As stated above the growth technique used is PVD. In this technique pure (6N) elemental sources are melted or sublimated from the solid phase to produce a vapor. Attempting to evaporate alloys will typically lead to non-stoichiometric films since there are differing vapor pressures of the constituents. When the sources vapor pressure reaches $\sim 10^{-3}$ Torr there are appreciable evaporation rates ($\geq 0.1\mathring{A}/s$). There are useful vapor pressure curves which can be used to determine if PVD growth is feasible. If the temperature at which the vapor pressure is $\sim 10^{-3}$ Torr is above the melting point the material will melt then evaporate. If it is below then it sublimates. In my research I used three different evaporation sources: thermal evaporation from boats, effusion cells, and electron beam evaporators.

Thermal evaporation boats, typically made out of Tungsten, are used by running a current through them and resistively heating them to a point where the source material evaporates. The boats are made of metals with low vapor pressure so there is no concern of contamination. Thermal boats are best to evaporate high vapor pressure materials at low temperatures. Trying to grow materials with high melting points will sometimes alloy to the metal boat which changes the mechanical materials properties and lead to cracking. Coating thermal boats in materials such as Al_2O_3 can prevent alloying. It is best to just use electron beam evaporators when growing with high melting point materials.

Effusion cells are a way of using indirect resistive heating to grow. These are made up of long tungsten filaments wrapped around a Pyrolitic Boron Nitride ceramic crucible. These cells reach a temperature around $1200\,^{o}$C with a thermocouple to monitor the temperature and a PID control for accurate and stable growth rates. Bi, Se, Te, and I were all grown out of a K-cells. Sources that emit from a central point follow what is called the ”cosine distribution” characteristic flux. K-cells that aren’t fully filled don’t follow the same distribution and follow a more direct beam characteristic.

E-beam sources are evaporation sources that use field emission of an electron from a hot tungsten filament at 7kV below its anode to create an electron beam. This charged beam is steered by a magnetic field onto the source which is sitting in a copper crucible. The beam position and size is controlled by changing the current in the electromagnet sweep coils. Depending on if the source material sublimates or melts, the sweep coils need to be moved or can stay stationary. If the source sublimates then then beam spot must be moved to not drill through the source and crucible. If the source melts then the beam is moved on the first melt to homogenize the surface but then stays stationary until the source is refilled.

The growth rate is monitored by multiple quartz crystal monitors in the chamber. A quartz crystal sensor measures the mass of the material deposited over time using the piezoelectric effect to measure a shift in the resonant frequency of a standing shear wave in the crystal as mass is deposited. Prior to growth input parameters such as the molar mass and

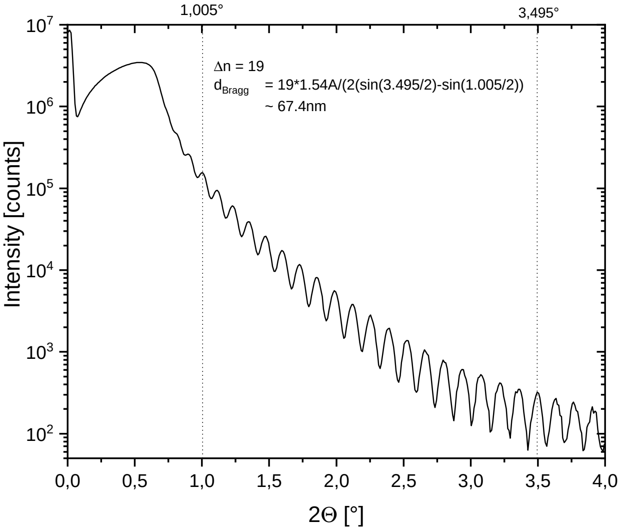

Figure 2.2: XRR scan for for an a-Co-Si thin film alloy of thickness determined to be 67.4 nm on a 300 nm thick a-SiN$_x$-covered Si substrate which would produce interference fringes at about 1/5 the angles seen here, and are unresolved in this scan. The interference fringes are seen which enable measurement of the thickness.

density are put into the rate monitor to convert the mass into a growth rate. When growing with more than one element, one must take into account the growth rate at the substrate will see flux from all of the sources. Also there are geometric factors in a chamber that lead to the growth rate at the source not equaling the growth rate at the substrate. For this reason the tooling factor is simply a geometric factor that accounts for this. Prior to doing a production run, one should calibrate the sources by determining the correct tooling factor, TF = (measured thickness/QCM thickness)×100. Once this is done you can grow any material composition with high accuracy.

Profilometry

It is important to have accurate readings of thickness for TF calibrations and for growing materials with desired properties. In my research I used KLA-Tencor ASIQ surface profiler. This rasters a fine tip across the sample and measures the vertical displacement from its baseline position with sub nanometer accuracy. There are inevitably thickness variations across a substrate so performing profilometry measurements along each edge of the film is important. The films are typically grown using a shadow mask, which should in principle create a sharp edge to measure using the profilometer. However depending on the shape of the evaporation flume there can be shadowing at the edges making it important to measure sufficiently far into the sample.

XRR

Another method to calculate thickness is using X-ray reflectivity measurements. This is a low angle X-ray diffraction technique. The X-rays scatter and reflect off the surface of the sample and interfere. The spacing between interference minima, called Kiessig fringes, are proportional to $1/t$ where t is the film thickness. This measurement is done using a 2θ-omega scan on a PANalytical X'pert system. Software such as GenX is used to analyze the XRR data. An example is shown in Fig. 2.2. The film has to be very flat to get many fringes/make this technique work. Typically nanocrystalline films won't work, but amorphous is generally flat enough to enable clear interference fringes.

2.2 Composition

It is important to grow materials with very accurate compositions since physical properties vary quite dramatically with even small changes in composition. Multiple composition characterization techniques were used to ensure the composition was accurate in addition to tooling factor calibrations. Additional uses are to look for composition gradients, clustering, and even valence state bonding characteristics.

XPS

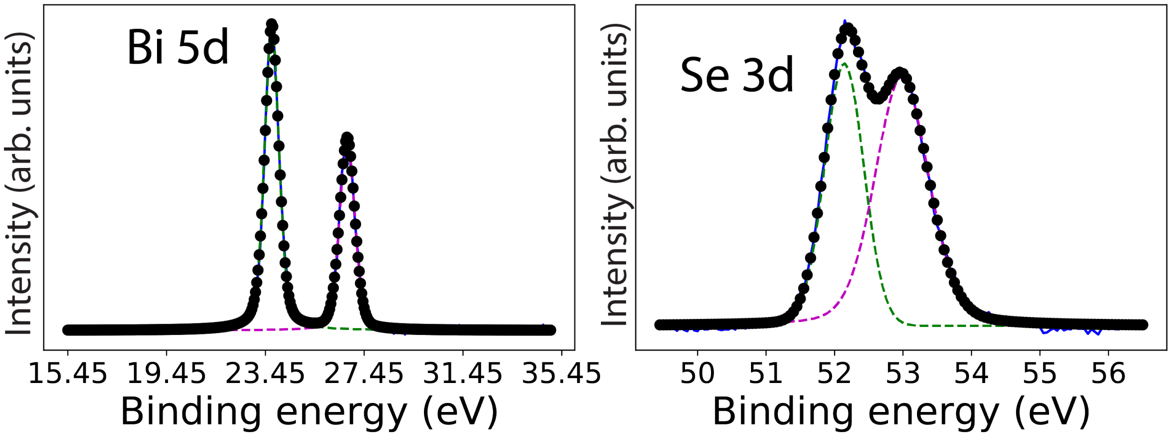

Figure 2.3: Bi 5d and Se 3d core levels. The peaks are spin-orbit split and are fit (pink and green Gaussian curves) to determine the composition. The position of the peaks also give information about bonding.

X-ray photoelectron spectroscopy is a powerful tool not only for composition but also for understanding bonding and the electronic structure. It also can be thought of as the angle-integrated version of ARPES presented below. XPS involves irradiating the sample surface with soft X-rays (typically using Al-Kα $h\nu = 1486.6$ eV) and analyzing the emitted electrons (photoelectric effect) based off their binding energy ($E_B = KE - h\nu + \phi$). Each element has a unique spectrum (unique set of binding energies of energy levels) therefore this method is used for identification of elements in your sample and the spectrum of a mixture of elements is the sum of the peaks of the individual constituents. The mean free path of the electrons in the sample is small so XPS is a very surface sensitive technique. Quantitative analysis is done by considering the height of the peaks and the integrated area under the peaks. Additional processes such as Auger electrons are a result of the photoionizing process. Variations in the elemental binding energies (the chemical shifts) arise from differences in the chemical potential and polarizability of compounds. These shifts elucidate the chemical state the material is in. An example is shown in Fig. 2.3.

EDS

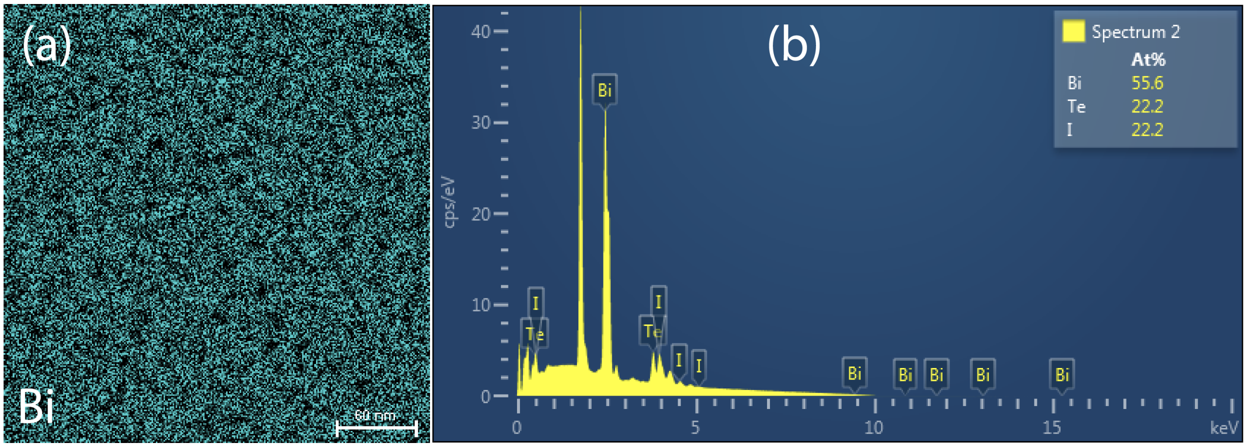

Figure 2.4: (a) Bi elemental map taken in a TEM from a 10 nm nanocrystalline Bi_2TeI film grown at room temperature. The scale bar is 60 nm. (b) EDS spectrum for a $Bi_{2.5}TeI$ film. The peaks correspond to characteristic radiation from each element and are fit to determine composition.

This technique is opposite to XPS, where it is a high energy electron beam hits your sample, electrons are ejected from an inner shell, an electron falls to fill that shell giving off characteristic radiation. Practically speaking an electron goes in and a photon is emitted in the X-ray regime. The characteristic X-ray again is unique to the elements in your material enabling composition analysis. This is done in the lab by placing a sample in an SEM or a TEM with an EDS (X-ray) detector. One benefit of EDS is in a TEM you can measure the composition with spatial resolution. A benefit of EDS over XPS is it is less surface sensitive and depending on the energy of the electron beam you can begin to see the substrate. An example is shown in Fig. 2.4.

RBS

The golden standard for composition analysis in the Hellman lab is Rutherford Backscattering spectroscopy (RBS). The technique involves shooting a beam of alpha particles ($^4He^{++}$) at your sample at high energy (2-3 MeV). The alpha particles will undergo Rutherford backscattering from the atomic nuclei of the constituents in the sample. The scattering is related to the Z of the atomic nuclei. One benefit of RBS is the depth analysis that the technique provides. The energetic alpha particles pass through the sample and into the substrate losing energy the entire way from the backscattering processes. Therefore the RBS spectrum gives the ability to depth profile the film and works even better when considering heterostructures. The spectrum is then simulated using the SIMNRA software to determine the atomic density (density determination requires combining RBS with thickness measurement) and composition. An example is shown in Fig. 2.5.

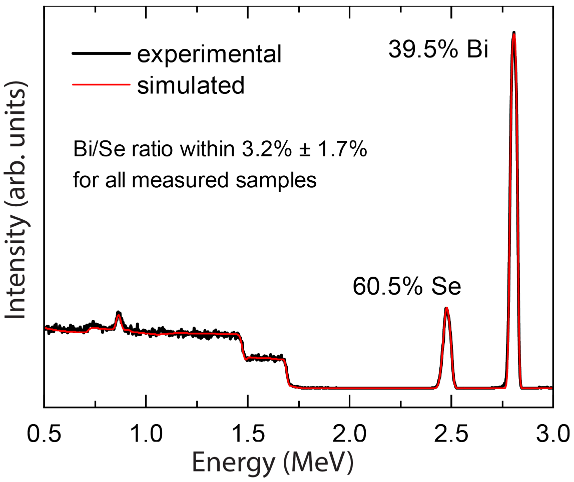

Figure 2.5: Bi_2Se_3 RBS Spectrum. The simulated curve gives information on composition and atomic density. The sample is 100 nm on a-SiN_x.

2.3 Structure

XRD

X-ray diffraction is one of the most common methods for characterizing the crystal structure of single crystals. The principles of XRD are built upon Bragg's law which states $n\lambda = 2dsin\theta$

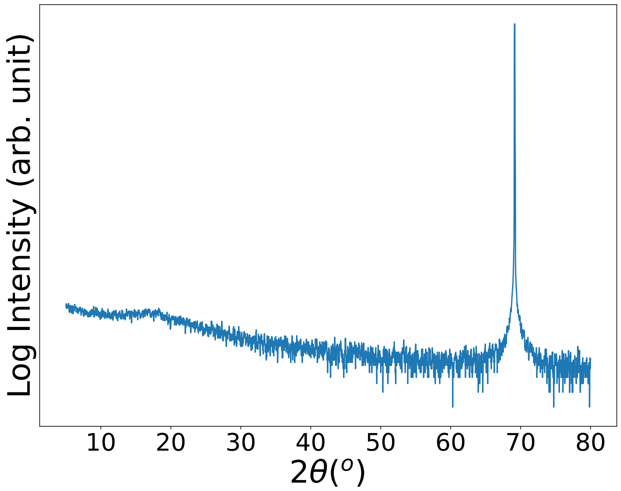

Figure 2.6: Amorphous Bi_2Se_3 2θ-ω scan with $\lambda = 1.5406\,\text{Å}$. The peak at 69^o is due to to the substrate. The hump around 17^o is related to diffraction from the short range order in the amorphous film. The film is 100 nm.

where n is an integer, λ is the wavelength of radiation, d is the interatomic spacing between planes, and θ is the angle of incidence of the X-rays on the sample. To summarize, two parallel waves reflecting off adjacent planes separated by d will constructively interfere if the path extra path traveled is an integer number of wavelengths. In practice we align our samples by using known d-spacing for the substrates so the X-ray scattering vector is aligned normal to the planes being measured. Measurement and analysis of the diffracted X-ray intensity allows us to extract structural information from the peaks in diffraction pattern.

Perfect crystals will diffract X-ray in relatively few directions because there is destructive interference among waves that do not satisfy Bragg's condition, the so called structure factor. As stated in the background section on amorphous materials, they tend to arrange themselves where there is a well defined nearest neighbor, and even second or third nearest neighbors depending on the medium range order. Therefore incident X-rays diffract and constructively interfere to produce one or two broad maxima in the diffracted intensity. In practice performing XRD on amorphous materials is beneficial to inform whether there are large crystalline grains. The absence of peaks does not mean the material is definitely amorphous. This is because of the Abbe diffraction limit. Essentially the wavelength of the incident X-ray radiation isn't small enough to resolve small crystallites in the film. Therefore it is necessary to perform other techniques to ensure your sample is amorphous such as TEM or synchrotron based techniques. An example is shown in Fig. 2.6.

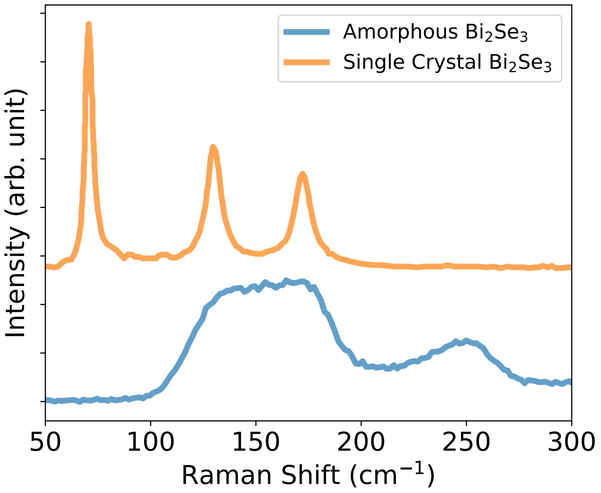

Figure 2.7: Bi_2Se_3 Raman Spectrum. The Raman spectrum, Fig. 1(f), shows one broad peak between 135 cm^{-1} and 174 cm^{-1} which correspond to the broadened bulk E_g^2 and A_{1g}^2 vibrational modes, respectively. The A_{1g}^1 van der Waals mode at ∼72 cm^{-1}, which is created by the layered structure of the crystal, is absent in our amorphous samples. Instead, we observe a peak at 238 cm^{-1} not present in crystalline Bi_2Se_3, which we attribute to amorphous Se-Se bonding.

Raman

Raman spectroscopy is a method that relies on the inelastic scattering of light with matter. It is a versatile method as it does not depend on whether the material has a crystalline or non-crystalline structure. The incident light induces a rotational, vibrational, or electronic transition in the material. In my research we used Raman to probe the vibrational modes of a material to understand the structure and bonding. It should be noted that performing Raman in metallic samples is not possible due to screening from the conduction electrons which hinders the excitation of vibrational modes (there are exceptions). In the lab monochromatic light is shined on your sample, some of which is inelastically scattered (Raman scattering vs elastic Rayleigh Scattering). The resulting Raman spectrum plots the intensity of the inelastically scattered light as a function of the wavenumber shift from the incident light. The peaks in the spectrum correspond to the vibrational modes in your material. In crystalline materials, Raman is an effective tool to probe the symmetry of the structure as different vibrational modes are allowed by symmetry. In amorphous materials Raman is useful technique to first give a rough idea if your sample is amorphous and then to understand the local environment and bonding characteristics. Since amorphous materials have short and medium range order the Raman spectrum sheds light on a few interesting properties. Due to the distribution of bond length, angles, and coordinations the Raman modes change. Depending on the bond strength the peak in your Raman spectrum shifts. Since there is a distribution of bonds, the Raman modes typically broaden. Observing broad, shifted peaks in the Raman spectrum of your amorphous film enables you to make statements regarding the local ordering in your material. An example is shown in Fig. 2.7.

TEM

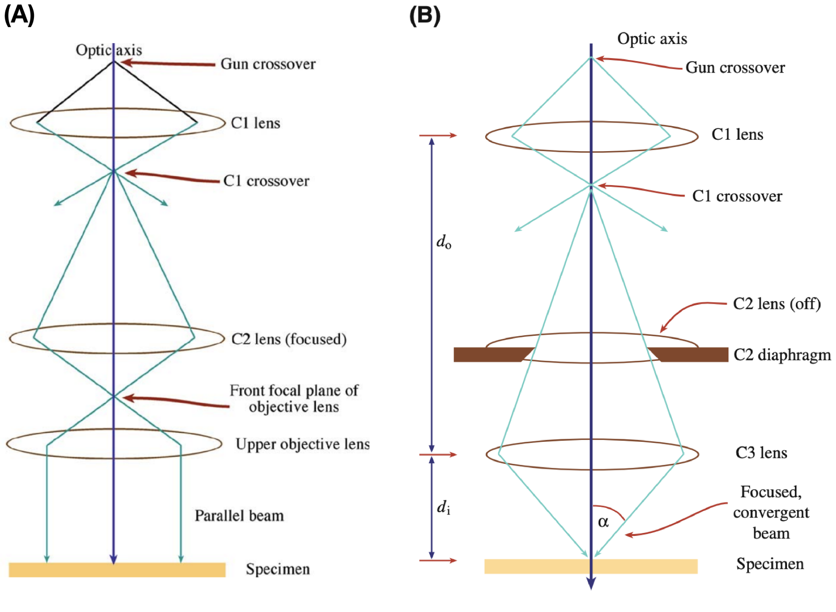

Figure 2.8: TEM modes. (A) Parallel beam. (B) Convergent beam. Image used from [34].

Transmission electron microscopy (TEM) is arguably the best technique for understanding the structure of any material. As stated earlier to perform these measurements we grew thin films, approximately 10-25 nm, on amorphous SiN_x membranes. These are then placed into the TEM column and pumped down in vacuum. This enables transmission of the electron beam through the sample to be captured on the screen.

There are two main modes to operate a TEM, parallel beam or convergent beam operation, Fig. 2.8. The first mode is primarily used for imaging and selected area diffraction. The second mode which is typically referred to as STEM is primarily used for scanning images, analysis such as EELS, and scanning nanodiffraction. In the parallel mode the incident beam of electrons is μm in diameter and then the electrons scatter (directly or through appreciable angles) from the sample to be collected by a detector for imaging or diffraction patterns. The parallel mode is best used for producing the sharpest diffraction patterns and traditionally has the best image contrast. If you wish to focus the beam more to observe a specific area or perform elemental analysis on a small part of the sample then convergent beam mode is the best option. In this mode the converged nature of the beam destroys image contrast which means to get an image you must scan across the sample. The convergent beam can be thought more of as a probe that must be scanned across the sample.

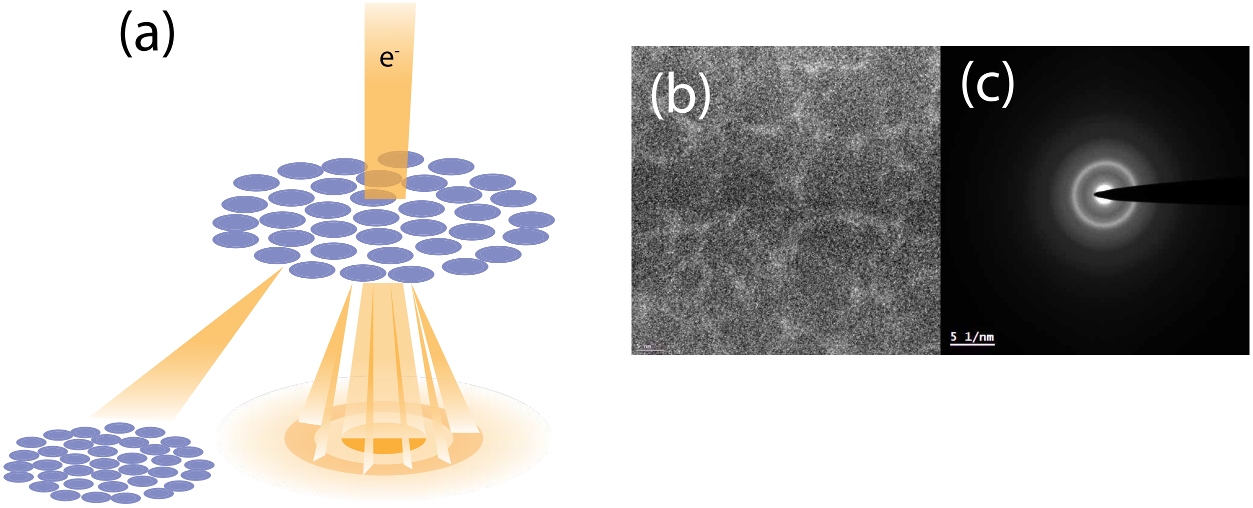

Figure 2.9: Parallel TEM modes. (a) A cartoon of a parallel beam measurement. Parallel beams of electrons are incident on the sample, then depending on the mode the diffraction pattern or real space image can be taken. (b) High resolution real space image of amorphous Bi_2Se_3. (c) Diffraction pattern of of amorphous Bi_2Se_3.

In parallel mode, the objective lens takes the emerging electrons from the sample and disperses them to create a diffraction pattern in the back focal plane or recombines them to create an image in the image plane. To form an image we can insert an aperature in the back focal plane of the objective lens. The image is made out of the central direct beam of electrons or by using some of the scattered electrons. This is called either bright field or dark field imaging, Fig. 2.9

In convergent or STEM mode the beam must be scanned parallel to the optical axis to ensure the same scattering processes. To create an image the detector picks up intensity from the direct beam which varies depending on where is illuminated on the sample. Both bright and dark field imaging are possible in STEM. Additionally, diffraction patterns can be generated in STEM mode, this is called convergent beam electron diffraction, Fig. 2.10.

Another method of electron microscopy is fluctuation electron microscopy (FEM). This method studies the medium range order in amorphous materials. In this method fluctuation refers to the changes in local structure and orientation of the atoms in the amorphous material. We perform FEM by doing STEM diffraction with a beam size of 2 nm (which is

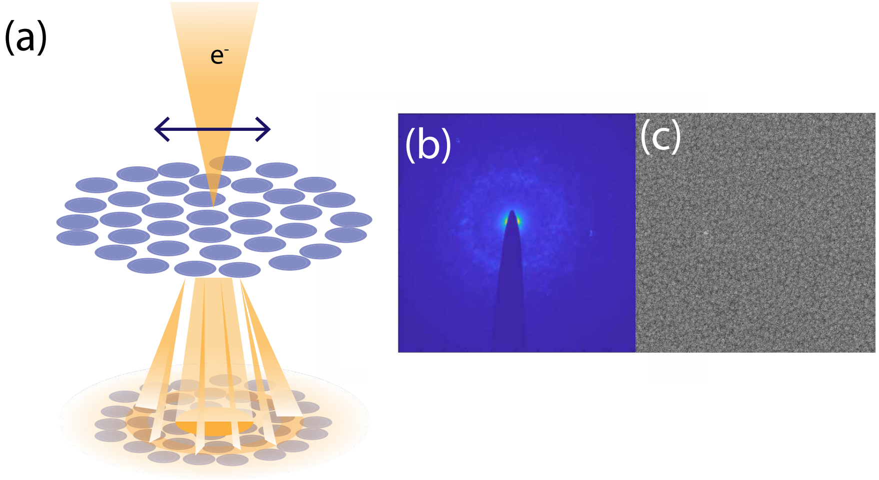

Figure 2.10: Convergent TEM modes. (a) A cartoon of a convergent beam measurement. A convergent beams of electrons are incident on the sample, the diffraction pattern and real space image can be taken simultaneously. (b) Scanning nanodiffraction pattern of of amorphous Bi_2Se_3. (c) Real space STEM image of amorphous Bi_2Se_3.

on the order of the length scale of medium range order) and rastering it across the sample. The normalized variance in the diffracted intensity gives the relevant information on the MRO, Fig. 2.11. The speckle visible in the scanning nanodiffraction images is associated with local ordering and orientations of clusters of atoms, which correspond to near- and off-Bragg conditions. The diffracted intensity originates from nanoscale volumes within the sample. When the speckle observed across the diffraction images is highly uniform, this is indicative of many randomly oriented nanoscale clusters of atoms with short range ordering in the amorphous structure. If the speckle varies greatly in intensity then this originates from more ordered structures.

One consideration when doing TEM on amorphous materials is that the beam can crystallize the films, Fig. 2.12. To achieve atomic scale images some TEM operate at 300 kV, which depending on your measurement, can lead to large electron doses in your material. The high energy of the incident electrons can promote growth kinetics when interacting with the amorphous sample such as nucleation of crystallites. Ways to mitigate this are to use lower energy electron beams (although this affects resolution and contrast), lower exposure times, and not letting the beam stay parked on your sample before measurement.

Finally, it is possible to obtain the radial distribution function from parallel beam TEM diffraction patterns. This is done by radially integrating the the diffraction pattern to obtain the radially integrated diffraction intensity this gives you $I(q)$ where I is the intensity and q

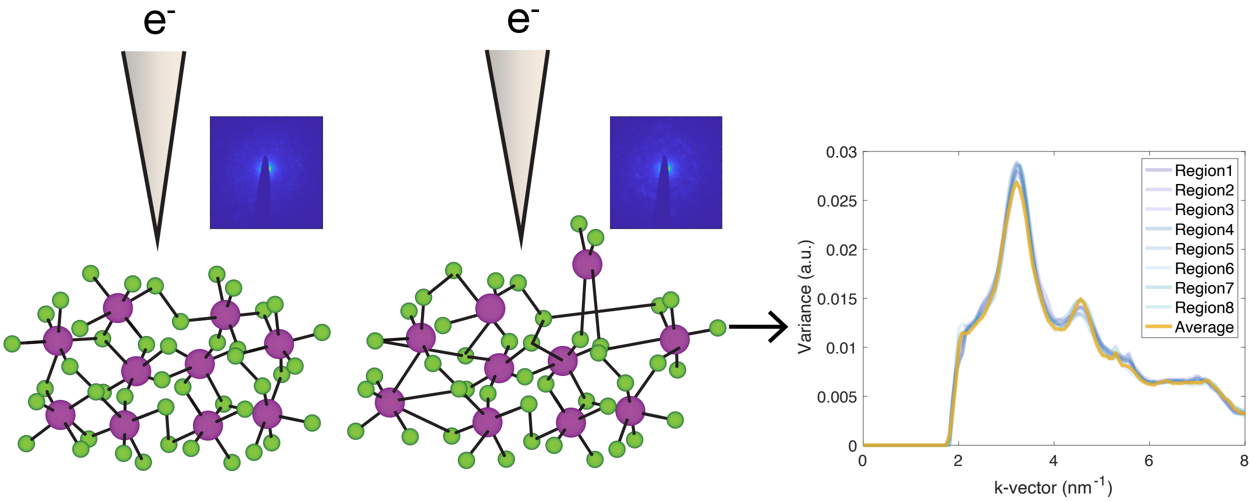

Figure 2.11: Cartoon FEM experiment. The convergent beam is rastered across the sample taking nanodiffraction patterns and the variance in intensity is computed. Variations in medium range order give rise to peaks in the $V(k)$.

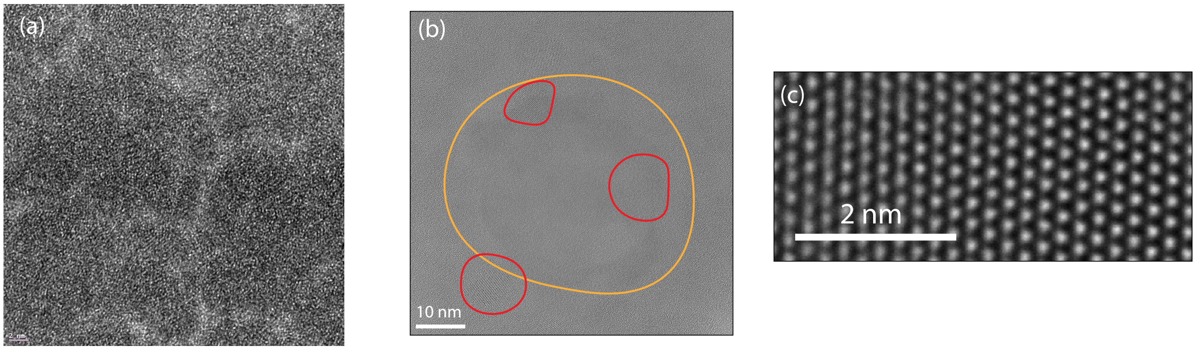

Figure 2.12: Beam crystallization in Bi_2Se_3. (a) Amorphous Bi_2Se_3 (b) After the beam has been left stationary which produces large electron doses in the sample. There is obvious beam damage and incipient crystallization. Orange circle indicates beam damage and red circle are nucleated nanocrystals. (c) Atomic resolution HRTEM of Bi_2Se_3 after beam crystallization.

is the scattering vector. To then obtain the structure factor, we subtract off the single atom scattering factors for the atomic species in the material, now we have $\phi(q)$.

$$\phi(q) = \left[\frac{I(q) - Nf^2(q)}{Nf^2(q)}\right] q \tag{2.1}$$

Then we can mask out the high/low angle noise. Finally the RDF, $g(r)$, is calculated from the structure factor using

$$4\pi r\left[g(r)-\rho_0\right]=\int_0^\infty \phi(q)\sin(qr)dr \tag{2.2}$$

.

2.4 Transport

Transport measurements provide a great deal of information regarding the electronic structure and carrier dynamics whether the sample is under an applied electric field, magnetic field, thermal gradient, or some combination. Transport provides insight into the scattering mechanisms and the electronic band structure. These measurement are one of the best ways to study and observe quantum properties like superconductivity. Measuring the longitudinal resistivity gives insight into low temperature quantum corrections, electron interactions, and even the Fermi surface. The transverse resistance give insight into the carrier concentration and type via the Hall effect. The measurements enable the utilization of structures that are easily implemented into technological devices. We use transport measurements to shine light on the spin orbit entanglement in the materials of interest and to understand different length scales in the films.

Lithography

The first step for transport measurements is to fabricate the thin film into a device structure that enables the study of the physical mechanisms of interest. The two measurement configurations performed in the thesis research were Hall bar and Van der Pauw configurations. Van der Pauw measurements required no lithography and processing post growth. There are a variety of ways to to create Hall bars using lithography such as wet etching, plasma etching, or electron beam lithography. A majority of the Hall bar devices fabricated in this thesis were made using a lift-off technique for which I will go the most into detail. The main difference the former growth methods and lift-off is related to whether the photoresist is developed pre- or post-growth, Fig. 2.13

A common feature to both conventional lithography and lift-off processes are the use of photoresist. There are different types of photoresist (positive or negative) that can best suit your needs. In this work we use LOR5A and MIR701. The difference between standard and lift-off is in standard the photoresist coats the sample where in lift-off it coats the substrate. One key consideration for standard lithography is that the photoresist needs to bake after being spun on. Therefore if you plan to study amorphous films you must pick your photoresist carefully and bake at temperatures below the crystallization temperature. For this reason we opted to use the lift-off technique where there is no post growth processing other than stripping the resist.

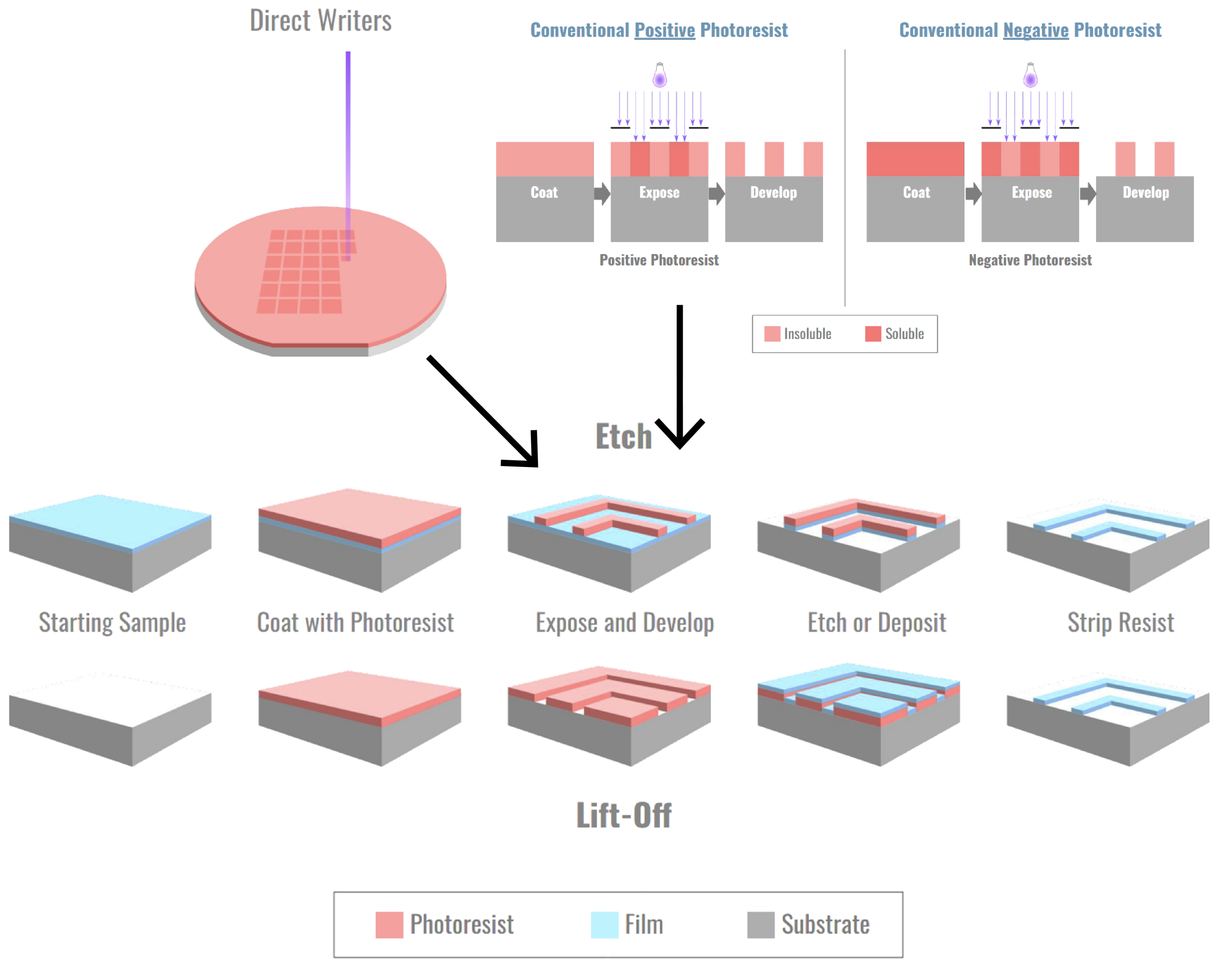

Figure 2.13: Standard steps in a lithography process. Image courtesy of the Berkeley Nanolab.

Once the photoresist has been spun on you must expose it to pattern your sample. Typically this is done by exposing your film to light in the UV range. There are different ways to produce the device structure that is needed (such as a Hall bar). They range from masks patterned in the shape of your device, direct writers, or even electron beams. Electron beams have the highest resolution with features of the order of ~10 nm. Once the film has been exposed it must be developed to dissolve portions of the photoresist. This is where standard and liftoff techniques diverge. At this point for lift-off techniques we simply grow on the developed pattern and then post growth we strip the photoresist and we have a beautiful Hall Bar, Fig. 2.14. If we do standard lithography we now have to find a way to etch our film. This is done by wet etching using liquid chemicals to remove the film from the substrate. This process requires development to figure out the best etch times and solvent concentrations. A good place to start is the Handbook for Metal Etchants. Another method of etching is dry etching where a plasma is used instead of liquid chemicals where the ions in the plasma will hit the sample and dislodge the sample that isn't covered in photoresist. There are some considerations here for amorphous films since this process can impart some energy/heating. After removing the film we remove the resist and then we have a Hall bar device used for transport measurements.

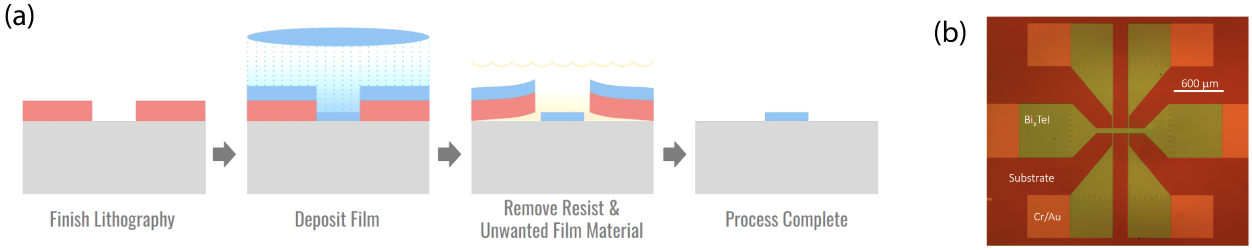

Figure 2.14: (a) Liftoff process. Image courtesy of the Berkeley Nanolab. (b) Example liftoff hall bars used in this thesis.

The final method used in my research was to pre-pattern Cr/Au contacts onto a SiN$_x$ substrate with 2 large current pads and two voltage pads. We then grow our material of interest in a long bar using a metal shadow mask, Fig. 2.15. This method enabled quick and accurate results that were similar to Hall bar devices (used to measure V_{xx} only, for magnetotransport we need to use a Hall bar or Van der Pauw) without the need to perform lithography steps. It should be noted that scratching the films into a hall bar device also work but it quite brute force. However, the first observation of the QAHE was using this method.

Contacts

Having ohmic contacts is critical for performing any transport measurement to get sensible results. The low resistance contacts allow easy flow of electrons into your sample with an immediate response of the voltage with change in the current, the I-V characteristic should be linear. The way in which charge carriers enter the material depends on how large the barrier height is from the contact to material (Fermi level matching). If the barrier is large then there must be thermionic emission over the barrier because the depletion region is large (to equilibriate the Fermi level carriers move from region near the interface). The I-V characteristic is Schotkey like. If the barrier is small then the depletion region is small and the carriers can tunnel through the barrier, this is Ohmic. In all transport measurements we checked that the I-V characteristic is linear throughout the entire measurement. Interfaces, defects, and dopants can pin the Fermi level in the material which makes injecting a current into it harder. Therefore it is beneficial to make deposit contacts onto your thin film in-situ or to grow onto pre-patterned contacts. We do this by growing a sticking layer of Cr (2nm)/ Au (8nm) pre thin film deposition to ensure high quality interfaces between the thin film and contacts. We then wirebond contacts from the measurement puck to the gold pads to ensure high quality contacts. Much of this does not need to be taken into consideration if you are measuring a metallic thin film, the semiconductor is highly doped, or you are not doing high frequency applications. If the above conditions are satisfied then there are a few methods to produce contacts that work reasonably. The first is pressing soft metallic indium blobs onto the film then contacting those blobs with the wire. This should be done carefully by not making the contacts too large (if performing Van der Pauw). Also, depending on the purity, Indium can be superconducting at low temperatures. Another method is using silver paint that works quite well.

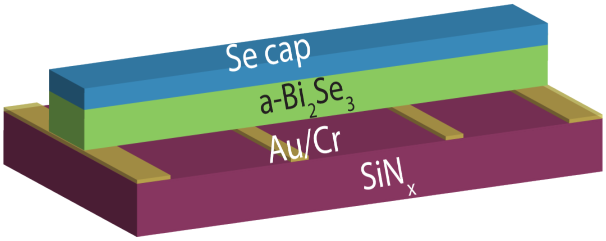

Figure 2.15: (a) Schematic of Bi_2Se_3 bars used in this thesis.

Measurement

Configurations

The first four point measurement configuration is the Van der Pauw configuration to measure the sheet resistance (Ohms/square) of thin film. This method is nice because it means there is no need to performing any patterning prior to measurement. The method works for a thin film or arbitrary shape, however growing the thin film into a square using a shadow mask makes measurement and contacts quite easy. Contacts are meant be as small as possible and located on the perimeter of the thin film. Using complex analysis and the conformal mapping theorem Van der Pauw showed that the sheet resistance is calculated using the following equation:

$$e^{-\pi R_{ab,cd}/R_s} + e^{-\pi R_{bc,da}/R_s} = 1 \tag{2.3}$$

where $R_{ab,cd} = (V_d - V_c)/I_{a\to b}$, t is the film thickness, and R_s is the resistivity [35]. This is then made into a resistivity by $\rho = R_s t$. In practice for for $\rho\,(T)$ and $\rho\,(B)$ measurements we inject current into two of the leads then measure the voltage in the other two, then we permute the configuration clockwise and measure again. This is done at each T or B. If the ratio of $R_{ab,cd}/R_{bc,da}$ is large then the validity of this equation becomes questionable. For Hall measurements, the $\rho_{xy} = \frac{t}{4}\left(R_{ac,bd} + R_{bd,ac} + R_{db,ca} + R_{ca,bbd}\right)$.

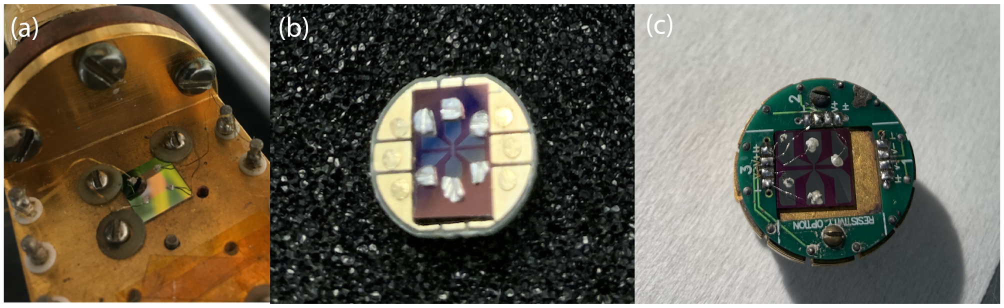

Figure 2.16: (a) Indium blobs in Van der Pauw configuration. (b) Hall bar with indium blobs on a PPMS puck. (c) Hall bar with silver paint on a PPMS puck. Wired bonded sample not shown.

The other measurement configuration is using a Hall bar which has two current pads and four voltage pads. The aspect ratio used in all of our samples was 3. This method enables simultaneous measurement of the V_{xx} and V_{xy}. Due to the design of the Hall bar there should be little to no longitudinal component in the Hall signal and vice versa. To calculate resistance values with a Hall bar you simply do $R = V/I$ for longitudinal and transverse components. Examples are shown in Fig. 2.16

Equipment

Many of the room temperature to 3 K $\rho(T)$ measurements done in my thesis were done in a custom built Janis closed cycle refrigerator. This system is dry with a cold head that recirculates helium gas. The closed cycle has 8 pins for contact to samples enabling measuring two samples at once. It has a quick prep, pumpdown, and cooldown time which cuts down on the time from when the samples leave the UHV chambers to when they are being measured under vacuum. We perform these measurements using DC current with a Keithley 2400 sourcemeter and measuring the voltage using a four-point probe. The temperature is measured using a Silicon thermometer and a Lakeshore. The closed cycle is a workhorse in the Hellman lab. There are a lot of insights into the bandstructure and quantum interference effects that can be extracted from only an $R(T)$ curve.

While the closed cycle is great it lacks a magnetic field which enables the measurement of carrier density and is a probe to understand quantum interference. For magnetotransport measurements I used the Hellman lab MPMS and the Analytis Lab PPMS. The MPMS has a 7 T magnet and the PPMS has a 14 T. Measurements were done using AC techniques which provides a better SNR and higher sensitivity. In these measurements a constant AC voltage is applied which induces a current in the sample, this current is deduced by placing a resistor (much larger than the resistance of the sample) in series with the sample. Then V_{xx} and V_{xy} are measured with two lock-in amplifiers. It is important for these measurements the contact resistance is not excessively large and the impedance if the sample is small. It is also important for high resistance samples, which is common for amorphous and disordered systems, to use a low lock-in frequency. This is because the wire connecting to the sample acts as a capacitor to ground therefore making RC circuit or a low pass filter.

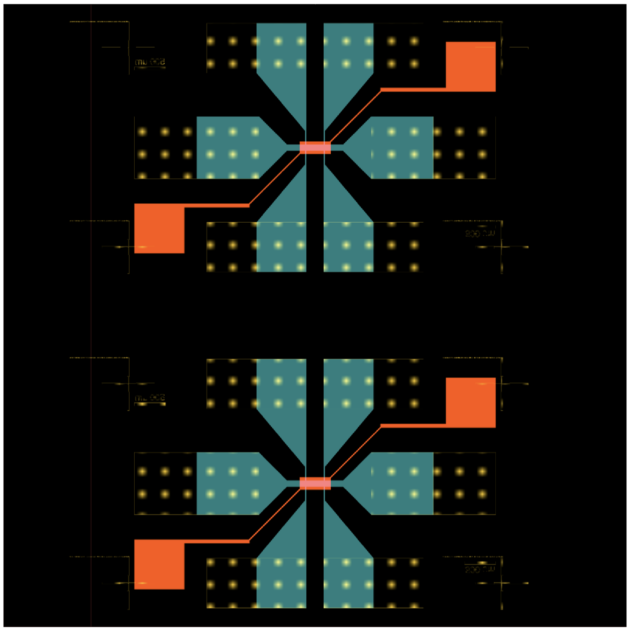

Figure 2.17: GDS pattern for Hall bars used in this thesis.

2.5 Angle resolved photoemission spectroscopy

The beauty of ARPES is that one can use the kinematics of the electron in the material before it has been ejected to map the crystal momentum $\hbar\mathbf{k}$ to binding energy E_B. It has been the gold standard measurement for topological materials and quantum materials for this reason [36]. Similar to XPS (described above), Angle-resolved photoemission spectroscopy utilizes the photoelectric effect. The electrons photoemit in all directions and an analyzer captures the kinetic energy and the emission angles. From the emission angles (θ is the polar angle from the surface normal and ϕ is the azimuthal angle) one can determine the components of $\mathbf{k}$, Fig. 2.18. Using energy and momentum conservation:

$$E_{kin} = h\nu - \phi_{wf} - E_B \tag{2.4}$$

$$\hbar \mathbf{k}_{||} = \sqrt{2mE_{kin}} sin\theta \tag{2.5}$$

where $\mathbf{k}_{||}$ is the crystal momentum parallel to the photoemission surface and is conserved in the photoemission process. The photoemission process is described by the transition probability of an N electron initial state to excited final state ($\Psi_i^N \rightarrow \Psi_f^N$):

$$w_{fi} = \frac{2\pi}{\hbar} \left| \langle \Psi_f^N | H_{int} | \Psi_i^N \rangle \right|^2 \delta(E_f^N - E_i^N - h\nu) \tag{2.6}$$

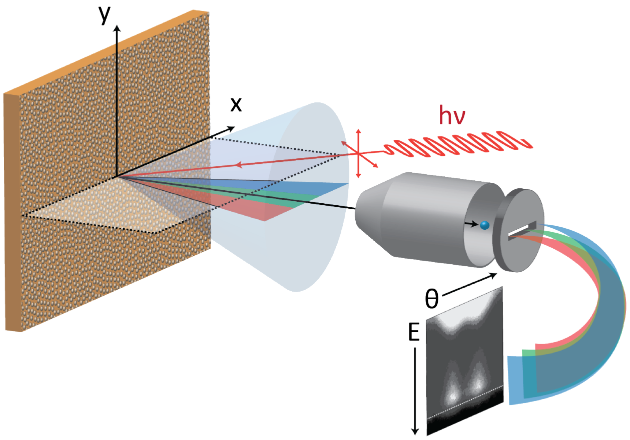

Figure 2.18: Amorphous ARPES experimental setup

where the interaction Hamiltonian for the electron-photon perturbation can be approximated as $H_{int} \sim \frac{e}{mc} \mathbf{A} \cdot \mathbf{p}$ with $\mathbf{A}$ being the vector potential. This is a single step process where ARPES has been more practically described as a three step process: (1) The photon drives and optical transition for the electron in the bulk, (2) the electron travels to the surface dependent on the mean free path l_{mfp}, (3) the electron moves through the surface barrier and is described by a plane wave in vacuum. An approximation can be made for non-interacting systems. The N-electron system can be factorized:

$$|\Psi_{i,j}^N\rangle = A \, |\psi_{i,j}^N\rangle \otimes |\Psi_{i,j}^{N-1}\rangle \tag{2.7}$$

where A is an antisymmetric operator enforcing the Pauli principle. The ψ are the wavefunctions of the photoelectron before and after absorbing the photon and the N-1 system remain unchanged. The non-interacting limit provides a great simplification, now the intensity measured goes as:

$$I_{i \rightarrow f}(\mathbf{k}, \epsilon_f) \propto \left| \langle \psi_f^N | H_{int} | \psi_i^N \rangle \right|^2 \delta(E_f^N - E_i^N - h\nu) \tag{2.8}$$

. The ARPES spectrum for noninteracting materials has a sharp peak that traces out the electronic band dispersion ϵ_k for the single particle wavefunction ψ. Due to the fact the surface breaks translational symmetry the out of plane components of $\mathbf{k}$ are not conserved, however one can recover $k_\perp$ by parameterizing the photoelectron with a free electron dispersion modified by the inner potential V_0. The inner potential can be thought of as the average potential an electron feels in the solid. Therefore,

$$\hbar\mathbf{k}_\perp = \sqrt{2m[E_{kin}cos^2\theta + V_0]}. \tag{2.9}$$

Because E_{kin} depends on the photon energy, we can use a synchrotron with tunable energies to probe the out of plane component and the inner potential is determined employing the fact $E_B(\mathbf{k}_{||}, \mathbf{k}_\perp) = E_B(\mathbf{k}_{||}, \mathbf{k}_\perp + n\mathbf{G}_\perp)$. Because two-dimensional states don't have an out of plane component, changing the photon energy and measuring whether the states disperse or not is a way to distinguish bulk vs surface states. Finally the dipole matrix element, M, was introduced above in the non-interacting picture. Manipulating this matrix element with different polarization's of light is used to understand the orbital character of the bands in the material. Incorporating spin-dependent reflections from a magnetic thin-film due to the exchange interaction enables spin-resolution of the ARPES spectrum.

2.6 Density Functional Theory

One goal of materials science and condensed matter physics is to understand the electronic structure of a material, specifically the properties of electrons and atoms in the material. We do this by calculating the many body wavefunction Ψ, where Ψ contains all the information of the system. The Hamiltonian (in order to solve $\hat{H}\Psi = E\Psi$) for many electrons and nuclei goes as:

$$\hat{H} = -\frac{\hbar^2}{2m_e}\sum_i \nabla_i^2 - \sum_n \frac{\hbar^2}{2M_n}\nabla_n^2 - \sum_{n,i}\frac{Z_n e^2}{|\mathbf{r}_i - \mathbf{R}_n|} + \frac{1}{2}\sum_{i\neq j}\frac{e^2}{|\mathbf{r}_i - \mathbf{r}_j|} + \frac{1}{2}\sum_{n\neq m}\frac{Z_n Z_m e^2}{|\mathbf{R}_n - \mathbf{R}_m|} \tag{2.10}$$

where electrons are denoted by i, j and nuclei by n, m. The terms in Eq. 2.10, left to right, are the kinetic energy of the electrons, the kinetic energy of the nuclei, the interaction between electrons and nuclei, the Coulomb interaction between electrons, and the Coulomb interaction between nuclei. An additional term is added to Eq. 2.10 for relativistic effects such as spin orbit coupling. The term with M_n in the denominator is small meaning it can be discarded, this is the Born-Oppenheimer approximation where the nuclei are treated as fixed and provide a static potential V the electrons feel. Focusing on the Hamiltonian of the electrons (nuclei information taken as parameters) we get:

$$\hat{H}_e = -\frac{\hbar^2}{2m_e}\sum_i \nabla_i^2 - \sum_{n,i} V\left(|\mathbf{r}_i - \mathbf{R}_n|\right) + \frac{1}{2}\sum_{i\neq j}\frac{e^2}{|\mathbf{r}_i - \mathbf{r}_j|} + E_H \tag{2.11}$$

where V is the potential acting on the electrons from the nuclei and E_H are interactions resulting from the nuclei but not critical for describing the electrons. Now with the mean field potential V one can solve for Ψ and given Ψ we obtain observables. The density, $n(\mathbf{r})$, is one such observable defined as:

$$n(\mathbf{r}) = N \int d^3r_2...d^3r_N \Psi^* \left(\mathbf{r}, \mathbf{r}_2, \ldots, \mathbf{r}_N\right) \Psi \left(\mathbf{r}_1, \mathbf{r}_2, \ldots, \mathbf{r}_N\right). \tag{2.12}$$

Using this definition of the density, the total energy is:

$$\langle H \rangle = \langle T \rangle + \langle V_{int} \rangle + E_H + \int d^3r V(\mathbf{r}) n(\mathbf{r}) \tag{2.13}$$

with V_{int} representing the Coulomb interaction among electrons and T is the kinetic energy operator. The ground state energy E_0 corresponding to the the ground state wavefunction Ψ_0 is the one with lowest energy. From this ground state we derive properties such as total energy, electron density, correlation functions, and materials properties. Formulated by Hohenberg, Kohn, and Sham, density functional theory (DFT) has been shown to reduce the quantum many-body problem to one of solving a self consistent field one particle problem [37, 38]. They showed that for an interacting electron system in a static potential the ground state energy can be expressed as a functional of the charge density rather that $E[\Psi\left(\mathbf{r}_1, \mathbf{r}_2, \ldots, \mathbf{r}_N\right)]$. There are a few important statements regarding DFT:

- The ground state energy is written as $E_0[n] = \int d\mathbf{r} v(\mathbf{r}) n(\mathbf{r}) + F[n]$ where $n(\mathbf{r})$ is the electron density, $F[n]$ is a universal functional of density, and $v(\mathbf{r})$ is an external static potential
- $E_0[n]$ is at a minimum for the correct physical ground state density with $N = \int n(\mathbf{r}) d\mathbf{r}$
- $E_0[n]$ and $n(\mathbf{r})$ can be exactly obtained from an associated one body problem in an effective potential $v_{eff}(\mathbf{r})$
- The ground state wavefunction Ψ_0 is uniquely determined by the ground state density n_0

The Kohn-Sham formulation [38] is the most widely used approach to find the one-body equations to exactly determine $n(\mathbf{r})$. The resulting Kohn-Sham equations give the same ground state density and energy as the many-body problem. First the $F[n]$ term contain contributions from the kinetic energy and the electron-electron interaction energy. This can now be split up as:

$$E_0[n] = \int d\mathbf{r} v(\mathbf{r}) n(\mathbf{r}) + T_s[n] + E_{xc}[n] + \frac{e^2}{2} \int \frac{n(\mathbf{r}') n(\mathbf{r}')}{|\mathbf{r} - \mathbf{r}'|} d\mathbf{r} d\mathbf{r}' \tag{2.14}$$

where $T_s[n]$ is the kinetic energy for the non-interacting system and the last term in 2.14 is the interaction energy if exchange and correlations are neglected, $E_{Hartree}$ (self interaction energy of the density). The sum of these two terms should be close to $F[n]$ and the term E_{xc} (the exchange-correlation functional) now contains contains everything beyond $E_{Hartree}$ +

$T_s[n]$. Every term other than E_{xc} in 2.14 involves independent particles. Now we can use the electron density of the fictitious system that is non-interacting coupled with the fact that $E_0[n]$ is minimum for the correct density to vary the non-interacting density to minimize the the energy functional.This this leads to the Kohn-Sham equations:

$$\left(-\frac{\hbar^2}{2m_e}\nabla_i^2 + v(\mathbf{r}) + v_{Hartree}(\mathbf{r}) + v_{xc}(\mathbf{r}) - \epsilon_i\right)\psi_i(\mathbf{r}) = 0 \tag{2.15}$$

with $v_{xc}(\mathbf{r}) = \delta E_{xc}/\delta n(\mathbf{r})$.

This formulation has removed the need for a very complex $3N$ many-body wavefunction however we still don't know E_{xc}. One approach is the local density approximation (LDA) where $E_{xc}[n] = \int n(\mathbf{r})\epsilon_{xc}(n(\mathbf{r}))d\mathbf{r}$ where the exchange correlation energy density is ϵ_{xc} for a uniform electron gas. Another approach is called Generalized gradient approximation (GGA) which accounts for some spatial variation in the functional, $E_{xc}[n] = \int f\left(n(\mathbf{r}), \nabla n(\mathbf{r})\right)d\mathbf{r}$. PBE functionals are one particular approach to GGA [39]. These functionals do not describe strongly correlated electrons well, such as d and f electrons which are localized. LDA and GGA fail because they do not contain orbital information and underestimate the localization. A formulation of E_{xc} called LDA+U takes into account the orbital dependence.

In order to solve the Kohn-Sham equations, the Kohn-Sham orbitals need to be expanded in a set of basis functions. The most common option is to expand in a plane wave basis:

$$\psi_{n,\mathbf{k}}(\mathbf{r}) = \frac{1}{\Omega^{1/2}}\sum_{\mathbf{G}} C_{\mathbf{G}n\mathbf{k}} e^{i(\mathbf{G}+\mathbf{k})\cdot\mathbf{r}} \tag{2.16}$$

where Ω is the volume of the cell, $\mathbf{k}$ is the wavevector, and $\mathbf{G}$ is the reciprocal lattice vector. To be exact the sum over $\mathbf{G}$ would be to infinity, but typically a plane wave cutoff energy is specified that includes enough $\mathbf{G}$ that a total energy convergence is reached. Another approximation introduced in DFT is the psuedopotential method which approximates the core states. The core states contribution to binding energy and bonding in a crystal are negligible. In order to accurately describe the highly spatially varying wavefunctions near the core, many plane waves are needed. By constructing smooth pseudopotentials from the all-electron wave function the number of plane waves is greatly reduced and the computational demand is reduced. The Projector augmented wave (PAW) approach generalizes this by creating an augmentation sphere that smoothly matches to the wavefunctions outside the sphere [40]. A typical DFT workflow goes as: Initial guess of the charge density $n(\mathbf{r})$, then calculate the effective potential v_{KS}, the solve the Kohn-Sham equations 2.15, evaluate the density and total energy, check if it has converged, if yes then output quantities or if no then return to initial guess. This was done using the VASP code [41, 42] on different supercomputers around the country, mainly NERSC and Lawrencium.

2.7 Tight-Binding Hamiltonians

DFT provides full calculations and very accurate results with chemical specificity. However, sometimes it is more useful to consider a simpler representation that provides more physical intuition of the low energy physics. This is a situation where tight-binding models using localized orbitals is beneficial. For a 3D periodic system we can choose the tight-binding orbitals to be

$$\phi_{\mathbf{R}j}(\mathbf{r}) = \varphi(\mathbf{r} - \mathbf{R} - \boldsymbol{\tau}_j) \tag{2.17}$$

where φ is an atomic-like orbital typically s, p, or d-like orbitals with the form of a radial function times a spherical harmonic, $\mathbf{R}$ is a lattice vector, and $\boldsymbol{\tau}$ is a basis vector for where the orbital sits in the unit cell. The tight-binding orbitals are orthonormal $\langle\phi_{\mathbf{R}i}|\phi_{\mathbf{R}'j}\rangle = \delta_{\mathbf{R}\mathbf{R}'}\delta_{ij}$. The Hamiltonian matrix elements are:

$$H_{ij}(\mathbf{R}) = \langle\phi_{\mathbf{R}'i}|H|\phi_{\mathbf{R}'+\mathbf{R}j}\rangle = \langle\phi_{\mathbf{0}i}|H|\phi_{\mathbf{R}j}\rangle \tag{2.18}$$

This matrix element corresponds to a hopping from orbital j in cell $\mathbf{R}' + \mathbf{R}$ to orbital i in $\mathbf{R}'$ (in second quantized notation this is $c^{\dagger}_{\mathbf{R}'i}c_{\mathbf{R}'+\mathbf{R}j}$). We can construct Bloch-like basis functions:

$$|\chi^{\mathbf{k}}_j\rangle = \sum_{\mathbf{R}} e^{i\mathbf{k}\cdot(\mathbf{R}+\boldsymbol{\tau}_j)}\,|\phi_{\mathbf{R}j}\rangle \tag{2.19}$$

with $\langle\chi^{\mathbf{k}}_i|\chi^{\mathbf{k}}_j\rangle = \delta_{ij}$. the Bloch eigenstates expanded in this basis are

$$|\psi_{n\mathbf{k}}\rangle = \sum_j C^{n\mathbf{k}}_j\,|\chi^{\mathbf{k}}_j\rangle \tag{2.20}$$

. The Hamiltonian in this basis is

$$H^{\mathbf{k}}_{ij} = \sum_{\mathbf{R}} e^{i\mathbf{k}\cdot(\mathbf{R}+\boldsymbol{\tau}_j-\boldsymbol{\tau}_i)} H_{ij}\left(\mathbf{R}\right) \tag{2.21}$$

Solving this Hamiltonian reduces to solving the eigenvalue equation $H_{\mathbf{k}} \cdot C_{n\mathbf{k}} = E_{n\mathbf{k}} \cdot C_{n\mathbf{k}}$. To generalize this so we are not just studying spinless electrons, we can double each tight-binding orbital. Now each term has an additional index s to spin up or down along the z axis. The Hamiltonian is now an $L \times L$ matrix with 2×2 blocks and is written as

$$H_{ijss'} = \sum_a h_{ija}\sigma_{ass'} \tag{2.22}$$

where σ are the Pauli matrices.

Chapter 3

Spin-momentum locked surface states in amorphous Bi_2Se_3

This chapter is based on an accepted paper in Nature Materials with explicit permission from all co-authors. The full reference is P. Corbae, S. Ciocys, D. Varjas, E. Kennedy, S. Zeltmann, M. Molina-Ruiz, S. Griffin, C. Jozwiak, Z. Chen, L.-W. Wang, A. M. Minor, M. Scott, A. G. Grushin, A. Lanzara, and F. Hellman, Observation of spin-momentum locked surface states in amorphous $\mathbf{Bi_2Se_3}$ (2020), arXiv:1910.13412 [cond-mat.mtrl-sci].

Much of materials science and condensed matter physics has focused on exploiting crystal symmetries to understand physical properties, headlined by topological phases and spontaneously broken symmetries in quantum materials. The unusual properties of topological materials, such as the robustness to disorder and their quantized electromagnetic responses, have prompted extensive efforts to classify crystalline topological matter. Non-magnetic crystalline topological insulators and metals with topological bands close to the Fermi level are relatively abundant, representing ∼50% of all materials [1, 2, 3], a number that may increase by including magnetic space groups [43]. To identify topological crystals one asks if the band representations of a particular space group admit a trivial insulator limit compatible with the crystal symmetries; if not, the material is labeled topological. The absence of a crystal lattice places amorphous matter outside this classification, even though it is a subset of materials of comparable size to their crystalline counterpart. This raises the question we have set to answer in this work: is there an amorphous topological insulator in the solid state?

Theoretically, amorphous matter can be topological since there are non-spatial symmetries, such as time-reversal symmetry, that protect topological phases. Topological insulator crystals are robust against disorder; topological states do not rely on a periodic crystal lattice at all. In the presence of time reversal invariant disorder the topological states will remain robust and not localize, unless the disorder closes the bulk energy gap, [16, 44]. Therefore, amorphous materials, which lack translational symmetry and cannot be understood in the context of Bloch states, can still present topological properties. Specifically, electrons in a lattice of randomly distributed atoms with strongly disordered electron hoppings—so strong that no memory of a lattice can be used to label the sites—can present topologically protected edge states and quantized Hall conductivity, hallmarks of topological insulators [45, 25, 26, 19, 27, 28, 29, 30, 31]. As a proof of principle, a random array of coupled gyroscopes [19] was designed to act as a mechanical analogue of an amorphous topological state with protected edge oscillating modes, but there has so far been no experimental realization in a solid state material system.

In this work, we have grown and characterized thin films of amorphous Bi_2Se_3. The temperature and field dependent resistance reveals the existence of low dimensional carriers with a reduced bulk contribution. Angle-resolved photoemission (ARPES) and spin-resolved ARPES show a two dimensional surface state with strong spin-momentum locking, the spin-polarization changes with ARPES detection angle which is proportional to the plane-wave momentum k. In its crystalline form Bi_2Se_3 is a textbook three-dimensional topological insulator [46]. We find that amorphous Bi_2Se_3, despite being strongly disordered and lacking translational invariance, hosts two dimensional spin-momentum locked surface states, while nanocrystalline Bi_2Se_3 does not. By numerically simulating a model for amorphous Bi_2Se_3 with trivial and topological phases, we show that dispersive spin-locked surface states exist in amorphous matter with strong spin-orbit coupling, allowing us to discuss their origin.

3.1 Growth and Structure

Amorphous Bi_2Se_3 thin films were thermally evaporated in a UHV chamber with base pressure of 10^{-9} Torr. The films were grown at room temperature from high purity (99.999%) elemental Bi and Se single sources. Stoichiometry of the films was confirmed using XPS (X-ray photoelectron spectroscopy), EDS (Energy dispersive X-ray spectroscopy), and RBS (Rutherford backscattering spectroscopy). High resolution TEM and Fluctuation electron microscopy (FEM) were performed on 10 nm thick Bi_2Se_3 films deposited on a 10 nm thick SiN window. FEM experiments were performed using an FEI TitanX operated at an acceleration voltage of 200 kV. Diffraction images were collected on an Orius CCD system with an exposure time of 0.3 seconds and a camera length of 300 mm. The probe convergence angle was set to 0.51 mrad by adjusting the third condenser lens current, resulting in a probe diameter of 2.2 nm and a probe current of 15.5 pA. Nanodiffraction data were collected as 15-by-15 image stacks (225 total images). Multiple 225-image datasets were collected for both the amorphous and polycrystalline Bi_2Se_3 for statistical averaging. Each data set covered an area on the film of approximately 77-by-77 nm. The first image from each dataset was excluded to avoid including any potential sample damage or contamination in the data resulting from the parked beam. The central beam was covered using a beam stop and the beam position remained constant across all FEM images for each sample. Variation in peak positions and intensities were negligible across data from different locations on a single film. Imaging conditions were held constant for all data collection to prevent variations in microscope alignment. The amorphous structure of the film was confirmed with XRD, Raman spectroscopy, and TEM.

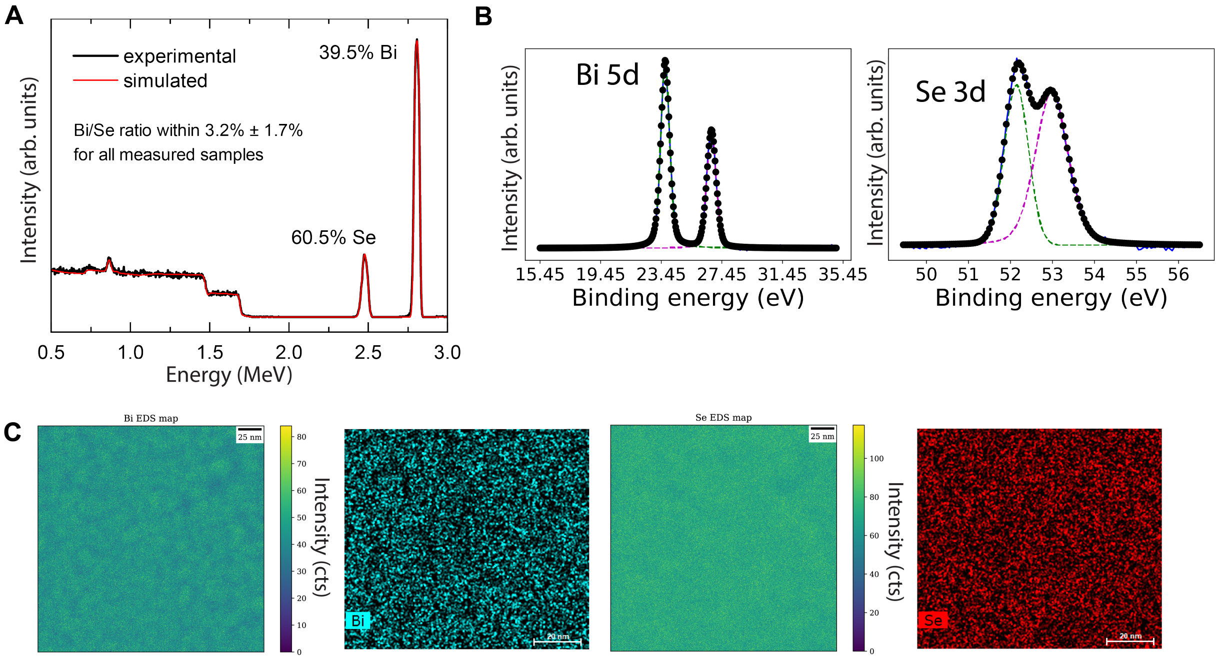

Figure 3.1: Compositional characterization. (a) RBS spectrum fit indicating near stoichiometric films. 0.8 MeV peak is from Oxygen from the thermal oxide between the nitride and the silicon wafer. (b) XPS spectra of the Bi 5d and Se 3d core levels indicating stoichiometric films; the quantitative comparison of these intensities allow us to confirm stoichiometry. (c) EDS compositional mapping performed from STEM HAADF showing no composition gradients and only statistical variations in composition across the sample. There are two Bi maps and two Se maps.

The Bi$_2$Se$_3$ films used for this study were grown on 300 nm of amorphous SiN$_x$ on top of 500 micron Si(100) (10x10x0.5mm^3) using a standard thermal evaporation technique. The films were grown at room temperature with fluxes to match the stoichiometric ratio. The use of an amorphous substrate, low base pressure to reduce impurities, and high growth rates enabled us to grow amorphous films where previous studies only produced nanocrystalline films. Rutherford Backscattering Spectroscopy (RBS) was used to characterize the composition and to look for impurities. RBS, Fig. 3.1(a), shows our films are within ±3% of the exact stoichiometry of 40/60%. X-ray photoemission spectroscopy (XPS) measurements, Fig. 3.1(b), of the Bi 5d and Se 3d core levels prove we are in fact measuring Bi$_2$Se$_3$ films. EDS compositional map characterization, with a lateral resolution of 5 $\AA$, were taken via Scanning transmission electron microscopy high-angle annular dark field (STEM HAADF) show there is no clustering or composition gradients in the films (Fig. 3.1(c)). The EDS results constrain the size of possible Se clusters to be less than or equal to 5 $\AA$. Large-scale real space images are shown in Fig. 3.2(a) to show the lack of crystalline order, such as grain

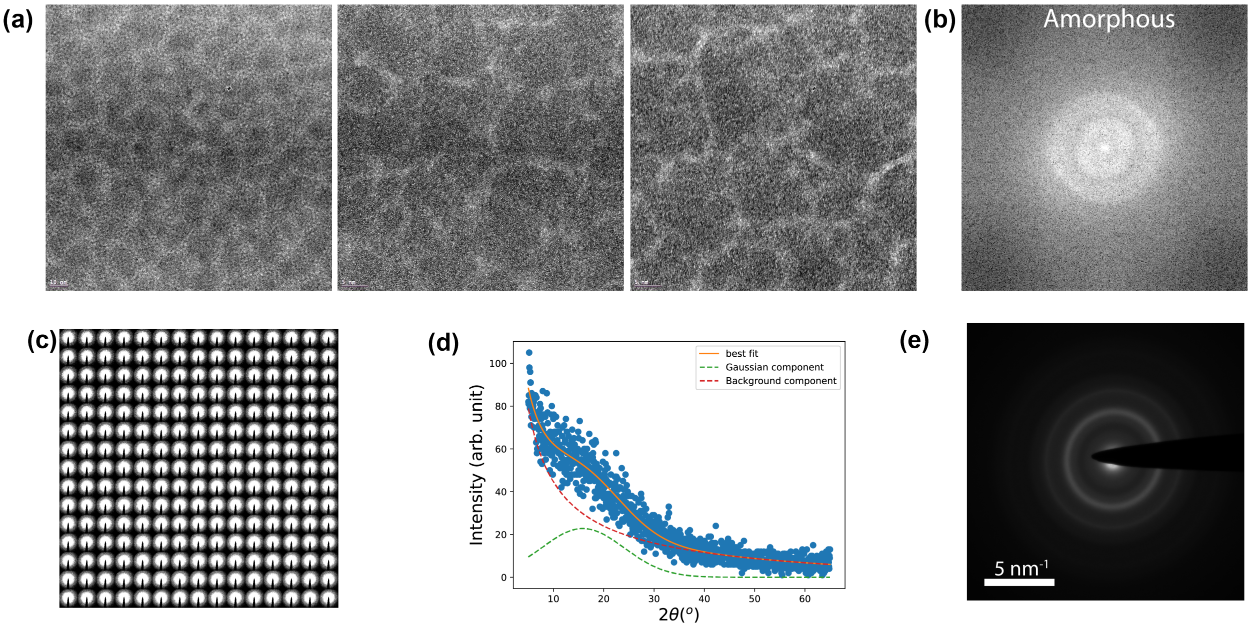

Figure 3.2: Structural characterization. (a) Larger scale HRTEM images showing an absence of any long-range order and the tops of a columnar microstructure (”web”) which is common in amorphous thermally evaporated films such as these and should not be mistaken for grains. Light/dark regions correspond to less/more Bi_2Se_3. (b) FFT of HRTEM in (a). (c) Scanning nanodiffraction with a 2.2 nm diameter probe and a 5 nm step size resulting in areas of approximately 77 nm by 77 nm each. The films are amorphous in all the regions. A diffuse ring attributed to the amorphous structure are observed at each spot. There are no signs of any nanocrystalline order or puddling of crystalline Bi_2Se_3. (d) XRD patterns showing a broad bump at low angle, associated with the short range nearest neighbor ordering of an amorphous films (the amorphous halo, green line), and the contribution from the background (red line). (e) Diffraction pattern of a decapped sample.

boundaries, nanocrystallites, etc. (FFT shown in Fig. 3.2(b)). Given HRTEM probes a very small fraction of the sample, we performed scanning nanodiffraction to determine if the sample is locally amorphous across the entire sample. A montage of all diffraction patterns covering a 77 nm by 77 nm area is shown in Fig. 3.2(c). Each diffraction pattern shows a diffuse ring and no diffraction spots, proving our sample isn't just locally amorphous but amorphous across the entire sample. The diffraction patterns showed the same ring pattern that was seen in other HRTEM samples. XRD, Fig. 3.2(d), shows no peaks in the spectrum that correspond to crystalline Bi_2Se_3 interatomic planes and at low 2θ values, where θ is the incident angle, there is an amorphous hump. In order to check that the decap process was not crystallizing our films we performed HRTEM on samples undergoing the same decap procedures Fig. 3.2(e). Raman was performed with a Renishaw inVia 488 nm Ar/Ne laser using linearly polarized light and operating at 7-60 $\mu W/\mu m^2$.

High resolution transmission electron microscopy (HRTEM) on amorphous Bi_2Se_3 thin films, Fig. 3.3(a), shows no signs of crystalline order or even precursor lattice fringes which would have suggested incipient nanocrystals were starting to form. The diffraction pattern in the Fig. 3.3(a) inset is typical of amorphous materials with well-defined nearest neighbor coordination and inter-atomic distance. There is a diffuse but well-defined inner ring corresponding to the short-range ordering of nearest neighbors. To further ensure we are not probing nanocrystalline regions, scanning nanodiffraction was performed and shown in Fig. 3.3(b). Four select beam spots each separated by 5 nm show amorphous speckle [48] and no signs of Bragg peaks. The speckle visible in the scanning nanodiffraction images from Bi_2Se_3 is associated with local ordering and orientations of clusters of atoms, which correspond to near- and off-Bragg conditions. The diffracted intensity originates from nanoscale volumes within the sample. The speckle observed across the Bi_2Se_3 diffraction images is highly uniform, which is indicative of many randomly oriented nanoscale clusters of atoms with short range ordering in the amorphous structure. The diffracted intensity versus scattering vector k for eight different regions is shown in Fig. 3.3(c), with a single peak corresponding to the diffuse diffraction ring. The nearest neighbor spacing set by the ring is 2.39 Å, compared to 3.2 Å in crystalline Bi_2Se_3 [49]. To further investigate the structure, fluctuation electron microscopy (FEM) was used to determine the variance of the diffracted intensity, from which medium range order (MRO) can be extracted and compared to that of nanocrystalline Bi_2Se_3. FEM is a scanning nanodiffraction technique that probes MRO in amorphous materials through statistical analysis of the variance in diffracted intensity as a function of scattering vector across many diffraction patterns. Fig. 3.3(d) presents the normalized variance of the diffracted intensity for amorphous Bi_2Se_3 and nanocrystalline Bi_2Se_3. The variance in diffracted intensity is a measure of the squared deviation (or fluctuations) in the intensity from the mean intensity at a specific scattering vector. The variance is normalized by dividing by the mean intensity for the specific scattering vector [50]. Bragg scattering from crystalline regions induces large variations in intensity compared to scattering from amorphous materials. The nanocrystalline sample shows a very large variance with multiple strong peaks due to crystalline order while the amorphous sample does not, providing clear evidence the amorphous samples are indeed amorphous. The electron diffraction scan shows a diffuse diffraction ring over the entire sample; together with the HRTEM images which show no sign of nanocrystals or precursor lattice fringes, these prove the amorphous nature of the film. The samples require selenium capping and subsequent decapping in order to preserve the surface for ARPES. To verify that the decapping process does not generate nanocrystalline regions, Fig. 3.3(e) displays a XRD 2θ scan for amorphous Bi_2Se_3, showing a strong substrate peak and a low angle bump typical of amorphous materials which lack long range order but still maintain a well defined interatomic spacing. Electron diffraction confirms the decapped film is still amorphous. The Raman spectrum, Fig. 3.3(f), shows one broad peak between $135\,\mathrm{cm}^{-1}$ and $174\,\mathrm{cm}^{-1}$. As the laser power increases two peaks

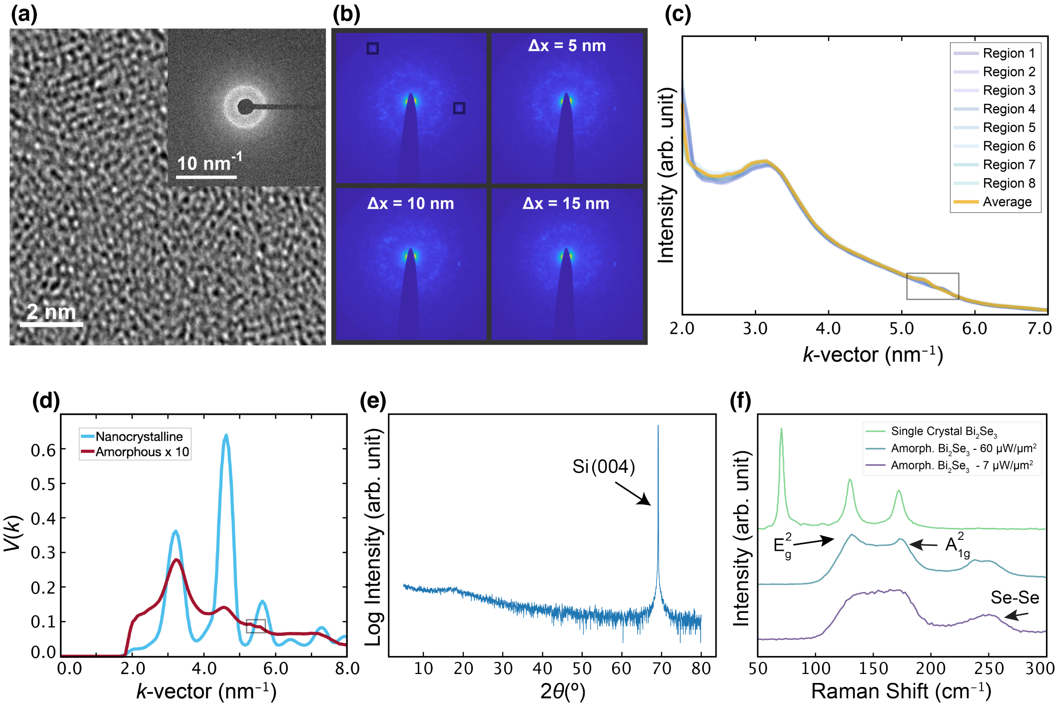

Figure 3.3: Structural and spectral evidence for the amorphous atomic structure of Bi_2Se_3. (a) HRTEM image. Inset: Diffraction pattern for the amorphous Bi_2Se_3 films. We observe a diffuse ring due to the amorphous nature of the film. (b) Scanning nanodiffraction patterns taken with a beam spot of 2 nm separated by 5 nm. Each spot shows a speckled ring and no signs of crystallinity. Detector defects are highlighted by a box throughout the figure. (c) A 1D intensity cut, $I(k)$, for 8 different regions as well as the average intensity. A peak is observed $\sim 3.2\,\text{nm}^{-1}$. Detector defects are highlighted by a box. (d) FEM variance, $V(k)$, as a function of scattering vector k for amorphous and nanocrystalline Bi_2Se_3. The nanocrystalline sample exhibits substantial variation in intensity for a given k-vector from crystalline Bragg diffraction peaks, the amorphous sample shows little variation. Detector defects are highlighted by a box. (e) A XRD 2θ scan for amorphous Bi_2Se_3 after the Se decap showing the same broad low angle peak near 17 ^{o} and no signs of incipient crystallization. The substrate peak is labeled. (f) Raman spectra for 50 nm amorphous Bi_2Se_3 films using a 488 nm laser. The peaks are labeled with their respective Raman mode. Different curves (blue and purple) correspond to different laser powers, showing the bulk Raman modes become more well-defined and do not shift. Crystalline data [47] (green curve) is overlayed to show the lack of a Van der Waal mode at $\sim$72 cm^{-1} in the amorphous films and the extra peak in the amorphous film at $\sim$250 cm^{-1} which is associated with Se-Se bonding.

can be resolved, which correspond to the bulk E_g^2 and A_{1g}^2 vibrational modes, respectively. The A_{1g}^1 van der Waals mode at $\sim 72\,\mathrm{cm}^{-1}$, which is created by the layered structure of the crystal, is absent in our samples. Instead, we observe a peak at $238\,\mathrm{cm}^{-1}$ not present in crystalline Bi_2Se_3, which we attribute to amorphous Se-Se bonding as seen in Se films [51]. The Raman peaks broaden compared to the crystalline system; the full width half maximum of the E_g^2 mode is $23.7\,\mathrm{cm}^{-1}$ compared to $8.0\,\mathrm{cm}^{-1}$ [52]. Additionally, EDS maps confirm there is no clustering of Bi and Se in our films and show minimal spatial variations, further confirming that the films do not contain clusters or nanocrystals. These results show that our samples are amorphous and, while lacking a layered structure with a van der Waals gap, have a local bonding environment similar to the crystalline phase. Moreover, the decapping process important for the following sections does not induce crystallization.

Fig. 3.4 presents structural data regarding the nanocrystalline Bi_2Se_3 thin films we grew at slower rates. We find that the films are within 1 at% of stoichiometric. These films show obvious lattice fringes and Bragg diffraction in the scanning nanodiffraction. The $R(T)$ curve has an insulating behaviour and no metallic component (3.5(e)). The weak antilocalization does not produce a sharp cusp at low fields as we see in our amorphous films and the fitting doesn't produce α values that correspond to two dimensional conductance channels. Finally, there is no dispersion in the ARPES spectrum and no obvious midgap states (3.10(f)). These results are in stark contrast to our amorphous data, further solidifying the fact we are probing the spin-momentum locked surface states in amorphous Bi_2Se_3.

3.2 Transport

The amorphous Bi_2Se_3 samples $\rho(T)$ was measured using a four point probe. The samples were grown as a bar using a metal mask onto pre-deposited Au(5 nm)/Cr(2 nm) contacts to ensure ohmic contact (shown in Fig. 3.5(a) inset). Magnetrotransport was measured in the Van der Pauw configuration with samples grown onto pre-deposited Au(5 nm)/Cr(2 nm) contacts.

Figure 3.5(a,b) shows the temperature dependent transport data for different thicknesses in amorphous Bi_2Se_3, as well as that for the nanocrystalline Bi_2Se_3 (Fig. 3.5(e)). The resistivity, $\rho(T)$, is shown in Fig. 3.5(a). The $\rho(T)$ values (~70-140mΩ·cm) are larger than the crystalline system (~1-2mΩ·cm [53]). The amorphous system also demonstrates a much weaker T dependence than the crystalline counterpart [54]. As is typical in amorphous metals, the carrier mean free path is determined more by disorder-driven localization than phonon interactions, leading to a largely temperature independent resistivity [55]. Moreover the high ρ and the weak temperature dependence is inconsistent with either a purely metallic or purely insulating material, and suggestive of a metallic surface on a localized bulk state. Due to the potential metallic surface, we consider the resistance in Fig. 3.5(b), $R(T) = \rho(T) \cdot L/wt$, where t is the film thickness. Again, the $R(T)$ values are greatly increased compared to the crystal (~5-250mΩ for similar thicknesses [53]). While $R(T)$ is largely temperature independent, the thicker films show a more pronounced bulk behavior at high

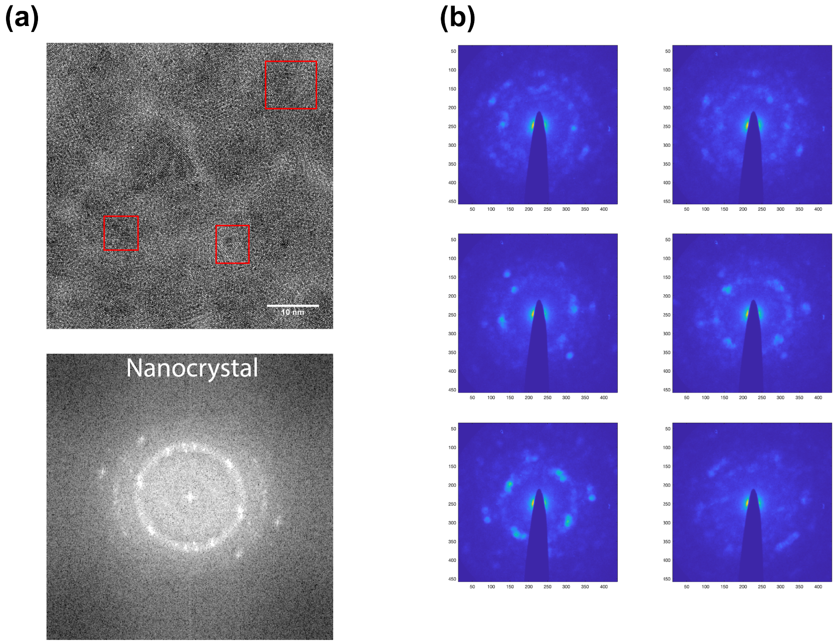

Figure 3.4: Structural data for nanocrystalline Bi_2Se_3. (a) Real space HRTEM image showing lattice fringes and crystalline order (red box) and FFT of HRTEM showing bright spots from crystalline order. (b) Scanning nanodiffraction patterns from several places in the sample (2 nm spot size as discussed above) with obvious Bragg diffraction spots.

temperature [56], seen in the inset of Fig. 3.5(b). $R(T)$ for each thickness saturates at low temperature; this is in contrast to crystalline Bi_2Se_3 which shows a low temperature upswing. The low temperature values range from $\sim \frac{h}{3e^2}$ to $\frac{h}{e^2}$, similar to bulk insulating topological insulators when gated to bring the Fermi level into the bulk gap [57, 58, 59, 60, 61]. The low temperature $R(T)$ values vary with thickness, possibly a result of small variations in composition between sample thicknesses ($<$ 1 at% deviation) or thickness dependent defect formation [53]. The effect of composition needs to be explored further. Transport and ARPES results were reproducible on different samples. The $R(T)$ data was fit using a two channel conductance model [62] represented by the dashed curves in Fig. 3.5(b). The model requires parallel contributions from an insulating, variable range hopping bulk and metallic surface states, and provides an overall good fit to the data. Below around 150 K, the surface contribution dominates for films of all thicknesses. These results indicate that the surface state contribution to conduction is metallic and dominant over a large temperature range for the amorphous samples. The conductivity in nanocrystalline Bi_2Se_3 (shown in Fig. 3.5(e)) drops over the entire temperature range and does not display any metallic behavior with temperature.

The magnetoconductance (MC) provides another means to probe the transport. Fig.

3.5(c) shows MC data for a 140 nm film, revealing a sharp decrease in the low field ΔG (< 2 T) at low temperatures which is typical of weak anti-localization (WAL), consistent with a metallic surface state in amorphous Bi_2Se_3 [63]. This is in contrast to other non-magnetic amorphous systems which are topologically trivial and show a MC increase due to weak localization [64]. The case of positive MC is likely due to a diminished spin-orbit coupling (SOC) effect where disorder closes the mobility gap or a local environment that does not produce topological states. In amorphous Bi_2Se_3 the nearest neighbor distance is smaller than in the crystal, acting similar to pressure, which has been shown to lead to a topological gap [65]. In amorphous Bi_2Se_3, due to strong SOC, backscattering is suppressed when a field is absent and time reversal symmetry is present. When time-reversal symmetry is broken with the application of a magnetic field, backscattering increases leading to a positive MR. The magnetoconductance can be fit with the standard Hikami-Larkin-Nagaoka (HLN) formula for WAL [66], $\Delta G\left(B\right) = \alpha\frac{e^2}{\pi h}\left[\Psi\left(\frac{\hbar}{4eBl_\phi^2}+\frac{1}{2}\right) - \ln\left(\frac{\hbar}{4eBl_\phi^2}\right)\right]$ where Ψ is the Digamma function, B is the out-of-plane field, l_ϕ (the phase coherence length) and α are used as fitting parameters. According to this model, each conductance channel with a π Berry phase should contribute an $\alpha = -1/2$ factor to ΔG [67]. Fitting our low field data, Fig. 3.5(d), at 2 K gives a value of $\alpha = -0.81$, suggesting we have two decoupled surface states [68]. At 20 K, $\alpha = -0.51$ suggesting the surface states are coupled to a bulk state, causing the entire film to act effectively as one channel, as seen in crystalline Bi_2Se_3 from 2 nm to 100 nm [69, 70]. As the temperature increases the WAL contribution is diminished. Based on Hall measurements, the two-dimensional carrier density is $n_{2D} = 2.8 \times 10^{14}$ cm^{-2} and the three-dimensional carrier density is $n_{3D} = 1.9 \times 10^{19}$ cm^{-3}, leading to a mobility of 21.8 cm^2/Vs. According to the Ioffe-Regel criterion amorphous Bi_2Se_3 has $k_F l \sim 1$ [71] and have similar μ,n_{3D} values reported in the bulk insulating BiSbTeSe solid solution [72]. Additionally, the calculated mean free path at 2 K is $\sim$ 1 nm. This n_{3D} likely places E_F into the conduction band (seen in ARPES presented below), although the depth depends on the effective mass [71]. Since our system is amorphous the bulk carriers are expected to be localized and provide little contribution to the transport, leading to the observed high ρ. The observed behavior in the amorphous Bi_2Se_3 sheet resistance and MR is a result of metallic surface states that dominates over a wide range of temperatures.

The $R\left(T\right)$ data was fit using a two-channel conductance model. The total conductance is the parallel sum of bulk conductance and a metallic surface conductance. The bulk conductance consists of variable range hopping, while the surface conductance is metallic,

$$\begin{aligned} G_T &= 1/R(T) = G_{Bulk} + G_{Surface} &\quad (3.1)\\ G_{Bulk} &= Ce^{(-T_0/T)^{1/4}} &\quad (3.2)\\ G_{Surface} &= (A + BT)^{-1}. &\quad (3.3) \end{aligned}$$

This model gives good fits to the resistance data and allows us to extract the surface state contribution, $G_{surface}/G_{total}$, as seen in Fig. 3.6(c).

The bulk conductance behaves as expected for different thicknesses, especially at low temperature where extrinsic effects have been frozen out, as seen in Fig. 3.6(a). As thickness

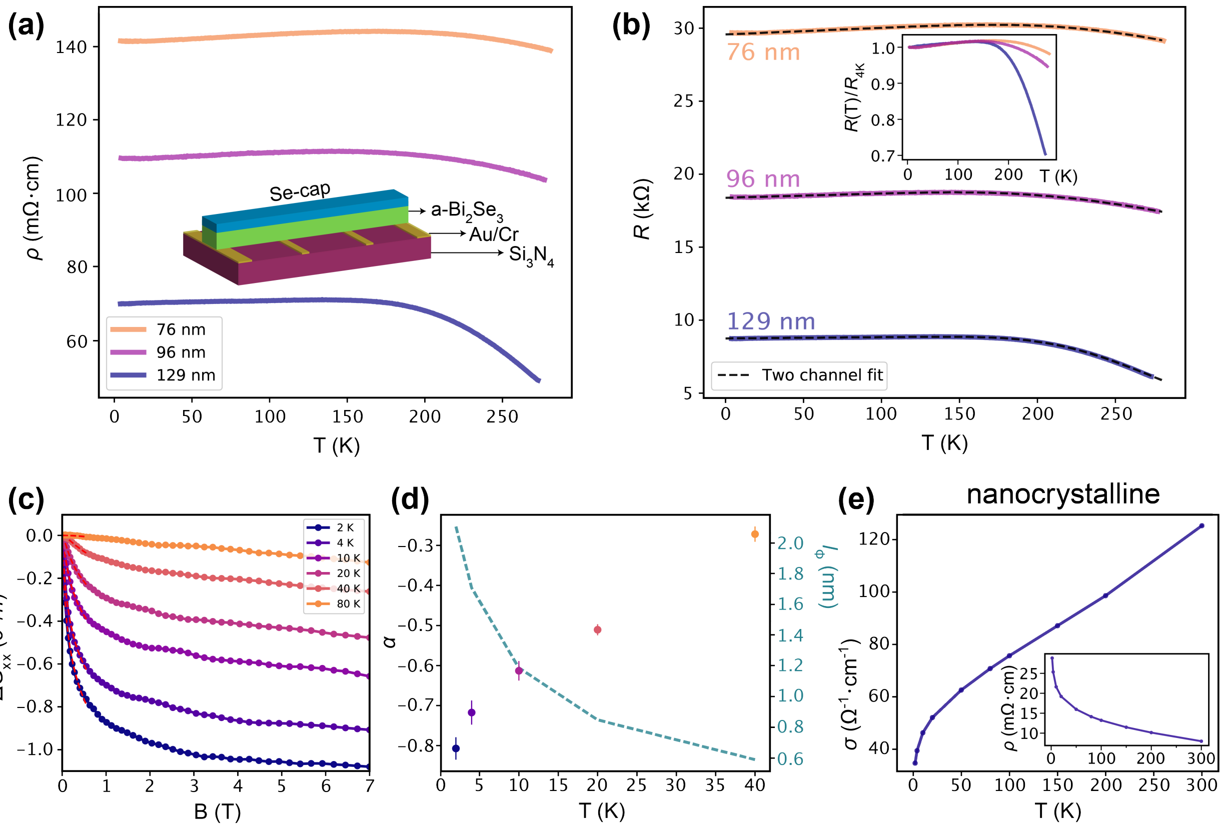

Figure 3.5: Electron transport in amorphous Bi_2Se_3 (a) $\rho(T)$ for 76 nm, 96 nm and 129 nm films. All films show a high resistivity with little temperature dependence. Inset: Schematic of the structure used to measure resistivity. (b) The resistance for 76 nm, 96 nm and 129 nm films. All films show high temperature VRH behavior (inset) and low temperature metallic behavior in R with a low temperature saturation. Two-channel conductance fits the data reasonably well indicating a metallic surface and insulating VRH bulk behavior. (c) Conductance change as a function of the magnetic field for a 120 nm film, measured at 2 K, 4 K, 10 K, 20 K, 40 K and 80 K, where $\Delta G_{xx} = G(B) - G(0)$. The deep cusp in the low field regime is characteristic of the WAL effect. (d) Magnetoconductance HLN fits showing α values indicating decoupled surface surface states at 2 K and a single conduction channel at 20 K. The dephasing length l_ϕ decreases with increasing temperature. (e) Nanocrystalline Bi_2Se_3 conductivity as a function of temperature. The conductivity drops with decreasing temperature. Resistivity is shown in the inset.

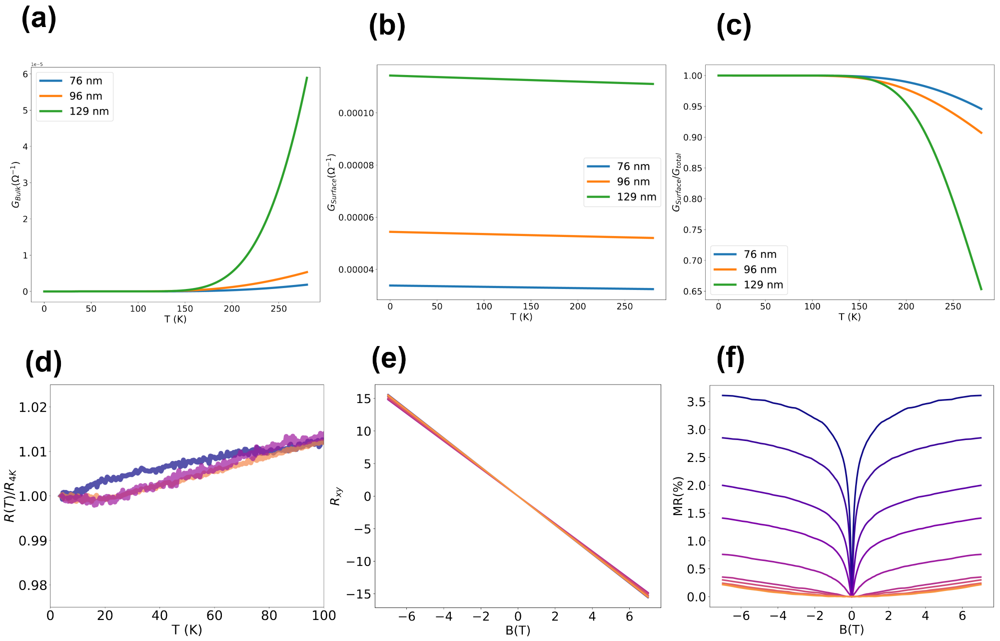

Figure 3.6: Resistivity analysis for the three films of different thicknesses using a two-conductance channel fit as described in the text, with the bulk modeled as VRH and the surface as a metallic layer. (a) Bulk conductance as a function of temperature for various thicknesses of amorphous Bi$_2$Se$_3$. The bulk conductance goes to 0 as the temperature decreases, indicating a localized bulk. (b) G$_{surface}$ vs. temperature. (c) Surface state conductance contributions taken from the ratio of G_{surf}/G_{total}. Below ~150K, the metallic surface dominates the total conductance. (d) At low temperatures the resistance saturates indicative of conduction dominated by the surface. (e) The variation of Hall resistance as a function of magnetic field at various temperatures (2-300 K)in amorphous Bi$_2$Se$_3$ showing a linear behavior indicative of electron carriers in the surface (metallic) layer. (f) Magnetoresistance in 140 nm amorphous Bi$_2$Se$_3$ (dark to light is increasing temperature).

goes from 129 nm to 76 nm the bulk conductance drops (bulk resistance increases). The surface conductance is separated by a factor of three, Fig. 3.6(b). We find for the 76 nm, 96 nm, and the 129 nm the B (electron-phonon coupling) parameter to be 4.4, 3.4, and 1.3 Ω/K, respectively. These values are smaller than previously reported value of $\sim 6\Omega/K$ in the bulk insulating TI BiSbTeSe$_2$ [56]. At low temperatures (<20 K), resistivity values begin to decrease in slope and level off indicating at lower temperatures the values saturate, Fig. 3.6(d). The resistivity data exhibits metallic and low temperature behavior that is consistent with multiple channels of conduction. Fig. 3.6(e) shows the Hall resistance as a function of magnetic field at various temperatures in amorphous Bi$_2$Se$_3$. Hall resistance is linear with magnetic field and is nearly temperature independent. This indicates that transport is determined by a single carrier (electron type) and the lack of temperature dependence implies that carrier density is unaffected by temperature as expected for a metallic surface state. The magnetoresistance is shown in Fig. 3.6(f).

3.3 Theory

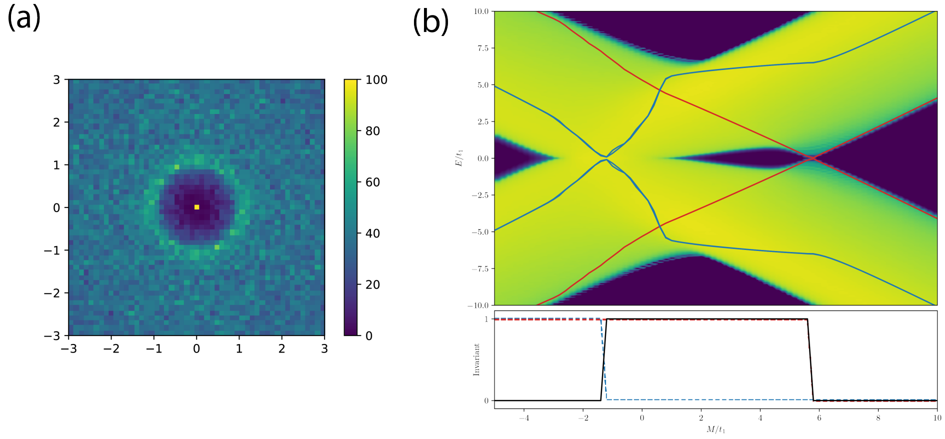

Figure 3.7: (a) Tight Binding Structure. Histogram of the relative positions of atoms in the xy plane for a one-unit thick slice of the amorphous lattice structure used in the numerics. The correlation hole for distances under one and an annular peak corresponding to close packing are visible. (b) Topological phase transitions in the tight-binding model. Top panel: total density of states as a function of onsite potential M in a sample with periodic boundary conditions, brighter colors indicate higher density on a logarithmic scale. Overlaid the eigenvalues of the effective Hamiltonian $H_{\mathrm{e}ff}(\mathbf{0})$ (red) and $H_{\mathrm{e}ff}(\infty)$ (blue). Bottom panel: number of pairs of occupied inversion odd states in $H_{\mathrm{e}ff}(\mathbf{0})$ (red dashed), $H_{\mathrm{e}ff}(\infty)$ (blue dashed) and their total modulo 2 giving the $\mathbb{Z}_2$ topological invariant (solid black).

Amorphous materials are not expected to have any electronic states with well-defined momenta, but are nonetheless known to support metallic conduction and superconductivity. However, since the nearest neighbor distance is well defined (inset Fig. 3.3(a)), there exists a good reciprocal length scale. If sharp spectral features are observed, which is the case in our ARPES measurements, there exist states with good momentum quantum numbers since this corresponds to the overlap of the electronic wave-functions with plane waves of well defined k, modulated by matrix elements. The coordinates θ and ϕ are experimentally measured and refer to the respective angles of photoemission from the sample surface. The plane wave components k_x and k_y are proportional to θ and ϕ at small angles, where θ is the azimuthal angle and ϕ is the polar angle. In our work we refer to spin-momentum locking as the spin asymmetry around zero angle since at small angles, the momentum of the plane wave and the detection angle are proportional.

To interpret our experimental data and determine if it is consistent with a topological bulk we developed a numerical model that realizes a Dirac-like state in the absence of crystalline symmetry. Motivated by the similarity of local environments between the crystalline and amorphous Bi$_2$Se$_3$ found in Fig. 3.6, we use an amorphous variant of the three-dimensional four-band (spin-1/2 x 2-orbital) BHZ model [46, 45]. From the model we numerically obtain a spin resolved spectral function, shown in Fig. 3.10(a,b), for both the trivial and topological phase of amorphous Bi$_2$Se$_3$, respectively. While inversion is expected to be an average bulk symmetry in amorphous solids, it will be broken by the surface, allowing us to include a surface onsite potential that breaks this symmetry. As for the crystal surface states, this term spin-splits trivial surface states at E_F. This surface potential depends on the details of the surface termination (such as dangling bonds, Se vacancies, or surface reconstruction [73, 74]) and can tune the Dirac point to arbitrary binding energies [75, 76, 77]. However, it does not affect the bulk topological properties. In the trivial phase we observe spin-split states symmetric around $\phi = 0$ above the gap, while in the topological state a Dirac cone pinned to $\phi = 0$ is visible, guaranteed by time-reversal symmetry, spanning the bulk gap (see Fig. 3.10(a,b)).

The Hamiltonian used to describe amorphous Bi$_2$Se$_3$ features direction-dependent spin-orbit hoppings set by the normalized hopping vector $\hat{\mathbf{d}}$ and is the sum of onsite and hopping terms

$$H_{\text{onsite}} = m\sigma_0\tau_z, \tag{3.4}$$

$$H_{\text{hop}}(\hat{\mathbf{d}}) = it_1(\hat{\mathbf{d}}\cdot\boldsymbol{\sigma})\tau_x + t_2\sigma_0\tau_z \tag{3.5}$$

where σ_i and τ_i are the spin and orbital Pauli matrices respectively, m sets the splitting between the local s and p-like orbitals, t_1 is the spin-orbit hopping, and t_2 is the normal hopping amplitude. In the crystalline case this Hamiltonian correctly reproduces key features of the topologically nontrivial bands closest to the Fermi level [46]. We implement this tight-binding model on large systems of short-range correlated amorphous structures and investigate the topological surface states by calculating spectral functions using the Kernel Polynomial Method [78, 79].

To construct an amorphous system, we randomly add atomic sites in a fixed volume from an uncorrelated uniform distribution. Treating atoms as hard spheres, we reject atoms closer than distance one to existing atoms and this procedure is performed until the goal density is reached. This procedure minimizes density fluctuations and produces a peak in the radial distribution function at the typical nearest neighboring distance, matching the distribution function of an amorphous system more closely than independent uniformly distributed points, see Fig. 3.7(a). We then connect each neighbor to its 6 other nearest neighbors with hoppings of fixed magnitude, preserving the key features of octahedral coordination and fixed bond lengths, as in crystalline Bi$_2$Se$_3$. We do not distinguish Bi and Se atoms in this simplified effective model. The Hamiltonian of the system contains an onsite and a hopping term,

$$\begin{aligned} H &= H_{\text{onsite}} + H_{\text{hop}}(\hat{\mathbf{d}}) && (3.6)\\ H_{\text{onsite}} &= m\sigma_0\tau_z, && (3.7)\\ H_{\text{hop}}(\hat{\mathbf{d}}) &= it_1(\hat{\mathbf{d}}\cdot\sigma)\tau_x + t_2\sigma_0\tau_z. && (3.8) \end{aligned}$$

where $\hat{\mathbf{d}}$ is the normalized nearest neighbor vector.

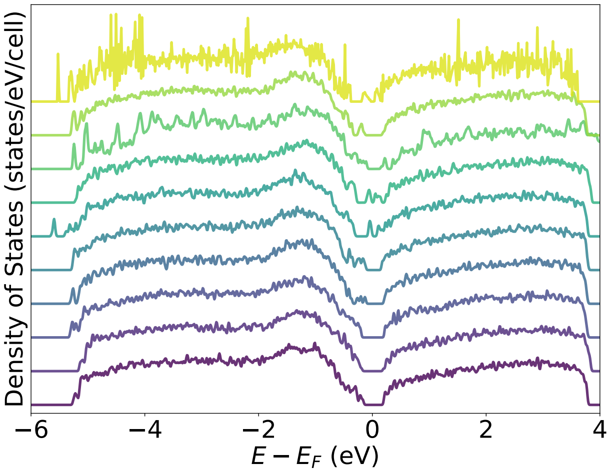

Figure 3.8: Density of states for ten amorphous structures. The mean bulk gap is ~ 300 meV.

To calculate the ground state (or finite temperature) expectation values of observables in large systems we use the Kernel Polynomial Method (KPM) [80]. The observable relevant to photoemission spectroscopy, sensitive to the topological nature of the system, is the energy E and momentum $\mathbf{k}$ dependent surface spectral function,

$$A(\mathbf{k}, E) = \sum_l \langle \mathbf{k}, l|\delta(H - E)|\mathbf{k}, l\rangle \qquad (3.9)$$

where $|\mathbf{k}, l\rangle$ is a plane wave state of wavevector $\mathbf{k}$ nonzero only in the local orbital l. When we restrict the local part of the plane wave vectors to a certain spin or orbital polarization the spectral function is spin-resolved, we consider the ±1 eigenstates of the local spin y operator $\sigma_y\tau_z$. We use the Kwant [81] software package to generate the tight-binding Hamiltonians and calculate spectral functions using the code published in Ref. [79]. The results shown were obtained using a sample of dimensions $80 \times 80 \times 20$ and 0.4 average density, 51200 sites in total. The bulk parameter values are (in arbitrary units) $t_1 = 1$, $t_2 = 1$, $M = 4$ for the topological and $M = 6.5$ for the trivial case, and we use a constant electric field in the surface layer of thickness $d = 3$ with electric field strengths $E_z = -1$. To obtain the surface spectral function we used plane waves with constant $|k| = 7.5$ in the xz plane and exponential decay in the z direction with $\mathrm{I}mk_z = 0.5i$.

The emergence of a single cone around Γ in the topological case can be understood as a consequence of average rotational invariance. This average imposes a rotationally symmetric dispersion relation of the topological surface state. The existence of a single topological state with an averaged Fermi velocity in amorphous topological insulators has been observed in simulations and in synthetic systems, see e.g. Refs [45, 19].

Lastly, we point out that our 3D amorphous topological insulator model is adiabatically connected to others discussed in the literature [45, 82]. Nontrivial bulk topology (beyond the presence of edge states) in these systems has been demonstrated by calculating the Witten effect [83, 82]. Here we take a different approach to demonstrate bulk topology, based on effective momentum-space Hamiltonian invariants [24, 30, 31]. We rely on the average inversion symmetry of the bulk amorphous model, with the local inversion operator given by τ_z. Similar to inversion-symmetric crystalline topological insulators, the ± 1 inversion eigenvalues at time-reversal invariant momenta (TRIM) come in Kramers-pairs. Counting the number of pairs of -1 eigenvalues at all TRIM in the occupied subspace modulo 2 gives the $\mathbb{Z}_2$ topological invariant. In the amorphous system, momentum-space has the topology of a 3-sphere [30, 31], with the only two TRIM being $\mathbf{k} = \mathbf{0}$ and $\boldsymbol{\infty}$. Hence we calculate the topological invariant by the number of pairs of occupied inversion-odd states in the effective Hamiltonians $H_{eff}(\mathbf{0})$ and $H_{eff}(\boldsymbol{\infty})$. We illustrate this in Fig. 3.7(b), where we show the topological phase transitions through the gap closings in the total density of states, as well as the effective Hamiltonian eigenvalues at the TRIM. These gap closings coincide with the changes in the number of inversion odd occupied states, clearly indicating a topological regime for intermediate values of the on-site term M. The numerical calculations were performed using KPM, with Fermi level at $E_F = 0$, on a sample of size $50 \times 50 \times 50$ with periodic boundary conditions. The structure and parameter values are the same as above.

Ten representative amorphous structures were set up by constructing a box with 54 Bi atoms and 81 Se atoms which underwent a melting step (at 2000 K), a quenching step, and an annealing step (at 200 K) in a canonical ensemble, followed by a further relaxation step. To calculate the band gap we performed Density Functional Theory calculations of 10 representative amorphous structures. The results of our calculations are shown in Fig. 3.8. Several of the structures have mid- gap defect states (the upper five), which are often present in the electronic structure of amorphous materials [84]. Therefore, to estimate the bandgap, we neglected any structures with clear mid-gap states as their appearance is not uniform across the series. Averaging the bandgaps of the five remaining structures gives a bandgap of 299 meV. We note that many of these also contain extended Urbach tails and so this value is a lower bound. Finally, since GGA typically underestimates the bandgap we also compare previous calculations of crystalline Bi_2Se_3 for different exchange correlation functionals and experimentally determined values. Surprisingly, Park et al. [85] found that the PBE gap of crystalline Bi_2Se_3 is 336 meV while HSE06 underestimates the gap at 37 meV compared to the experimental gap of 300 meV. We conclude, therefore, that PBE is an appropriate choice for accurate gap calculations.

3.4 ARPES

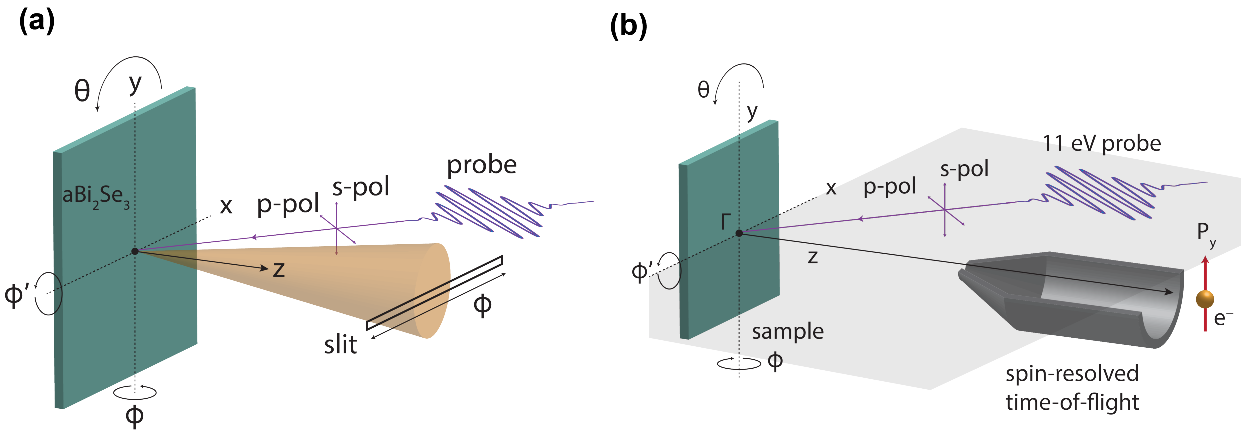

Figure 3.9: ARPES/SARPES experimental geometry. ϕ is the detector angle away from the z-axis in which the z-axis is defined as the normal vector from the sample surface. ϕ' is the sample tilt angle and θ is the azimuthal angle. The measured spin polarization is P$_y$ in which y points along the axis of rotation used in the experiment, parallel to the sample surface.

We performed ARPES at the Advanced Light Source MAESTRO (7.0.2) and MERLIN (4.0.3) beamlines with photon energies in the range of 65 - 125 eV. The experimental geometry used to obtain the ARPES/SARPES spectra is shown in Fig. 3.9. ϕ is the detector angle away from the z-axis, ϕ' is the sample tilt angle, and θ is the azimuthal rotation angle. ARPES results taken on different samples and at different beamlines produce the same results. The decap procedure does not create any crystalline order in our samples. The spin-resolved spectra were acquired from a high-efficiency and high-resolution spin-resolved time-of-flight (TOF) spectrometer that utilizes the spin-dependent reflection from a magnetic thin-film due to the exchange interaction [86]. The light source for the spin measurements was a Lumeras 11eV Xenon gas-cell laser with 1MHz repetition rate [87]. Synchrotron ARPES measurements and spin-resolved measurements were taken at 20K and 75K, respectively. ARPES was analyzed using the PyARPES software package [88].

Fig. 3.10(c) displays the raw ARPES spectrum as a function of energy and emission angle ϕ at a specific θ, a momentum space slice that intersects Γ $(\phi = 0^o)$. The dispersion revealed here in amorphous Bi$_2$Se$_3$ marks the first observation of an amorphous band structure with sharp, momentum-dependent features. Notably, the dispersion exhibits two vertical features at the Fermi level crossing the bulk gap. The raw spectrum reveals an intensity peak near E_F starting at $-0.2\,$eV and a sharp rise in intensity below $-0.5\,$eV. The increased intensity of the surface states near E_F may be due to photoemission enhancement from the less-visible bulk conduction band. The increased intensity below $-0.5\,$eV coincides with a less-dispersive

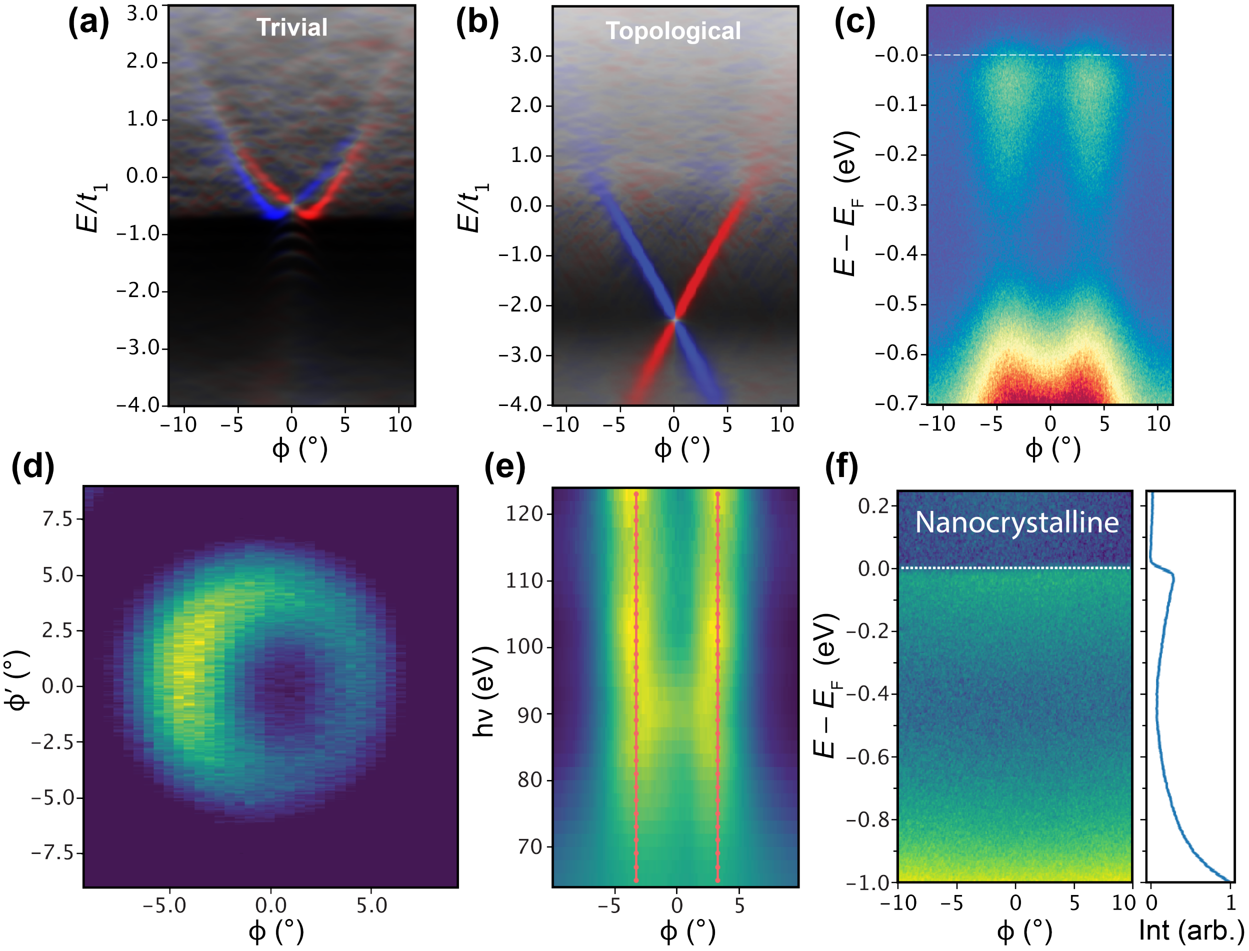

Figure 3.10: ARPES spectra of electronic states in amorphous Bi$_2$Se$_3$ A calculated spin-resolved surface spectral function as a function of ϕ for the (a) trivial and (b) topological phase. In the topological phase the Dirac point is low in binding energies and Rashba spin-split states develop near the Fermi level. (c) ARPES spectrum E vs. ϕ taken at normal emission at $h\nu = 117.5\,\text{eV}$. The spectrum reveals vertical states that cross the bulk gap and meet at $-0.6\,\text{eV}$ near the bulk valence states. (d) The ring-like in-plane Fermi surface. ϕ are the angles simultaneously collected by the detector referenced to normal incidence at a given sample tilt ϕ'. (e) $h\nu$ vs. ϕ with binding energy integrated from $-0.6\,\text{eV}$ to the Fermi level and normalized by photon energy. The $h\nu$ vs. ϕ plot displays no photon energy dependence of the photoemission angle. Red dotted lines are fit to intensity peaks in the $h\nu$ vs. ϕ spectrum. (f) ARPES spectrum E vs. ϕ for nanocrystalline Bi$_2$Se$_3$ showing an obvious lack of dispersion.

band which is most likely the bulk valence band. The exact bottom of the conduction band

and top of the valence band is obscured in the ARPES spectra due to intrinsic broadening. However, using angle-integrated photoemission, we can roughly estimate the band gap to be ~350 meV, consistent with the calculated DOS from amorphous structures using ab-initio molecular dynamics (299 meV).

Fig. 3.10(d) presents the experimental in-plane Fermi surface in amorphous Bi_2Se_3. The annular Fermi surface is consistent with crystalline Bi_2Se_3, where the dispersion associated surface state in Fig. 3.10(c) produces a ring at the Fermi surface. The dot product of the p-orbital axis and the experimental coordinates is well defined and should lead to a similar scenario as seen in the crystalline case in which p-polarized light couples asymmetrical across $k = 0$, leading to the observed orbital effect in the Fermi surface. To confirm that these states are localized to the surface, in Fig. 3.10(e) we show the photon energy plotted versus emission angle ϕ. Due to conservation of energy, photon energy ($h\nu$) and k^2 of the photoemitted electron are nearly-proportional for large $h\nu$, and related by $\hbar^2k^2/2m = h\nu - W - E_b$ where W is the work function of the material and E_b is the binding energy. In the plane (k^2, ϕ) the states are nearly independent of photon energy (red lines in Fig. 3.10(e)). For a 3D amorphous system (or even a 3D polycrystalline system), bulk states must be spherically symmetric and independent of ϕ due to the absence of an average preferred direction. Therefore the strong ϕ-dependence and $h\nu$-independence suggests the electrons are not from the bulk and instead originate from surface states. These observations motivate us to interpret these states as two-dimensional surface states. It is important to note that there exist significant density of states at the Fermi energy associated with the 2D surface states, confirming a two-dimensional transport channel as determined by our magnetoresistance measurements.

In order to understand the size of the bulk electronic energy gap, we consider the photoemission spectrum seen in Fig. 3.11. Fig. 3.11(a) presents the ARPES spectrum at a photon energy of 72 eV which demonstrates a bulk band gap as seen by the absence of intensity in the blue area and exhibits strong surface state intensity as seen by the presence of the broad vertical feature at an emission angle of -3 degrees. The black arrows indicate an additional flat band feature near the Fermi level that we attribute to the bulk conduction band. Fig. 3.11(b) provides the angle integrated intensity curves (integrating over -12 to 12 degrees) for three ranges of photon energy: 55 – 79 eV (dark grey), 80 – 96 eV (blue), 97 – 125 eV (red). The dark grey and red curves show heightened surface state intensity seen in the intensity near the Fermi level and between binding energies -0.1 and -0.5 eV. The surface state intensity is not present in the blue curves due to photon energy dependent matrix elements, revealing the true bulk valence band below -0.5 eV. By taking the energy derivative of these curves, Fig. 3.11(c) better illustrates the band edge energy for the bulk conduction and valence bands by revealing the onset of changes in the spectral intensity as a function of binding energy. The flat bulk conduction band is visible in the dark grey energy range and upturn near -0.03 eV marks the band edge as indicated by the top arrow. The bottom arrow points to the downturn just above -0.5 eV marking the valence band edge. The Fermi energy appears as a sharp dip centered at 0.0 eV and should be ignored. This provides a rough estimate of the band gap as approximately 350 meV and is subject

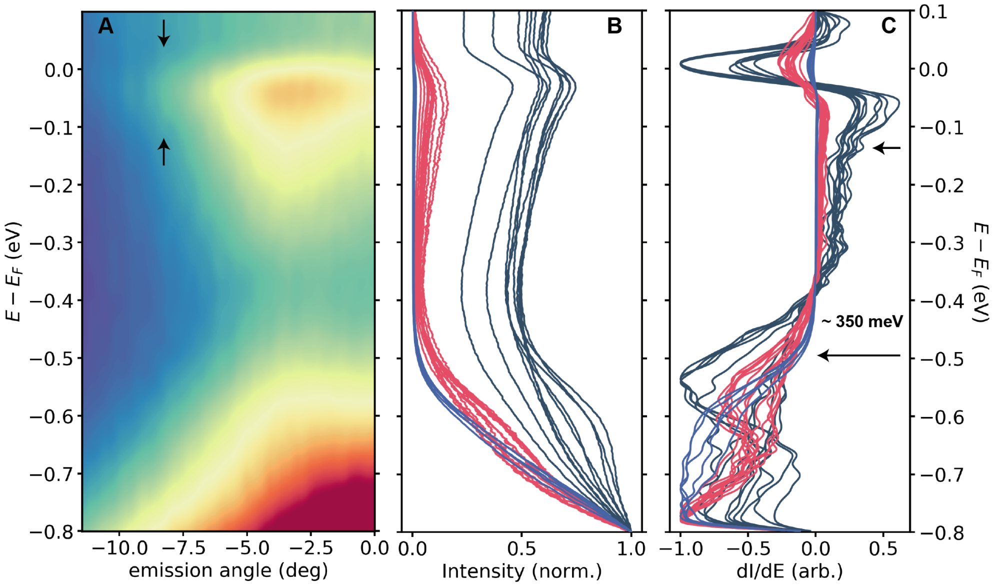

Figure 3.11: (a) ARPES spectra at 72 eV demonstrating strong spectral intensity of surface features as well as a bulk band gap shown as an absence of intensity in the blue region. Arrows indicate a flat band near the Fermi level that we attribute to the bulk conduction band enhanced by the overlap with the surface state at the Fermi level. (b) Angle integrated spectral intensity vs. binding energy for photon energies between 55-125 eV. Dark grey (55-75 eV) and red (98-125 eV) exhibit strong surface state intensity as observed by the intensity near the Fermi level and the onset of spectral weight near -0.6 eV. Blue (76-97 eV) demonstrates very little surface state intensity revealing the bulk valence band below -0.5 eV. (c) dI/dE vs. binding energy allows us to extract estimates for the bulk E_g. The arrows indicate an upturn near -0.03 eV which corresponds to the flat conduction band edge and a downturn near -0.5 eV which corresponds to the valence band edge suggesting a bulk band gap of roughly 350 meV.

to intrinsic energy broadening which would lead to an underestimation of the band gap as well as possible unobserved bulk bands due to poor photoemission matrix elements which (if lying within the presumed band gap region) would lead to an overestimation of the band gap. Momentum distributions curves (MDC) are presented in Fig. 3.12(a). The MDCs show two peaks in spectral intensity in the bulk gap corresponding to the surface state dispersion, providing evidence that these surface states are not gapped. The large peak in intensity at lower binding energies can be attributed to the valence states. To get a better view of the surface states, Fig. 3.12(b) presents an ARPES spectrum normalized by binding energy in the gap and Fig. 3.12(c) presents the peak location and angular width of the intensity across binding energy. If the increased intensity of these vertical features, at the Fermi level and again near -0.4 eV seen in the raw spectrum (see Fig. 3.12(d)), were due to surface Rashba

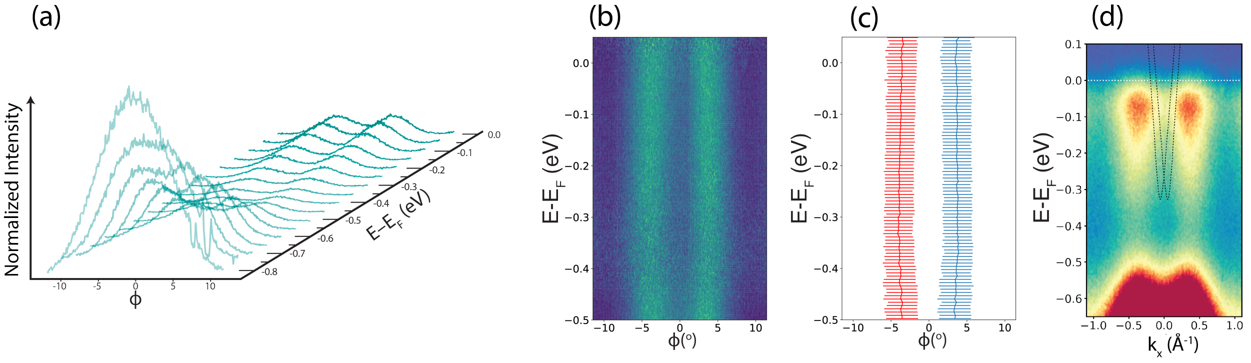

Figure 3.12: Midgap surface states. (a) MDCs of the surface state dispersion taken at $h\nu =$ 117.5 eV. Increasing spectral intensity at higher binding energies is associated with the bulk valence state. (b) Emission angle of surface states across the gap. ARPES spectrum taken at $h\nu = 117.5$ eV normalized by binding energy to show the binding energy independence of the photoemission clearly. (c) Fits to the peak locations and widths across binding energy to the spectral intensity in (b). (d) Comparison between BiTeI Rashba bands from [89](dashed lines) which have a Rashba splitting of $0.051\mathring{A}^{-1}$, and the present data for amorphous $\mathrm{Bi_2Se_3}$. This comparison shows that the Rashba splitting would have to be drastically larger than any reported value to match our observed spectra.

states and not a topological state, then the Rashba splitting of the conduction band near the Fermi level would be larger than the Rashba splitting in the valence band, since the orbitals contributing to the conduction band are of different orbital character, they experience stronger Rashba splitting from the SOC [90]. Fig. 3.12, on the other hand demonstrates that the vertical features comprising the surface state remain at a constant photoemission angle over greater than 500 meV on both sides of the gap, indicating that the intensity near the valence band and near the conduction band are of the same origin. For this reason, the ARPES is consistent with a topological surface state crossing the gap with a Dirac node buried in the valence and not to energy broadened conduction and valence Rashba states. This is further confirmed by the spin-ARPES data, which shows that the spin polarization in the gap region flips towards the valence band. The distinct spin-polarization of the in-gap states from the near-E_F states indicates that the spin signal in the gap is not from inelastic scattering smearing the conduction band states. The spin-integrated ARPES spectrum taken in the spin time-of-flight system is shown in figure 3.13(a). The spectrum is broadened at low photon energy, a feature of the amorphous electronic structure that will addressed in future works (Fig. 3.13(d,e)). Photon energy dependent broadening and the 11eV spectrum are consistent with our higher energy spectra, the spin degree of freedom allows us to disentangle the key features in the electronic structure. Fig. 3.13(b,c) shows the spectrum E vs. $k \cdot a$ where a is the nearest neighbor distance for both amorphous and crystalline samples.

Multiplying k by a allows us to compare the dispersions and effective "Brillouin zone" sizes since $k \cdot a$ is adimensional. The amorphous Fermi surface is about double the crystalline.

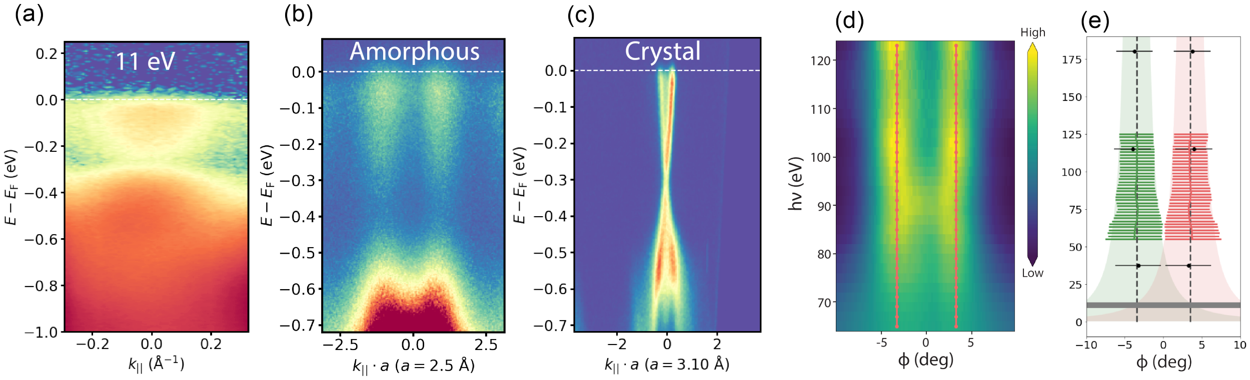

Figure 3.13: Additional ARPES data on Bi_2Se_3. (a) Spectrum taken at 11 eV in the spin-TOF system. The spectrum broadens substantially at low photon energy. (b) Comparing the "Brillouin zones" for amorphous and crystalline Bi_2Se_3. The momentum is scaled by the nearest neighbor distance. (c) Momentum broadening as a function of photon energy. Second panel shows MDC linewidth of Fig. 3.10(e) (green and red). The broadening increases at lower photon energies and can be extrapolated by an inverse square root dependence on photon energy. At 11 eV (grey bar) the two independent features are blurred together to form a single broad Fermi surface feature. This explains the reason for the observed 11eV spectrum in (a)

3.5 SARPES

The presence of strong SOC added to broken inversion symmetry at the surface in our system should lead to a spin texture. Fig. 3.14 shows spin-resolved angle-resolved photoemission spectroscopy taken with 11 eV photons. We observe an anti-symmetric spin-polarization, the first observation in an amorphous system to the best of our knowledge. The spin-polarized energy distribution curves (EDCs) with p-polarized light are shown in Fig. 3.14(a) at $\phi = -6,\ 0$ and 6^o. The spin-polarization is measured by the relative difference between spin-up and spin-down photoelectrons weighted by the Sherman function (S) of the detector in the form $P_y = S * (I_\uparrow - I_\downarrow) / (I_\uparrow + I_\downarrow)$. The most evident feature from the three spin-polarized EDCs is the large positive polarization between -0.6 and 0.0 eV that reaches a maximum of $\sim$50%. This large polarization offset is due to spin-dependent photoemission matrix elements (SMEs) in which SOC leads to selective emission of electrons with a particular spin-state. This is observed in crystalline Bi_2Se_3 near the upper Dirac cone with similar intensity [91].

In order to uncover the intrinsic spin texture (i.e. the sign of the polarization) within the SME background we follow a similar background subtraction to Ref. [91]. Fig. 3.14(b)

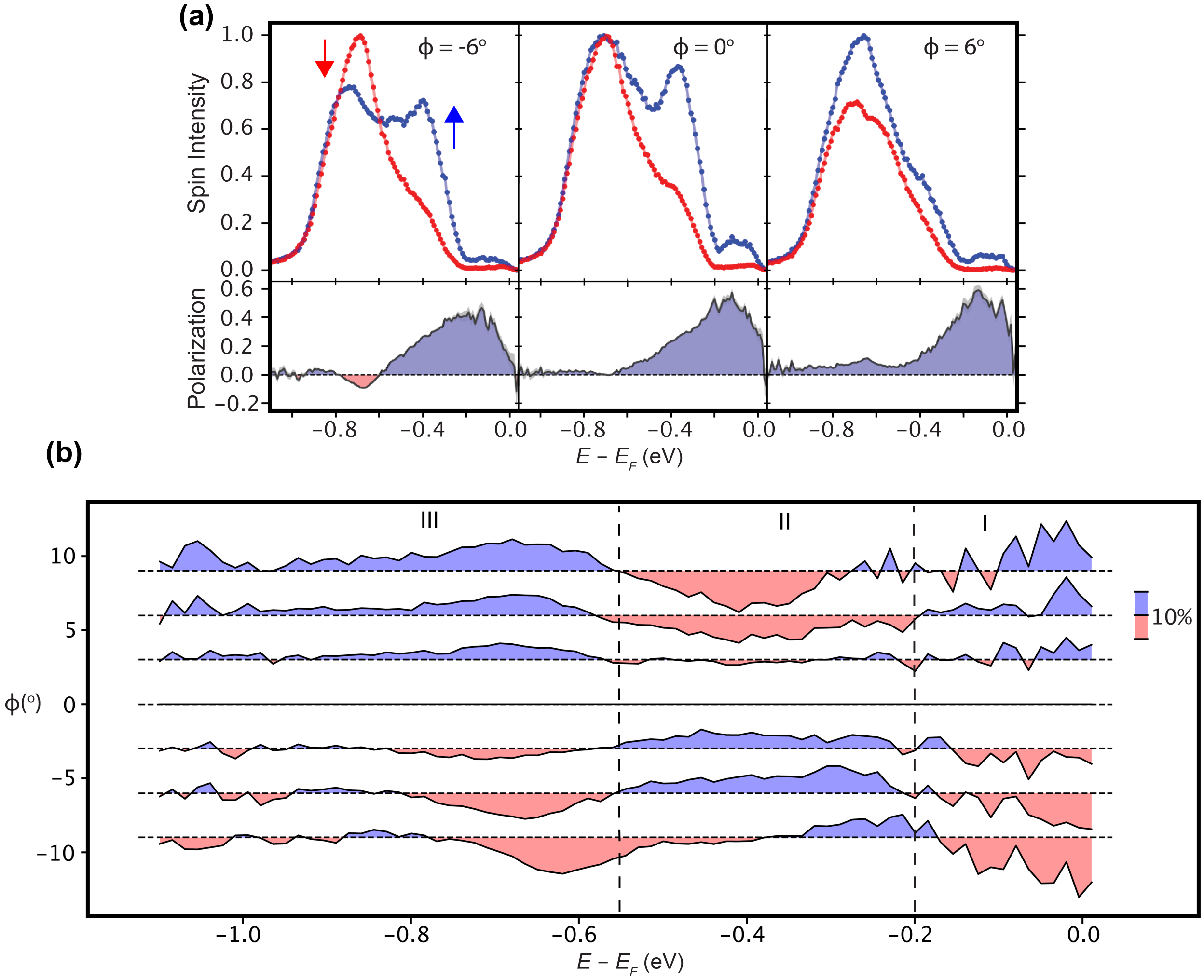

Figure 3.14: Spin-resolved ARPES spectra of electronic states in amorphous Bi_2Se_3 (a) Spin-resolved EDC's taken at $\phi = -6^o$, Γ, and $\phi = 6^o$, respectively. The spin contributions at each binding energy vary with respect to $\phi = 0^o$. (b) Spin-resolved EDC map of E vs ϕ with SME background subtraction taken from $\phi = -9^o$ to $\phi = 9^o$. The spin polarization switches from red to blue (or vice versa on the other side of Γ) at $-0.2\,\text{eV}$ and from blue to red at $-0.55\,\text{eV}$.

presents the spin polarization as a function of binding energy and ϕ after performing the background subtraction. From this spin-polarized map, three ranges of binding energy demonstrate distinct anti-symmetric spin polarizations with respect to ϕ: E_F to $-0.20\,\mathrm{eV}$ (region I), $-0.20\,\mathrm{eV}$ to $-0.55\,\mathrm{eV}$ (region II), and $-0.55\,\mathrm{eV}$ to $-0.75\,\mathrm{eV}$ (region III). The spin polarization has a magnitude of $\pm 15\%$ and changes sign between these ranges as a function of binding energy. By comparing Fig. 3.14(b) with the spin-integrated spectrum in Fig. 3.10(c) we see that region I corresponds to the conduction band, region III corresponds to the valence band, and region II corresponds to the in-gap states. The in-gap states of region II have opposite spin-polarization to both the conduction band and valence band, suggesting that these states are indeed separate features from region I and III and not a consequence of inelastic scattering from region I states or from local variations in composition. The measured spin-polarization matches the expected spin-polarization from our tight-binding model shown in Fig. 3.10(b) for the topological case with region I representing the spin texture of the trivial Rashba split bulk states near the Fermi level, region II representing the spin texture of the upper Dirac cone of the topological surface state in the bulk band-gap, and region III representing the spin texture of the lower Dirac cone within the bulk valence band. We conclude that the two-dimensional surface states form a node around $-0.55\,\mathrm{eV}$, and the anti-symmetric spin-resolved spectrum around Γ at E_F is associated with trivial states with a large component at the surface stemming from Rashba-type spin-splitting in our system, as seen also in crystalline $\mathrm{Bi_2Se_3}$ [92].

The raw spin-polarized spectrum collected from the S-ARPES contains a large spin-polarized background associated with spin matrix elements (SME) from -600 meV to 0 meV that reaches approximately 60% at maximum. The magnitude of the SME is an interesting phenomenon on its own with possible applications, needing further investigation. Moreover, over the course of the entire measurement (the spectra at each angle took approximately 3 hours), the background maximum increased slightly. We captured each spectra in non-sequential order with respect to angle in order to determine that the increase in background was due to time-related changes to the sample in vacuum and was not dependent on emission angle. Since the underlying spin signal is a fraction of the SME background, normalizing by the SME peak value provides a more accurate spin-map after background subtraction. Similar to Fig. 3.14(c), Fig. 3.15 displays four spin-polarized maps on amorphous $\mathrm{Bi_2Se_3}$. Fig. 3.15(a) is the total spin polarization including the SME after normalizing to the SME peak intensity. Only the spin polarization of the bands near -700 meV are distinguishable. To remove the SME to determine the underlying spin-polarization, we subtract the spin-polarized spectra at $\phi = 0$ since time-reversal symmetry requires spin-degeneracy at zero-momentum. Fig. 3.15(b) and Fig. 3.15(c) show the SME subtracted spin-maps without and with SME peak normalization, respectively. The difference between these two maps is subtle and suggests that the normalization process is not drastically affecting the results. Lastly, if, instead of subtracting the normalized map with the $\phi = 0$ spectrum, we subtract off the averaged spectrum with respect to ϕ, then we get Fig. 3.14(c). The difference between Fig. 3.14(c) and Fig. 3.14(d) are even less noticeable, suggesting that the final spin-maps are robust to background subtraction methods. Fig. S12 and S15 show additional ARPES data.

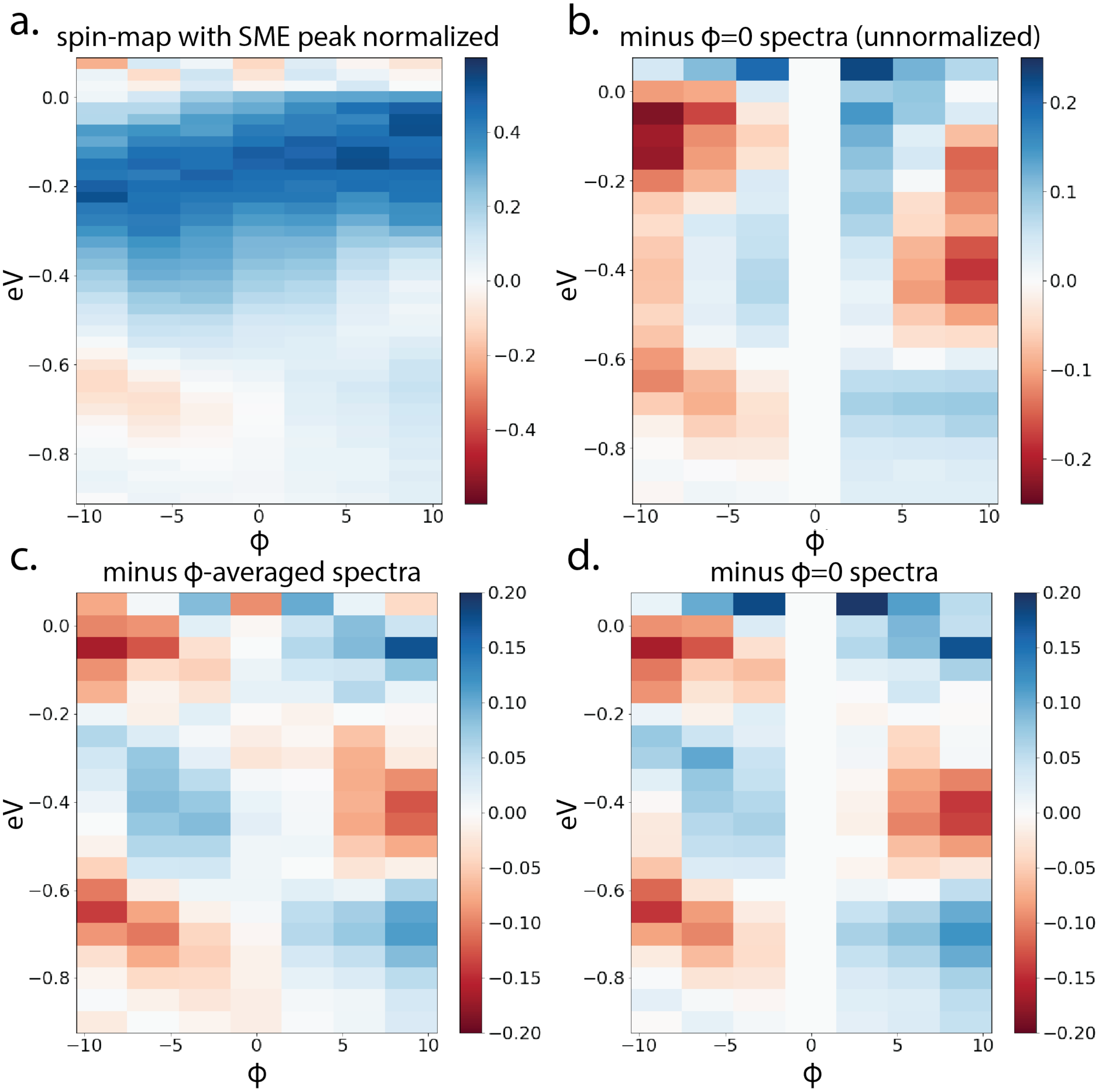

Figure 3.15: Spin map background subtraction. (a) spin-map before SME subtraction in which the spectra at each ϕ are normalized by peak SME value. (b) SME subtracted spin-map using $\phi = 0$ spectrum for subtraction, no SME peak normalization. (c) SME subtracted spin-map using ϕ-integrated spectrum as background, SME peak normalized. (d) SME subtracted spin-map using $\phi = 0$ spectrum as background, SME peak normalized.

3.6 Conclusions

Electron microscopy in Fig. 3.3 confirms the structure is amorphous with a shortened interatomic spacing. Fig. 3.5 shows the carriers in the system are weakly anti-localized, suggesting two-dimensional decoupled metallic conductance channels. ARPES, Fig. 3.10, shows dispersive surface states that cross the bulk gap. The midgap states are spin polarized shown via SARPES in Fig. 3.14. Our data is consistent with a spin-momentum locked two-dimensional surface state for which we discuss two main origins: non-topological and topological. In the latter, a topological bulk state in amorphous Bi_2Se_3 would produce the dispersive, spin-momentum locked surface states we observe. In this interpretation, the topological surface states cross the bulk gap, as in Fig. 3.10(b), forming a Dirac state similar to the surface states observed in related topological insulator crystals [93]. In the amorphous case however, the Dirac point can be hidden underneath the bulk valence band due to a strong surface potential, as discussed above (recall that, although a Dirac node crossing is a protected feature of topological insulators, the binding energy of the node is not). Additionally, from our tight-binding model, we expect trivial spin-split states of Rashba-type to develop at the Fermi level, with opposite polarization from the topological surface state, due to broken inversion symmetry at the surface, as observed in Ref. [92]; this will be discussed below. For the topological explanation to be viable, we need to discard that the amorphous spectrum is a result of averaging over nanocrystalline domains. Fig. 3.10(f) shows the resulting spectrum from nanocrystalline Bi_2Se_3 in which averaging over randomly rotated domains leads to angle-independent photoemission. Our spectra is also distinct from the crystalline spectrum [92], where the amorphous Bi_2Se_3 spectral features extend further in ϕ than the crystalline case.

Although the topological origin of the surface state is consistent with our data, it is important to discuss non-topological origins like two-dimensional Rashba states, and features that are not captured by our model. Spin resolved ARPES shows an anti-symmetric spin-polarization on either side of the nodal region observed at $-0.55\,\mathrm{eV}$. In the topological scenario these would be attributed to a spin-polarized two-dimensional topological surface state. Another possible explanation is that the lack of inversion symmetry at the surface gives rise to trivial Rashba states, as in Fig. 3.10(a), and a spin-polarization in the bulk conduction and valence bands. If the spin texture were a result of Rashba splitting, then each near-vertical branch would need to be a single parabolic-like band that returns to the Fermi level. This is because each near-vertical feature has only one spin character. This Rashba interpretation could be plausible if the parabolic dispersion was obscured by the momentum broadening. Indeed, the spectra are broadened by the atomic disorder as well as the presence of vacancies and dangling bonds at the surface, which are a significant source of final state scattering. However, it would also imply a gigantic Rashba momentum offset of $k_0 \approx 0.4$ Å^{-1}. For reference, the giant Rashba splitting in bulk BiTeI is demonstrated by $k_0 = 0.051$ Å^{-1} [94], nearly a factor of 10 smaller. While we cannot definitively settle on either explanation, the topological scenario seems simpler as it could explain the spin switching of all regions in Fig. 3.14, and because it seems that a gigantic Rashba splitting is needed to explain our results otherwise. Regardless of the explanation, our observation of well-defined, spin-momentum locked dispersing surface states opens a new direction to characterize amorphous matter, and to search for new materials with advantageous properties, such as spin-momentum locking.

In the raw spectra ARPES features are perceived as near-vertical, yet the underlying bands need not have infinite electron velocity. They are broadened to the point that the electron velocity is hard to quantify yet we can appreciate that they do have an increased Fermi velocity compared to the crystal. It is known that the surface environment can affect the location of the Dirac node and the curvature of the bands significantly in the crystalline case [95]. We expect that this is exacerbated in the amorphous case due to the presence of dangling bonds. In fact, amorphous materials have been predicted to experience large band renormalizations that lead to backbending of the dispersions as well as vertical features [96, 97, 98]. Combining these factors, it is reasonable to expect large deviations in the amorphous surface state dispersion from the crystalline case, both in the observed band velocity from renormalizations and burying of the Dirac node in the valence band. However, the spin-polarization allowed us to argue that states crossing the gap-like region (II) are unrelated to broadening caused by inelastic scattering of conduction band electrons. Specifically, the spin polarization reverses sign going down in energy from the conduction band (I) at E_F into the the gap-like region (II), reversing again in the valence band (III) states (i.e. unrelated to broadening caused by inelastic scattering of conduction band electrons) lie within the gap. We do this by revealing the sign reversals of the spin near E_F, in the gap-like region, and again in the valence band.

TEM and Raman data suggests that the typical local structure of the amorphous system are comparable to the crystalline case, indicating that a possible condition to preserve the topological nature of the bulk in the amorphous state is to retain a local ordering similar to that of the crystal [30]. However, it should be noted that there is no continuous pathway from the crystalline phase to amorphous phase but instead a discontinuous phase transformation associated with the nucleation of crystalline domains [99]. The nucleation process explains why nanocrystalline $\mathrm{Bi_2Se_3}$ has been shown to be topologically trivial, Fig. 3.5(e), due to the presence of grain boundaries and other structural defects [100]. The impact of coupling strengths and local field environments can be assessed theoretically via ab-initio calculations to refine the Hamiltonian modeling of amorphous topological materials [46]. This approach can be extended to amorphous material systems without topological crystalline counterparts, where local ordering coupled with disorder and strong SOC can mix energy levels to produce a topologically nontrivial electronic structure.

In conclusion, we have found that amorphous $\mathrm{Bi_2Se_3}$ hosts a dispersing two-dimensional metallic surface state with spin-momentum locking. This experimental observation of spin-momentum locked surface states in an amorphous solid state system highlights that searching for new quantum materials with advantageous properties, such spin-momentum locked states, or topological properties should not be restricted to crystalline solids. Our work provides a study of an amorphous solid state system with chemical specificity and local bonding environments, a system which can be implemented into devices. To the best of our knowledge there have been no previous reports of ARPES/SARPES on an amorphous solid. Our results represent the first step towards realizing, in real materials, recently proposed non-crystalline topological phases [24, 30] that lie outside the known classification schemes for topological crystalline matter [101, 2, 3, 43, 102] and that may be more robust than their crystalline counterparts [31]. We expect our work to motivate an effort to understand topological amorphous matter, enabling materials discovery that can provide a path towards affordable and better implementation into modern thin film processes.

Chapter 4

ARPES study of dispersive features in amorphous materials

This chapter is based on a submitted manuscript with explicit permission from all co-authors. The author list is Samuel T. Ciocys, Quentin Marsal, Paul Corbae, Daniel Varjas, Ellis Kennedy, Mary Scott, Frances Hellman, Adolfo G. Grushin, and Alessandra Lanzara.

How the atomic arrangement of an amorphous solid affects its electronic properties is a challenging problem with implications ranging from technology [103] to the discovery of new topological phases of matter [104, 105, 106, 107]. For crystalline solids, the foundations are well established since the early days of quantum mechanics: translational symmetry leads to well-defined peaks in the lattice structure factor, Fig. 7.1(a) top, that determine where Bragg scattering of electrons occurs. The scattering planes are determined by the periodic atomic potential, and define the edges of the Brillouin zone. Through Bloch's theorem, the crystalline momentum precisely describes electronic states within a Brillouin zone.

In the case of non-crystalline solids, the Brillouin zone description is less clear due to the absence of long-range order. Indeed, the structure factor of random atomic positions, such as an electron gas, is uniformly distributed, Fig. 7.1(a) middle, and lattice disorder is expected to localize the electronic states, leading to a structureless dispersion relation (i.e. featureless momentum-space) [108, 109, 110]. However, realistic amorphous solids are not random. Often, the chemical bonding retains the local ordering(short and medium range) [4, 111, 112, 113], even if long-range atomic order is absent. Structurally, this results in an atomic arrangement which is locally similar to the crystal (bond lengths, angles, and coordination) but globally the atomic sites demonstrate no periodic behavior [114, 115, 116, 4]. In this case, the diffraction pattern is not uniformly distributed, but rather presents a set of rings, Fig. 7.1(a) bottom, each corresponding to characteristic real-space scales, such as a well-defined nearest neighbour distance.

Whether long-range order is a necessary condition for structured momentum space is an open discussion. Can an amorphous material, void of long range order but with correlated local structure produce momentum-dependent electronic states? This question is motivated by the recent experimental observation of strongly dispersive surface states in a purely amorphous Bi_2Se_3 (a-Bi_2Se_3)[117]. While it is established that topology can survive in amorphous matter, the difference between crystalline and amorphous spectra poses the more fundamental question of how to characterize the electronic structure of amorphous solids. These are crucial questions since many technologically important materials are amorphous and many other systems lack long range order but exhibit well defined structural length scales such as quasicrystals, high-entropy alloys, and even dynamic systems such as liquids [118, 119, 120].

Here, we reveal novel and generic characteristics of an amorphous electronic momentum space, demonstrating highly dispersive surface states that form repeated annular zones analogous to Brillouin zones. The key insight is that the correlated structural disorder of amorphous materials leads to characteristic real-space scales, which in turn translates into characteristic momentum-space scales.

The phenomenology we observe is strongly reminiscent of the decades-old predictions concerning the dispersion of electrons in liquid metals [121, 96, 122, 123, 124, 125, 126, 97, 127]. In liquids dispersive electronic features were predicted to remain contingent on the presence of a well-defined nearest neighbor distance. They were recently used to explain why disordered dopants on the surface of a crystal can lead to pseudo-gap-like band structures [98]. However, this phenomenology has never been directly observed in an amorphous solid. We report the first observation in amorphous materials of Brillouin-zone like repetitions and present theoretical insights to interpret the photoemission spectra of electronic systems that lack long-range translational symmetry, thus expanding the material pool to uncover novel physics from these unexplored dispersions.

4.1 Structure

In this work, we utilize angle resolved photoemission spectroscopy (ARPES) on amorphous Bi_2Se_3 (a-Bi_2Se_3) to identify generic momentum space features that result from electron coherence in a system that lacks long-range order. Our findings will have consequences for, but it is not restricted to, the spectrum of topological surface states.

To begin, it is useful to recall that crystalline Bi_2Se_3 (c-Bi_2Se_3) features a quintuple layer structure of alternating selenium and bismuth planes with bismuth atoms octohedrally coordinated with six adjacent selenium atoms. The quintuple layers are bonded by van der Waals forces, the stacking of which defines the c-axis lattice constant (see top panel in Fig. 7.1 (f)).

The accumulated knowledge on amorphous systems suggests that a realizable structure for a-Bi_2Se_3 can share certain traits with c-Bi_2Se_3. For example, in elemental amorphous materials, such as Si, Ge and monolayer carbon, or bi-elemental amorphous compounds such as SiO_2 and GaAs, the coordination of atoms and the nearest neighbor distances remain peaked at the values of their crystalline counterparts. The structural disorder stems from small variations in bond angles and smaller variations in bond lengths, which are peaked at the crystalline values[116, 128, 129, 130]. Following suit, a-Bi_2Se_3 is expected to also possess octohedrally coordinated bismuth atoms and similar local environment to c-Bi_2Se_3.

The propensity for amorphous systems to retain the crystalline local order means that the amorphous system has a tendency to retain a well defined length-scale. A notable difference between the c-Bi_2Se_3 and a-Bi_2Se_3 however is that the van der Waals gap in c-Bi_2Se_3 is an inherently 2D structure with no obvious analog in the amorphous case. Indeed, in Ref. [117] we have demonstrated through Raman spectroscopy that the van der Waals gap no longer exists in a-Bi_2Se_3. Using ab-initio molecular dynamics to generate realistic a-Bi_2Se_3 amorphous structures, we observe a peak in the coordination number at six (Fig. 7.1(e)), representing the existence of majority octahedral environments.

To elucidate the real-space structure, we grew a-Bi_2Se_3 using physical vapor deposition from two elemental effusion cells and characterized the structure using high-resolution transmission electron microscopy (HRTEM) in shown in Fig. 7.1(b). The large scale HRTEM image indicates no regions exhibiting crystalline order or even nano-crystalline precursors. The inset displays a 2 nm × 2 nm field of view displaying phase contrast resulting from the lack of long-range periodicity.

Fig. 7.1(c) shows TEM diffraction from the same film exhibiting the characteristic diffuse rings of amorphous systems lacking long range order. The presence of rings is indicative of well-preserved real-space length-scales. Using parallel-beam diffraction, we compute the reduced radial distribution function, $G(r)$, shown in Fig. 7.1(d). The a-Bi_2Se_3 film shows clear peaks at 2.4 Å, 3.5 Å, and 4.9 Å, indicating well-defined real and reciprocal length-scales in the system.

4.2 ARPES

Figure 4.2 summarizes the momentum-space structure from the electronic dispersion we obtain from ARPES on a-Bi_2Se_3. Panel (a) displays a momentum-slice spectrum cutting through $(k_x, k_y) = (0, 0)$ at a photon energy of 120 eV revealing remarkably dispersive band structure manifesting as vertical column-like features and an M-shaped valence band [117]. The near-vertical features are in stark contrast to the expectation that disordered and localization lead to a broadened, momentum-independent electronic dispersion [108, 109, 110].

At large momentum, the band structure is replicated, resulting in copies of the electronic states at -1.75 and 1.75 Å^{-1} with reduced intensity. The replicas occur at a characteristic momentum, $k^* = 2\pi/a^* \approx 1.75$ Å^{-1} corresponding to $a^* \approx 3.6$ Å, which closely matches the second peak in the radial distribution function from Fig. 7.1(d). The consequent Fermi surface, seen in Fig. 4.2(b) and visually enhanced by taking $\nabla^2 I$ (where I is photoemission intensity), confirms that the momentum space structure is rotationally symmetric in the form of concentric rings. Therefore, the dispersive structure is only repeated along the radial direction, forming annular regions at larger momenta.

The repetition phenomenon is reminiscent of that occurring in crystalline systems, which feature duplicated dispersions commensurate with reciprocal lattice vectors, outside of the first Brillouin zone. Hence, we refer to the regions where duplicates appear as "Brillouin-like zones" (BLZ) because they demonstrate repetition akin to crystalline fermiology. Unlike

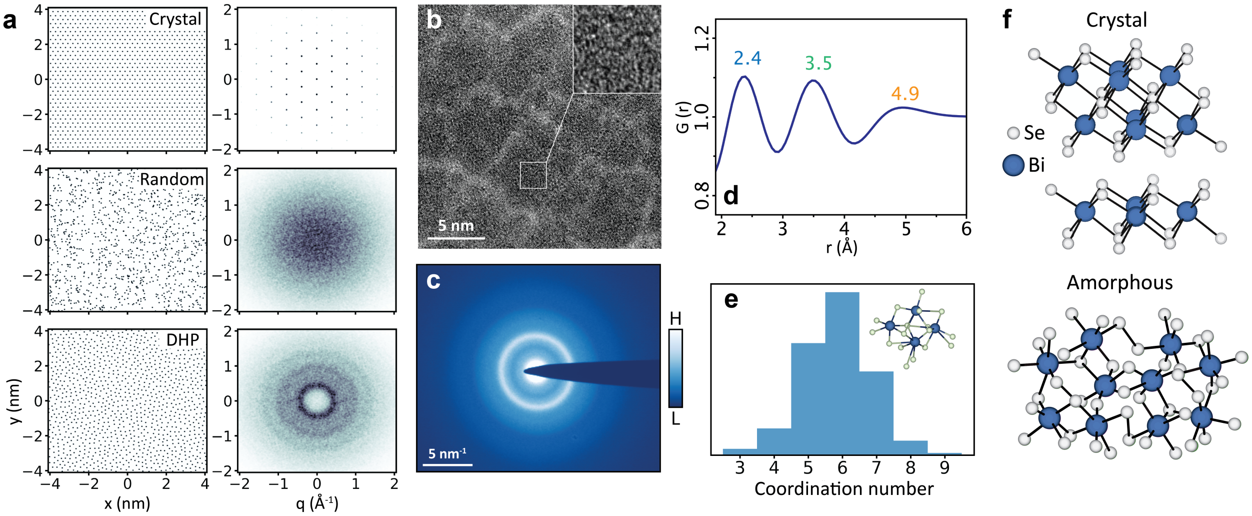

Figure 4.1: Well-defined reciprocal length scale from real-space short-range order. (a) Fourier transforms for three real-space point distributions (crystalline, normal random, and disordered hard pack) demonstrates that reciprocal-space structure persists in the presence of well defined nearest-neighbor distance. (b,c) The large scale HRTEM image indicates no regions exhibiting crystalline order or even nano-crystalline precursors (the contrast visible in the main image is associated with columnar microstructure that is common in thermally evaporated amorphous materials). The inset displays an expanded 2 nm x 2 nm field of view displaying a speckle pattern due to phase contrast resulting from the lack of long-range periodicity, but has no sign of any nanocrystalline or even precursor nanocrystallites. The electron diffraction pattern shows broad diffuse rings corresponding to short range order and no high intensity spots from long range order. (d) The reduced radial distribution function, $G(r)$, has three peaks from a well defined nearest neighbor (2.4 Å), next nearest neighbor (3.5 Å), and third nearest neighbor (4.9 Å). (e) Coordination number for amorphous Bi_2Se_3 calculated using a 200 atom cell and ab-intio molecular dynamics. The CN is peaked at 6. Inset: an example coordination environment in amorphous Bi_2Se_3. (f) Ball-and-stick model of crystalline and amorphous Bi_2Se_3. For the amorphous structure, van der Waals separation is absent and majority sites are octahedral coordinated, implying an isotropic nearest neighbor distance.

for crystals, the repetitions occur only along the radial direction, which we interpret as a manifestation of the rotational symmetry expected in amorphous structures. Fig. 4.2(c) conceptualizes the BLZ, showing the typical BZ-relationship of the replicated bands with respect to a reciprocal lattice constant (upper panel) and the annular zones in the Fermi surface (lower panel). The essential difference in the amorphous case is that its uniformity at long length-scales implies that reciprocal-space structure is rotational symmetric. Therefore reciprocal lattice vectors cannot exist, otherwise there would be well defined preferential directions and therefore long-range order. However preferential momentum scalars, can exist since local ordering, such as typical bond lengths, can persist in randomized directions. As a note, an effect which is absent in our spectra is the possible long-range nematic ordering. This can occur for instance via a compression or a strain which modifies the nearest-neighbor distances along one axis resulting in an elliptic transformation of the BLZ [98, 131].

Expanding further out in momentum space exposes higher order BLZ. Fig. 4.2(f) shows the photon energy dependence of the dispersion at the Fermi level along the same radial direction panels as a and b at large detection angles. The white dashed lines represent the photon energy dependence for 2D states at four different k_z-independent momenta, indicating that the features are in fact photoemission from 2D surface states as opposed artifacts from photon energy-dependent matrix elements. The first two curves from the top-left follow the 1st order BLZ (0th order being at Γ_0) and the last two curves follow the 2nd order BLZ. Panel (g) displays the momentum space converted spectrum for $h\nu = 120$ eV (shaded region in (f)) in which the bright 0th order dispersion is cutoff on the left edge and the 2nd order BLZ can be seen near 3 Å^{-1}. The intensity of the BLZs decrease and the dispersions broaden at larger momenta.

To determine the origin of the BLZ we compare the results of the ARPES experiment on a-$\mathrm{Bi_2Se_3}$ to a numerical simulation with a tight-binding Hamiltonian of a-$\mathrm{Bi_2Se_3}$ introduced in [117]. However, to explain our ARPES observations we need to ensure that a degree of local order is preserved when defining the atomic arrangement. To do so we construct a 3D arrangement of amorphous sites using thermalized hard packed spheres as in Ref. [117] to which we add a relaxation step, resulting in a radial distribution function with peaks corresponding to nearest, second-nearest, and third-nearest neighbours. The peak locations define the characteristic length scales of the system. We use the nearest-neighbour average distance r^* to set the scale of the plots in position space. This choice defines the characteristic momentum scale $k^* = \frac{2\pi}{r^*}$, which we use to normalize momentum space.

On this atomic site distribution, we define a model with a spin $\frac{1}{2}$ degree of freedom and two orbitals per site, to generalize the crystalline Bernevig-Hughes-Zhang (BHZ) model [132], For each site in the amorphous structure we find the six closest neighbours. We then choose the coupling between neighbouring sites so that, if the lattice was cubic, it would result in the original BHZ model. Because the hoppings are assigned sequentially for every site, the six-fold coordination is preserved on average. The hopping term of the Hamiltonian depends on the relative position of the two sites $\mathbf{d}_{ij}$ according to

$$\langle i|H|j\rangle = it_1(\hat{\mathbf{d}}_{ij} \cdot \sigma)\tau_x - t_2\sigma_0\tau_z, \tag{4.1}$$

while the onsite energy of a single site reads

$$\langle i|H|i\rangle = M\left(\sigma_0\tau_z + \alpha e^{-\frac{\delta_i}{2r^*}}\sigma_0\tau_0\right). \tag{4.2}$$

This system shows a topologically non-trivial gap that hosts a Dirac cone surface state for M positive and close enough to zero[117]. The parameter α controls the strength of a symmetry-allowed surface on-site potential that shifts the surface Dirac cone away from $E = 0$, where δ_i is the distance from site i to the surface.

We compute the spectral function of this system by projecting into a basis of plane waves of light momentum k, illuminating a single surface with a finite penetration depth, simulating an ARPES experiment. One can then define the two parallel and the perpendicular components of the momentum without ambiguity. Due to the isotropy of amorphous systems, the problem is invariant up to an in-plane rotation. One can thus only focus on the incident plane of light.

The ARPES spectra of a-Bi_2Se_3 and the numerical model (Fig. 4.2(d)) both show the bulk gap, and within it a dispersive surface states that cross the gap around the Γ point. Around each momenta comensurate with the characteristic momenta k^*, $\left\|\mathbf{k}_{\|}\right\| = k^*$, $2k^*$... a copy of the central bulk states and surface Dirac cone appears. This is the amorphous equivalent of the Brillouin zones of a crystal, enabled by the characteristic nearest-neighbour distance retained by the amorphous structure. This suggests that in Figs. 4.2(a) and (b), the repetitions we observe originate in the local order of the atomic sites. Fig. 4.2(e) shows that the expected spectrum is isotropic in the two components of the momentum that are parallel to the illuminated surface, as also observed experimentally. This theoretical analysis combined with the experimental spectra strongly supports the conclusion that ARPES can be used as a tool to extract the scale of local order of any non-crystalline solid by observing BLZ repetitions.

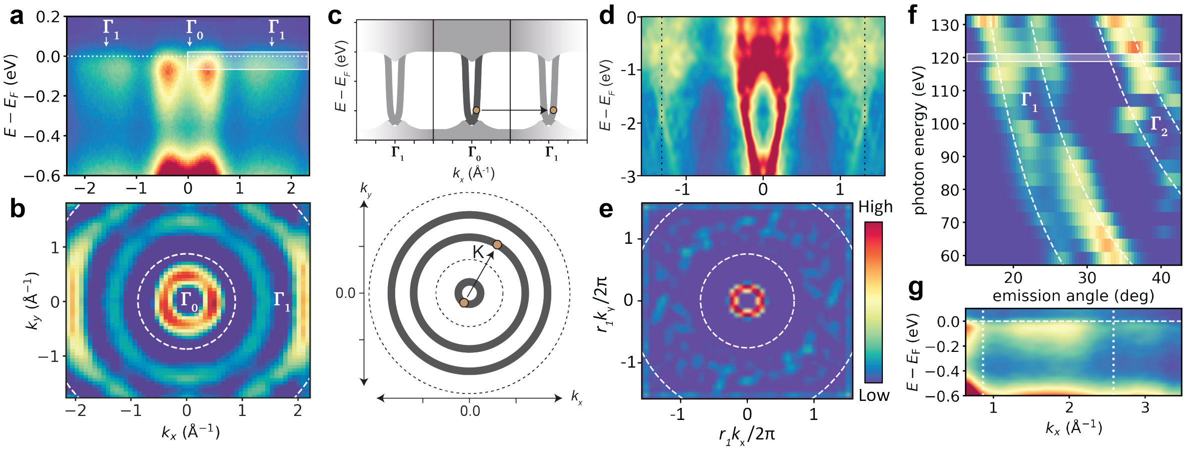

Figure 4.2: Amorphous surface state dispersion. (a) Large momentum range ARPES spectrum uncovers duplicate dispersions approximately 1.75 $\mathring{A}^{-1}$ from Γ. (b) The Fermi surface ($\nabla^2 I$ of the raw intensity for visibility) demonstrates rotational symmetry of the primary and duplicated dispersion. (c) Illustration of amorphous dispersion and Brillouin zone-like repetition contingent on a characteristic momentum. (d) Simulated dispersion along $k_{\|}$ through Γ showing duplicated structures. (e) Fermi surface from simulations showing repeated annuli. (f) Photon energy dependence of the 2nd and 3rd BZ dispersion, obeying k_z-independent photoemission (dashed white). (g) ARPES spectrum at $h\nu = 120$ eV with repeated dispersions separated by 1.75 $\mathring{A}^{-1}$.

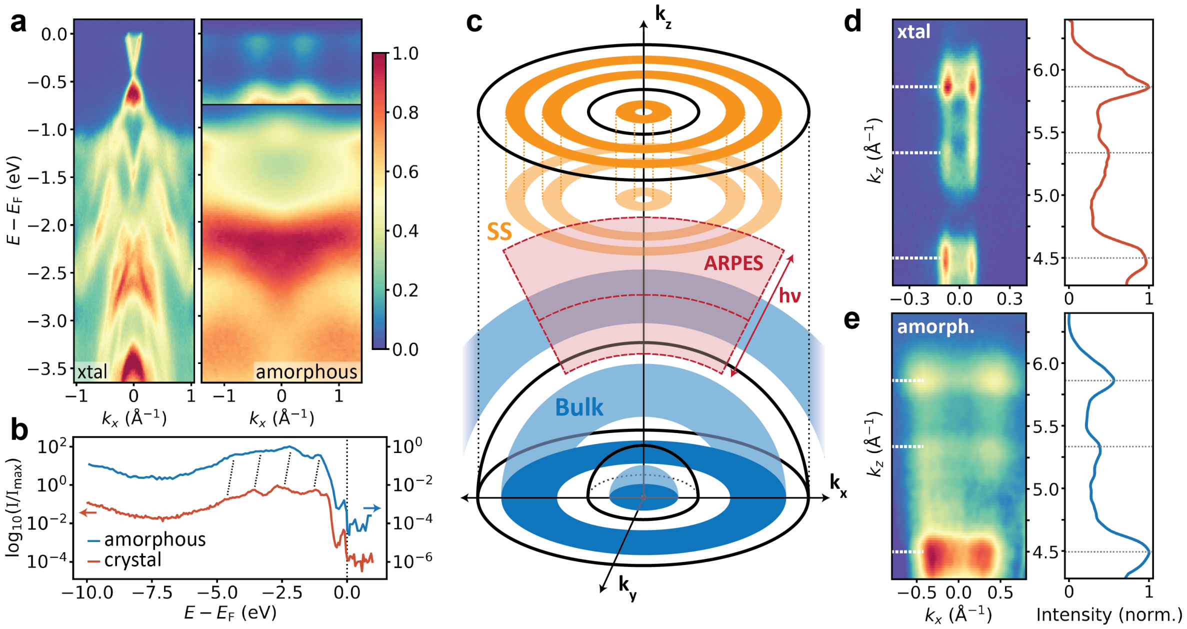

Figure 4.3: Amorphous versus crystalline Bi_2Se_3 (a) Deep binding energy ARPES spectra for c-Bi_2Se_3 ($\Gamma - K$) and a-Bi_2Se_3. (b) XPS on a-Bi_2Se_3 (blue) and c-Bi_2Se_3 (red) displays similar spectra for valence bands. Dashed lines indicate corresponding peaks, and the spectral hump of the upper energy portion of the surface state can be seen near E_F in both samples. (c) Diagram of amorphous band structure geometry. Bulk states form spherical shells around $\vec{k} = (0, 0, 0)$ (blue), whereas surface states form cylindrical shells around the k_z axis (orange). For a single photon energy, ARPES probes a section of an approximately spherical shell about $\vec{k} = (0, 0, 0)$ (red). (d,e) Surface state spectrum at E_F as a function of k_z for c-Bi_2Se_3 (d) and a-Bi_2Se_3 (e). k_x-integrated intensity shown to the left with 3 characteristic peaks marked by arrows.

It is illustrative to compare the momentum space structure of a-Bi_2Se_3 with c-Bi_2Se_3 and to separate the roles of bulk and surface states. In Fig. 4.3(a), we show deep binding-energy ARPES spectra at $h\nu = 120$ eV for c-Bi_2Se_3 along the $\Gamma - K$ direction and for a-Bi_2Se_3 radial from Γ. The intensity of the features near the Fermi level in a-Bi_2Se_3 has been enhanced by 10× for visibility. The most notable difference close to the Fermi level is that the Dirac state in the crystal and the vertical features in the amorphous system have markedly different Fermi wave vectors (k_F), 0.08 Å^{-1} and 0.4 Å^{-1}, respectively. We identify several factors that can contribute to this difference. First, a surface potential (captured by α in Eq. (4.2)) can shift the Dirac point downwards in energy, changing k_F significantly. Second, the surface state Fermi velocity is not universal, and can be strongly affected by disorder, as we will exemplify later on.

Turning back to Fig. 4.3(a), and looking deeper in binding energy we see that the crystalline sample maintains strongly dispersive features, whereas the amorphous sample demonstrates flattened and broadened bulk band structure. Notably there is a broad nearly-flat structure near -2 eV. Even though the curvature of the deep binding energy band structure is reduced in the a-Bi_2Se_3, the angle integrated spectral response is intriguingly similar. In Fig. 4.3(b) we plot the x-ray photoemission spectroscopy (XPS) spectra for c-Bi_2Se_3(red) and a-Bi_2Se_3(blue) on shifted y-axes for visibility. The overall intensity as a function of binding energy follows nearly identical large-scale behavior with a dip near -8 eV and a broad shoulder with substructure at -3 eV. The crystalline sample exhibits four peaked features in the shouldered region that correspond to four peaks in the amorphous spectrum shifted by ~ 0.5 eV. The similarity between the spectra indicates that the deep binding energy band structure of the amorphous sample appears as the momentum averaged band structure in the crystal.

The peculiar difference between the highly dispersive bands near the Fermi level and the weakly dispersive bands at high binding energy in a-Bi_2Se_3 can be explained by reflecting on the uncommon features that a rotationally symmetric system imprints in ARPES. Fig. 4.3(c) illustrates the 3D momentum space structure of bulk bands and surface states given the symmetry of an amorphous system. The bulk bands (blue) are rotationally symmetric and are allowed to vary along the radial direction contingent on a well-defined characteristic momentum, thereby forming repeated spherical shells at constant energy within BLZs. Surface states (orange), spatially localized at the surface, are k_z-independent and forming cylindrical shells oriented along the k_z-axis. ARPES is well suited for studying k_z-dependence in crystals with cartesian Brillouin zones by varying the photon energy, since:

$$k_z \propto \frac{1}{\hbar}\sqrt{2 * m_e(h\nu - E - \phi + V_0)}. \tag{4.3}$$

where E is the binding energy of the electron, V_0 is the fixed inner potential of the material, ϕ is the material work function, $h\nu$ is the photon energy, and m_e is the mass of the electron. However, in a spherically symmetric momentum-space, ARPES faces an additional challenge to observe k_z-dependent bulk states. In ARPES, $k_{x,y} \propto \sin\theta$ and $k_z \propto \cos\theta$, where θ is the angle of photoemission, such that ARPES probes an approximately spherical crossection in momentum space for a given photon energy. The solid red arcs in Fig. 4.3(c) illustrate variable ARPES crossections given fixed photon energies. Moreover, typical inner potentials, V_0, are of order 10 eV, limiting the minimum probable k_z to approximately 2 Å^{-1} so that the concentric structure at $k_z = 0$ is out of reach. All in all, this means that ARPES probes approximately spherical cross-sections of the spherically-invariant bulk band structure. Therefore bulk dispersive features will still disperse along k_z-axis by varying the photon energy (shaded red region) but features in k_x and k_y will appear flat.

In contrast, surface states are k_z independent and the concentric structure can be accessed by ARPES at any photon energy (see red shaded region meets orange), revealing dispersive bands in k_x and k_y. In panels (d) and (e), we display the k_z-dependence of the c-Bi_2Se_3 and a-Bi_2Se_3 surface states near E_F, respectively. In the crystalline case, k_F remains fixed for all k_z at 0.08 Å^{-1}, manifesting as narrow vertical pillars in k_z vs. k_x with variable intensity due to photon energy dependent matrix elements.

Curiously, the amorphous surface state bands expand outward with increasing k_z (Fig. 4.3(e)). This is a non-periodic dispersive feature that occurs over the full measured 2.5 inverse angstroms in k_z. The lack of periodicity over this range indicates that this momentum space feature cannot be due to a crystalline bulk structure since any such structure would need to repeat on smaller intervals than 2 Å ($\pi/2.25$ Å^{-1}). Moreover, this peculiarity does not affect the conclusion that these are surface states since, given the lack of long-range order, bulk states would necessarily form rotationally symmetric shells centered at (k_x, k_y, k_z) = (0, 0, 0) and would appear nearly horizontal in panel (e). Therefore these states must be of surface state origin since they are coherent across many k_z values.

Crucially, the momentum integrated intensity as a function of k_z (panels (e) and (d), right plots) are nearly identical, with intensity peaks occurring at the same three k_z values (horizontal lines). This indicates that the photon energy dependent matrix elements are comparable in the two systems, advocating for similar orbital character.

Using the BHZ model defined by Eqs. (4.1) and (4.2), we can compare the localization of the bulk and surface wavefunctions. Fig. 4.4(a) shows the average wavefunction site occupation within a 2 Å slice of the amorphous cube for surface states between $E - E_\mathrm{D} = -1.0$ and 0 eV (yellow) and bulk states between $E - E_\mathrm{D} = -9.5$ and -4.0 eV (blue), where E_D marks the center of the band gap. The in-gap surface states are localized to the system edges whereas the bulk states evenly fill the interior appearing completely delocalized. However, the singular wavefunctions tell a different story. Fig. 4.4(b) shows a single wavefunction at -0.45 eV (yellow), again localized to the surface but delocalized along the 2D surfaces. A random selection of three bulk wavefunctions between -9.5 and 4.0 (red, green, and blue) show a localized behavior, constrained to a small number of sites.

In fact, we are able to deduce a lower limit on the coherence length of the electronic order from the momentum broadening of the states in Fig. 4.3(d) [119, 133, 134]. The momentum Lorentzian linewidth of the two peaks in each case serve as a measure of the electronic real space ordering, in so much as perfect electronic order leads to delta functions in momentum (ignoring lifetime broadening) and spatial incoherence leads to smearing across the full BZ. This represents a lower limit for the coherence length since final state effects, spatial variations in doping, or lifetime broadening could introduce additional extrinsic broadening.

Fig. 4.4(c) plots the k_z-dependence of the coherence length (or mean free path, MFP) as $2\pi/\Gamma_k$ where Γ_k is the Lorentzian line-width. For c-Bi_2Se_3, MFP is largest at small k_z at nearly 400 Å, serving as our estimate of the lower limit of the coherence length in the crystal. The MFP then linearly decreases towards larger k_z suggesting a possible photon energy dependence of the momentum resolution. In a-Bi_2Se_3 the maximal determined MFP is near $k_z \approx 5.2$ Å^{-1} which gives a value of 13 Å for the MFP. This is a markedly reduced coherence to the crystal yet coherent beyond three nearest neighbors, $3a^*$. Interestingly, the measured coherence length reduces towards lower and higher k_z values indicating an additional broadening mechanism in the low momentum regime as compared to c-Bi_2Se_3.

The delocalization of the surface state along the surface planes enables the electronic wavefunction to encompass many atomic sites, which in turn enables dispersive coherent structure in momentum space. In contrast, the localization of the bulk bands, inferred

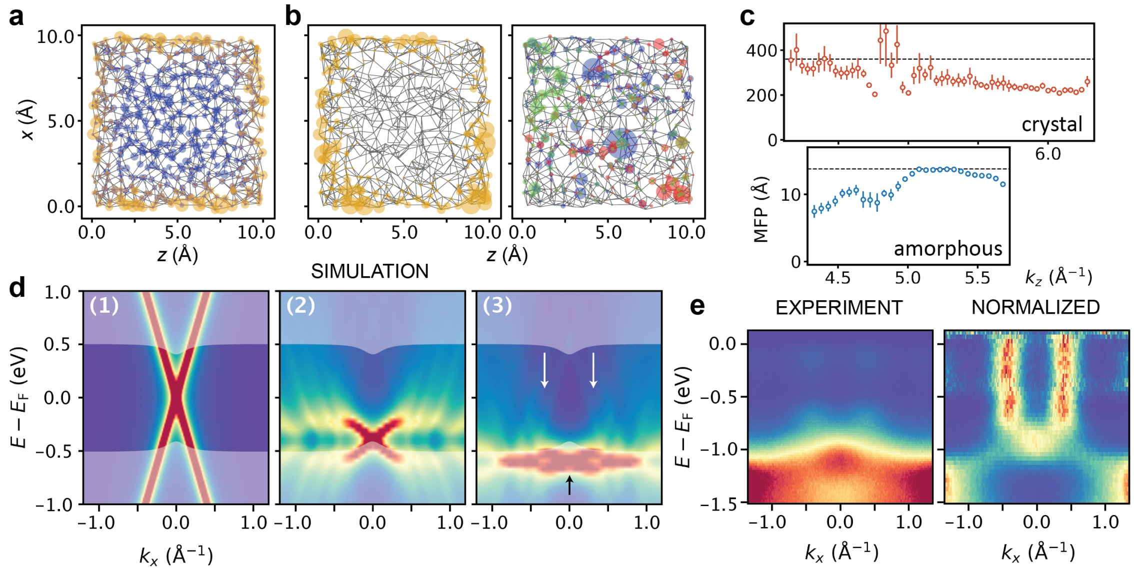

Figure 4.4: (a) Average site occupations for wavefunctions with energy within the bulk gap (yellow) and below the bulk gap (blue). (b) Single surface state wavefunction ($E - E_{\mathrm{F}} = 0$ yellow) is delocalized along the surface plane, spreading across multiple unit cells. Single bulk state wavefunctions ($E - E_{\mathrm{F}} < -0.5$ eV red, green blue) are localized within the bulk. (c) Measure of mean free-path (or spatial coherence) of surface state electrons as a function of k_z as determined from $2\pi/\sigma_{\mathrm{MDC}}$ for c-$\mathrm{Bi_2Se_3}$ and a-$\mathrm{Bi_2Se_3}$ from Fig. 3d. (d) Spectral function of a linear dispersing state scattered on a disordered array of atoms with interacting strengths (1)$v_0 = 0$, (2) $v_0 = 2$, (3) $v_0 = 3$. When the interaction with scattering centers increases, copies of the central Dirac cone appear at the peaks of c_2, i.e. around $k = \pm 0.4$ $\mathring{\mathrm{A}}^{-1}$. For strong enough scattering potential, the dispersion is pushed into the valence and vertical features form that cross the bulk band gap. (e) Experimental ARPES spectrum and normalized along energy-axis spectrum for comparison with simulation.

from Fig. 4.4(b) would suggest a flattened band structure. This is indeed the case for the amorphous structure in Fig. 4.3(a), in which strong dispersion occurs for the surface state near E_{F} and bulk bands deeper in binding energy are flat. It is possible that either topological protection or spin-momentum locking of the surface states may enhance the in-plane coherence for a-$\mathrm{Bi_2Se_3}$ surface states, making it a particular good material for observing a defined amorphous band structure.

Lastly we discuss why the amorphous surface state may exhibit broad near-vertical dispersive features at a dramatically enhanced k_F with respect to the crystalline spectrum (see Fig. 4.3(a)). These broad vertical features, particular to a-$\mathrm{Bi_2Se_3}$, are not fully explained by our tight-binding model used in Fig. 4.2. A tantalizing additional effect neglected in the tight-binding approximation is that scattering on a disordered array of atoms can significantly alter the dispersion of a propagating state, creating the effect of a broad and vertical dispersion [96, 122]. This is believed to be the case of liquid metals and surface electrons propagating within a disordered but correlated array of atoms on crystal surfaces [98]. Translated to our situation, the hypothesis is that the surface Dirac propagating state experiences scattering due to the correlated disorder intrinsic to amorphous structure. This weak scattering effect is not captured by the tight-binding approximation [96, 122]. To explore this possibility, we calculate the disorder induced self-energy caused by the experimental radial density function of Fig. 7.1(d) to determine how a linearly dispersing surface state is affected by this spatial distribution of atoms. Following Ref. [96], the scattering effect introduces a self-energy that reads

$$\Sigma_s(\mathbf{k}) = v_0 \sum_{s'} \int c_2(\mathbf{k}-\mathbf{k}') F_{ss'}(\mathbf{k},\mathbf{k}') G_{0s'}(\mathbf{k}') \mathrm{d}\mathbf{k}', \tag{4.4}$$

where v_0 is the strength of the disorder, $F_{ss'}(\mathbf{k},\mathbf{k}')$ is the overlap factor between the two bands (labeled by $s = \pm$) of the Dirac Hamiltonian, $c_2(\mathbf{k})$ is the Fourier transform of the radial distribution function shown in Fig. 7.1(d), and $G_{0s} = (E - s v_F |\mathbf{k}|)^{-1}$ is the bare Green's Function of the surface Dirac cone in the diagonal basis.

Fig. 4.4(d) shows that indeed correlated structural disorder reshapes the linear dispersion for increasing disorder strengths v_0. Without interaction, the spectral function only shows a Dirac cone centered around Γ. When the interaction with scattering centers increases, copies of the central Dirac cone appear at the peaks of c_2, i.e. around $k = \pm 0.4$ Å^{-1}. For strong enough scattering potential, the dispersion and node (black arrow) is pushed into the valence (shaded white region) and vertical features form that cross the bulk band gap (white arrows). Thus the exact shape of the dispersion can be strongly affected by the surface disorder, a mechanism that could explain why the ARPES spectrum measured in Fig. 4.3 differs significantly from the crystalline spectrum.

Comparing Fig. 4.4(d) with Fig. 4.4(e) (where the ARPES spectrum near E_F is shown along with the spectrum normalized along binding energy) demonstrates how both the experiment and simulation exhibit broad vertical features that cross the gap, as well as an apparent band crossing and node at the valence band edge.

4.3 Conclusions

The features we see arise from well defined short-range length scales, hinting at the possibility of widely overlooked momentum-space structure in all non-crystalline solids with this property, such as other amorphous materials, quasicrystals, and liquids. Diagnosing them with further photoemission studies complemented by other probes, such as scanning tunneling spectroscopy, has the potential to change significantly the landscape of solid-state properties. The presence of highly dispersive features in a-$\mathrm{Bi_2Se_3}$ motivate the generalization of momentum-dependent phenomena to glassy systems, including spin-momentum locking [117], momentum-based paring in superconductivity, or new avenues to engineer flat-bands in amorphous phase-change materials [135].

Based on a-$\mathrm{Bi_2Se_3}$ specifically, another direction of further study is the origin of the appreciable monotonic k_z-dependence of the surface states of Fig. 4.3(d), which clearly differs from bulk states, but is not completely k_z-independent. A possible cause is the lack of translational symmetry itself. ARPES is based on the notion that translational symmetry conserves the in-plane crystalline momentum following photoemission. This may no longer be the case in amorphous samples; while continuous translations can be recovered on average to explain most of our results, discrete translational symmetry is lost, which may result in more subtle k_z dependencies, and may be a unique feature of non-crystalline media.

This work reveals dispersive surface electronic states on the surface of an amorphous material, amorphous $\mathrm{Bi_2Se_3}$, that exhibit a rotationally symmetric Fermi surface with repeated Brillouin zone-like repetitions. This is made possible by the presence of a well-defined real-space length scale from the disordered hard packing of atoms in the amorphous structure, which corresponds to a well-defined reciprocal length scale. The amorphous analog to crystalline $\mathrm{Bi_2Se_3}$ preserves the angle-integrated XPS spectral features yet exhibits remarkably different valence state behavior, manifesting as vertical-like features with large Fermi wavevectors. Since the presence of local chemical order is ubiquitous in solids, our work calls for a retrospective investigation of amorphous and other non-crystalline systems such as quasicrystals, in search for dispersive features that reveal novel quantum effects in momentum space, previously reserved for crystals alone.

Chapter 5

Structural disorder driven topological phase transition in BiTeI

This chapter is based on a published paper with explicit permission from all co-authors. The full reference is P. Corbae, F. Hellman, and S. M. Griffin, Phys. Rev. B 103, 214203 (2021).

The discovery of nontrivial topological phases in materials has been at the forefront of condensed matter physics for both their fundamental importance and their potential in applications ranging from low-power electronics to quantum computing. High-throughput searches and classification schemes for topological materials exploit crystalline symmetries, and how these symmetries determine band connectivity [136, 2, 3, 43, 15, 137, 138]. Such symmetry indicators have enabled the prediction of thousands of crystalline topological materials. However, materials without intrinsic or long-range crystalline symmetries, such as amorphous and quasicrystalline materials [139, 24], have no such classification scheme. Nonetheless, evidence for topological surface states has been experimentally and theoretically observed in an amorphous topologically insulating system [117, 18]. Recently, Marsal et al., [30] exploited local environments to compute the topological phase diagram in a coordinated amorphous structure. These works find that local interactions and connectivity determine the relevant features in the electronic structure to produce topological phases, and emphasize the importance of local chemical environments in topological materials. Understanding how structural disorder contributes to and enhances topological phases will drive predictions of disordered and amorphous topological materials based on local structural properties.

Small gap semiconductors with strong spin-orbit interactions (SOI) are ideal systems to probe how local environments affect the band topology. In such systems, a band inversion and a topological phase can be induced by tuning the chemical environment to modify the crystal-field splitting (CFS) [75]. Systems with a strong SOI and no inversion are subject to Rashba spin-splitting: without I-symmetry, the degeneracy between $\psi_{-k,\uparrow}$ and $\psi_{k,\uparrow}$ is lifted so that the bands split at non-specific k-points, and a resulting band inversion can occur away from Γ in the Brillouin zone (BZ). If the states near the Fermi level are of the same orbital character and also close in energy, they can couple together effectively through a Rashba Hamiltonian, further reducing the band gap at relevant points in the BZ [140].

Several routes to inducing topological phase transitions (TPTs) from normal to topological insulator (TI) have been proposed in solid-state systems, including using temperature[141, 142], pressure [143] and strain [144]. Topological Anderson insulators are an example where onsite disorder pushes a trivial insulator through a gapless state into a topologically nontrivial state [145, 17]. Typically, Anderson models incorporate an onsite disorder term which can be applied to non-crystalline solids [7], however here we incorporate disorder with perturbations to the atomic positions. No studies to date have looked at the effect of this random structural disorder on the topological character.

In this work, we study how local structural disorder affects the CFS and SOI in the small-gap semiconductor BiTeI and identify the structural motifs that play a crucial role in producing the nontrivial band topology. First, we present our scheme for introducing structural disorder in BiTeI and analyze the subsequent charge redistribution upon symmetry breaking. Using first-principles calculations we show that, as bond lengths change, the CFS is enhanced leading to a bandgap reduction. We observe a TPT from trivial insulator to Weyl semimetal to TI originating from a bulk band inversion when spin-orbit coupling (SOC) is included. These topological phases emerge in a crystalline material with reduced crystalline symmetries. We confirm the TPT by studying the surface state spectrum and calculating topological invariants from Wannier charge centers, observing a Dirac cone on the surface resulting from a strong $\mathbb{Z}_2$ index. This work provides a pathway to understanding local chemical environments in topological materials and their extension to amorphous systems by using disorder in crystalline systems to elucidate the physical origin of the TPT, prompting a route for materials discovery [117].

5.1 Structure

BiTeI is a trigonal, noncentrosymmetric material adopting the $P3m1$ space group (No. 156). The primitive unit cell contains a single Bi, Te, and I configured in layers of triangular networks along the c-axis (Fig. 5.1(a)), resulting in a C_{3v} rotational symmetry about the c-axis. The Te-Bi-I network forms a trigonal prism surrounding the Bi atoms, which are separated by a van der Waals gap. In this undisordered structure the equilibrium Bi-Te bond length is 3.07 Å and the Bi-I bond length is 3.29 Å, bond lengths in the PBE framework are typically within $1-2\%$ (experimental values are 3.04 Å and 3.27 Å respectively). This structure is a trivial insulator with an experimental bandgap of 0.36 eV [146]. To understand how topology is influenced by the local chemical environment we generated disordered structures as follows: We pull a random number from a uniform distribution between -0.15 Å and 0.15 Å and add it to each Wyckoff position in the unit cell for each direction. This generated a disordered structure with an average atomic displacement d_{av}=0.62 Å per unit cell, similar in value to the change in interatomic spacing between the crystalline and amorphous phases of Bi2Se3 in experiment[117]. From this disordered structure, we created interpolated snapshots between the undisordered and fully disordered crystal with d_{av}=0.62 Å to track the electronic and topological properties with increasing disorder. The final structure is in the $P1$ space group

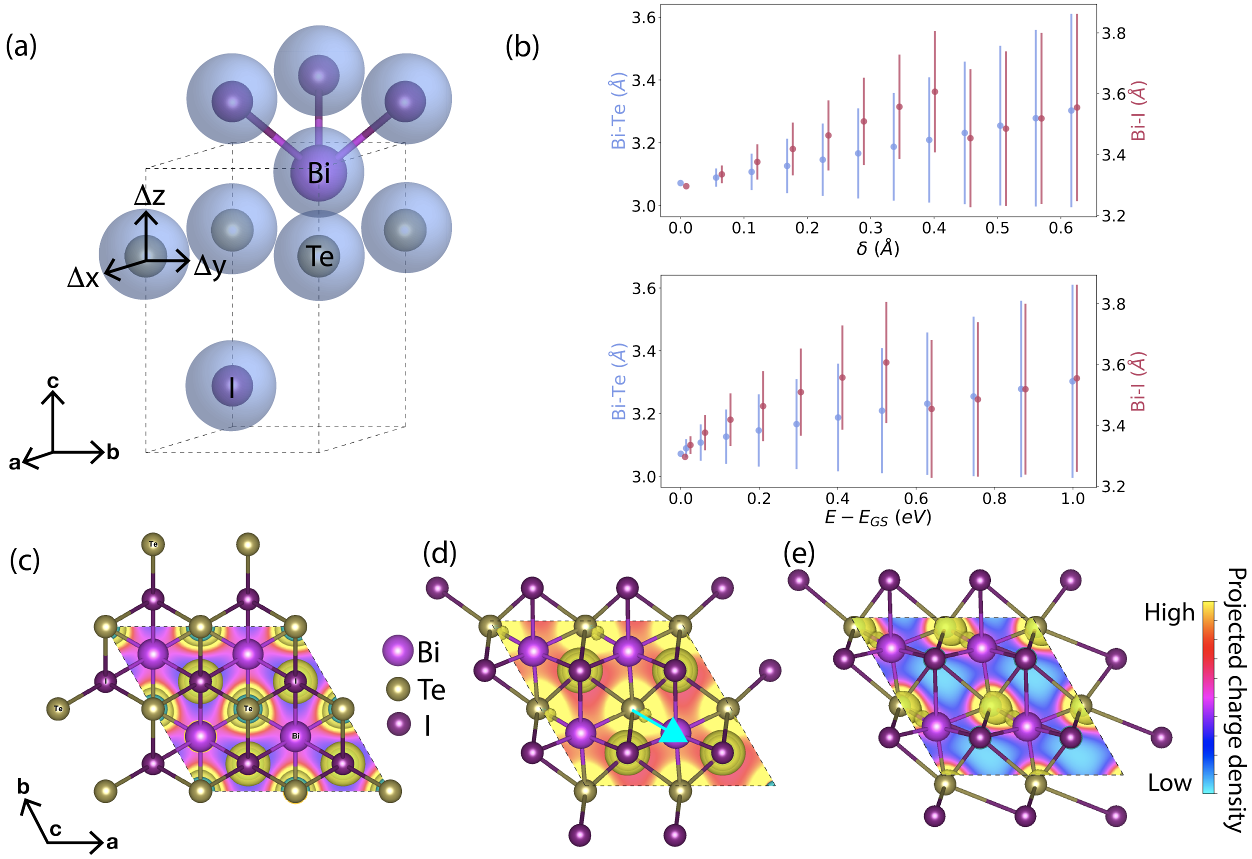

Figure 5.1: Structural disorder induced charge redistribution. (a) BiTeI primitive unit cell. Blue spheres represent the allowed random displacements Δx, Δy, and Δz. (b) Bi-Te and Bi-I bond lengths vs. disorder/energy per unit cell. The Bi-Te bonds shift to a higher mean length and develop a larger σ. The important bond for the TPT, Bi-Te = 2.9 Å, can be seen developing around 0.4 Å. The Bi-I bonds initially develops a higher mean length with large σ and then drops around 3.50 Å with low σ after the TPT. (c-e) Partial charge density of the (001) plane for bands near the Fermi level in structures with d_{av}=0.00 Å, d_{av}=0.28 Å, and d_{av}=0.56 Å, respectively. As the structures become more disordered the charge density distorts into the y-direction (indicated by the blue arrow in (d)) and the charge moves to the Bi-Te bond.

after the C_{3v} and remaining symmetry elements are removed by the structural disorder.

Fig. 5.1(b) shows the distributions (mean bond lengths with bars representing the standard deviation) for Bi-Te and Bi-I bond lengths for our disordered structures as a function of average displacement and energy difference from the ground state. We see that with increasing disorder, the distribution of Bi-Te bond lengths develops a larger standard deviation while the mean bond length becomes larger. The smaller Bi-Te bonds shift to a value of

BiTeI interpolation and $\mathbb{Z}_2$ Invariant												
	Crystal	S1	S2	S3	S4	S5	S6	S7	S8	S9	S10	S11
d_{av}	0.00 Å	0.06 Å	0.11 Å	0.17 Å	0.22 Å	0.28 Å	0.34 Å	0.39 Å	0.45 Å	0.50 Å	0.56 Å	0.62 Å
Bi u_x	0.00 Å	0.005 Å	0.009 Å	0.014 Å	0.019 Å	0.024 Å	0.028 Å	0.033 Å	0.038 Å	0.042 Å	0.047 Å	0.052 Å
Bi u_y	0.00 Å	0.004 Å	0.009 Å	0.013 Å	0.017 Å	0.022 Å	0.026 Å	0.030 Å	0.035 Å	0.039 Å	0.043 Å	0.048 Å
Bi u_z	0.00 Å	0.001 Å	0.003 Å	0.004 Å	0.005 Å	0.007 Å	0.008 Å	0.009 Å	0.011 Å	0.012 Å	0.013 Å	0.015 Å
Te u_x	0.00 Å	−0.002 Å	−0.003 Å	−0.005 Å	−0.006 Å	−0.008 Å	−0.010 Å	−0.011 Å	−0.013 Å	−0.014 Å	−0.016 Å	−0.017 Å
Te u_y	0.00 Å	0.011 Å	0.022 Å	0.033 Å	0.044 Å	0.055 Å	0.066 Å	0.077 Å	0.088 Å	0.099 Å	0.109 Å	0.120 Å
Te u_z	0.00 Å	0.006 Å	0.011 Å	0.017 Å	0.022 Å	0.028 Å	0.033 Å	0.039 Å	0.044 Å	0.050 Å	0.055 Å	0.061 Å
I u_x	0.00 Å	−0.003 Å	−0.006 Å	−0.009 Å	−0.013 Å	−0.016 Å	−0.019 Å	−0.022 Å	−0.025 Å	−0.028 Å	−0.031 Å	−0.034 Å
I u_y	0.00 Å	−0.015 Å	−0.031 Å	−0.046 Å	−0.061 Å	−0.076 Å	−0.092 Å	−0.107 Å	−0.122 Å	−0.137 Å	−0.153 Å	−0.168 Å
I u_z	0.00 Å	−0.007 Å	−0.014 Å	−0.021 Å	−0.027 Å	−0.034 Å	−0.041 Å	−0.048 Å	−0.055 Å	−0.061 Å	−0.068 Å	−0.075 Å
$\mathbb{Z}_2$	0; (000)	0; (000)	0; (000)	0; (000)	0; (000)	0; (000)	0; (000)	1; (001)	1; (001)	1; (001)	1; (101)	1; (100)

Table 5.1: Atomic displacements for interpolated BiTeI structures

2.9 Å – this Bi-Te bond plays an important role in the TPT as discussed later. Additionally, the distribution of Bi-I bond lengths spread out with large deviation and then moves to 3.5 Å with lower deviation.

The Bi-Te bond shortening and Bi-I bond lengthening has important implications on the charge density. Fig. 5.1(c) plots the charge density of bands at the Fermi level near the A point which are involved in the TPT for the undisordered crystal. We also plot the charge density for the bands projected onto the (001) plane depicting the C_{3v} symmetry and the charge sitting on the Te and I atoms. As we disorder crystalline BiTeI, Fig. 5.1(d-e), the charge density moves from being centered on the Te and I ions to the Bi-Te bond. This is important because, as we will describe later, the TPT band inversion occurs between the Bi and Te p orbitals near the Fermi level. The charge density is redistributed in the y-direction due to the increased p_y orbital presence at the Fermi level. This increase is attributed to the shortening of the Bi-Te bonds, which happens primarily in the y-direction. The y-direction is not specific, rather the important feature is a shortening of the Bi-Te bond and the subsequent charge redistribution. In summary, in our disordered BiTeI, the Bi-Te bond gets shorter causing a charge redistribution along the Bi-Te bond, resulting in a broken 3-fold rotation symmetry and a new crystal-field environment for the states near the Fermi level.

Our crystal structure was obtained from the Materials project (mp-22965), which was derived from ICSD no. 79364 with standard Materials Project settings.

To track the topological properties of BiTeI, eleven disordered structures were produced by randomly displacing the atoms from their equilibrium positions. The average displacement as well as the atomic displacements ($u_{x,y,z}$) for each atom in the primitive cell are shown in Table 5.1. The reason for the band inversion and topological phase transition is the shortening of the Bi-Te bond and subsequent charge redistribution to this bond due to the new crystal-field environment. From the $u_{x,y,z}$'s shown in the table, it can be seen the Bi and Te atoms get closer together in the x, y directions shortening the bond.

5.2 Electronic Structure

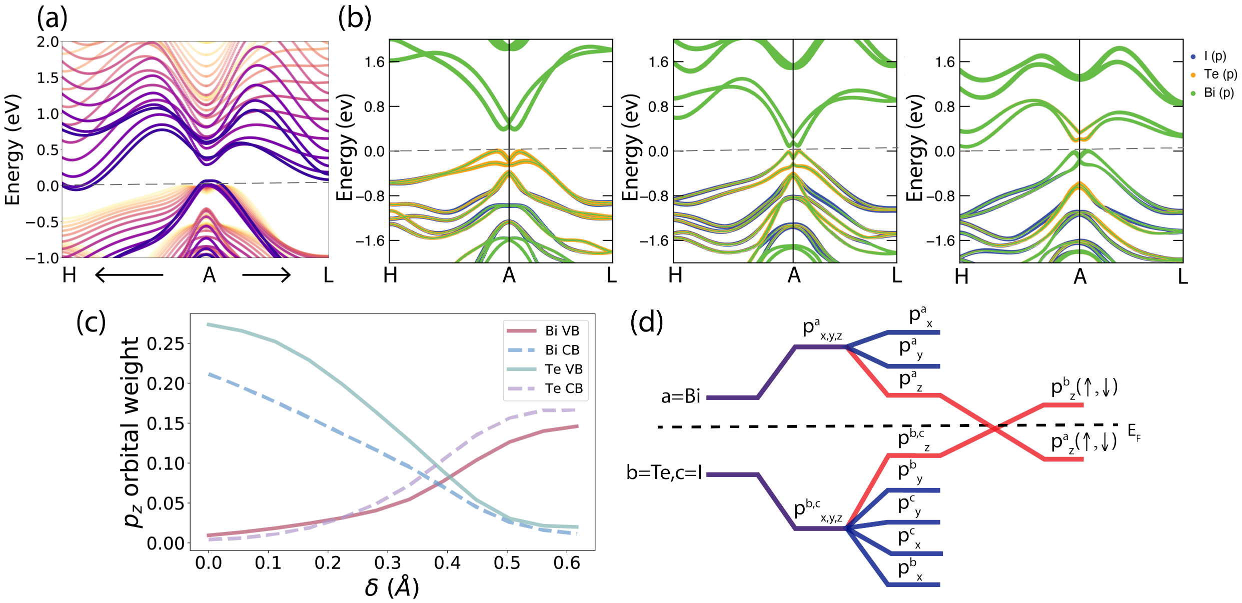

Figure 5.2: Bulk electronic bandstructure. (a) Bulk bandstructure in the $H-A-L$ direction without SOC. Structural disorder modifies the CFS pushing bands near the Fermi level closer and reducing the energy gap. Darker colors represent more disordered structures. (b) The bandstructure with SOC for d_{av}=0.00 Å, d_{av}=0.28 Å, and d_{av}=0.45 Å, respectively. The Bi weight in green moves from the CB to VB and vice versa for Te in orange. (c) The Bi/Te p_z orbital weight at A as a function of average atomic displacement. With increasing displacement the Bi and Te weight of the VB (CB) switch around 0.4 Å. (d) Energy level splitting diagram for disordered BiTeI after the TPT. The three splittings represent chemical bonding, crystal field, and SOC. By breaking the C_{3v} symmetry the $p_{x,y}$ orbitals are no longer degenerate.

Our electronic structure calculations were performed using Density Functional Theory (DFT) with the projector augmented wave (PAW) formalism in the Vienna ab initio Simulation Package (VASP)[41, 42]. The exchange-correlation potentials were treated in the framework of generalized gradient approximation (GGA) of Perdew-Burke-Ernzerbof (PBE)[39]. Bi (6s, 6p), Te (5s,5p), and I (5s, 5p) electrons were treated as valence, and their wavefunctions expanded in plane waves to an energy cutoff of 600 eV. A k-point grid of 6x6x4 with Gamma sampling was used. Spin-orbit coupling was added self-consistently.

Based on our first-principles results, we construct a Wannier function based tight-binding model using the WANNIER90 code [147]. We include the Bi, Te, and I p orbitals in the model. We then calculated the topological invariants for different structures using the WANNIERTOOLS package [148].

Next, we examine the influence of the structural changes on the electronic and topological properties of disordered BiTeI. The calculated electronic structure is shown in Fig. 5.2 with and without SOC included to disentangle how crystal-field effects and SOC change with atomic displacement. Due to the lack of a center of inversion, we examine the states along the $H - A - L$ direction to track topological band inversion. Fig. 5.2(a) shows the calculated electronic bandstructure for increasing values of d_{av} without SOC. We find that for increasing d_{av}, the resulting changes in the CFS at A reduces the band gap and pushes the bands at the Fermi level closer together. This large crystal-field enhancement is a result of the lifting of the degeneracy between the p_x and p_y orbitals upon displacement when the three-fold rotational symmetry is broken. This causes an increased p_y orbital contribution near the Fermi level, seen in the partial charge density. The orbital overlap produces large splitting pushing states near the Fermi level closer together as shown in Fig. 5.1(e) and Fig. 5.2(a).

To understand the role of SOC on the disordered electronic structure, Fig. 5.2(b) plots the bandstructure for $d_{av} = 0.0\,\text{Å}$, $d_{av} = 0.3\,\text{Å}$, and $d_{av} = 0.5\,\text{Å}$, respectively, with SOC included. SOC breaks the spin degeneracy giving rise to splitting at positions in the Brillouin zone away from high-symmetry points and causes a large Rashba spin-splitting near the Fermi level in all structures [149]. Importantly, by incorporating SOC we observe a reduction of the bandgap, and, with increasing d_{av}, a band inversion occurs at the A point. This band inversion produces the TPT in disordered BiTeI. The origin of the band inversion can be understood by considering the p-orbital projections of Bi, Te, and I onto the bandstructure. Initially the Te (orange) and I (blue) weight is concentrated in the valence band (VB) and the Bi weight (green) in the conduction band (CB). After the transition the Bi weight is in the VB and the Te weight is in the CB, which is quantitatively shown in Fig. 5.2(c). The Bi and Te p_z orbital weights switch at $d_{av} \sim 0.4\,\text{Å}$ with the Bi weight decreasing in the CB and the Te weight increasing (vice versa for the VB). Importantly, the average atomic displacement of $0.4\,\text{Å}$ is observed in amorphous TI systems and so is a physically reasonable amount of disorder that could be induced in amorphous materials [117]. This allows us to reasonably assume the electronic structure of the disordered crystal could reflect an amorphous phase. Additionally, the peak in the distribution of coordination numbers in the disordered structures moves from six to five exactly at the TPT, producing a new crystal field. A minimal tight binding model incorporating disorder reproduces our results. The generality of this model capturing the TPT with disorder can be applied to other structurally disordered materials systems with strong SOC.

The electronic structure results are summarized in Fig. 5.2(d). We find the states at the Fermi level, namely Bi-p in the CB and Te/I-p in the VB, dominate the TPT. As previously noted, the in-plane C_{3v} rotational symmetry in crystalline BiTeI results in degenerate $p_{x,y}$ orbitals split in energy from the p_z orbital due to the semi-ionic polar trigonal prismatic coordination of the Bi [150]. This results in Bi-p_z and Te-p_z states at the edge of the CB and VB respectively [132], separated by a calculated band gap of $0.38\,\text{eV}$. Introducing disorder that shortens Bi-Te bonds results in greater orbital overlap between the Bi-p_z and Te-p_z

states, pushing bands near the Fermi level closer together. This disorder-induced reduction in bandgap is then sufficient, once SOC is included, to cause a band inversion of the two opposite polarity bands, resulting in a TPT to a TI.

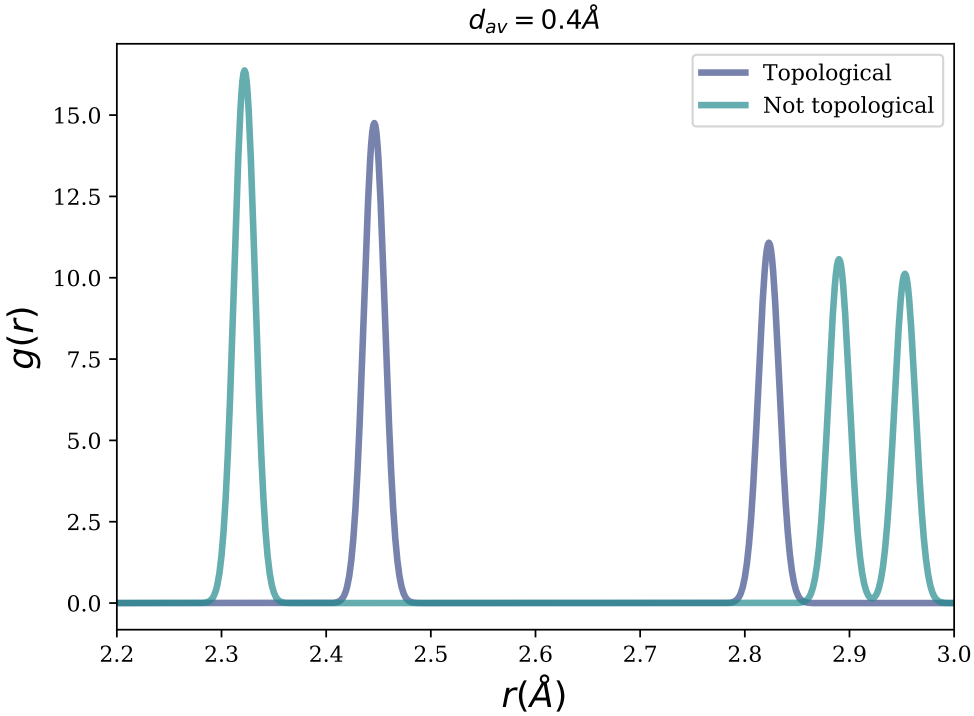

Figure 5.3: Computed RDF for different realizations of structural disorder in BiTeI. The structure labeled topological corresponds to structure S7 in Table S1. The structure labeled not topoligcal has $d_{av} = 0.4$ Å but does not possess the required Bi-Te bond shortening and charge redistribution for a topological phase transition.

Different realizations of structural disorder in BiTeI lead to non-topological systems. In one set of ten randomly disordered interpolations the shortening of the Bi-Te bond and charge redistribution causes a reduction in the band gap, but the crystal field splitting isn't enough to cause a band inversion, but larger amounts of disorder could potentially drive it past a TPT. The radial distribution function is shown in Fig. 5.2 for another realization of disordered BiTeI with similar average displacement to the topological structure. The shortening of the Bi-Te bond and the corresponding charge redistribution was not present in this set of ten disordered interpolations, owing to the different local environments from nearest and next-nearest neighbor atoms seen in the radial distribution function. The topological structure has peaks in the RDF at $\sim 2.5Å$ and $\sim 2.8Å$. The different local environment leads to different modifications of crystal-field environment that push the bands near the Fermi level farther apart. This is shown in Fig. 5.4, the energy gap at the A point in the

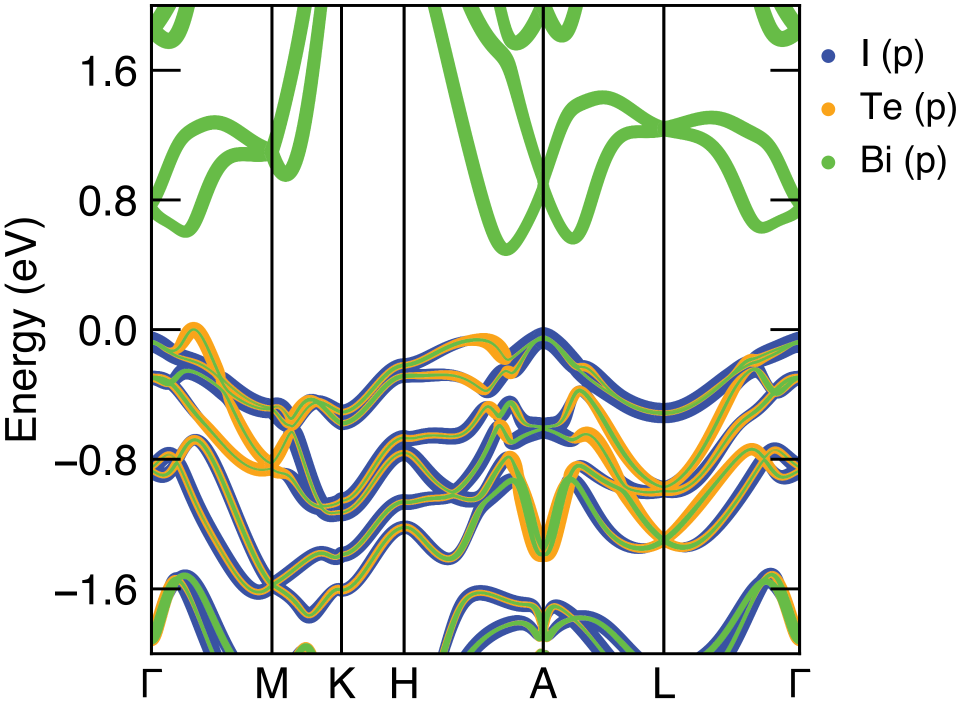

Figure 5.4: Electronic bandstructure for non-topological BiTeI with orbital projections with the Fermi level set to 0 eV. As the structural disorder becomes larger the Rashba splitting is greatly increased. The conduction band splitting at the A point has $E_R = 0.4\,\text{eV}$ and the momentum offset $k_o = 0.17\,\text{Å}^{-1}$.

BZ is larger than it is in the undistorted crystal. This different crystal field results from random atomic displacements that do not produce the relevant orbital overlaps required for topology (such as the p_z orbital overlap). This can be seen in the Bi, Te, and I orbital projections, these states reside in the same bands as the non-topological crystal. Although the system doesn't undergo a topological phase transition it develops an even greater Rashba splitting seen in Fig. 5.4. In these non-topological structures $E_R = 0.4\,\text{eV}$ and the momentum offset $k_o = 0.17\,\text{Å}^{-1}$, larger than any previously reported in literature [89]. These results demonstrate that structural disorder can generate both TPTs and colossal Rashba splitting in SOC materials making it a new tuning parameter for quantum properties in small gap semiconductors with large SOC.

5.3 Topology

Since the TPT is that of an ordinary insulator to a TI in a noncentrosymmetric crystal upon structural disorder, we calculate the $\mathbb{Z}_2$ topological invariant for the TR-invariant planes in the BZ [14]. After the TPT $\mathbb{Z}_2 = 1; (001)$ indicating a strong TI. Fig. 5.5(a) presents the surface state calculations performed on a slab of structurally disordered BiTeI after the TPT. The presence of a Dirac cone at the surface Γ confirms the nontrivial bulk $\mathbb{Z}_2$ invariant. The Dirac cone sits mid gap and passes through the top of the Rashba split VB as $\Gamma \rightarrow M$ before connecting to the VB at M. This complex surface spectrum allows for the interplay of bulk Rashba split bands with the topological surface state. We plot the spin-momentum locking of the surface states with $H \propto \sigma \times \boldsymbol{k}$ in Fig. 5.5(b). The annular structure is distorted in momentum space due to the structural disorder in real space. Increasing structural disorder produces a TPT leading to a strong TI with a spin-polarized Dirac cone.

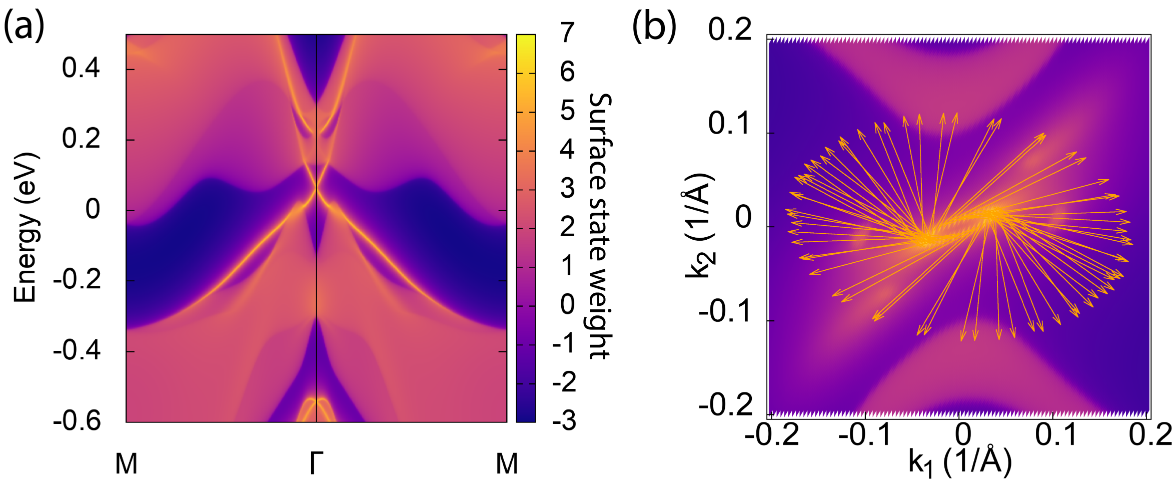

Figure 5.5: Calculated surface state spectrum for disordered BiTeI. (a) The momentum dependent local density of states shows a topological Dirac cone around the surface Γ point. (b) The Fermi surface of the topological surface state. The Dirac cone is distorted due to the structural disorder, the resulting Fermi surface is stretched in k_x, k_y in momentum space, a result of the structural disorder in real space. Arrows correspond to the spin texture of the Fermi surface. Brighter colors represent a higher local density of states.

The WCC for the $k_3 = 0.5$ plane is shown in Fig. 5.6, there is clearly a single crossing of the line cut with a WCC giving a $\mathbb{Z}_2$ index of 1. In conjunction with all the other planes, this shows the system is in a topologically insulating phase. The $\mathbb{Z}_2$ index set for all structures is shown in the last row of Table 5.1.

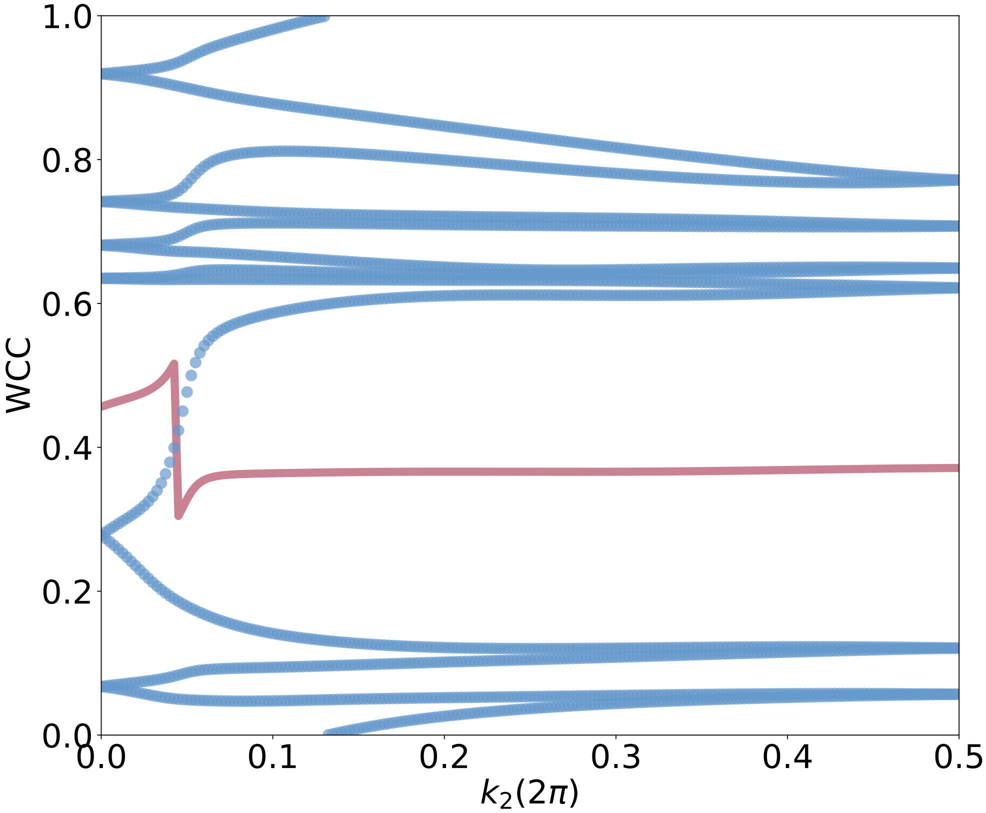

Figure 5.6: Hybrid WCC evolution for the $k_3 = 0.5$ plane. The red line is the largest gap between WCC's and the blue lines are the WCC's. There is a single crosses indicating this plane has $\mathbb{Z}_2 = 1$ and the system is topologically insulating.

These topological phases have been discussed before as intermediate phases between a trivial $\mathbb{Z}_2$ insulator and a nontrivial $\mathbb{Z}_2$ insulator which lacks a center of inversion [151]. As BiTeI becomes more structurally disordered, the crystal-field splitting increases and the bands approach a band inversion. When the valence and conduction bands touch at the A point in the BZ, a pair of Weyl nodes should emerge. Calculating the Chern number for the $k_x = 0$ plane gives $C = 1$ meaning an intermediate Weyl phase in the structurally disordered BiTeI. Since pairs Weyl nodes are sources and sinks of Berry curvature, we should observe this phase by looking at the real part of Ω. Fig. 5.7 shows the real part of Ω_x (x-component of the Berry curvature). There are two nodes in the BZ, each with opposite Berry curvature from the other (red vs. blue). This, in addition to the non-zero Chern number, signifies the presence of a Weyl phase as BiTeI transitions from a trivial insulator to topological insulator.

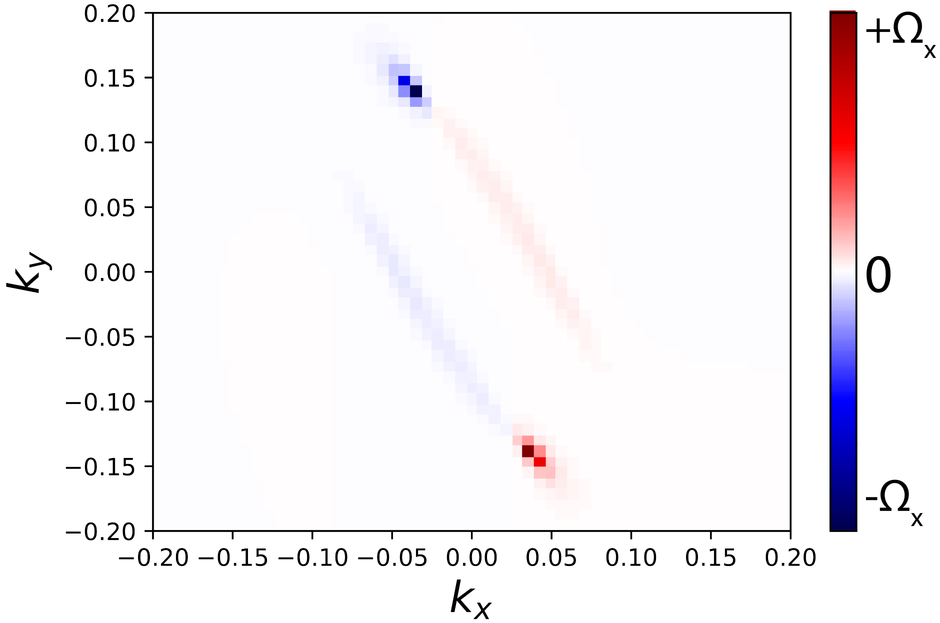

Figure 5.7: Real Ω_x at the topological phase transition. Two nodes with opposite Berry curvature are observed in the BZ at the Fermi level. Red and blue denote opposite Berry Curvature.

5.4 Conclusions

The local structure and its disorder play a key role in the TPT. We generated several sets of disordered interpolations via our random displacement process, different from the set presented. In these, the bonds lengths develop different distributions leading to varying local chemical environments and orbital overlaps. In one set, the shortening of the Bi-Te bond brought the structures close to a TPT. In another set the charge redistribution to the Bi-Te bond was not present, but led to a very large Rashba splitting in the bulk. These trivial electronic structures show not all disorders and subsequent local environments produces a TPT, highlighting the need for identifying key structural markers in TPTs. Our results demonstrate that structural disorder can generate both TPTs and colossal Rashba splitting in SOC materials making it a new tuning parameter for quantum properties in small gap semiconductors with large SOC.

Studying the influence of random structural disorder in SOC systems has implications for topological materials. We find that crystal-field engineering can be achieved with structural disorder as a new theoretical tuning parameter for topological phases. Furthermore, disorder can be employed to identify the physical origin of the TPT, making it also a marker for topological phases. This leads us to a systematic prescription for inducing TPT in material as follows: (i) identify the orbital character of the states near the Fermi level, (ii) add random atomic disorder to break the degeneracy of the states and distort along the corresponding orbital direction to reduce the gap, (iii) close the gap and cause a band inversion. By incorporating tight-binding models and topological markers [79, 24, 152], we can potentially discover many disordered and amorphous topological materials candidates. The topological phase and local environment in BiTeI, probed in our study via random atomic disorder, could be realized in amorphous thin films grown via physical vapor deposition. Short range ordering coupled with the atomic displacement in disordered or amorphous BiTeI could potentially show a topological phase in experiment.

In conclusion, we show that by randomly introducing structural disorder a TPT from a normal insulator to TI is achieved. Disordered BiTeI shows a bulk band inversion at the A point in the BZ which manifests as a spin-polarized topological Dirac cone with a strong topological invariant. The physical mechanism for this is broken crystalline symmetries which produce a unique crystal-field environment that pushes the states near the Fermi level closer together, inducing a band inversion. Our work is a step towards understanding topological matter from a local bonding perspective and has implications for topological states that cannot be classified using crystalline symmetry indicators. They suggest a route to discovering topological states in disordered and amorphous materials by identifying the local mechanisms (orbital inversions, etc.) which produce a TPT in the crystal in the presence of disorder. Our work provides a study of disorder induced TPT in a real solid state system with chemical specificity and bonding environments via first principles, a system which can be readily synthesized and manipulated in the lab. Such small-gap systems with strong SOC and well defined local environments, are promising systems to study the interplay of structural disorder, symmetry breaking, and topology.

Chapter 6

Disorder-driven localization and electron interactions in Bi$_x$TeI thin films

This chapter is based on a manuscript in final preparation with explicit permission from all co-authors. The author list is Paul Corbae, Nicolai Taufertshöfer, Ellis Kennedy, Mary Scott, and Frances Hellman.

Quantum materials such as topological materials or correlated phases have revealed remarkable emergent properties such as robust spin-momentum locked surface states and unconventional superconductors, and have the potential to revolutionize technology with applications ranging from low power electronics to quantum computing. Many studies involve single crystals since disorder is typically seen as a drawback that hinders the emergence of interesting quantum properties in materials. However, disorder is in fact useful in quantum materials and the observation of certain phenomena rely on the presence of disorder, such as the quantum anomalous Hall effect [153]. Quantum properties that exist in the amorphous structure include superconductivity, magnetism, and topological phases, the latter seen via spin-momentum locked surface states in an amorphous analog of a 3D topological insulator [117].

It is well understood that structural disorder can lead to electron localization, specifically via Anderson localization [6]. In these systems there is a finite density of states at the Fermi level, but the states are localized within a localization length that is typically much larger than the interatomic spacing. The Fermi energy is commonly tuned by composition and the correlation length diverges when the Fermi energy lies at the mobility edge [154]. When the Fermi energy passes through the mobility edge, the states become delocalized. This transition is understood if interactions are not present which enables a single particle description. However, in systems where carriers are charged (electrons or holes), then Coulomb interactions are important and these introduce many body correlation effects. Additionally, disorder also increases electron interactions, and in some cases interactions can dominate [155]. The presence of electron interactions opens a Coulomb gap in the density of states at the Fermi level [8]. The interplay of strong disorder and interactions is an open field of research [156].

Spin-orbit coupling (SOC) has a particularly strong effect on materials which are disordered, where localization increases the strength of SOC relative to electron kinetic energy [157]. On the metallic side of the metal-insulator transition (MIT), the presence of disorder leads to the suppression of the conductance due to the constructive quantum interference of time reversed paths in zero magnetic field and is known as weak-localization (WL). In the presence of strong SOC, the spins of time reversed paths rotate and destructively interfere leading an enhancement of the conductance known as weak-antilocalization (WAL) [158, 66]. WAL and WL will manifest itself in the scattering lifetimes which can be studied via magnetotransport [159]. One important consideration is the dephasing time which corresponds to the time an electron will stay in an energy eigenstate in the presence of disorder. Another consideration is the spin orbit scattering time, which is the time it takes to randomize the spin-orientation during scattering events. On the insulating side, carriers exhibit variable range hopping (VRH) between sites which can be spin-dependent [160, 64].

The Bi$_x$TeI system contains several distinct quantum materials with different emergent properties. BiTeI is a small gap Rashba semiconductor with a very large spin splitting [89]. BiTeI can be tuned by disorder or pressure to different ground states, specifically a topological insulator or Weyl semimetal phase [161, 65]. Bi$_2$TeI is a weak topological insulator due to an even number of band inversions which results in surface states on a distinct set of surfaces [162]. It also is a topological crystalline insulator from a mirror symmetry in the crystal structure with protected surface states on a set of surfaces, both which have been seen in experiment [163]. Finally, Bi$_3$TeI is metallic, and has been proposed to be a topological metal [164]. In BiTeI, the layers are van der Waals (vdW) bonded together, leading to a vdW gap. The Bi$_2$TeI and Bi$_3$TeI structures incorporate one and two Bismuth bilayers, respectively, in the van der Waals gap of BiTeI. In single crystal form, Bi$_x$TeI with $x = 1, 2, 3$ is experimentally found to show metallic behaviour with $\rho(T)$ decreasing with decreasing temperature and $\rho \sim 0.5\,\mathrm{m}\Omega\cdot\mathrm{cm}$ at low temperature [165, 89]. The metallic behaviour has been discussed as a result of non-stoichiometry leading to an n-type semiconductor for $x = 1, 2$. This Bi$_x$TeI system thus presents an opportunity to study the effects of disorder in a material with a wide range of topological and quantum states.

In this paper we grow Bi$_x$TeI thin films at both room temperature and 230 K with varying levels of structural disorder to study how transport mechanisms are affected by disorder. Electron diffraction is used to characterize the structure and shows that both a reduced growth temperature and reduced Bi concentration x cause increased structural disorder. Transport properties were measured as a function of temperature and magnetic field for an extensive range of compositions and disorder. A metal-insulator transition is seen with decreasing composition for both cold and warm grown samples. With increased structural disorder from growth temperature, the MIT occurs at larger values of x. Temperature and magnetic field dependent transport provides evidence for weak antilocalization associated with strong spin-orbit coupling, which disappears with increased disorder, and evidence for electron interaction effects. The dephasing length is extracted from the field dependence and decreases as a function of increased disorder with the dominant dephasing mechanism changing from electron-phonon interactions to electron-electron interactions. Our work signals that strong disorder can localize spin-orbit entangled states and increase interactions in the complex electronic structure in quantum materials, such as the BiTeI family.

6.1 Structure

We grew 100 nm thin films of Bi$_x$TeI with various Bi concentrations on a-SiN$_x$ covered Si substrates at room temperature (RT) and 230 K (LT). The films were grown out of three effusion cells (Bi,Te,BiI$_3$) in a UHV chamber with a base pressure of 10^{-10} Torr. Different compositions were achieved by varying the Bi rate relative to the Te and I rate. The film thicknesses were confirmed using profilometry and the compositions were determined by energy dispersive spectroscopy (EDS) and x-ray photoelectron spectroscopy (XPS). The structure of the room temperature and cold grown Bi$_x$TeI films was characterized using high resolution TEM, parallel beam diffraction, and scanning nanodiffraction. For transport measurements the films were patterned into Hall bar devices ($l = 600\mu$m, $w = 200\mu$m) using conventional photolithography techniques. The films were measured in a custom closed cycle cryostat and a Quantum Design PPMS using standard four-point DC and low frequency lock-in techniques. We used pre-patterned thin Cr/Au (2 nm+8 nm) contacts on the substrates on which the films were grown and subsequently ex situ patterned into Hall bars using lift-off techniques. The structure and electronic properties of this material is badly influenced by any sort of annealing, which induces crystallization. The choice of pre-made Cr/Au contact pads and a lift-off technique was made to eliminate any annealing. Large Cr/Au contact pads were used to reduce contact resistance which can be significant on highly insulating films.

Both growth temperature and composition affect the level of structural disorder. In Fig. 6.1(a) high resolution real space images of room temperature BiTeI (RT-BiTeI) show nanocrystals approximately 5-10 nm in size embedded in an amorphous matrix. In RT-Bi$_2$TeI and RT-Bi$_3$TeI, the nanocrystalline regions approximately double in size with RT-Bi$_3$TeI having a larger volume fraction of nanocrystals. Low temperature BiTeI (LT-BiTeI) grows amorphous, LT-Bi$_2$TeI has $5-10$ nm precursors in an amorphous matrix, and LT-Bi$_3$TeI is entirely nanocrystalline with nanocrystals $\sim 10-20$ nm. Fig. 6.1(b) shows parallel beam electron diffraction patterns for BiTeI, Bi$_2$TeI, and Bi$_3$TeI grown at RT and 230 K. RT-BiTeI has two diffuse rings resulting from the amorphous matrix and the embedded nanocrystals. RT-Bi$_2$TeI and RT-Bi$_3$TeI are nanocrystalline, indicated by the sharp rings in the diffraction patterns, with a larger crystallite size compared to RT-BiTeI and a decrease in the amount of amorphous phase from $x = 2$ to $x = 3$. The LT-BiTeI diffraction pattern shows diffuse rings which confirms the film is fully amorphous. In LT-Bi$_2$TeI there is a single sharp ring in addition to the diffuse ring from the amorphous matrix. In LT-Bi$_3$TeI, the number of rings increases and the rings appear sharper corresponding to the large crystalline domains. The level of structural disorder in RT and LT $x = 1, 2$ is greatly affected by growth temperature

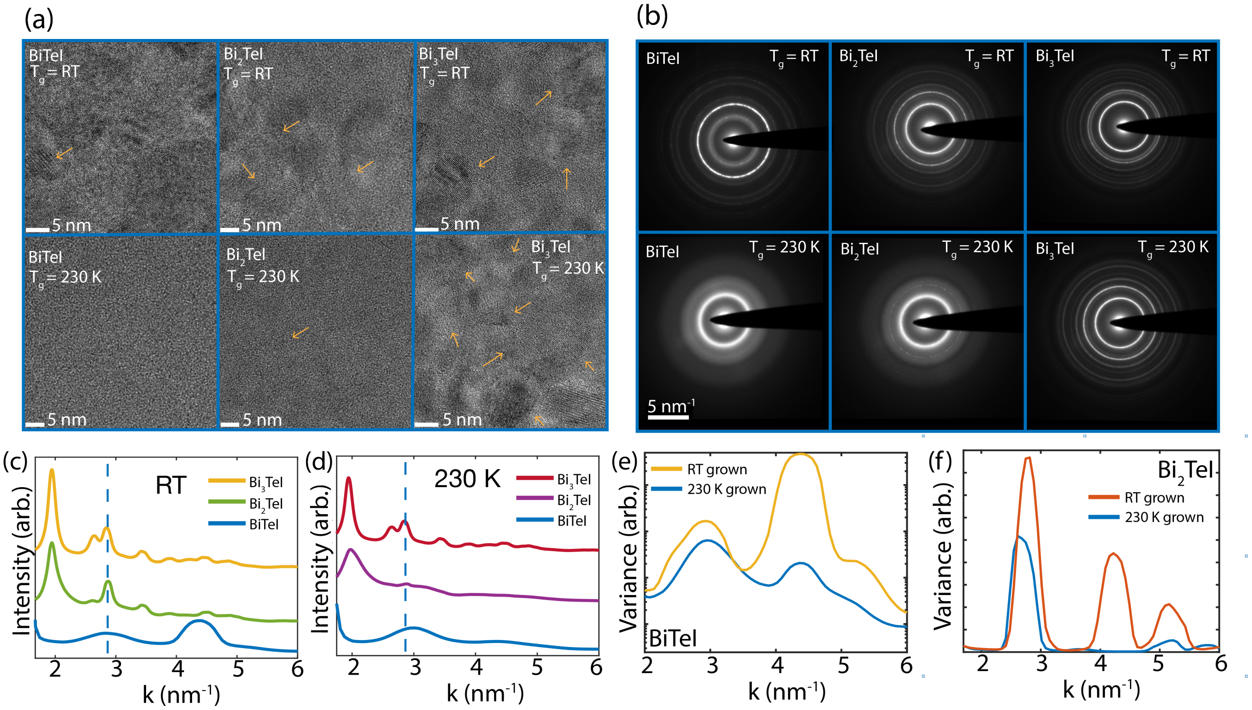

Figure 6.1: Structural disorder in BiTeI thin films. (a) HRTEM images Bi$_x$TeI for varying composition and growth temperature. RT-BiTeI is amorphous with nanocrystals embedded in the matrix. RT $x = 2 - 3$ are nanocrystalline showing crystallites larger in size compared to $x = 1$. The volume fraction of nanocrystals is greater for $x = 3$. Cold grown (230 K) films are amorphous for low x then nucleate crystallites with larger size as Bi concentration is increased. Example nanocrystallites indicated by arrows. (b) The diffraction patterns for RT-BiTeI has broad rings from small nanocrystals and the amorphous matrix, then as Bi concentration is increased there is an increase in the intensity of the rings. LT-BiTeI is amorphous with braod rings then LT-Bi$_2$TeI, LT-Bi$_3$TeI nucleate crystallites leading to sharp rings with increasing x. (c) Radially integrated diffraction intensity for RT grown samples. Higher intensity is seen for increased Bi concentration from an increased crystallite size. Dashed line corresponds to dominant single crystal BiTeI diffraction peak. The peak at $k \sim 2$ nm^{-1} is from the Bi bilayer. (d) Radially integrated diffraction intensity for cold grown samples. The peaks become sharper and more frequent for increased Bi concentration. (e) Variance in the diffracted intensity as a function of scattering vector k for warm and cold grown BiTeI, the film grown at higher T has more MRO and less disorder, evidenced by the large second peak in the variance. (f) Variance in the diffracted intensity as a function of scattering vector k for warm and cold grown Bi$_2$TeI, the film grown at higher T has more MRO and less disorder, evidenced by the large second peak in the variance.

where RT and LT $x = 3$ the structure is unaffected by growth temperature with the levels of disorder being the same.

These results are also seen in the radially integrated intensity, $I(k)$, shown in Fig. 6.1(c,d) which show additional features. For RT-BiTeI there are two broad peaks which correspond to the diffuse rings in the diffraction pattern, of a sample which is largely amorphous. For RT-Bi$_2$TeI and RT-Bi$_3$TeI there is an increase in the peak intensity observed with increasing Bi concentration, indicating a larger fraction of nanocrystals in RT-Bi$_3$TeI. Peaks at similar k are observed in both RT-Bi$_2$TeI and RT-Bi$_3$TeI, indicating a similar structural order in both films arising from the incorporation of Bi bilayers ($2\,\mathrm{nm}^{-1}$ peak seen in crystalline diffraction [165]) into the host BiTeI structure. The peak at $3.1\,\mathrm{nm}^{-1}$ in RT-BiTeI corresponds to the amorphous matrix and the $4.4\,\mathrm{nm}^{-1}$ peak corresponds to a real space length scale of 2.3 Å coming from the (110) or (003) planes in the single crystal [161]. The amorphous LT-BiTeI has a broad peak at $3.1\,\mathrm{nm}^{-1}$ from the diffuse halo corresponding to local medium-range ordering of 3.4 Å. In LT samples, with increasing Bi concentration the nucleation of crystallites in an amorphous matrix are evidenced by the LT-Bi$_2$TeI peaks that arise out of the broad amorphous peak as well as the Bi bilayer peak. The LT-Bi$_3$TeI films are completely nanocrystalline with a large crystallite size and many peaks. Fits to the $k = 2\,\mathrm{nm}^{-1}$ peak show a smaller FWHM as the composition increases from $x = 2$ to $x = 3$ indicating smaller crystallite size in LT-Bi$_2$TeI. The relative peak heights of the variance in diffracted intensity between RT and 230 K BiTeI, Bi$_2$TeI are shown in Fig. 6.1(e,f). Fig. 6.1(e) compares $V(k)$ for the BiTeI films grown at RT and 230 K, and shows that they have peaks at approximately the same k's, consistent with them both being amorphous as previously discussed, but the RT has a significantly enhanced second peak, at $4.4\,\mathrm{nm}^{-1}$, which indicates an increased MRO in the RT film compared to the LT film. Similarly, RT-Bi$_2$TeI has pronounced MRO at $4.4\,\mathrm{nm}^{-1}$ compared to RT-Bi$_2$TeI. Thus we see that growth temperature directly affects disorder for these two amorphous samples, specifically visible in this $V(k)$ data, and can be used to tune structural disorder. Growth at colder temperatures increases the level of structural disorder in the films, and enables the growth of amorphous films. Fig. 6.1 shows we are able to tune the amount of structural disorder in Bi$_x$TeI films which will have important implications on the electronic structure and transport.

The rotational symmetries of the amorphous and nanocrystalline films can be extracted using electron nanodiffraction [166, 167]. The sharp diffraction ring and peak at 4.4 nm^{-1} in RT grown BiTeI arises from a structure with 2-, 3-, and 6-fold rotation symmetry as seen in Fig. 6.2(a). A phase that is structurally close to the P3m1 space group with 6-fold rotation symmetry is P6$_3$mc [168]. The amorphous BiTeI system does not show such a defined rotational symmetry associated with the dominant k seen in Fig. 6.2(d). The dominant diffraction peak shows the dominant symmetry to be a 2-fold rotation with both 4 and 6-fold rotations also present. The secondary diffraction peak shows both 2-fold and 6-fold symmetries present, implying 3-fold is also present. Warm Bi$_2$TeI shows a dominant 2-fold symmetry as well as 3, 4, and 6 fold angular symmetries. The case is the same for the cold grown Bi$_2$TeI as well as warm Bi$_3$TeI. Angular symmetries larger than 6 stem from dynamical effects [166].

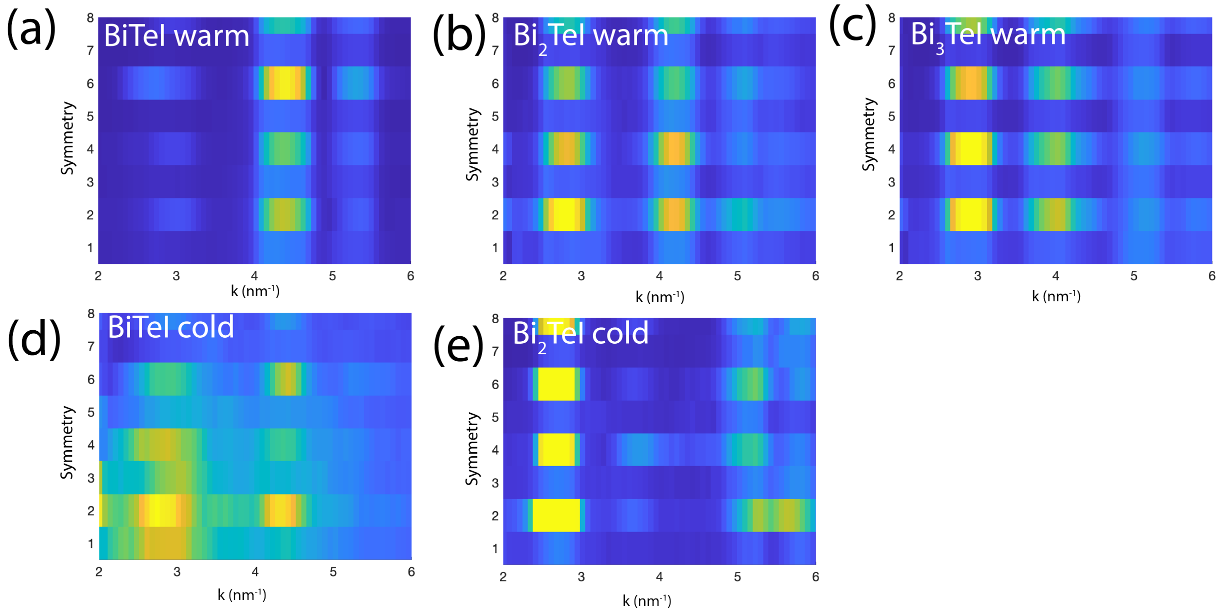

Figure 6.2: Angular symmetries in Bi$_x$TeI thin films. (a,b,c) Angular symmetries in warm grown Bi$_x$TeI, the dominant symmetries are 2-, 3-, and 6-fold. 4-fold symmetries show up at different k with decreasing disorder. (d,e) Angular symmetries in cold grown Bi$_x$TeI. The dominant symmetry is 2-fold for the main amorphous diffraction peak. There are also 3, 4, and 6-fold symmetries.

6.2 Transport

Turning now to the electrical transport properties of these films, we find a transition from insulating to metallic behavior with increasing x, for both RT and LT samples. Fig. 6.3(a,b) shows the conductivity of RT and LT Bi$_x$TeI samples versus temperature for a range of x, showing clear evidence of a MIT in Bi$_x$TeI for both RT and 230 K grown films at different x. All samples are plotted here on log scales (a,b) or linear scales (c,d) of σ vs T in order to display the transition from metallic behavior at high x to insulating behavior at lower x. The high x samples (both RT and LT) show a nearly temperature independent conductivity, with $\sigma \sim 800\Omega{\cdot}\text{cm}^{-1}$, which increases slightly with increasing temperature, a common feature of amorphous metals above but near the MIT, and a sign of WL and quantum correction effects. We note again that for single crystal $x = 3$, the $\sigma \sim 2000\Omega{\cdot}\text{cm}^{-1}$, and decreases slightly with increasing temperature. With decreasing x, σ decreases and becomes increasingly temperature dependent, with increasingly sharp downturns seen at lower temperatures, particularly in the LT samples. By fitting the data to $\sigma_0 + AT^{1/2}$, an expression appropriate to metals near the MIT, values for σ_0 vs. x are extracted and plotted in Fig. 6.3(c). These figures show σ_0 vanishing for x near 1.5 (RT) and 2.4 (LT). For lower x (lower σ), the data

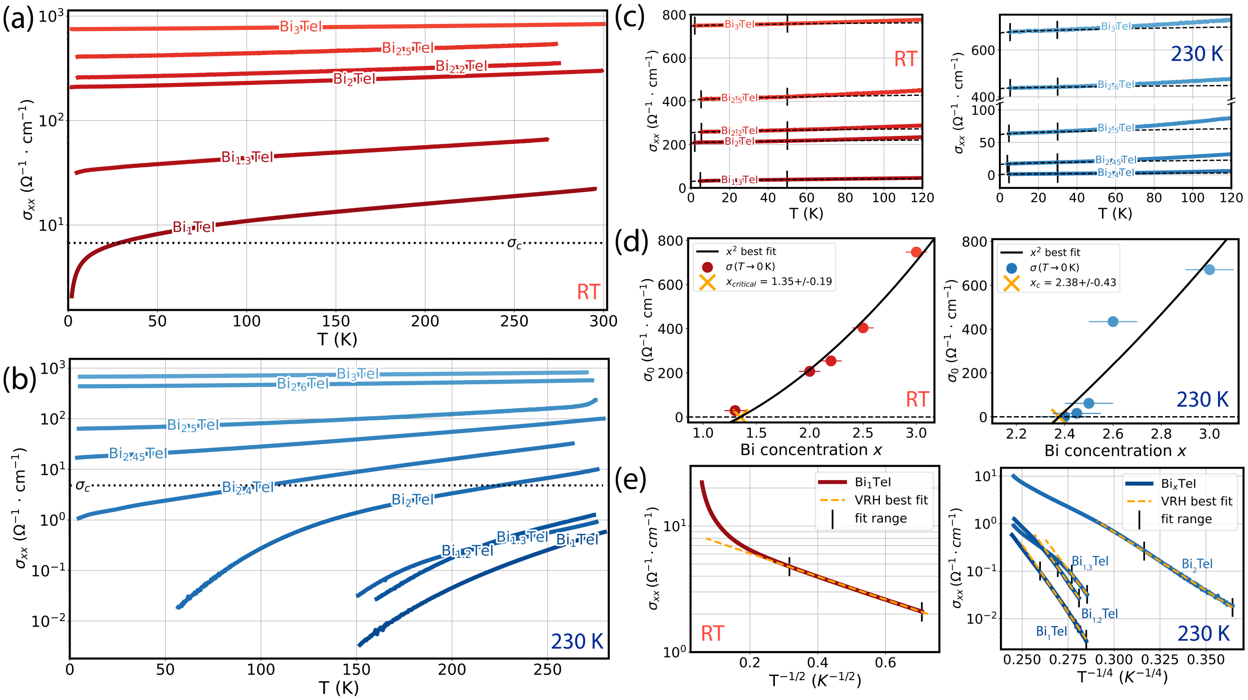

Figure 6.3: Metal-insulator transition in Bi$_x$TeI for $x = 1 - 3$. (a) Conductivity σ vs. temperature for Bi$_x$TeI films grown at room temperature (RT) and (b) with substrates cooled down to $\approx 230\,\mathrm{K}$ (LT). (c-e) left RT, right 230K (or LT). (c) Fits to the conductivity based on the presence of interactions, $\sigma(T) = \sigma_0 + aT^{1/2}$, where $\sigma_0 = \sigma(T = 0\,\mathrm{K})$ and the $T^{1/2}$ term is due to Coulomb interactions in a disordered system. (d) σ_0 vanishes as a power law for the metal-insulator transition approached from the metallic side. The critical Bi composition x for RT grown is $x_c = 1.35 \pm 0.19$ and for films grown at 230 K is $x_c = 2.38 \pm 0.43$. This significant difference in x_c displays how the increased disorder in films grown at reduced temperature affects the electronic properties of the material. (e) VRH fits $\propto e^{-(T_0/T)^{\nu}}$ to Bi$_x$TeI films that show insulating behaviour. The fit range is indicated by the black bars. The RT Bi$_1$TeI curve (red) is close to the metal-insulator transition and therefore best described for a temperature up to 10 K by $\nu = 1/2$. The insulating films grown at reduced temperature (blue) are well described within a Mott-type VRH with $\nu = 1/4$ for a large T range.

is best viewed on a log scale, with a fit to VRH, as shown in 6.3(e). Cold grown samples with $x < 2.4$ were not measured below 50 or 150 K (depending on x) because their resistance exceeded MΩ, the limit of the measurement setup.

We now look in greater detail at the temperature dependence of $\sigma(T)$. Altshuler and Aronov [169] described the effect of Coulomb interactions between electrons in a disordered system which carve out a $\sqrt{E}$ gap in the density of states and cause a $T^{1/2}$ term in the conductivity for metallic systems, with a non-zero conductivity in the limit as T approaches zero. Fig. 6.3(c) shows the low temperature fit including a $T^{1/2}$ term for both warm and cold grown samples on the metallic side. Curves with nonzero $\sigma_0 = \sigma(T = 0\,\mathrm{K})$ allows us to make an estimate of the composition x of Bi$_x$TeI films where the MIT occurs. From scaling theory of localization it is assumed that σ_0 vanishes continuously when being approached from the metallic side with a critical exponent ν such that $\sigma_0 \propto (x - x_c)^\nu$. In literature a scatter of results for ν ranging from 0.5 to 2 is found, and a debate about the interpretation of the transition is ongoing [170]. σ_0 values for both warm and cold grown films were fit to this expression, with a best fit value of with $\nu = 2$ shown in Fig. 6.3(d). From this data we report a critical composition x_c of $x_{c,warm} = 1.35 \pm 0.19$ and $x_{c,cold} = 2.38 \pm 0.43$.

On the insulating side of the MIT, localized states contribute to conductivity by hopping to states near the Fermi level. σ is proportional to $e^{-(T_0/T)^\nu}$ where T_0 is a temperature which can be related to the localization length (length scale over which the amplitude of the electron wavefunction decays) and $\nu = 1/4$. Efros and Shklovskii showed that when Coulomb interactions are taken into account the exponent is $\nu = 1/2$ [8]. $\nu = 1/4$ is normally obeyed except near the metal-insulator transition where the Coulomb gap becomes large compared to the hopping energy and $\nu = 1/2$ is observed [8]. Fig. 6.3(e) shows curves with insulating character ($x < x_c$) for warm and cold grown films where the fits indicate the hopping regime. In the warm grown films only RT-BiTeI is insulating and is well described by a VRH model with $\nu = 1/2$ up to 10 K, indicating Coulomb effects are important. The cold grown samples with a composition below $x_{c,cold}$ show highly insulating behaviour which is well described within the $\nu = 1/4$ model for a large temperature range (χ^2 is better for $\nu = 1/4$ fit vs. $\nu = 1/2$ fit).

The magnetoresistance (MR) is a probe of the different dephasing mechanisms from the hopping to diffusive regimes in RT grown Bi$_x$TeI films. Low temperature MR measurements are sensitive to quantum corrections in the diffusive regime such as WAL or WL which manifest as positive or negative MR (negative or positive magnetoconductance). In a magnetic field the electrons acquire an additional phase which reduces the destructive (constructive) interference of WAL (WL). In systems with WAL, the increased backscattering in a magnetic field leads to a positive, sharp increase of the MR. Fig. 6.4 shows the magnetoconductance (MC) curves as a function of temperature and field. RT-BiTeI, which is an insulator, has a positive, linear MR even when it is in the hopping regime where previous works have shown negative magnetoresistance [160, 64]. RT-Bi$_2$TeI shows the onset of WAL with a larger decrease of the MC with applied field compared to RT-BiTeI. RT-Bi$_3$TeI shows a sharp, clear WAL cusp indicated by the rapid decrease of the MC at small magnetic fields. More quantitative estimations of WAL effects can be made by fitting our data to the three dimensional

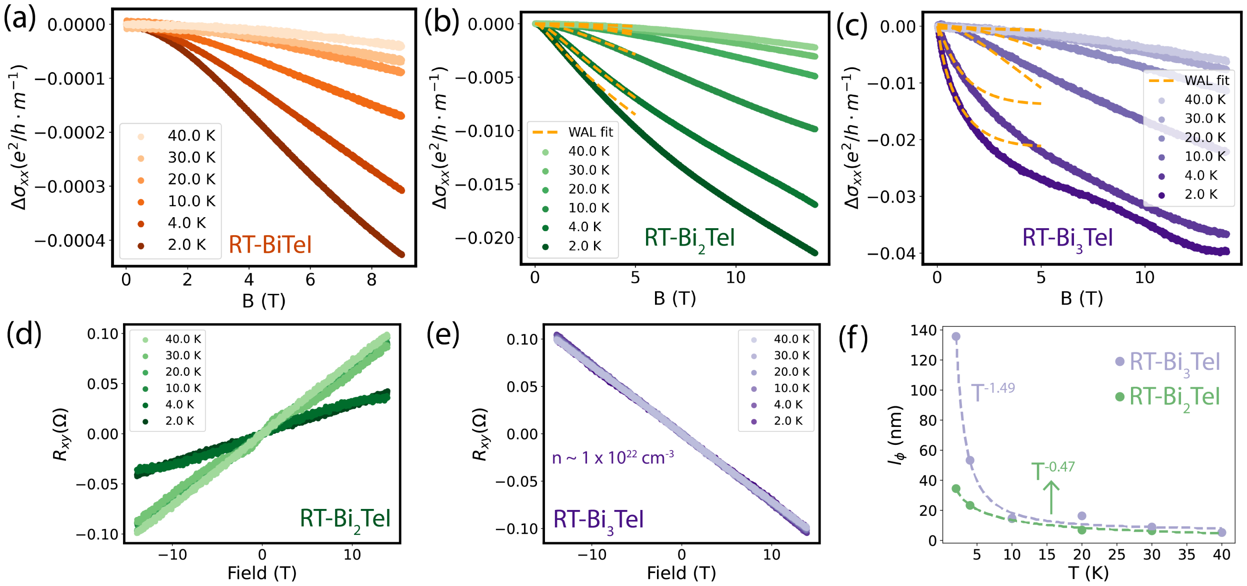

Figure 6.4: Magnetotransport in RT Bi$_x$TeI thin films (a) Magnetoconductance of RT-BiTeI as a function of temperature. The film is highly resistive in the hopping regime and shows a small negative MC that decreases with increasing measurement temperature. (b) Magnetoconductance of RT-Bi$_2$TeI, again negative and decreasing in magnitude with increasing measurement temperature but two orders of magnitude larger than in x=1. Fits shown are 3D weak antilocalization. (c) Magnetoconductance of RT-Bi$_3$TeI with 3D weak antilocalization fits. The sharp dip in the MC with field for 2 K data is from the WAL effect. (d) Hall resistance for RT-Bi$_2$TeI. R_{xy} is nonlinear and the Hall coefficent is small below 5 K. (e) Hall resistance for RT-Bi3TeI. R_{xy} is linear, electron-like, and temperature independent. (f) Dephasing length versus temperature for RT-Bi$_2$TeI and RT-Bi$_2$TeI. The RT-Bi$_2$TeI data is fit best as l_ϕ proportional to $T^{-0.47\pm0.12}$ indicating dephasing due to electron interactions. For RT-Bi$_3$TeI the data is fit best as l_ϕ proportional to $T^{-1.49\pm0.16}$ indicating dephasing due to electron-phonon interactions.

theory of WAL [171]. In three dimensions, the extension of the HLN [66] WAL goes as:

$$\Delta\sigma\left(B\right) = N\frac{e^2}{4\pi h l_B}\left[2\zeta\left(\frac{1}{2},\frac{1}{2}+\frac{l_B^2}{l^2}\right)+\zeta\left(\frac{1}{2},\frac{1}{2}+\frac{l_B^2}{l_\phi^2}\right)-3\zeta\left(\frac{1}{2},\frac{1}{2}+4\frac{l_B^2}{l_{SO}^2}+\frac{l_B^2}{l_\phi^2}\right)\right] \quad (6.1)$$

with ζ being the Hurwitz-Zeta function and where N, l_B, l, l_ϕ, and l_{SO} are the number of channels, magnetic length, mean free path, dephasing length, and spin-orbit scattering length, respectively. N, l, l_ϕ, and l_{SO} are used as fitting parameters. The MC for RT-BiTeI is shown in 6.4(a) without a fit since it is in the hopping regime where the 3D WAL theory is not applicable (see discussion). The fits to the 3D WAL theory for RT-Bi$_2$TeI and RT-Bi$_3$TeI are shown in Fig. 6.4(b,c). The fitting range was up to 1 T where the l_B is $\sim$ 13 nm and greater than the mean free path of our films. By reducing structural disorder, l_ϕ rises to values of 35 nm and then 136 nm in RT-Bi$_2$TeI and RT-Bi$_3$TeI respectively (both magnitudes larger than l_{SO}). This explains the emergence of WAL. Hall effect data on RT samples is shown in Fig. 6.4(d,e). Since RT-BiTeI is in the hopping regime, we don't extract a carrier concentration because the Hall effect is difficult to interpret in this regime, however the Hall voltage is linear and temperature independent. The RT-BiTeI Hall voltage is shown in Fig. 6.5. Below 5 K, the RT-Bi$_2$TeI Hall resistance R_{xy} is nonlinear signaling multiple types of carriers. The Hall coefficient in RT-Bi$_2$TeI is temperature dependent and below 5 K is a factor if two smaller than above 5 K; this can be a linked to the presence of electron interactions since $\delta R_H/R_H = 2\delta R/R$ [172]. The ratio of $(\delta R_H/R_H)/(\delta R/R)$ gives 2.8 for RT-Bi$_2$TeI. For this reason we do not extract a carrier density as the Drude picture is based on a single particle picture. RT-Bi$_3$TeI shows a temperature independent, negative (electron-like) carrier concentration of $n_{3D} \sim 1\times10^{22}$ cm^{-3}. The dependence of the dephasing length l_ϕ on temperature gives insights into the dominant dephasing mechanisms. The dephasing length in RT-Bi$_2$TeI follows a $T^{-0.47\pm0.12}$ scaling, Fig. 6.4(e), indicating the dominant dephasing mechanism is likely stemming from electron interactions. This is because the exponent p is smaller than the value of $p \sim 1-3$ for electron-phonon interactions in 3D disordered systems [173]. This is also the expected exponent for electron dephasing in two dimensions. In RT-Bi$_3$TeI, l_ϕ follows the scaling of $T^{-1.49\pm0.16}$ indicating the dephasing mechanism is dominated by electron-phonon interactions [158], Fig. 6.4(f).

The role of enhanced correlations from disorder can be studied further in Bi$_x$TeI films on the metal side. The application of a magnetic field will suppress quantum interference effects but not electron interactions since interaction effects occur through a particle-hole diffusion channel that is insensitive to magnetic flux [158]. In Fig. 6.6(a) the RT-Bi$_2$TeI samples have a low temperature decrease in the conductivity while the MR is positive, indicating the decrease is a result of electron interactions not WL, which is line with the dephasing length power law. The slope of the line between 2 K and 4 K increases as quantum interference effects are suppressed with increasing field (also seen by the decrease in conductivity above 10 K), indicating the EEI is dominant and the cause of the low temperature conductivity drop. The RT-Bi$_3$TeI sample shows a low temperature upturn in the conductivity which is destroyed with applied field and the breaking of time reversal symmetry, Fig. 6.6(b). This

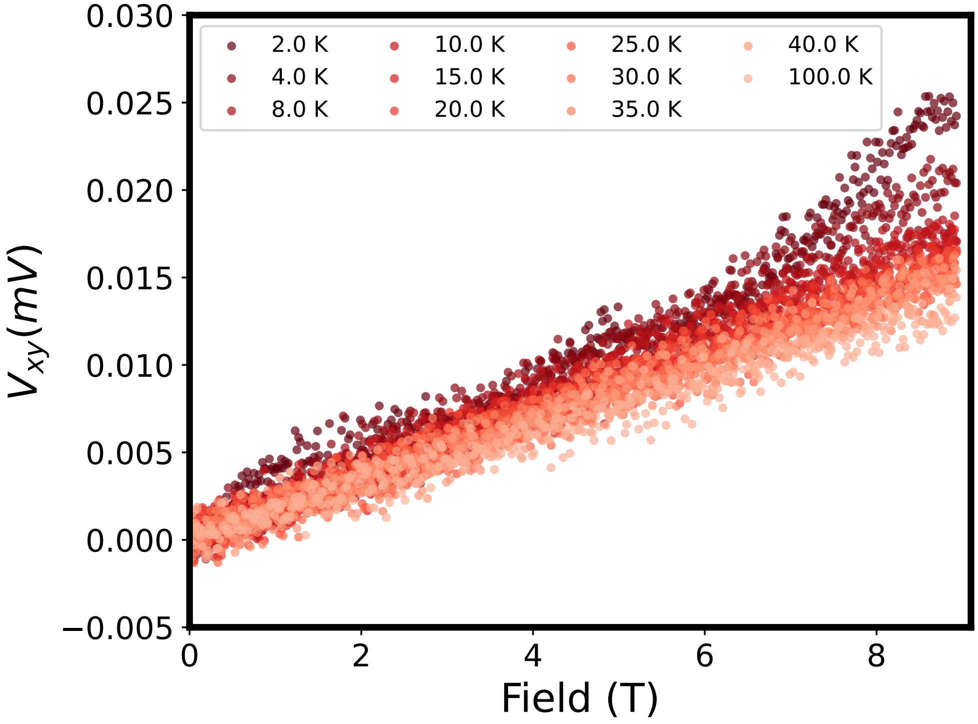

Figure 6.5: Hall voltage in RT-BiTeI thin films. The films are in the hopping regime where the Hall effect is difficult to interpret yet the data looks linear in field and temperature independent. The noise in the data is a result of using a low lock-in frequency which means low frequency noise likely pervaded the measurement.

is consistent with the observation of weak-antilocalization in these films as well as our WAL fitting. The observation of electron interactions in RT-Bi$_2$TeI and not RT-Bi$_3$TeI indicates the electron interactions emerge as x approaches x_c for the MIT in RT-Bi$_x$TeI.

One of the most striking results is that the amorphous (grown at 230 K) LT-BiTeI has a conductivity that is orders of magnitude smaller than RT-BiTeI (grown at RT). There is no change in composition, allowing the direct comparison of the structure in each system and to quantify disorder. The relative peak height of the variance in diffracted intensity between warm and cold grown BiTeI is shown in Fig. 6.1(e). The peak at $2.98\,\mathrm{nm}^{-1}$ for RT-BiTeI has 3 times the intensity of LT-BiTeI and the peak at $4.35\,\mathrm{nm}^{-1}$ for RT-BiTeI has 128 times the intensity of LT-BiTeI. The same comparison between RT and LT-Bi$_2$TeI is seen in 6.1(f). The peak at $2.8\,\mathrm{nm}^{-1}$ for RT-Bi$_2$TeI has 2 times the intensity of LT-Bi$_2$TeI and the peak at $4.2\,\mathrm{nm}^{-1}$ for RT-Bi$_2$TeI has 100 times the intensity of LT-Bi$_2$TeI. In both BiTeI and Bi$_2$TeI, the crystallites that nucleate out of the amorphous matrix order on the length scale corresponding to $k = 4.35\,\mathrm{nm}^{-1}$. The magnitudes increase in the variance peak intensity between LT and RT grown films means the structural disorder is much larger in

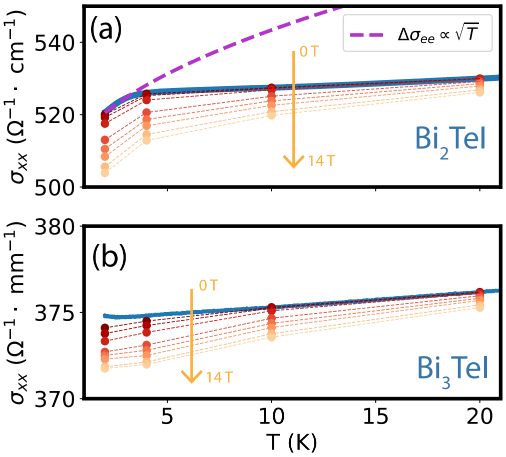

Figure 6.6: Electron interactions in RT Bi$_x$TeI thin films. (a) σ_{xx} vs T for different applied fields in warm Bi$_2$TeI films. The low temperature conductivity dip below 5 K increases with increasing applied field and scales as $\sqrt{T}$, indicating electron interactions. (b) σ_{xx} vs T for different applied fields in warm Bi$_3$TeI films. The low temperature $B = 0$ T conductivity increase as $T \to 0$ is destroyed with increasing applied field because the WAL effect is suppressed.

the LT grown films. This observation is in line with the order of magnitude increase in the conductivity between the LT and RT films seen in 6.3(a,b) showing that increased structural disorder dramatically increases carrier localization.

The MR in RT-BiTeI is positive and linear in the VRH regime, meaning it cannot be explained by a Drude model. In a system with ES VRH and a Coulomb gap the MR scales as B^2 at low fields and becomes exponentially large at large fields and low temperatures [8]. This is a result of the wave function shrinkage effect which leads to a positive MR due to a decrease in localization length with applied field which reduces the probability of a hop [174, 175, 176]. The RT-BiTeI data can be explained by this model, Fig. 6.4(a). In addition, it has been seen that backscattering in the presence of strong spin-orbit scattering in the VRH regime can cause positive MR rather than negative MR from forward scattering mechanisms [177, 178]. Given that RT-BiTeI is close to the to MIT and it has been shown that in RT-Bi$_{2,3}$TeI backscattering in the presence of strong spin-orbit coupling leads to a positive MR (Fig. 6.4(b,c)), it is reasonable to assume this can lead to positive MR in RT-BiTeI. Future experiments studying the anisotropy of the MR could shed light on which effects are dominant. Linear magnetoresistance has been ascribed to linear features of the electronic structure like Dirac cones or Weyl points, but it has also been shown to be the product of disordered current paths and fluctuations in mobility [179, 180, 181, 182].

The presence of nanocrystals has been shown to detrimentally affect the topological properties of some materials [100, 117]. This is due to the large amount of atomic disorder at the grain boundary. The local atomic environment is critical in determining the DOS and topological band inversions [183] and grain boundaries alter the local environment. This can explain why RT-BiTeI and LT-Bi$_2$TeI are highly insulating with no observed transport evidence of topological surface states, such as the saturation of the conductivity at low temperature. LT $x = 1 - 1.3$ films are fully amorphous with no grain boundaries, yet their $\sigma(T) \to 0$ indicating they are trivial insulators. Further spectroscopic measurements are required to determine if there are any topological aspects to the bandstructure in Bi$_x$TeI films.

6.3 Conclusions

In conclusion, we have found that the strong SOC material Bi$_x$TeI undergoes a disorder-driven metal-insulator transition with varying x that is dependent on the structure of the films. The metal-insulator transition is accompanied by weak antilocalization on the metallic side and hopping transport on the insulating side. As structural disorder is increased, increased electron interactions in room temperature grown films are evidenced by Efros-Shklovskii hopping and a reduction in the low temperature conductivity on the metallic side. Power-law fits suggest the dephasing mechanisms are consistent with the observed conductivity as a function of temperature and field. Given the many exotic phases of Bi$_x$TeI and the observation of interactions with increased disorder, this system lends itself to the study of the convergence of many-body physics and topological phases. Our work highlights how an amorphous solid state system can be tuned into a functional quantum material with disorder. To the best of our knowledge this is the first study to grow Bi$_x$TeI thin films. We expect our work to motivate an effort to understand disorder in quantum materials, enabling materials discovery that can provide a path towards scalable quantum devices.

Chapter 7

Structural Spillage

This chapter is based on a manuscript in final preparation with explicit permission from all co-authors. The author list is Daniel Muñoz-Segovia, Paul Corbae, Daniel Varjas, Frances Hellman, Sinead Griffin, and Adolfo G. Grushin.

Predicting which solids are in a topological phase is a central problem of condensed matter physics. For crystalline solids, numerical methods based on first-principles calculations [184] take advantage of symmetries [185, 186, 187, 118] to efficiently screen topological materials. Whether a crystal is topological or not can be answered in most cases by simply consulting online databases [184]. However, there is no computationally efficient method to determine which amorphous materials are topological. Solving this challenge would open up a material class at least as large as crystals [188, 117] in which to explore topological phenomena [189, 45, 106, 117, 105, 29, 191, 189, 135, 190, 191] and novel phenomenology unique to amorphous matter [192, 193, 194, 195, 190, 196, 197, 198, 135].

To overcome this methodological problem, we introduce the structural spillage. It is based on the idea that a reference system whose topological state is known can be used to determine the topological state of a second, unknown system. For crystals, Liu and Vanderbilt [199] proposed to compare the overlap between wavefunctions with and without spin-orbit coupling, which they called the spin-orbit spillage, to signal topological band inversions efficiently. Here, we build on this idea by defining the structural spillage, which measures the overlap between wavefunctions with different atomic configurations. The structural spillage allows then to compare the wavefunctions of crystals, whose topological state can be efficiently calculated using standard tools [184], with those of amorphous solids, whose topological state is unknown and challenging to determine.

To exemplify the potential of the structural spillage, we benchmark its ability to detect topological phase transitions upon amorphization, using both the tight-binding approximation and density functional theory (DFT). Specifically, the structural spillage confirms that amorphous bismuthene is topological [200, 201], and predicts that amorphous bilayer bismuth is a novel topological material. Our results indicate that the structural spillage is suitable to establish a high-throughput catalogue of potential amorphous topological materials, using currently available DFT codes based on plane waves [41, 42, 202]

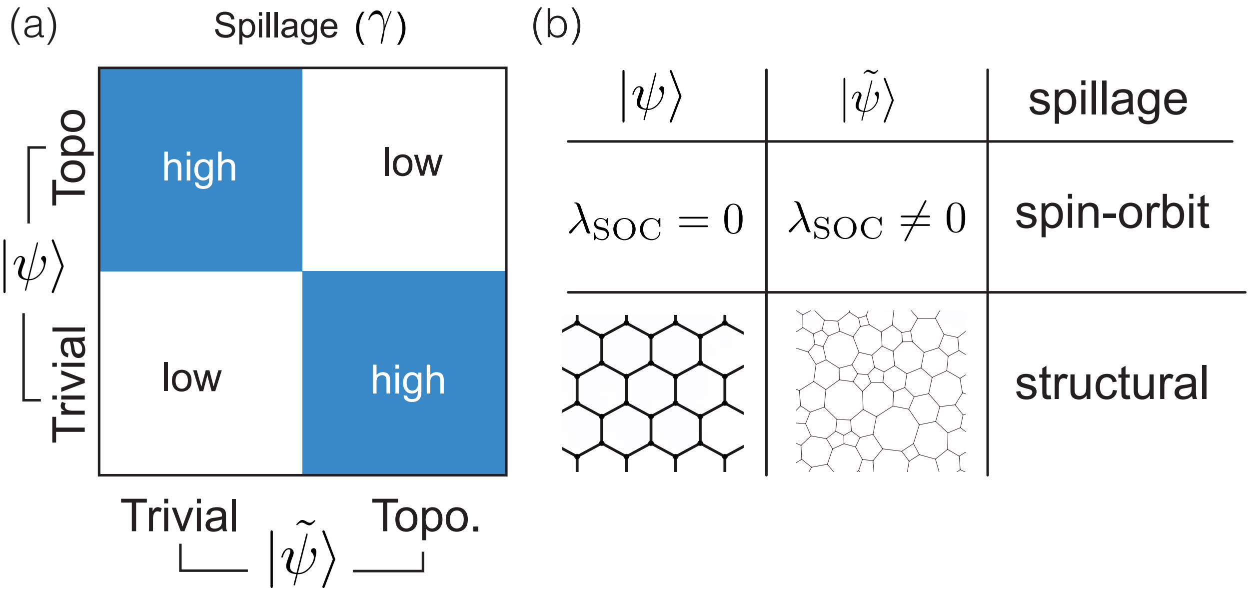

Figure 7.1: (a) The spillage γ is high or low depending on whether a test wavefunction $|\psi\rangle$ is in the same or different topological state compared to a known reference wavefunction $|\tilde{\psi}\rangle$. (b) The spin-orbit spillage [199] compares wavefunctions with and without spin-orbit coupling. The structural spillage takes advantage of the knowledge of the topological state of a crystalline solid to find the topological state of an amorphous solid.

7.1 Structural spillage

The total spillage γ measures the mismatch between two projectors P and $\tilde{P}$ into occupied states [199]:

$$\gamma = \frac{1}{2}\mathrm{Tr}\left[\left(P - \tilde{P}\right)^2\right] = \mathrm{Tr}\left[P(1 - \tilde{P})\right], \tag{7.1}$$

where the trace acts on the entire Hilbert space, and the last equality holds under the assumption that both systems have the same total number of occupied states $N_{\mathrm{occ}} = \mathrm{Tr}[P] = \mathrm{Tr}[\tilde{P}]$. By definition, $\gamma \geq 0$. From the first equality, γ can be viewed as the variance between two distributions with the same average. When $P = \tilde{P}$ the spillage vanishes. In contrast, it equals the total number of occupied states N_{occ} when the overlap between the two projectors is zero. Therefore, γ acts as an indicator of band inversions caused by the parameters that differ in P and $\tilde{P}$ [199].

To predict topological crystals, Liu and Vanderbilt [199] chose P and $\tilde{P}$ to be projectors onto the subspace of occupied states of crystalline insulators with and without spin-orbit coupling, respectively. Lattice periodicity allows then to resolve the projectors in Bloch momentum $\boldsymbol{k}$ as $P(\boldsymbol{k}) = \sum_{n\in\text{occ}} |\psi_{n\boldsymbol{k}}\rangle\langle\psi_{n\boldsymbol{k}}|$, which we can use to define a $\boldsymbol{k}$-resolved spin-orbit Bloch spillage, $\gamma_{\text{B}}(\boldsymbol{k}) = n_{\text{occ}} - \text{Tr}[P(\boldsymbol{k})\tilde{P}(\boldsymbol{k})]$, where $n_{\text{occ}} = N_{\text{occ}}/N_{\text{cells}}$ is the number of occupied bands. The total spillage is recovered by summing over all momenta in the Brillouin zone (BZ), $\gamma = \sum_{\boldsymbol{k}} \gamma_{\text{B}}(\boldsymbol{k})$. The spin-orbit Bloch spillage $\gamma_{\text{B}}(\boldsymbol{k})$ measures the amount of band inversion caused by spin-orbit coupling at each $\boldsymbol{k}$; it is large at points in the BZ where the band inversion is sizable. Ref. [199] showed that at certain points in the BZ the spin-orbit Bloch spillage has to be larger than some given value if the spin-orbit coupling induces a topologically non-trivial phase. For instance, this lower bound is two for a time-reversal symmetric topological insulator. Their proof relies on the so-called Wannier obstruction, which prevents a topologically non-trivial system from being described by symmetric and exponentially localized Wannier functions.

Due to the above properties, $\gamma_{\text{B}}(\boldsymbol{k})$ can be used to signal topological band inversions in crystals. It is currently implemented in the Materials Project database [203], as it is easy to compute using DFT [199]. Indeed, it has recently been applied to high-throughput searches for topological crystals [204, 205]. However, a large spillage is a necessary but not a sufficient condition for topology: in certain cases, e.g., when many bands close to the Fermi level are slightly mixed by spin-orbit coupling, the spillage may be fooled by trivial insulators [199]. Consequently, modern searches for topological crystals favor symmetry based methods. In most practical cases the spillage is expected to be an accurate indicator of a topological state [199].

Unlike for crystals, there is no efficient and model-independent method to predict which amorphous solids are topological. While symmetry indicators can efficiently diagnose topological states of simple model tight-binding Hamiltonians of amorphous matter with average and local symmetries [191], it is unclear how they would diagnose realistic materials. Without symmetry-based methods and the lack of periodicity, the main alternative is to compute real-space invariants [206, 207, 208, 209], which are often computationally costly and not well integrated within *ab-initio* codes.

In this work, we propose a spillage that compares an amorphous system with its crystalline counterpart. In this way, we take advantage of the fact that the topological phase of crystals can be efficiently determined using standard tools [184]. To this end, let us write the total spillage γ in the plane wave basis $|\boldsymbol{p}\alpha\rangle$, where $\boldsymbol{p}$ is the plane-wave momentum (not necessarily restricted to the first BZ) and α denotes the spin degree of freedom. The plane-wave basis is convenient because it is well-defined for both crystalline and amorphous systems, and it is used in several *ab-initio* codes [41, 42, 202]. In order to compute the spillage, we need the projector onto occupied states of the amorphous and reference systems, $P = \sum_{N\in\text{occ}} |\psi_N\rangle\langle\psi_N|$, where $|\psi_N\rangle$ are the eigenstates. By projecting them onto plane waves, we have access to the projector matrix elements $P^{\alpha\beta}_{\boldsymbol{p},\boldsymbol{p}'} = \langle\boldsymbol{p}\alpha|\, P\, |\boldsymbol{p}'\beta\rangle$, which are well-defined for crystalline and amorphous systems. By noting that any plane-wave momentum $\boldsymbol{p}$ can be uniquely decomposed as $\boldsymbol{p} = \boldsymbol{k} + \boldsymbol{G}$, the sum of a crystal momentum $\boldsymbol{k}$ in the first BZ plus a reciprocal lattice vector $\boldsymbol{G}$, both of the reference crystal, we can define the quasi-Bloch spillage as

$$\gamma_{\mathrm{qB}}(\boldsymbol{k}) = \frac{1}{2}\sum_{\boldsymbol{k}'}\sum_{\boldsymbol{G}\boldsymbol{G}'}\sum_{\alpha\beta}\left[P^{\alpha\beta}_{\boldsymbol{k}+\boldsymbol{G},\boldsymbol{k}'+\boldsymbol{G}'}P^{\beta\alpha}_{\boldsymbol{k}'+\boldsymbol{G}',\boldsymbol{k}+\boldsymbol{G}} - P^{\alpha\beta}_{\boldsymbol{k}+\boldsymbol{G},\boldsymbol{k}'+\boldsymbol{G}'}\tilde{P}^{\beta\alpha}_{\boldsymbol{k}'+\boldsymbol{G}',\boldsymbol{k}+\boldsymbol{G}}\right] + \left[P \leftrightarrow \tilde{P}\right] = \tag{7.2a}$$

$$= \frac{1}{2}\left\{\left[\sum_{\boldsymbol{G}\alpha}P^{\alpha\alpha}_{\boldsymbol{k}+\boldsymbol{G},\boldsymbol{k}+\boldsymbol{G}}\right] + \tilde{n}_{\mathrm{occ}}(\boldsymbol{k}) - \sum_{\boldsymbol{G}\alpha}\sum_{\boldsymbol{G}'\beta}\left[P^{\alpha\beta}_{\boldsymbol{k}+\boldsymbol{G},\boldsymbol{k}+\boldsymbol{G}'}\tilde{P}^{\beta\alpha}_{\boldsymbol{k}+\boldsymbol{G}',\boldsymbol{k}+\boldsymbol{G}} + \tilde{P}^{\alpha\beta}_{\boldsymbol{k}+\boldsymbol{G},\boldsymbol{k}+\boldsymbol{G}'}P^{\beta\alpha}_{\boldsymbol{k}+\boldsymbol{G}',\boldsymbol{k}+\boldsymbol{G}}\right]\right\} \tag{7.2b}$$

In Eq. (7.2b) we have used the fact that the reference projector $\tilde{P}$ corresponds to a crystal, which allows us to set $\boldsymbol{k}' = \boldsymbol{k}$ in terms involving at least one $\tilde{P}$, since there is no scattering between different crystal momenta due to the discrete translational symmetry. Note that $\gamma_{\mathrm{qB}}(\boldsymbol{k})$ fulfills the same sum rule as the Bloch spillage, $\gamma = \sum_{\boldsymbol{k}}\gamma_{\mathrm{qB}}(\boldsymbol{k})$. Therefore, applied to two insulating crystals, $\gamma_{\mathrm{qB}}(\boldsymbol{k})$ recovers the Bloch spillage. Moreover, it can also be applied to semimetallic systems with the advantage of it being bounded by zero, in contrast to recent extensions to semimetallic materials [204, 205].

The main result of this paper is to show that the structural quasi-Bloch spillage, defined by Eq. (7.2), can be used as an efficient topological indicator in amorphous systems. Crucially, it can be efficiently computed with plane-wave-based DFT methods, since the projector matrix elements are an output of the calculation. Consequently, this method is suitable for high-throughput screening of amorphous topological materials.

7.2 Structural spillage in DFT: free-standing Bi bilayer

To show that Eq. (7.2) is well suited for high-throughput screening of amorphous topological materials, we calculate the structural spillage from the output wavefunctions using first-principles codes. To this end we use the free-standing Bismuth (111) bilayer as an example. This 2D Bi allotrope, whose crystalline phase consists of a buckled honeycomb lattice with lattice constant $a = 4.33\mathring{A}$, is also predicted to be a strong topological insulator crystal with $\mathbb{Z}_2 = 1$ [210, 211, 212, 213]. However, no prediction exists for its amorphous counterpart.

In order to accurately represent amorphous structures, we create $5 \times 5 \times 1$ supercells of the Bi bilayer, whose electronic structure is computed for a single supercell momentum, the center of the supercell BZ. Starting from a crystalline supercell, the disordered structure is then created by adding random disorder in the x, y, and z directions, sampled from a Gaussian distribution. The structures and their corresponding radial distribution functions are shown in Fig. 7.2.

To predict the topological phase of an amorphous Bi bilayer with spin-orbit coupling we compute Eq. (7.2) with plane-wave-based DFT to compare it with its crystalline counterpart without and with spin-orbit coupling. When the crystal has no spin-orbit coupling (Fig. 7.3,

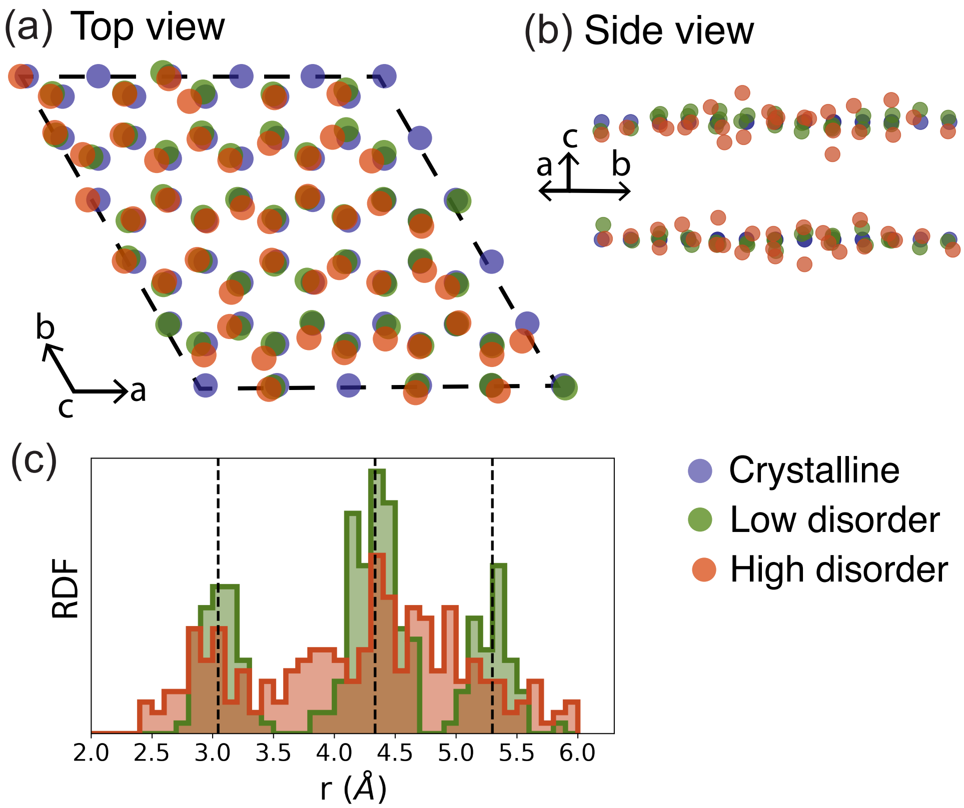

Figure 7.2: Bismuth bilayer DFT supercells. (a) and (b) show in-plane and out of plane views of the super-cell lattice, respectively. The three colors indicate different degrees of disorder: crystal (blue), low disorder (green) and high-disorder (orange). (c) Statistics on the bond lengths in the disordered Bismuth bilayer and their deviations from the perfect crystal (vertical dashed lines). The disorder is sampled from a Gaussian distribution.

first row), $\gamma_{\mathrm{qB}}(\boldsymbol{k})$ is peaked at $\boldsymbol{k} = 0$, with $\gamma_{\mathrm{qB}}(\boldsymbol{k} = 0) > 2$. Increasing disorder smooths $\gamma_{\mathrm{qB}}(\boldsymbol{k})$, yet it remains peaked at Γ with a value greater than 2. In contrast, when both the disordered Bi bilayer and the pristine crystal have spin-orbit coupling (Fig. 7.3, second row) the spillage is always small. Both rows together show that amorphous Bismuth bilayer with spin-orbit coupling is in the same state as the crystal with spin-orbit coupling, a strong topological insulator crystal with $\mathbb{Z}_2 = 1$.

The last column of Fig. 7.3, compares our DFT results with those obtained using a tight-binding model for the amorphous Bi (111) bilayer. For comparable disorder strengths, $\gamma^{\mathrm{TB}}_{\mathrm{qB}}(\boldsymbol{k})$ is broader and its maximum value is smaller than $\gamma_{\mathrm{qB}}(\boldsymbol{k})$. It is thus apparent that, due to the approximations in the tight-binding calculation of the spillage, the spillage method is more suitable for DFT, an advantageous feature compared to other topological indicators available for amorphous systems.

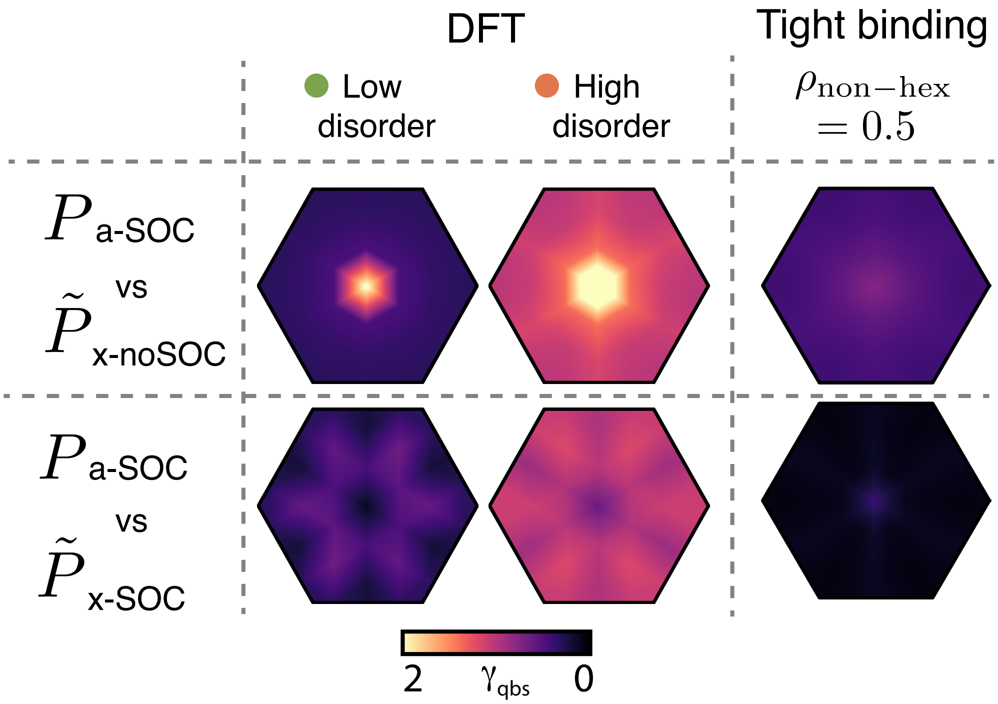

Figure 7.3: Structural quasi-Bloch spillage $\gamma_{\text{qB}}(\boldsymbol{k})$ for the Bismuth bilayer. First row: comparison between an amorphous system with spin-orbit coupling (a-SOC) and a crystalline system without spin-orbit coupling (x-noSOC). Comparing an amorphous system without spin-orbit coupling with a crystalline sample with spin-orbit coupling leads to similar results. Second row: comparison between the amorphous and crystalline systems with spin-orbit coupling (a-SOC and x-SOC, respectively). $\gamma_{\text{qB}}(\boldsymbol{k})$ is high at $\boldsymbol{k} = 0$ for the first row while small for the second row, indicating that amorphous bismuth bilayer is a topological insulator. The last column shows a comparison with the tight-binding quasi-Bloch spillage $\gamma_{\text{qB}}^{\text{TB}}(\boldsymbol{k})$.

7.3 Discussion

We have introduced the structural spillage as an efficient method to signal amorphous topological phases, compatible with tight-binding and *ab-initio* simulations. We have used it to predict amorphous bismuthene as a novel topological insulator.

As for crystals, we expect the spillage to signal a large fraction of promising materials, but not to be infallible: if multiple band inversions are physically expected upon amorphization, the spillage might also be artificially large. However, unlike for crystals, the spillage seems to be the only model-independent method that is systematic and compatible with existing *ab-initio* packages. Additionally, we observe that, for different disorder realizations, its fluctuations are smaller compared to scattering methods like calculating the conductance. It can also be applied to systems without a spectral gap, where the effective Hamiltonian approach [214] can fail [191]. Lastly, while Eq. (7.2) is general, the definition of the spillage is relatively versatile and can accommodate less standard cases. For example, when no crystalline counterpart exists, one may define a plane-wave-resolved spillage by using Eq. (7.2a) without the sum over $\boldsymbol{G}$, a modification worth studying in the future. Lastly, the spillage can also be applied to indicate topology in other non-crystalline solids, including quasicrystals.

In conclusion, the structural spillage suggests a clear road-map to establish a high-throughput candidate-material catalogue by screening existing amorphous databases, or by scrutinizing realistic structures obtained using existing *ab-initio* molecular dynamics packages [215]. This methodology may enable for the first time the systematic prediction and discovery of a potentially large number of amorphous materials that are currently inaccessible, suitable to develop affordable and scalable topological devices.

Chapter 8

Conclusions and outlook

The most important conclusion from this work is that interesting physics and the search for quantum materials should not be restricted to crystalline materials with long-range order. This work has shown that the local ordering in amorphous materials enables these materials to host a myriad of interesting phenomena that is traditionally observed in systems with a periodic arrangement of atoms. The observation of quantum phenomena like spin-momentum locked surface states in amorphous materials should motivate the fields of materials science and condensed matter physics to look to amorphous materials for quantum and topological states that most scientists think require crystalline periodicity and symmetries [117].

Regarding topology in amorphous solid state materials, studying amorphous Bi_2Se_3 has highlighted that the local environment in the amorphous system influences the topological properties of the electronic structure and surface states. When going from a topological crystal to an amorphous system, if the local environment can be preserved then the system is likely to retain its topological bulk with the resultant physical properties useful for quantum information and low power electronics. It was shown that by simply modifying the local environment in BiTeI, we could induce a topological phase transition from trivial to nontrivial [161]. Therefore we conclude that the local environment leads to an understanding of the coarse density of states. Using this DOS, especially in the context of topological insulators, we can classify whether the energy gap is a topological or trivial one. Therefore, when studying amorphous topological materials we need to take a local perspective. One of the interesting findings of this work is that nanocrystalline systems seem to be devoid of topological properties, a result of the disorder at the grain boundaries. Further studies into the atomic and electronic structure at the grain boundary using set of measurement techniques different than the ones presented in this thesis would shed light on whats happening at the grain boundary regarding topology.

Regarding amorphous materials, especially with our ARPES measurements, is it shown that there is electron coherence and momentum space structure arising from the local structural order. Considering that dispersive features exist in amorphous momentum space, we can reevaluate the use of amorphous materials for novel phases. Additionally we showed that electrons in a quantum material with an interesting momentum space dispersion can be localized by structural disorder and electron interactions. We hope this work motivates understanding more than just topology in amorphous systems.

Looking forward there is a need to develop efficient ways to predict and measure amorphous topological phases. The absence of translational symmetry and the Bloch wavevector is pushing the limits of the field theoretically. New methods have been developed but the field needs to go further to characterize amorphous topological matter as well as develop a classification scheme of amorphous matter. The normal insulator to topological insulator transition via amorphization would be an exciting experimental realization, and the motivation of the experimental work on $\mathrm{Bi}_x\mathrm{TeI}$ films. Unfortunately the films grew mostly nanocrystalline, but the growth temperature is a powerful tool to modify the structure. The structural spillage is a theoretical tool that can be used to predict topological properties of realistic amorphous materials which will then guide experiments. This will supplement our understanding of topological matter based on model Hamiltonians. This method will enable the broad search for new materials that can be topological as well help develop theoretical indicators comparable to those that we know in crystals based on the results. One of the unresolved and open materials science questions is what materials can be made amorphous by PVD. Therefore, we believe there are exciting experimental prospects to this field. The structural spillage can be combined with high throughput methods to identify which materials can host topological phases in the amorphous phase, hopefully discovering many materials. Once new amorphous topological phases have been identified, developing a suitable workflow of experimental techniques can aid in the experimental discovery. Transport is a good measurement technique for amorphous materials, however directly diagnosing topological phases in transport is not easy. Performing a nanoribbon experiment where the magnetic flux threaded through the amorphous nanoribbon competes with the π Berry phase would be an interesting experiment. Gating experiments would also be interesting to measure the conductivity when the Fermi-level is in the mid-gap states. ARPES has been the go-to measurement for topological states due to bulk-boundary correspondence and its direct measurement of $E(k)$. It worked very well for measuring amorphous $\mathrm{Bi}_2\mathrm{Se}_3$ when we took into account all considerations of a system which lacks long range order. Other measurement such as STM which can directly measure the electronic structure and real space structure would be invaluable for amorphous materials. Nano-ARPES is moving in this direction as well. With these measurements we could correlate the electronic structure to the local environment which produces the topological phase. In our ARPES measurements we had to be very careful to not crystallize the film when performing the decap process, therefore moving to systems where the films could be grown in-situ and transferred would make a more efficient measurement process. The possibilities are endless with amorphous materials!

Bibliography

[1] Tiantian Zhang et al. “Catalogue of topological electronic materials”. In: *Nature* 566.7745 (2019), pp. 475–479. ISSN: 1476-4687. DOI: `10.1038/s41586-019-0944-6`. URL: `https://doi.org/10.1038/s41586-019-0944-6`.

[2] M G Vergniory et al. “A complete catalogue of high-quality topological materials”. English. In: *Nature Publishing Group* 566.7745 (Feb. 2019), pp. 480–485. DOI: `10.1038/s41586-019-0954-4`. URL: `https://www.nature.com/articles/s41586-019-0954-4`.

[3] Feng Tang et al. “Comprehensive search for topological materials using symmetry indicators”. English. In: *Nature Publishing Group* 566.7745 (Feb. 2019), pp. 486–489. DOI: `10.1038/s41586-019-0937-5`. URL: `https://www.nature.com/articles/s41586-019-0937-5`.

[4] Richard Zallen. *The Physics of Amorphous Solids.* Wiley, 1998.

[5] G. Bergmann. “Amorphous metals and their superconductivity”. In: *Physics Reports* 27.4 (1976), pp. 159–185. ISSN: 0370-1573. DOI: `https://doi.org/10.1016/0370-1573(76)90040-5`. URL: `https://www.sciencedirect.com/science/article/pii/0370157376900405`.

[6] P. W. Anderson. “Absence of Diffusion in Certain Random Lattices”. In: *Phys. Rev.* 109 (5 Mar. 1958), pp. 1492–1505. DOI: `10.1103/PhysRev.109.1492`. URL: `https://link.aps.org/doi/10.1103/PhysRev.109.1492`.

[7] N.E. Mott and E.A. Davis. *Electronic Processes in Non-Crystalline Materials.* Oxford Classic Texts in the Physical Sciences. Oxford University Press, 1979. ISBN: 9780199645336.

[8] Alex L. Efros Boris I. Shklovskii. *Electronic Properties of Doped Semiconductors.* 1st ed. Springer Berlin, Heidelberg, 1984. ISBN: 978-3-662-02405-8.

[9] M. Z. Hasan and C. L. Kane. “Colloquium: Topological insulators”. In: *Rev. Mod. Phys.* 82 (4 Nov. 2010), pp. 3045–3067. DOI: `10.1103/RevModPhys.82.3045`. URL: `https://link.aps.org/doi/10.1103/RevModPhys.82.3045`.

[10] M. V. Berry. “Quantal Phase Factors Accompanying Adiabatic Changes”. In: *Proceedings of the Royal Society of London. A. Mathematical and Physical Sciences* 392.1802 (1984). read, pp. 45–57. DOI: `10.1098/rspa.1984.0023`. eprint: `http://rspa.royalsocietypublishing.org/content/392/1802/45.full.pdf+html`. URL: `http://rspa.royalsocietypublishing.org/content/392/1802/45.abstract`.

[11] F. D. M. Haldane. “Model for a Quantum Hall Effect without Landau Levels: Condensed-Matter Realization of the "Parity Anomaly"”. In: *Phys. Rev. Lett.* 61 (18 Oct. 1988), pp. 2015–2018. DOI: `10.1103/PhysRevLett.61.2015`. URL: `https://link.aps.org/doi/10.1103/PhysRevLett.61.2015`.

[12] Liang Fu and C. L. Kane. “Topological insulators with inversion symmetry”. In: *Phys. Rev. B* 76 (4 July 2007), p. 045302. DOI: `10.1103/PhysRevB.76.045302`. URL: `https://link.aps.org/doi/10.1103/PhysRevB.76.045302`.

[13] J. E. Moore and L. Balents. “Topological invariants of time-reversal-invariant band structures”. In: *Phys. Rev. B* 75 (12 Mar. 2007), p. 121306. DOI: `10.1103/PhysRevB.75.121306`. URL: `https://link.aps.org/doi/10.1103/PhysRevB.75.121306`.

[14] Alexey A. Soluyanov and David Vanderbilt. “Computing topological invariants without inversion symmetry”. In: *Phys. Rev. B* 83 (23 June 2011), p. 235401. DOI: `10.1103/PhysRevB.83.235401`. URL: `https://link.aps.org/doi/10.1103/PhysRevB.83.235401`.

[15] Barry Bradlyn et al. “Topological quantum chemistry”. In: *Nature* 547.7663 (July 2017), pp. 298–305. DOI: `10.1038/nature23268`. URL: `https://www.nature.com/articles/nature23268`.

[16] M. Z. Hasan and C. L. Kane. “Colloquium: Topological insulators”. In: *Rev. Mod. Phys.* 82 (4 Nov. 2010), pp. 3045–3067. DOI: `10.1103/RevModPhys.82.3045`. URL: `https://link.aps.org/doi/10.1103/RevModPhys.82.3045`.

[17] C. W. Groth et al. “Theory of the Topological Anderson Insulator”. In: *Phys. Rev. Lett.* 103 (19 Nov. 2009), p. 196805. DOI: `10.1103/PhysRevLett.103.196805`. URL: `https://link.aps.org/doi/10.1103/PhysRevLett.103.196805`.

[18] Adhip Agarwala and Vijay B. Shenoy. “Topological Insulators in Amorphous Systems”. In: *Phys. Rev. Lett.* 118 (23 June 2017), p. 236402. DOI: `10.1103/PhysRevLett.118.236402`. URL: `https://link.aps.org/doi/10.1103/PhysRevLett.118.236402`.

[19] Noah P Mitchell et al. “Amorphous topological insulators constructed from random point sets”. In: *Nature Physics* 14.4 (Apr. 2018), pp. 380–385.

[20] Yan-Bin Yang et al. “Topological Amorphous Metals”. In: *Phys. Rev. Lett.* 123 (7 Aug. 2019), p. 076401. DOI: `10.1103/PhysRevLett.123.076401`. URL: `https://link.aps.org/doi/10.1103/PhysRevLett.123.076401`.

[21] Jiong-Hao Wang et al. “Structural-Disorder-Induced Second-Order Topological Insulators in Three Dimensions”. In: *Phys. Rev. Lett.* 126 (20 May 2021), p. 206404. DOI: `10.1103/PhysRevLett.126.206404`. URL: `https://link.aps.org/doi/10.1103/PhysRevLett.126.206404`.

[22] Adhip Agarwala, Vladimir Juri či ć, and Bitan Roy. “Higher-order topological insulators in amorphous solids”. In: *Phys. Rev. Research* 2 (1 Mar. 2020), p. 012067. DOI: `10.1103/PhysRevResearch.2.012067`. URL: `https://link.aps.org/doi/10.1103/PhysRevResearch.2.012067`.

[23] Citian Wang et al. “Structural Amorphization-Induced Topological Order”. In: *Phys. Rev. Lett.* 128 (5 Feb. 2022), p. 056401. DOI: `10.1103/PhysRevLett.128.056401`. URL: `https://link.aps.org/doi/10.1103/PhysRevLett.128.056401`.

[24] Dániel Varjas et al. “Topological Phases without Crystalline Counterparts”. In: *Phys. Rev. Lett.* 123 (19 Nov. 2019), p. 196401. DOI: `10.1103/PhysRevLett.123.196401`. URL: `https://link.aps.org/doi/10.1103/PhysRevLett.123.196401`.

[25] Shampy Mansha and Y D Chong. “Robust edge states in amorphous gyromagnetic photonic lattices”. English. In: *Physical Review B* 96.12 (Sept. 2017), p. 121405. DOI: `10.1103/PhysRevB.96.121405`. URL: `https://link.aps.org/doi/10.1103/PhysRevB.96.121405`.

[26] K. Pöyhönen et al. “Amorphous topological superconductivity in a Shiba glass”. In: *Nature Communications* 9, 2103 (May 2018), p. 2103. DOI: `10.1038/s41467-018-04532-x`. arXiv: `1712.07486 [cond-mat.mes-hall]`.

[27] Huaqing Huang and Feng Liu. “Quantum Spin Hall Effect and Spin Bott Index in a Quasicrystal Lattice”. English. In: *Physical Review Letters* 121.12 (Sept. 2018), p. 126401. DOI: `10.1103/PhysRevLett.121.126401`. URL: `https://link.aps.org/doi/10.1103/PhysRevLett.121.126401`.

[28] Huaqing Huang and Feng Liu. “Theory of spin Bott index for quantum spin Hall states in nonperiodic systems”. English. In: *Physical Review B* 98.12 (Sept. 2018), p. 125130. DOI: `10.1103/PhysRevB.98.125130`. URL: `https://link.aps.org/doi/10.1103/PhysRevB.98.125130`.

[29] Chris Bourne and Emil Prodan. “Non-commutative Chern numbers for generic aperiodic discrete systems”. English. In: *Journal of Physics A: Mathematical and Theoretical* 51.23 (June 2018), p. 235202. DOI: `10.1088/1751-8121/aac093`. URL: `http://iopscience.iop.org/article/10.1088/1751-8121/aac093`.

[30] Quentin Marsal, Dániel Varjas, and Adolfo G. Grushin. “Topological Weaire–Thorpe models of amorphous matter”. In: *Proceedings of the National Academy of Sciences* 117.48 (2020), pp. 30260–30265. ISSN: 0027-8424. DOI: `10.1073/pnas.2007384117`. eprint: `https://www.pnas.org/content/117/48/30260.full.pdf`. URL: `https://www.pnas.org/content/117/48/30260`.

[31] Helene Spring, Anton R. Akhmerov, and Daniel Varjas. “Amorphous topological phases protected by continuous rotation symmetry”. In: *SciPost Phys.* 11 (2 2021), p. 22. DOI: `10.21468/SciPostPhys.11.2.022`. URL: `https://scipost.org/10.21468/SciPostPhys.11.2.022`.

[32] Xiao Liu et al. “Hydrogen-Free Amorphous Silicon with No Tunneling States”. In: *Phys. Rev. Lett.* 113 (2 July 2014), p. 025503. DOI: `10.1103/PhysRevLett.113.025503`. URL: `https://link.aps.org/doi/10.1103/PhysRevLett.113.025503`.

[33] Shakeel S. Dalal et al. “Tunable molecular orientation and elevated thermal stability of vapor-deposited organic semiconductors”. In: *Proceedings of the National Academy of Sciences* 112.14 (2015), pp. 4227–4232. DOI: `10.1073/pnas.1421042112`. eprint: `https://www.pnas.org/doi/pdf/10.1073/pnas.1421042112`. URL: `https://www.pnas.org/doi/abs/10.1073/pnas.1421042112`.

[34] C. Barry Carter David B. Williams. *Transmission Electron Microscopy.* Springer, 2009.

[35] L. J. van der Pauw. “TA Method of Measuring Specific Resistivity and Hall Effect of Discs of Arbitrary Shape”. In: *Philips Research Reports* 13 (1958), pp. 1–9.

[36] Jonathan A. Sobota, Yu He, and Zhi-Xun Shen. “Angle-resolved photoemission studies of quantum materials”. In: *Rev. Mod. Phys.* 93 (2 May 2021), p. 025006. DOI: `10.1103/RevModPhys.93.025006`. URL: `https://link.aps.org/doi/10.1103/RevModPhys.93.025006`.

[37] P. Hohenberg and W. Kohn. “Inhomogeneous Electron Gas”. In: *Phys. Rev.* 136 (3B Nov. 1964), B864–B871. DOI: `10.1103/PhysRev.136.B864`. URL: `https://link.aps.org/doi/10.1103/PhysRev.136.B864`.

[38] W. Kohn and L. J. Sham. “Self-Consistent Equations Including Exchange and Correlation Effects”. In: *Phys. Rev.* 140 (4A Nov. 1965), A1133–A1138. DOI: `10.1103/PhysRev.140.A1133`. URL: `https://link.aps.org/doi/10.1103/PhysRev.140.A1133`.

[39] John P. Perdew, Kieron Burke, and Matthias Ernzerhof. “Generalized Gradient Approximation Made Simple”. In: *Phys. Rev. Lett.* 77.18 (Oct. 1996), pp. 3865–3868. DOI: `10.1103/PhysRevLett.77.3865`.

[40] G. Kresse and D. Joubert. “From ultrasoft pseudopotentials to the projector augmented-wave method”. In: *Phys. Rev. B* 59 (3 Jan. 1999), pp. 1758–1775. DOI: `10.1103/PhysRevB.59.1758`. URL: `https://link.aps.org/doi/10.1103/PhysRevB.59.1758`.

[41] G. Kresse and J. Furthmüller. “Efficient iterative schemes for *ab initio* total-energy calculations using a plane-wave basis set”. In: *Phys. Rev. B* 54 (16 Oct. 1996), pp. 11169–11186. DOI: `10.1103/PhysRevB.54.11169`. URL: `http://link.aps.org/doi/10.1103/PhysRevB.54.11169`.

[42] G. Kresse and J. Hafner. “Ab initio molecular dynamics for liquid metals”. In: *Phys. Rev. B* 48.1 (Jan. 1993), p. 13115.

[43] Haruki Watanabe, Hoi Chun Po, and Ashvin Vishwanath. “Structure and topology of band structures in the 1651 magnetic space groups”. English. In: *Science Advances* 4.8 (Aug. 2018), eaat8685. DOI: `10.1126/sciadv.aat8685`. URL: `http://advances.sciencemag.org/lookup/doi/10.1126/sciadv.aat8685`.

[44] Xiao-Liang Qi and Shou-Cheng Zhang. “Topological insulators and superconductors”. In: *Rev. Mod. Phys.* 83 (4 Oct. 2011), pp. 1057–1110. DOI: `10.1103/RevModPhys.83.1057`. URL: `https://link.aps.org/doi/10.1103/RevModPhys.83.1057`.

[45] Adhip Agarwala and Vijay B Shenoy. “Topological Insulators in Amorphous Systems”. English. In: *Phys. Rev. Lett.* 118.23 (June 2017), p. 236402. DOI: `10.1103/PhysRevLett.118.236402`. URL: `http://link.aps.org/doi/10.1103/PhysRevLett.118.236402`.

[46] HaiJun Zhang et al. “Topological insulators in Bi_2Se_3, Bi_2Te_3 and Sb_2Te_3 with a single Dirac cone on the surface”. English. In: *Nature Physics* 5.6 (June 2009), pp. 438–442. DOI: `10.1038/nphys1270`. URL: `https://www.nature.com/articles/nphys1270`.

[47] Hanbum Park et al. “Disorder-induced decoupled surface transport channels in thin films of doped topological insulators”. In: *Phys. Rev. B* 98 (4 July 2018), p. 045411. DOI: `10.1103/PhysRevB.98.045411`. URL: `https://link.aps.org/doi/10.1103/PhysRevB.98.045411`.

[48] M M J Treacy et al. “Fluctuation microscopy: a probe of medium range order”. In: *Reports on Progress in Physics* 68.12 (Oct. 2005), pp. 2899–2944. DOI: `10.1088/0034-4885/68/12/r06`. URL: `https://doi.org/10.1088/0034-4885/68/12/r06`.

[49] Sarah E. Friedensen et al. “Transmission Electron Microscope Nanosculpting of Topological Insulator Bismuth Selenide”. In: *ACS Nano* 12.7 (2018). PMID: 29890079, pp. 6949–6955. DOI: `10.1021/acsnano.8b02377`. eprint: `https://doi.org/10.1021/acsnano.8b02377`. URL: `https://doi.org/10.1021/acsnano.8b02377`.

[50] P.M. Voyles and D.A. Muller. “Fluctuation microscopy in the STEM”. In: *Ultramicroscopy* 93.2 (2002), pp. 147–159. ISSN: 0304-3991. DOI: `https://doi.org/10.1016/S0304-3991(02)00155-9`. URL: `https://www.sciencedirect.com/science/article/pii/S0304399102001559`.

[51] G. Lucovsky et al. “Identification of the fundamental vibrational modes of trigonal, alpha - monoclinic and amorphous selenium”. In: *Solid State Communications* 5.2 (1967), pp. 113–117. ISSN: 0038-1098. DOI: `https://doi.org/10.1016/0038-1098(67)90006-3`. URL: `http://www.sciencedirect.com/science/article/pii/0038109867900063`.

[52] Jun Zhang et al. "Raman Spectroscopy of Few-Quintuple Layer Topological Insulator Bi2Se3 Nanoplatelets". In: *Nano Letters* 11.6 (2011). PMID: 21604748, pp. 2407–2414. DOI: `10.1021/nl200773n`. eprint: `https://doi.org/10.1021/nl200773n`. URL: `https://doi.org/10.1021/nl200773n`.

[53] Yong Seung Kim et al. "Thickness-dependent bulk properties and weak antilocalization effect in topological insulator Bi_2Se_3". In: *Phys. Rev. B* 84 (7 Aug. 2011), p. 073109. DOI: `10.1103/PhysRevB.84.073109`. URL: `https://link.aps.org/doi/10.1103/PhysRevB.84.073109`.

[54] James G. Analytis et al. "Two-dimensional surface state in the quantum limit of a topological insulator". In: *Nature Physics* 6.12 (Dec. 2010), pp. 960–964. ISSN: 1745-2473. DOI: `10.1038/nphys1861`. URL: `http://www.nature.com/articles/nphys1861`.

[55] O. Gunnarsson, M. Calandra, and J. E. Han. "Colloquium: Saturation of electrical resistivity". In: *Rev. Mod. Phys.* 75 (4 Oct. 2003), pp. 1085–1099. DOI: `10.1103/RevModPhys.75.1085`. URL: `https://link.aps.org/doi/10.1103/RevModPhys.75.1085`.

[56] Yang Xu et al. "Observation of topological surface state quantum Hall effect in an intrinsic three-dimensional topological insulator". In: *Nature Physics* 10 (Nov. 2014). Article, 956 EP -. URL: `https://doi.org/10.1038/nphys3140`.

[57] Dohun Kim et al. "Coherent topological transport on the surface of Bi2Se3". In: *Nature Communications* 4.1 (June 2013), p. 2040. ISSN: 2041-1723. DOI: `10.1038/ncomms3040`. URL: `https://doi.org/10.1038/ncomms3040`.

[58] Yang Xu et al. "Tuning Insulator-Semimetal Transitions in 3D Topological Insulator thin Films by Intersurface Hybridization and In-Plane Magnetic Fields". In: *Phys. Rev. Lett.* 123 (20 Nov. 2019), p. 207701. DOI: `10.1103/PhysRevLett.123.207701`. URL: `https://link.aps.org/doi/10.1103/PhysRevLett.123.207701`.

[59] Yang Xu, Ireneusz Miotkowski, and Yong P. Chen. "Quantum transport of two-species Dirac fermions in dual-gated three-dimensional topological insulators". In: *Nature Communications* 7.1 (May 2016), p. 11434. ISSN: 2041-1723. DOI: `10.1038/ncomms11434`. URL: `https://doi.org/10.1038/ncomms11434`.

[60] Stephane Yu Matsushita, Kim-Khuong Huynh, and Katsumi Tanigaki. "Ultrathin films of three-dimensional topological insulators by vapor-phase epitaxy: Surface dominant transport in a wide temperature range as revealed by measurements of the Seebeck effect". In: *Phys. Rev. B* 99 (19 May 2019), p. 195302. DOI: `10.1103/PhysRevB.99.195302`. URL: `https://link.aps.org/doi/10.1103/PhysRevB.99.195302`.

[61] Stephane Yu Matsushita et al. "Thermoelectric properties of 3D topological insulator: Direct observation of topological surface and its gap opened states". In: *Phys. Rev. Materials* 1 (5 Oct. 2017), p. 054202. DOI: `10.1103/PhysRevMaterials.1.054202`. URL: `https://link.aps.org/doi/10.1103/PhysRevMaterials.1.054202`.

[62] B. F. Gao et al. "Gate-controlled linear magnetoresistance in thin Bi2Se3 sheets". In: *Applied Physics Letters* 100.21 (2012), p. 212402. DOI: `10.1063/1.4719196`. eprint: `https://doi.org/10.1063/1.4719196`. URL: `https://doi.org/10.1063/1.4719196`.

[63] J. Chen et al. "Gate-Voltage Control of Chemical Potential and Weak Antilocalization in Bi_2Se_3". In: *Phys. Rev. Lett.* 105 (17 Oct. 2010), p. 176602. DOI: `10.1103/PhysRevLett.105.176602`. URL: `https://link.aps.org/doi/10.1103/PhysRevLett.105.176602`.

[64] Inna Korzhovska et al. "Spin memory of the topological material under strong disorder". In: *npj Quantum Materials* 5.1 (June 2020), p. 39. ISSN: 2397-4648. DOI: `10.1038/s41535-020-0241-5`. eprint: `1911.00070`. URL: `https://doi.org/10.1038/s41535-020-0241-5`.

[65] M. S. Bahramy et al. "Emergence of non-centrosymmetric topological insulating phase in BiTeI under pressure". In: *Nature Communications* 3 (Feb. 2012). Article, 679 EP -. URL: `https://doi.org/10.1038/ncomms1679`.

[66] Shinobu Hikami, Anatoly I. Larkin, and Yosuke Nagaoka. "Spin-Orbit Interaction and Magnetoresistance in the Two Dimensional Random System". In: *Progress of Theoretical Physics* 63.2 (Feb. 1980), pp. 707–710. ISSN: 0033-068X. DOI: `10.1143/PTP.63.707`. eprint: `http://oup.prod.sis.lan/ptp/article-pdf/63/2/707/5336056/63-2-707.pdf`. URL: `https://doi.org/10.1143/PTP.63.707`.

[67] E. McCann et al. "Weak-Localization Magnetoresistance and Valley Symmetry in Graphene". In: *Phys. Rev. Lett.* 97 (14 Oct. 2006), p. 146805. DOI: `10.1103/PhysRevLett.97.146805`. URL: `https://link.aps.org/doi/10.1103/PhysRevLett.97.146805`.

[68] Matthew Brahlek et al. "Emergence of Decoupled Surface Transport Channels in Bulk Insulating Bi_2Se_3 Thin Films". In: *Phys. Rev. Lett.* 113 (2 July 2014), p. 026801. DOI: `10.1103/PhysRevLett.113.026801`. URL: `https://link.aps.org/doi/10.1103/PhysRevLett.113.026801`.

[69] H. Steinberg et al. "Electrically tunable surface-to-bulk coherent coupling in topological insulator thin films". In: *Phys. Rev. B* 84 (23 Dec. 2011), p. 233101. DOI: `10.1103/PhysRevB.84.233101`. URL: `https://link.aps.org/doi/10.1103/PhysRevB.84.233101`.

[70] Jian Liao et al. "Enhanced electron dephasing in three-dimensional topological insulators". In: *Nature Communications* 8.1 (July 2017), p. 16071. ISSN: 2041-1723. DOI: `10.1038/ncomms16071`. URL: `https://doi.org/10.1038/ncomms16071`.

[71] Matthew Brahlek et al. "Transport properties of topological insulators: Band bending, bulk metal-to-insulator transition, and weak anti-localization". In: *Solid State Communications* 215-216 (2015), pp. 54–62. ISSN: 0038-1098. DOI: `https://doi.org/10.1016/j.ssc.2014.10.021`. URL: `http://www.sciencedirect.com/science/article/pii/S0038109814004426`.

[72] Zhi Ren et al. "Optimizing $\mathbf{Bi}_{2-x}\mathbf{Sb}_x\mathbf{Te}_{3-y}\mathbf{Se}_y$ solid solutions to approach the intrinsic topological insulator regime". In: *Phys. Rev. B* 84 (16 Oct. 2011), p. 165311. DOI: `10.1103/PhysRevB.84.165311`. URL: `https://link.aps.org/doi/10.1103/PhysRevB.84.165311`.

[73] S. R. Park et al. "Quasiparticle scattering and the protected nature of the topological states in a parent topological insulator Bi_2Se_3". In: *Phys. Rev. B* 81 (4 Jan. 2010), p. 041405. DOI: `10.1103/PhysRevB.81.041405`. URL: `https://link.aps.org/doi/10.1103/PhysRevB.81.041405`.

[74] D. Hsieh et al. "Observation of Time-Reversal-Protected Single-Dirac-Cone Topological-Insulator States in Bi_2Te_3 and Sb_2Te_3". In: *Phys. Rev. Lett.* 103 (14 Sept. 2009), p. 146401. DOI: `10.1103/PhysRevLett.103.146401`. URL: `https://link.aps.org/doi/10.1103/PhysRevLett.103.146401`.

[75] M. S. Bahramy et al. "Emergent quantum confinement at topological insulator surfaces". In: *Nature Communications* 3.1 (Oct. 2012). Article, 1159 EP -. ISSN: 2041-1723. DOI: `10.1038/ncomms1679`. URL: `https://doi.org/10.1038/ncomms2162`.

[76] Marco Bianchi et al. "Coexistence of the topological state and a two-dimensional electron gas on the surface of Bi2Se3". In: *Nature Communications* 1 (Nov. 2010). Article, 128 EP -. URL: `https://doi.org/10.1038/ncomms1131`.

[77] Marco Bianchi et al. "Simultaneous Quantization of Bulk Conduction and Valence States through Adsorption of Nonmagnetic Impurities on Bi_2Se_3". In: *Phys. Rev. Lett.* 107 (8 Aug. 2011), p. 086802. DOI: `10.1103/PhysRevLett.107.086802`. URL: `https://link.aps.org/doi/10.1103/PhysRevLett.107.086802`.

[78] Alexander Weiße et al. "The kernel polynomial method". In: *Reviews of Modern Physics* 78.1 (Mar. 2006), pp. 275–306.

[79] Dániel Varjas et al. "Computation of topological phase diagram of disordered $Pb_{1-x}Sn_xTe$ using the kernel polynomial method". In: *Phys. Rev. Research* 2 (1 Feb. 2020), p. 013229. DOI: `10.1103/PhysRevResearch.2.013229`. URL: `https://link.aps.org/doi/10.1103/PhysRevResearch.2.013229`.

[80] Alexander Weiße et al. "The kernel polynomial method". In: *Rev. Mod. Phys.* 78 (1 Mar. 2006), pp. 275–306. DOI: `10.1103/RevModPhys.78.275`. URL: `https://link.aps.org/doi/10.1103/RevModPhys.78.275`.

[81] Christoph W Groth et al. "Kwant: a software package for quantum transport". In: *New Journal of Physics* 16.6 (June 2014), p. 063065. DOI: `10.1088/1367-2630/16/6/063065`. URL: `https://doi.org/10.1088%2F1367-2630%2F16%2F6%2F063065`.

[82] Prateek Mukati, Adhip Agarwala, and Subhro Bhattacharjee. "Topological and conventional phases of a three-dimensional electronic glass". In: *Phys. Rev. B* 101 (3 Jan. 2020), p. 035142. DOI: `10.1103/PhysRevB.101.035142`. URL: `https://link.aps.org/doi/10.1103/PhysRevB.101.035142`.

[83] G. Rosenberg and M. Franz. “Witten effect in a crystalline topological insulator”. In: *Phys. Rev. B* 82 (3 July 2010), p. 035105. DOI: `10.1103/PhysRevB.82.035105`. URL: `https://link.aps.org/doi/10.1103/PhysRevB.82.035105`.

[84] Konstantinos Konstantinou et al. “Revealing the intrinsic nature of the mid-gap defects in amorphous Ge2Sb2Te5”. In: *Nature communications* 10.1 (2019), pp. 1–10.

[85] Sudong Park and Byungki Ryu. “Hybrid-density functional theory study on the band structures of tetradymite-Bi2Te3, Sb2Te3, Bi2Se3, and Sb2Se3 thermoelectric materials”. In: *Journal of the Korean Physical Society* 69.11 (2016), pp. 1683–1687.

[86] C. Jozwiak et al. “A high-efficiency spin-resolved photoemission spectrometer combining time-of-flight spectroscopy with exchange-scattering polarimetry”. In: *Review of Scientific Instruments* 81.5 (2010), p. 053904. DOI: `10.1063/1.3427223`. eprint: `https://doi.org/10.1063/1.3427223`. URL: `https://doi.org/10.1063/1.3427223`.

[87] Yu He et al. “Invited Article: High resolution angle resolved photoemission with tabletop 11 eV laser”. In: *Review of Scientific Instruments* 87.1 (2016), p. 011301. DOI: `10.1063/1.4939759`. eprint: `https://doi.org/10.1063/1.4939759`. URL: `https://doi.org/10.1063/1.4939759`.

[88] Conrad Stansbury and Alessandra Lanzara. “PyARPES: An analysis framework for multimodal angle-resolved photoemission spectroscopies”. In: *SoftwareX* 11 (2020), p. 100472. ISSN: 2352-7110. DOI: `https://doi.org/10.1016/j.softx.2020.100472`. URL: `https://www.sciencedirect.com/science/article/pii/S2352711019301633`.

[89] K. Ishizaka et al. “Giant Rashba-type spin splitting in bulk BiTeI”. In: *Nature Materials* 10.7 (July 2011). Article, pp. 521–526. ISSN: 1476-4660. DOI: `10.1038/nmat3051`. URL: `https://doi.org/10.1038/nmat3051`.

[90] Chris Jozwiak et al. “Spin-polarized surface resonances accompanying topological surface state formation”. English. In: *Nature Communications* 7 (Oct. 2016), p. 13143. DOI: `10.1038/ncomms13143`. URL: `https://www.nature.com/articles/ncomms13143`.

[91] Chris Jozwiak et al. “Photoelectron spin-flipping and texture manipulation in a topological insulator”. In: *Nature Physics* 9 (Mar. 2013), 293 EP -. URL: `https://doi.org/10.1038/nphys2572`.

[92] Chris Jozwiak et al. “Spin-polarized surface resonances accompanying topological surface state formation”. In: *Nature Communications* 7.1 (2016), p. 13143. ISSN: 2041-1723. DOI: `10.1038/ncomms13143`. URL: `https://doi.org/10.1038/ncomms13143`.

[93] L. Plucinski et al. “Robust surface electronic properties of topological insulators: Bi2Te3 films grown by molecular beam epitaxy”. In: *Applied Physics Letters* 98.22 (2011), p. 222503. DOI: `10.1063/1.3595309`. eprint: `https://doi.org/10.1063/1.3595309`. URL: `https://doi.org/10.1063/1.3595309`.

[94] K. Ishizaka et al. “Giant Rashba-type spin splitting in bulk BiTeI”. In: *Nat. Mater.* 10.7 (2011), pp. 521–526.

[95] Xiaoxiong Wang and T.-C. Chiang. "Topological states in Bi2Se3 surfaces created by cleavage within a quintuple layer: Analysis in terms of the Shockley criterion". In: *Phys. Rev. B* 89 (12 Mar. 2014), p. 125109. DOI: `10.1103/PhysRevB.89.125109`. URL: `https://link.aps.org/doi/10.1103/PhysRevB.89.125109`.

[96] S. F. Edwards. "The electronic structure of disordered systems". In: *The Philosophical Magazine: A Journal of Theoretical Experimental and Applied Physics* 6.65 (May 1961), pp. 617–638. DOI: `10.1080/14786436108244414`.

[97] J. J. Olson. "Anderson-McMillan prescription for the density of states of liquid iron". In: *Phys. Rev. B* 12 (8 Oct. 1975), pp. 2908–2916. DOI: `10.1103/PhysRevB.12.2908`.

[98] Sae Hee Ryu et al. "Pseudogap in a crystalline insulator doped by disordered metals". In: *Nature* 596.7870 (2021), pp. 68–73. DOI: `10.1038/s41586-021-03683-0`.

[99] "The Formation of Amorphous Solids". In: *The Physics of Amorphous Solids*. John Wiley I& Sons, Ltd, 1998. Chap. 1, pp. 1–32. ISBN: 9783527617968. DOI: `https://doi.org/10.1002/9783527617968.ch1`. eprint: `https://onlinelibrary.wiley.com/doi/pdf/10.1002/9783527617968.ch1`. URL: `https://onlinelibrary.wiley.com/doi/abs/10.1002/9783527617968.ch1`.

[100] Matthew Brahlek et al. "Disorder-driven topological phase transition in Bi_2Se_3 films". In: *Phys. Rev. B* 94 (16 Oct. 2016), p. 165104. DOI: `10.1103/PhysRevB.94.165104`. URL: `https://link.aps.org/doi/10.1103/PhysRevB.94.165104`.

[101] Yang Zhang et al. "Photogalvanic effect in Weyl semimetals from first principles". English. In: *Phys. Rev.* B97.24 (2018), p. 241118. DOI: `10.1103/PhysRevB.97.241118`. URL: `https://link.aps.org/doi/10.1103/PhysRevB.97.241118`.

[102] Hoi Chun Po, Ashvin Vishwanath, and Haruki Watanabe. "Symmetry-based indicators of band topology in the 230 space groups". In: *Nat. Commun.* 8.1 (June 2017). DOI: `10.1038/s41467-017-00133-2`. URL: `https://doi.org/10.1038/s41467-017-00133-2`.

[103] Matthias Wuttig and Noboru Yamada. "Phase-change materials for rewriteable data storage". In: *Nature Materials* 6.11 (2007), pp. 824–832. ISSN: 1476-1122. DOI: `10.1038/nmat2009`.

[104] Adhip Agarwala and Vijay B. Shenoy. "Topological Insulators in Amorphous Systems". In: *Phys. Rev. Lett.* 118 (23 June 2017), p. 236402. DOI: `10.1103/PhysRevLett.118.236402`. URL: `https://link.aps.org/doi/10.1103/PhysRevLett.118.236402`.

[105] Kim Pöyhönen et al. "Amorphous topological superconductivity in a Shiba glass". In: *Nature Communications* 9.1 (2018), p. 2103. DOI: `10.1038/s41467-018-04532-x`. URL: `https://doi.org/10.1038/s41467-018-04532-x`.

[106] Noah P. Mitchell et al. "Amorphous topological insulators constructed from random point sets". In: *Nature Physics* 14 (4 2018). DOI: `10.1038/s41567-017-0024-5`. URL: `https://www.nature.com/articles/s41567-017-0024-5`.

[107] Meng Xiao and Shanhui Fan. “Photonic Chern insulator through homogenization of an array of particles”. In: *Phys. Rev. B* 96 (10 Sept. 2017), p. 100202. DOI: `10.1103/PhysRevB.96.100202`. URL: `https://link.aps.org/doi/10.1103/PhysRevB.96.100202`.

[108] P. W. Anderson. “Absence of Diffusion in Certain Random Lattices”. In: *Phys. Rev.* 109 (5 Mar. 1958), pp. 1492–1505. DOI: `10.1103/PhysRev.109.1492`. URL: `https://link.aps.org/doi/10.1103/PhysRev.109.1492`.

[109] Sir Nevill Mott. “Electrons in glass”. In: *Rev. Mod. Phys.* 50 (2 Apr. 1978), pp. 203–208.

[110] J J Ludlam et al. “Universal features of localized eigenstates in disordered systems”. In: 17.30 (2005), pp. L321–L327.

[111] Zheng Yu et al. “Disordered hyperuniformity in two-dimensional amorphous silica”. In: *Science Advances* 6.16 (), eaba0826.

[112] G. Zhang, F. H. Stillinger, and S. Torquato. “The Perfect Glass Paradigm: Disordered Hyperuniform Glasses Down to Absolute Zero”. In: *Scientific Reports* 6.1 (2016), p. 36963.

[113] Devilal Dahal et al. “Hyperuniformity and static structure factor of amorphous silicon in the infinite-wavelength limit”. In: 1252.1 (2019), p. 012003.

[114] W. H. Zachariasen. “THE ATOMIC ARRANGEMENT IN GLASS”. In: *Journal of the American Chemical Society* 54.10 (Oct. 1932), pp. 3841–3851.

[115] R. L. C. Vink et al. “Device-size atomistic models of amorphous silicon”. In: *Phys. Rev. B* 64 (24 Dec. 2001), p. 245214.

[116] Volker L. Deringer et al. “Realistic Atomistic Structure of Amorphous Silicon from Machine-Learning-Driven Molecular Dynamics”. In: *The Journal of Physical Chemistry Letters* 9.11 (June 2018), pp. 2879–2885.

[117] Paul Corbae et al. *Observation of spin-momentum locked surface states in amorphous* Bi_2Se_3. 2020. arXiv: `1910.13412 [cond-mat.mtrl-sci]`.

[118] Dániel Varjas et al. “Topological Phases without Crystalline Counterparts”. In: *Phys. Rev. Lett.* 123 (19 Nov. 2019), p. 196401. DOI: `10.1103/PhysRevLett.123.196401`. URL: `https://link.aps.org/doi/10.1103/PhysRevLett.123.196401`.

[119] Hannah C. Robarts et al. “Extreme Fermi Surface Smearing in a Maximally Disordered Concentrated Solid Solution”. In: *Phys. Rev. Lett.* 124 (4 Jan. 2020), p. 046402.

[120] Jun Ding et al. “Second-Nearest-Neighbor Correlations from Connection of Atomic Packing Motifs in Metallic Glasses and Liquids”. In: *Scientific Reports* 5.1 (2015), p. 17429.

[121] J. M. Ziman. “A theory of the electrical properties of liquid metals. I: The monovalent metals”. In: *The Philosophical Magazine: A Journal of Theoretical Experimental and Applied Physics* 6.68 (Aug. 1961), pp. 1013–1034.

[122] Samuel Frederick Edwards and Nevill Francis Mott. “The electronic structure of liquid metals”. In: *Proceedings of the Royal Society of London. Series A. Mathematical and Physical Sciences* 267.1331 (2022/04/26 1962), pp. 518–540.

[123] G J Morgan. “Electron transport in liquid metals II. A model for the wave functions in liquid transition metals”. In: 2.8 (1969), pp. 1454–1464.

[124] B. L. Gyorffy. “Electronic States in Liquid Metals: A Generalization of the Coherent-Potential Approximation for a System with Short-Range Order”. In: *Phys. Rev. B* 1 (8 Apr. 1970), pp. 3290–3299.

[125] L Schwartz and H Ehrenreich. “Single-site approximations in the electronic theory of liquid metals”. In: *Annals of Physics* 64.1 (1971), pp. 100–148.

[126] K. S. Chang et al. “Density of states of liquid Cu”. In: *Phys. Rev. B* 12 (12 Dec. 1975), pp. 5506–5513.

[127] J Oglesby and P Lloyd. “Some single-site structure-independent approximations in condensed materials”. In: 9.15 (1976), pp. 2879–2886.

[128] M. C. Ridgway et al. “Characterization of the local structure of amorphous GaAs produced by ion implantation”. In: *Journal of Applied Physics* 83.9 (2022/04/26 1998), pp. 4610–4614.

[129] Yohei Onodera et al. “Structure and properties of densified silica glass: characterizing the order within disorder”. In: *NPG Asia Materials* 12.1 (2020), p. 85.

[130] Chee-Tat Toh et al. “Synthesis and properties of free-standing monolayer amorphous carbon”. In: *Nature* 577.7789 (Jan. 2020), pp. 199–203. ISSN: 1476-4687. DOI: `10.1038/s41586-019-1871-2`. URL: `https://doi.org/10.1038/s41586-019-1871-2`.

[131] Edith Perret and Rudolf Hufenus. “Insights into strain-induced solid mesophases in melt-spun polymer fibers”. In: *Polymer* 229 (2021), p. 124010.

[132] Haijun Zhang et al. “Topological insulators in Bi_2Se_3, Bi_2Te_3 and Sb_2Te_3 with a single Dirac cone on the surface”. In: *Nature Physics* 5.6 (May 2009), pp. 438–442. ISSN: 1745-2481. DOI: `10.1038/nphys1270`. URL: `https://doi.org/10.1038/nphys1270`.

[133] Baumberger F. et al. “Electron Coherence in a Melting Lead Monolayer”. In: *Science* 306.5705 (2022/04/26 2004), pp. 2221–2224.

[134] Keun Su Kim and Han Woong Yeom. “Radial Band Structure of Electrons in Liquid Metals”. In: *Phys. Rev. Lett.* 107 (13 Sept. 2011), p. 136402.

[135] Quentin Marsal, Dániel Varjas, and Adolfo G. Grushin. “Obstructed insulators and flat bands in topological phase-change materials”. In: *arXiv e-prints*, arXiv:2204.14177 (Apr. 2022), arXiv:2204.14177. arXiv: `2204.14177 [cond-mat.mes-hall]`.

[136] Tiantian Zhang et al. “Catalogue of topological electronic materials”. English. In: *Nature* 566.7745 (Feb. 2019), pp. 475–479. DOI: `10.1038/s41586-019-0944-6`. URL: `https://www.nature.com/articles/s41586-019-0944-6`.

[137] Jorrit Kruthoff et al. “Topological classification of crystalline insulators through band structure combinatorics”. In: *Physical Review X* 7.4 (2017), p. 041069.

[138] Kamal Choudhary, Kevin F Garrity, and Francesca Tavazza. “High-throughput Discovery of topologically Non-trivial Materials using spin-orbit spillage”. In: *Scientific reports* 9.1 (2019), pp. 1–8.

[139] Jeffrey D. Cain et al. “Layer-dependent topological phase in a two-dimensional quasicrystal and approximant”. In: *Proceedings of the National Academy of Sciences* (2020). ISSN: 0027-8424. DOI: `10.1073/pnas.2015164117`. eprint: `https://www.pnas.org/content/early/2020/10/02/2015164117.full.pdf`. URL: `https://www.pnas.org/content/early/2020/10/02/2015164117`.

[140] M. S. Bahramy, R. Arita, and N. Nagaosa. “Origin of giant bulk Rashba splitting: Application to BiTeI”. In: *Phys. Rev. B* 84 (4 July 2011), p. 041202. DOI: `10.1103/PhysRevB.84.041202`. URL: `https://link.aps.org/doi/10.1103/PhysRevB.84.041202`.

[141] Véronique Brousseau-Couture, Gabriel Antonius, and Michel Côté. “Temperature dependence of the topological phase transition of BiTeI from first principles”. In: *Phys. Rev. Research* 2 (2 May 2020), p. 023185. DOI: `10.1103/PhysRevResearch.2.023185`. URL: `https://link.aps.org/doi/10.1103/PhysRevResearch.2.023185`.

[142] Bartomeu Monserrat and Awadhesh Narayan. “Unraveling the topology of $ZrTe_5$ by changing temperature”. In: *Phys. Rev. Research* 1 (3 Dec. 2019), p. 033181. DOI: `10.1103/PhysRevResearch.1.033181`. URL: `https://link.aps.org/doi/10.1103/PhysRevResearch.1.033181`.

[143] Stephanie A. Mack, Sinéad M. Griffin, and Jeffrey B. Neaton. “Emergence of topological electronic phases in elemental lithium under pressure”. In: *Proceedings of the National Academy of Sciences* 116.19 (2019), pp. 9197–9201. ISSN: 0027-8424. DOI: `10.1073/pnas.1821533116`. eprint: `https://www.pnas.org/content/116/19/9197.full.pdf`. URL: `https://www.pnas.org/content/116/19/9197`.

[144] Shengli Zhang et al. “Semiconductor-topological insulator transition of two-dimensional SbAs induced by biaxial tensile strain”. In: *Phys. Rev. B* 93 (24 June 2016), p. 245303. DOI: `10.1103/PhysRevB.93.245303`. URL: `https://link.aps.org/doi/10.1103/PhysRevB.93.245303`.

[145] Jian Li et al. “Topological Anderson Insulator”. In: *Phys. Rev. Lett.* 102 (13 Apr. 2009), p. 136806. DOI: `10.1103/PhysRevLett.102.136806`. URL: `https://link.aps.org/doi/10.1103/PhysRevLett.102.136806`.

[146] J. S. Lee et al. “Optical Response of Relativistic Electrons in the Polar BiTeI Semiconductor”. In: *Phys. Rev. Lett.* 107 (11 Sept. 2011), p. 117401. DOI: `10.1103/PhysRevLett.107.117401`. URL: `https://link.aps.org/doi/10.1103/PhysRevLett.107.117401`.

[147] Arash A. Mostofi et al. "An updated version of wannier90: A tool for obtaining maximally-localised Wannier functions". In: *Computer Physics Communications* 185.8 (2014), pp. 2309–2310. ISSN: 0010-4655. DOI: `https://doi.org/10.1016/j.cpc.2014.05.003`. URL: `http://www.sciencedirect.com/science/article/pii/S001046551400157X`.

[148] QuanSheng Wu et al. "WannierTools : An open-source software package for novel topological materials". In: *Computer Physics Communications* 224 (2018), pp. 405–416. ISSN: 0010-4655. DOI: `https://doi.org/10.1016/j.cpc.2017.09.033`. URL: `http://www.sciencedirect.com/science/article/pii/S0010465517303442`.

[149] E. I. Rashba. "Properties of semiconductors with an extremum loop, 1. Cyclotron and combinational resonance in a magnetic field perpendicular to the plane of the loop". In: *Sov. Phys. Solid State* 2 (1960), pp. 1109–1122.

[150] K. Ishizaka and et. al. "Giant Rashba-type spin splitting in bulk BiTeI". In: *Nature Materials* 10.7 (July 2011), pp. 521–526. ISSN: 1476-4660. DOI: `10.1038/nmat3051`. URL: `https://doi.org/10.1038/nmat3051`.

[151] Jianpeng Liu and David Vanderbilt. "Weyl semimetals from noncentrosymmetric topological insulators". In: *Phys. Rev. B* 90 (15 Oct. 2014), p. 155316. DOI: `10.1103/PhysRevB.90.155316`. URL: `https://link.aps.org/doi/10.1103/PhysRevB.90.155316`.

[152] Q Marsal, D. Varjas, and A. Grushin. In: *arXiv:2003.13701* (). URL: `https://arxiv.org/pdf/2003.13701.pdf`.

[153] M. Winnerlein et al. "Epitaxy and structural properties of $(V,Bi,Sb)_2Te_3$ layers exhibiting the quantum anomalous Hall effect". In: *Phys. Rev. Materials* 1 (1 June 2017), p. 011201. DOI: `10.1103/PhysRevMaterials.1.011201`. URL: `https://link.aps.org/doi/10.1103/PhysRevMaterials.1.011201`.

[154] N. F. Mott and E. A. Davis. *Electronic processes in non-crystalline materials.* 2nd ed. Clarendon Press ; Oxford University Press Oxford : New York, 1979. ISBN: 0198512880.

[155] W. Teizer, F. Hellman, and R. C. Dynes. "Density of States of Amorphous Gd_xSi_{1-x} at the Metal-Insulator Transition". In: *Phys. Rev. Lett.* 85 (4 July 2000), pp. 848–851. DOI: `10.1103/PhysRevLett.85.848`. URL: `https://link.aps.org/doi/10.1103/PhysRevLett.85.848`.

[156] Byoung Hee Moon et al. "Soft Coulomb gap and asymmetric scaling towards metal-insulator quantum criticality in multilayer MoS2". In: *Nature Communications* 9.1 (May 2018), p. 2052. ISSN: 2041-1723. DOI: `10.1038/s41467-018-04474-4`. URL: `https://doi.org/10.1038/s41467-018-04474-4`.

[157] G. Singh et al. "Effect of disorder on superconductivity and Rashba spin-orbit coupling in $LaAlO_3$ /$SrTiO_3$ interfaces". In: *Phys. Rev. B* 96 (2 July 2017), p. 024509. DOI: `10.1103/PhysRevB.96.024509`. URL: `https://link.aps.org/doi/10.1103/PhysRevB.96.024509`.

[158] Patrick A. Lee and T. V. Ramakrishnan. “Disordered electronic systems”. In: *Rev. Mod. Phys.* 57 (2 Apr. 1985), pp. 287–337. DOI: `10.1103/RevModPhys.57.287`. URL: `https://link.aps.org/doi/10.1103/RevModPhys.57.287`.

[159] Gerd Bergmann. “Weak localization in thin films: a time-of-flight experiment with conduction electrons”. In: *Physics Reports* 107.1 (1984), pp. 1–58. ISSN: 0370-1573. DOI: `https://doi.org/10.1016/0370-1573(84)90103-0`. URL: `https://www.sciencedirect.com/science/article/pii/0370157384901030`.

[160] Johannes Reindl et al. “Persistence of spin memory in a crystalline, insulating phase-change material”. In: *npj Quantum Materials* 4.1 (Dec. 2019), p. 57. ISSN: 2397-4648. DOI: `10.1038/s41535-019-0196-6`. URL: `https://doi.org/10.1038/s41535-019-0196-6`.

[161] Paul Corbae, Frances Hellman, and Sinéad M. Griffin. “Structural disorder-driven topological phase transition in noncentrosymmetric BiTeI”. In: *Phys. Rev. B* 103 (21 June 2021), p. 214203. DOI: `10.1103/PhysRevB.103.214203`. URL: `https://link.aps.org/doi/10.1103/PhysRevB.103.214203`.

[162] Frank Schindler et al. “Higher-order topological insulators”. In: *Science Advances* 4.6 (2018), eaat0346. DOI: `10.1126/sciadv.aat0346`. eprint: `https://www.science.org/doi/pdf/10.1126/sciadv.aat0346`. URL: `https://www.science.org/doi/abs/10.1126/sciadv.aat0346`.

[163] Nurit Avraham et al. “Visualizing coexisting surface states in the weak and crystalline topological insulator Bi2TeI”. In: *Nature Materials* 19.6 (June 2020), pp. 610–616. ISSN: 1476-4660. DOI: `10.1038/s41563-020-0651-6`. URL: `https://doi.org/10.1038/s41563-020-0651-6`.

[164] Alexander Zeugner et al. “Modular Design with 2D Topological-Insulator Building Blocks: Optimized Synthesis and Crystal Growth and Crystal and Electronic Structures of BixTeI (x = 2, 3)”. In: *Chemistry of Materials* 29.3 (Feb. 2017), pp. 1321–1337. ISSN: 0897-4756. DOI: `10.1021/acs.chemmater.6b05038`. URL: `https://doi.org/10.1021/acs.chemmater.6b05038`.

[165] T. A. Elmslie et al. *Pressure-induced superconductivity in the weak topological insulator Bi2TeI and the topological metal Bi3TeI*. 2022. DOI: `10.48550/ARXIV.2209.02688`. URL: `https://arxiv.org/abs/2209.02688`.

[166] A C Y Liu et al. “Probing local order in glasses from limited-volume electron and x-ray diffraction”. In: *Journal of Statistical Mechanics: Theory and Experiment* 2016.5 (May 2016), p. 054046. DOI: `10.1088/1742-5468/2016/05/054046`. URL: `https://doi.org/10.1088/1742-5468/2016/05/054046`.

[167] Amelia C. Y. Liu et al. “Interpretation of angular symmetries in electron nanodiffraction patterns from thin amorphous specimens”. In: *Acta Crystallographica Section A* 71.5 (Sept. 2015), pp. 473–482. DOI: `10.1107/S2053273315011845`. URL: `https://doi.org/10.1107/S2053273315011845`.

[168] M. K. Tran et al. "Infrared- and Raman-Spectroscopy Measurements of a Transition in the Crystal Structure and a Closing of the Energy Gap of BiTeI under Pressure". In: *Phys. Rev. Lett.* 112 (4 Jan. 2014), p. 047402. DOI: `10.1103/PhysRevLett.112.047402`. URL: `https://link.aps.org/doi/10.1103/PhysRevLett.112.047402`.

[169] B.L. ALTSHULER and A.G. ARONOV. "CHAPTER 1 - Electron–Electron Interaction In Disordered Conductors". In: *Electron–Electron Interactions in Disordered Systems*. Ed. by A.L. EFROS and M. POLLAK. Vol. 10. Modern Problems in Condensed Matter Sciences. Elsevier, 1985, pp. 1–153. DOI: `https://doi.org/10.1016/B978-0-444-86916-6.50007-7`. URL: `https://www.sciencedirect.com/science/article/pii/B9780444869166500077`.

[170] A MacKinnon. "Critical exponents for the metal-insulator transition". In: *Journal of Physics: Condensed Matter* 6.13 (Mar. 1994), p. 2511. DOI: `10.1088/0953-8984/6/13/012`. URL: `https://dx.doi.org/10.1088/0953-8984/6/13/012`.

[171] H. Nakamura et al. "Robust weak antilocalization due to spin-orbital entanglement in Dirac material Sr3SnO". In: *Nature Communications* 11.1 (Mar. 2020), p. 1161. ISSN: 2041-1723. DOI: `10.1038/s41467-020-14900-1`. URL: `https://doi.org/10.1038/s41467-020-14900-1`.

[172] B. L. Altshuler et al. "Magnetoresistance and Hall effect in a disordered two-dimensional electron gas". In: *Phys. Rev. B* 22 (11 Dec. 1980), pp. 5142–5153. DOI: `10.1103/PhysRevB.22.5142`. URL: `https://link.aps.org/doi/10.1103/PhysRevB.22.5142`.

[173] J J Lin and J P Bird. "Recent experimental studies of electron dephasing in metal and semiconductor mesoscopic structures". In: *Journal of Physics: Condensed Matter* 14.18 (Apr. 2002), R501. DOI: `10.1088/0953-8984/14/18/201`. URL: `https://dx.doi.org/10.1088/0953-8984/14/18/201`.

[174] N M Pounder and M A Howson. "Negative magnetoresistance in NbSi amorphous alloys". In: *Journal of Physics: Condensed Matter* 3.13 (Apr. 1991), p. 2069. DOI: `10.1088/0953-8984/3/13/009`. URL: `https://dx.doi.org/10.1088/0953-8984/3/13/009`.

[175] Wu Jiang et al. "Variable-range hopping and positive magnetoresistance in insulating $Y_{1-x}Pr_xBa_2Cu_3O_7$ crystals". In: *Phys. Rev. B* 49 (1 Jan. 1994), pp. 690–693. DOI: `10.1103/PhysRevB.49.690`. URL: `https://link.aps.org/doi/10.1103/PhysRevB.49.690`.

[176] W. Schoepe. "Variable-range hopping conduction in doped germanium at very low temperatures and high magnetic fields". In: *Zeitschrift für Physik B Condensed Matter* 71.4 (Dec. 1988), pp. 455–463. ISSN: 1431-584X. DOI: `10.1007/BF01313932`. URL: `https://doi.org/10.1007/BF01313932`.

[177] Z Ovadyahu. “Quantum coherent effects in Anderson insulators”. In: *Waves in Random Media* 9.2 (1999), pp. 241–253. DOI: `10.1088/0959-7174/9/2/309`. eprint: `https://doi.org/10.1088/0959-7174/9/2/309`. URL: `https://doi.org/10.1088/0959-7174/9/2/309`.

[178] Y. Shapir and Z. Ovadyahu. “Effects of spin-orbit scattering on hopping magnetoconductivity”. In: *Phys. Rev. B* 40 (18 Dec. 1989), pp. 12441–12445. DOI: `10.1103/PhysRevB.40.12441`. URL: `https://link.aps.org/doi/10.1103/PhysRevB.40.12441`.

[179] Xiaolin Wang et al. “Room Temperature Giant and Linear Magnetoresistance in Topological Insulator Bi_2Te_3 Nanosheets”. In: *Phys. Rev. Lett.* 108 (26 June 2012), p. 266806. DOI: `10.1103/PhysRevLett.108.266806`. URL: `https://link.aps.org/doi/10.1103/PhysRevLett.108.266806`.

[180] T. Khouri et al. “Linear Magnetoresistance in a Quasifree Two-Dimensional Electron Gas in an Ultrahigh Mobility GaAs Quantum Well”. In: *Phys. Rev. Lett.* 117 (25 Dec. 2016), p. 256601. DOI: `10.1103/PhysRevLett.117.256601`. URL: `https://link.aps.org/doi/10.1103/PhysRevLett.117.256601`.

[181] Viktor Könye and Masao Ogata. “Magnetoresistance of a three-dimensional Dirac gas”. In: *Phys. Rev. B* 98 (19 Nov. 2018), p. 195420. DOI: `10.1103/PhysRevB.98.195420`. URL: `https://link.aps.org/doi/10.1103/PhysRevB.98.195420`.

[182] M. M. Parish and P. B. Littlewood. “Non-saturating magnetoresistance in heavily disordered semiconductors”. In: *Nature* 426.6963 (Nov. 2003), pp. 162–165. ISSN: 1476-4687. DOI: `10.1038/nature02073`. URL: `https://doi.org/10.1038/nature02073`.

[183] Quentin Marsal, Dániel Varjas, and Adolfo G. Grushin. “Topological Weaire–Thorpe models of amorphous matter”. In: *Proceedings of the National Academy of Sciences* 117.48 (2020), pp. 30260–30265. DOI: `10.1073/pnas.2007384117`. eprint: `https://www.pnas.org/doi/pdf/10.1073/pnas.2007384117`. URL: `https://www.pnas.org/doi/abs/10.1073/pnas.2007384117`.

[184] Benjamin J. Wieder et al. “Topological materials discovery from crystal symmetry”. In: *Nature Reviews Materials* 7.3 (2022), pp. 196–216. DOI: `10.1038/s41578-021-00380-2`. URL: `https://doi.org/10.1038/s41578-021-00380-2`.

[185] Jorrit Kruthoff et al. “Topological Classification of Crystalline Insulators through Band Structure Combinatorics”. In: *Phys. Rev. X* 7 (4 Dec. 2017), p. 041069. DOI: `10.1103/PhysRevX.7.041069`. URL: `https://link.aps.org/doi/10.1103/PhysRevX.7.041069`.

[186] Hoi Chun Po, Ashvin Vishwanath, and Haruki Watanabe. “Symmetry-based indicators of band topology in the 230 space groups”. In: *Nature Communications* 8.1 (June 2017), pp. 1–9. URL: `https://www.nature.com/articles/s41467-017-00133-2`.

[187] Zhida Song et al. “Quantitative mappings between symmetry and topology in solids”. In: *Nature Communications* 9.1 (2018), p. 3530. DOI: `10.1038/s41467-018-06010-w`. URL: `https://doi.org/10.1038/s41467-018-06010-w`.

[188] Richard Zallen. *The Physics of Amorphous Solids*. Wiley, 1998. ISBN: 9780471299417.

[189] Adolfo G. Grushin. “Topological phases of amorphous matter”. In: *arXiv e-prints* (2020). DOI: `10.48550/arxiv.2010.02851`. URL: `https://arxiv.org/abs/2010.02851`.

[190] Helene Spring, Anton R. Akhmerov, and Daniel Varjas. “Amorphous topological phases protected by continuous rotation symmetry”. In: *SciPost Phys.* 11 (2 2021), p. 22. DOI: `10.21468/SciPostPhys.11.2.022`. URL: `https://scipost.org/10.21468/SciPostPhys.11.2.022`.

[191] Quentin Marsal, Dániel Varjas, and Adolfo G. Grushin. “Topological Weaire–Thorpe models of amorphous matter”. In: *Proceedings of the National Academy of Sciences* (2020). ISSN: 0027-8424. DOI: `10.1073/pnas.2007384117`. URL: `https://www.pnas.org/content/early/2020/11/17/2007384117`.

[192] Yan-Bin Yang et al. “Topological Amorphous Metals”. In: *Physical Review Letters* 123.7 (Aug. 2019), p. 076401. DOI: `10.1103/PhysRevLett.123.076401`. URL: `https://link.aps.org/doi/10.1103/PhysRevLett.123.076401` (visited on 11/25/2021).

[193] Isac Sahlberg et al. “Topological phase transitions in glassy quantum matter”. In: *Phys. Rev. Research* 2 (1 Jan. 2020), p. 013053. DOI: `10.1103/PhysRevResearch.2.013053`. URL: `https://link.aps.org/doi/10.1103/PhysRevResearch.2.013053`.

[194] Adhip Agarwala, Vladimir Juričić, and Bitan Roy. “Higher-order topological insulators in amorphous solids”. In: *Physical Review Research* 2.1 (Mar. 2020), p. 012067. DOI: `10.1103/PhysRevResearch.2.012067`. URL: `https://link.aps.org/doi/10.1103/PhysRevResearch.2.012067` (visited on 06/16/2021).

[195] Prateek Mukati, Adhip Agarwala, and Subhro Bhattacharjee. “Topological and conventional phases of a three-dimensional electronic glass”. In: *Physical Review B* 101.3 (Jan. 2020), p. 035142. DOI: `10.1103/PhysRevB.101.035142`. URL: `https://link.aps.org/doi/10.1103/PhysRevB.101.035142` (visited on 11/19/2021).

[196] Bastien Lapierre, Titus Neupert, and Luka Trifunovic. “Topologically localized insulators”. In: *arXiv:2110.14651 [cond-mat]* (Oct. 2021). URL: `http://arxiv.org/abs/2110.14651` (visited on 11/29/2021).

[197] Jiong-Hao Wang et al. “Structural-Disorder-Induced Second-Order Topological Insulators in Three Dimensions”. In: *Physical Review Letters* 126.20 (May 2021), p. 206404. DOI: `10.1103/PhysRevLett.126.206404`. URL: `https://link.aps.org/doi/10.1103/PhysRevLett.126.206404` (visited on 02/16/2022).

[198] Citian Wang et al. “Structural Amorphization-Induced Topological Order”. In: *Physical Review Letters* 128.5 (Feb. 2022), p. 056401. DOI: `10.1103/PhysRevLett.128.056401`. URL: `https://link.aps.org/doi/10.1103/PhysRevLett.128.056401` (visited on 02/09/2022).

[199] Jianpeng Liu and David Vanderbilt. “Spin-orbit spillage as a measure of band inversion in insulators”. In: *Physical Review B* 90.12 (Sept. 2014), p. 125133. DOI: `10.1103/PhysRevB.90.125133`. URL: `https://link.aps.org/doi/10.1103/PhysRevB.90.125133` (visited on 10/22/2021).

[200] Marcio Costa et al. “Toward Realistic Amorphous Topological Insulators”. In: *Nano Letters* 19.12 (Dec. 2019), pp. 8941–8946. ISSN: 1530-6984. DOI: `10.1021/acs.nanolett.9b03881`. URL: `https://doi.org/10.1021/acs.nanolett.9b03881` (visited on 06/03/2021).

[201] Bruno Focassio et al. “Structural and electronic properties of realistic two-dimensional amorphous topological insulators”. en. In: *2D Materials* 8.2 (Feb. 2021), p. 025032. ISSN: 2053-1583. DOI: `10.1088/2053-1583/abdb97`. URL: `https://doi.org/10.1088/2053-1583/abdb97` (visited on 09/10/2021).

[202] Paolo Giannozzi et al. “QUANTUM ESPRESSO: a modular and open-source software project for quantum simulations of materials”. en. In: *Journal of Physics: Condensed Matter* 21.39 (Sept. 2009), p. 395502. ISSN: 0953-8984. DOI: `10.1088/0953-8984/21/39/395502`. URL: `https://dx.doi.org/10.1088/0953-8984/21/39/395502` (visited on 11/20/2022).

[203] Anubhav Jain et al. “The Materials Project: A materials genome approach to accelerating materials innovation”. In: *APL Materials* 1.1 (2013), p. 011002. ISSN: 2166532X. DOI: `10.1063/1.4812323`. URL: `http://link.aip.org/link/AMPADS/v1/i1/p011002/s1%5C&Agg=doi`.

[204] Kamal Choudhary, Kevin F. Garrity, and Francesca Tavazza. “High-throughput Discovery of Topologically Non-trivial Materials using Spin-orbit Spillage”. en. In: *Scientific Reports* 9.1 (June 2019), p. 8534. ISSN: 2045-2322. DOI: `10.1038/s41598-019-45028-y`. URL: `https://www.nature.com/articles/s41598-019-45028-y` (visited on 10/22/2021).

[205] Kamal Choudhary et al. “High-throughput search for magnetic topological materials using spin-orbit spillage, machine learning, and experiments”. In: *Physical Review B* 103.15 (Apr. 2021), p. 155131. DOI: `10.1103/PhysRevB.103.155131`. URL: `https://link.aps.org/doi/10.1103/PhysRevB.103.155131` (visited on 10/22/2021).

[206] Alexei Kitaev. “Anyons in an exactly solved model and beyond”. en. In: *Annals of Physics*. January Special Issue 321.1 (Jan. 2006), pp. 2–111. ISSN: 0003-4916. DOI: `10.1016/j.aop.2005.10.005`. URL: `https://www.sciencedirect.com/science/article/pii/S0003491605002381` (visited on 11/07/2021).

[207] Emil Prodan. "Non-commutative tools for topological insulators". en. In: *New Journal of Physics* 12.6 (June 2010), p. 065003. ISSN: 1367-2630. DOI: `10.1088/1367-2630/12/6/065003`. URL: `https://dx.doi.org/10.1088/1367-2630/12/6/065003` (visited on 11/08/2022).

[208] Raffaello Bianco and Raffaele Resta. "Mapping topological order in coordinate space". In: *Physical Review B* 84.24 (Dec. 2011), p. 241106. DOI: `10.1103/PhysRevB.84.241106`. URL: `https://link.aps.org/doi/10.1103/PhysRevB.84.241106` (visited on 11/07/2021).

[209] Julia D. Hannukainen et al. *Local topological markers in odd spatial dimensions and their application to amorphous topological matter*. July 2022. DOI: `10.48550/arXiv.2207.01646`. URL: `http://arxiv.org/abs/2207.01646` (visited on 07/06/2022).

[210] Shuichi Murakami. "Quantum Spin Hall Effect and Enhanced Magnetic Response by Spin-Orbit Coupling". In: *Physical Review Letters* 97.23 (Dec. 2006), p. 236805. DOI: `10.1103/PhysRevLett.97.236805`. URL: `https://link.aps.org/doi/10.1103/PhysRevLett.97.236805` (visited on 06/24/2021).

[211] M. Wada et al. "Localized edge states in two-dimensional topological insulators: Ultrathin Bi films". In: *Physical Review B* 83.12 (Mar. 2011), p. 121310. DOI: `10.1103/PhysRevB.83.121310`. URL: `https://link.aps.org/doi/10.1103/PhysRevB.83.121310` (visited on 06/24/2021).

[212] Zheng Liu et al. "Stable Nontrivial ${Z}_{2}$ Topology in Ultrathin Bi (111) Films: A First-Principles Study". In: *Physical Review Letters* 107.13 (Sept. 2011), p. 136805. DOI: `10.1103/PhysRevLett.107.136805`. URL: `https://link.aps.org/doi/10.1103/PhysRevLett.107.136805` (visited on 06/15/2021).

[213] Zhi-Quan Huang et al. "Nontrivial topological electronic structures in a single Bi(111) bilayer on different substrates: A first-principles study". In: *Physical Review B* 88.16 (Oct. 2013), p. 165301. DOI: `10.1103/PhysRevB.88.165301`. URL: `https://link.aps.org/doi/10.1103/PhysRevB.88.165301` (visited on 07/06/2021).

[214] Dániel Varjas et al. "Computation of topological phase diagram of disordered $\mathrm{Pb}_{1-x}\mathrm{Sn}_x\mathrm{Te}$ using the kernel polynomial method". In: *Phys. Rev. Research* 2 (1 Feb. 2020), p. 013229. DOI: `10.1103/PhysRevResearch.2.013229`. URL: `https://link.aps.org/doi/10.1103/PhysRevResearch.2.013229`.

[215] Thomas D. Kühne et al. "CP2K: An electronic structure and molecular dynamics software package - Quickstep: Efficient and accurate electronic structure calculations". In: *The Journal of Chemical Physics* 152.19 (2020), p. 194103. DOI: `10.1063/5.0007045`. URL: `https://doi.org/10.1063/5.0007045`.